I.R.Iran

ISSN:2423-5547
e-ISSN:2423-7469

Journal of Renewable Energy and Environment

Volume 8, Number 4, Autumn 2021

Materials and Energy Research Center

Iranian Association of Chemical Engineers

ISSN: 2423-5547; e-ISSN: 2423-7469

Journal of Renewable Energy and Environment (JREE): Vol. 8, No. 4, (Autumn 2021), 1-115

CONTENTS

AIMS AND SCOPE

Journal of Renewable Energy and Environment (JREE) publishes original papers, review articles, short communications and technical notes in the field of science and technology of renewable energies and environmental-related issues including:

- Generation
- Storage
- Conversion
- Distribution
- Management (economics, policies and planning)
- Environmental Sustainability

INSTRUCTIONS FOR AUTHORS

Submission of manuscript represents that it had neither been published nor submitted for publication elsewhere and is result of research carried out by author(s). Only the extended and upgraded articles presented in a conference and/or appeared in a symposium proceedings could be evaluated for publication.
Authors are required to include a list describing all the symbols and abbreviations in the paper. Use of the international system of measurement units is mandatory.

- On-line submission of manuscripts results in faster publication process and is recommended. Instructions are given in the JREE web sites: www.jree.ir
- References should be numbered in brackets and appear in sequence through the text. List of references should be given at the end of the paper. All journal articles listed in the References section must follow with article doi.
- Figure captions are to be indicated under the illustrations. They should sufficiently explain the figures.
- Illustrations should appear in their appropriate places in the text.
- Tables and diagrams should be submitted in a form suitable for reproduction.
- Photographs should be of high quality saved as jpg files.
- Tables' illustrations, figures and diagrams will be normally printed in single column width (8 cm). Exceptionally large ones may be printed across two columns (17 cm).

Journal of Renewable Energy and Environment

Research Article

Journal Homepage: www.jree.ir

Green Synthesis of Heteroatom Doped Graphene from Natural and Chemical Precursors for Oxygen Reduction Reaction

Sedigheh Sadegh Hassani [a], Leila Samiee [b*]

[a] *Catalysis Research Division, Research Institute of Petroleum Industry (RIPI), Tehran, Tehran, Iran.*
[b] *Energy Technology Research Division, Research Institute of Petroleum Industry (RIPI), Tehran, Tehran, Iran.*

PAPER INFO

Paper history:
Received 10 November 2020
Accepted in revised form 12 June 2021

Keywords:
Alkaline Fuel Cell,
Fuel Cell,
Graphene,
Electrocatalyst,
Natural Resources

ABSTRACT

In the present work, natural biomass and chemical materials were applied as the heteroatom resources for modifying the Porous Graphene (PG) structure by pyrolysis method at 900 ºC. The physical and chemical characterizatons were performed by means of Scanning Electron Microscopy (SEM), Brunauer–Emmett–Teller (BET), Raman Spectroscopy, N_2 Adsorption-Desorption, and X-ray Photo-electron Spectroscopy (XPS). Furthemore, the behavior of the prepared materials was investigated by Cyclic Voltammetry (CV) and Rotating Disk Electrode (RDE). The obtained results indicated that doping of heteroatoms into the graphene framework was possible using a low-cost and environment-friendly biomass material as well as chemical sources. Moreover, one-step quarternary and tersiary co-doped graphene could be acheived using natural biomass. The prepared electrocatalysts using grape leaves and sulfur trioxide pyridine complex exhibit higher electrocatalytic performance as exampled which conducted the electrocatalyst in $4e^-$ pathway and showed high stability in methanol solutions during the process, confirming their considerable potential to Oxygen Reduction Reaction (ORR) as an electro-catalyst. Moreover, the onset potential of Gl300G-900 and GSP 900 (0.93 V vs RHE) is almost equal to the Pt/C 20 wt % (0.99 V vs RHE). These optimal prepared cathodes (Gl300G-900 and GSP 900) in the Microbial Fuel Cell (MFC) test lead to considerable power densities of 31.5 mW m^{-2} and 30.9.mW m^{-2}, which are close to 38.6 mW m^{-2} for the Pt/C 20 wt % cathode.

https://doi.org/10.30501/jree.2021.255422.1157

1. INTRODUCTION

The demand for sustainable and clean energy technologies has been arising due to the growing energy consumption and environmental pollutions. Fuel cells, supercapasitors, and Li ion batteries as clean energy devices are able to transform the chemical energy to electricity [1, 2].

However, because of such problems as slow electron transfer kinetics for oxygen reduction reaction, this reaction is subject to limitations that cause performance losses [3, 4]. Therefore, development of highly efficient cathodic ORR catalysts is so necessary. Platinum and its derivities are the most active electrocatalysts for the ORR; however, their cost, limited Pt resources, susceptibility to methanol crossover, low durability, and slow electron transfer kinetics for ORR are the challenges that should be considered before large-scale use. Thus, a probe into finding new high-performance non-precious electrocatalyst for ORR has drawn greater interest [5-7].

Recently, for increasing electrical conductivity and activity, heteroatom-doped carbon materials were applied in electrocatalysis ORR, supercapacitors, and metal-air batteries. Doping the heteroatoms such as sulfur, nitrogen, phosphorus, and boron into the graphene nanosheets enhances electrical properties of the grapheneas and effectively creates more active sites in the elecatalyst towards the ORR [8, 9].

Due to the difference between the electronegativity of heteroatoms (N: 3.04, S: 2.58, I: 2.66, B: 2.04) and the carbon base (2.55), the electroneutrality of the adjacent carbon will change [10, 11]. Furthemore, the electronic density of states near the Fermi level will increse. Boron and phosphorus with lower electronegativity than carbon create a partial negative charge on the carbon atom. However, a partial positive charge will be obtained on the adjacent carbon atom. Moreover, upon introducing the heteroatoms in the carbon lattice, the C–C bond length may change, thus making the carbon surfaces asymmetrical and providing more defects as the active sites facilitate the O_2 adsorption during the ORR process [11-13].

Different approaches and many chemicals with high cost and hazardous properties have been used for introducing hetero-atoms within the graphene framework [14, 15]. In situ doping and post-synthesis methods are the two main techniques for doping heteroatoms in the carbon structres. Chemical vapor deposition, arc discharge, solvothermal approach, laser ablation, microwave irradiation, and segregation growth approach are used for insitu method. Thermal treatment of previously prepared carbon in the presence of a heteroatom source and wet chemical approach are the most important techniques for post-synthesis doping.

The details of the advantages and disadvantages of each method have been discussed in the literature. However, the

*Corresponding Author's Email: leila.samiee83@gmail.com (L. Samiee)
URL: http://www.jree.ir/article_131666.html

Please cite this article as: Sadegh Hassani, S. and Samiee, L., "Green synthesis of heteroatom doped graphene from natural and chemical precursors for oxygen reduction reaction", ***Journal of Renewable Energy and Environment (JREE)***, Vol. 8, No. 4, (2021), 1-11. (https://doi.org/10.30501/jree.2021.255422.1157).

post-synthesis doping technique will only lead to surface doping of the structure, while the in situ technique could lead to more homogeneous doping of the carbon material [16].

Moreover, due to economic and safety purpose, a few papers have been focused on green synthesis of ORR electrocatalysts using biomass resources such as mushroom and microalgae *Synechococcus elangatus* for investigating the possibility of introducing heteroatoms to carbon framework [17-19]. Therefore, this paper is focused on some available natural resources including garlic and Grape Leaves (Gl) as new and economic materials for ORR. The electrochemical performances were compared with our last works [19, 20], in which the microalgae Synechococcus elangatus and Sulfur Trioxide Pyridine (STP) complex were applied as the dopants. The studied electrode had superior stability to the conventional 20 wt %/C eletrocatalyst under alkaline conditions.

2. EXPERIMENTAL

2.1. Materials and reagents

The Garlic and grape leaves were obtained from Tehran garden in Iran. The Synechococcus elangatus cyanobacterium was prepared according to our last paper [19]. Sulfur trioxide pyridine complex, Nafion solution (5 wt % in alcohols-water), KOH, HCl (37 %), and Ethanol (99.8 %) were purchased from Sigma-Aldrich Company. Also, Pt/C 20 wt % was also obtained from Sigma-Aldrich Company.

2.2. Synthesis of samples

Porous graphene was synthesized by CVD method and its purification was made possible and used as a conductive support according to the litrature [20, 21]. The doped-graphene was synthasized using micro-algae according to the reported procedure [19]. Homogeneous carbonized microalgae at 300 °C at a ratio of 2:1 was ball milled with porous graphene at 300 rpm for 1 h and pyrolyzed under inert atmosphere at 900 °C for 2 h. The synthesized sample is J300G-900. The garlic and fresh grape leaves as the heteroatom sources were dried at 60 °C in a vacuum drying oven. The dried powders were ground into fine powder and carbonized at 300 °C, separately.

Homogeneous carbonized powders of these two natural sorces at a mass ratio of 2:1 were mixed with graphene and ground by ball-mill at 300 rpm for 1 h. The produced mixtures (Grape leaves@graphene and garlic@graphene) were subsequently pyrolyzed under N_2 atmosphere in a furnace at 900 °C for 2 h to synthesize a heteroatom-doped graphene Gl300G-900 and S300G-900, respectively. The PG and sulfur trioxide pyridine complex were mixed and dried according to our last work [20]. The dried powder was ground and pyrolyzed in the N_2 atmosphere at 900 °C for 2 h. The catalysts synthesized in this condition will be here referred with GSP 900. The overall synthesis process is shown in Figure 1.

3. METHOD

3.1. Methodology

3.1.1. Characterizations techniques

A Kemiat DX-27 device using CuK_α radiation was applied to obtain the XRD pattern between 10-80°. FESEM Mira-TSCAN equipped EDS mapping was used for morphology analysis. The nitrogen adsorption/desorption experiment was applied using a micromeritics Tristar 3000 instrument. The Raman spectroscopy Almega Thermo Nicolet with an Ar ion laser source (514 nm) was used. Furthermore, XPS Model 5700 by Al Kα (1486.6 eV photons) was utilized for surface chemical composition determination. Multipak™ software package was used for data processing and a Shirley background subtraction routine was applied throughout.

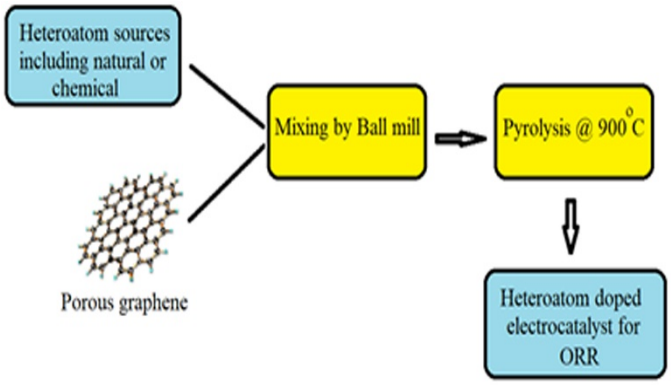

Figure 1. Schematic of heteroatom-doped graphene synthesis

3.1.2. Electrochemical measurements

A three-electrode Autolab potentiostat/galvanostat was applied to electrochemical evaluation. The Ag/AgCl and platinum wire were utilized as the reference and counter electrodes, respectively.

A 5 mg mL^{-1} suspension was prepared using sonicating of electrocatalyst in a ethanol-nafion solution for 30 minutes and pipetted onto glassy carbon electrode as a working electrode and dried in air at 60 °C to obtain 0.3 mg cm^{-2} electrocatalyst loading on the glassy carbon electrode.

Linear sweep voltammetry using a rotating disk electrode was applied in the O_2-saturated 0.1 M KOH solution (pH=13) in the potential ranges from -1 to 0.2 V at a scan rate of 5 mV s^{-1} and different rpms. Electron transfer was calculated using the Koutecky–Levich equation. Moreover, cyclic voltammetry tests were measured at a scan rate of 50 mV/s within a voltage range of 0.2 V to -1.0 V (vs. Ag/AgCl electrode).

4. RESULTS AND DISCUSSION

4.1. Electrochemical evaluation

4.1.1. Cyclic voltammetric results

The electrocatalytic evaluation of the synthesized electrocatalyst including chemical and natural pecursors (Gl300G-900, S300G-900 and J300G-900 and GSP 900) was conducted using CV in the O_2 saturated 0.1 M KOH solution and the results were compared with Pt/C 20 wt % and PG samples (Figure 2).

The onset potential of PG in the ORR (after about 20 CV cycles) was about 0.82 V (versus RHE), where the oxygen reduction peak appeared approximately at 0.73 V (versus RHE). All the prepared samples showed ORR reduction peak with greater intensity, improved onset potential, and increased peak current density than porous graphene. These obtained results showed that catalyst performance could be boosted by doping heteroatom into the graphene structure.

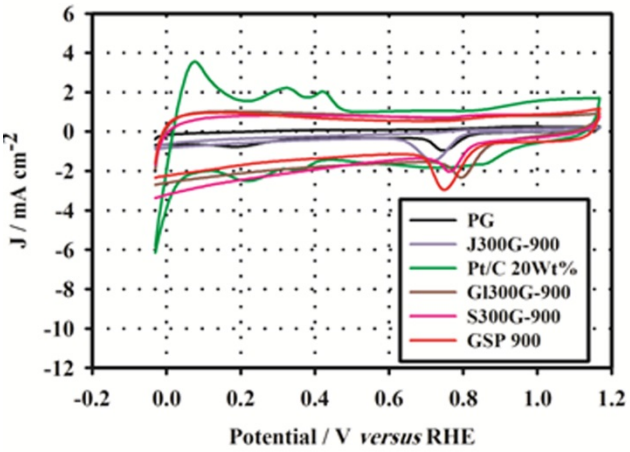

Figure 2. CV of samples for ORR in O_2 saturated 0.1 M KOH at a sweep rate of 50 mV/s on the: S300G-900, J300G-900, Gl300G-900, GSP 900 PG and Pt/C 20 wt %, electrodes

4.1.2. Rotating disk electrode test

The electrocatalytic performance of the synthesized samples was studied using an RDE in the range rotation speeds of 250 to 3500 rpm. Furthermore, the Koutechy–Levich equation was used to determine the number of electron transfer involved in the ORR. These equations are illustrated in the following [22, 23]:

$$\frac{1}{j} = \frac{1}{j_k} + \frac{1}{j_d} = \frac{1}{j_k} + \frac{1}{B\omega^{1/2}} \quad (1)$$

$$j_d = 0.62\, n \times F \times (C_0) \times (D_0)^{\frac{2}{3}} \times (A)^{\frac{-1}{6}} = B\omega^{\frac{1}{2}} \quad (2)$$

$$B = 0.62\, n \times F \times (C_0) \times (D_0)^{\frac{2}{3}} \times (A)^{\frac{-1}{6}} \quad (3)$$

The measured current density, diffusion, and kinetic limiting current densities are shown with J, J_L and J_K, respectively. F is the Faraday constant (96485 C/mol); n and ω are the electron transfer number and the rotation speed (rpm), respectively. Furthermore, the bulk concentration of O_2 (C_0), the diffusion coefficient of oxygen (D_0) in 0.1 M KOH as electrolyte, and kinetic viscosity (ν) are 1.2×10^{-6} mol/cm^3, 1.9×10^{-5} cm^2/s, and 0.01 cm^2/s, respectively.

The J^{-1} versus $\omega^{-0.5}$ plots in the potential range of 0.45 to 0.65 (V vs RHE) are shown in Figure 3 and Table 1, suggesting both $2e^-$ and $4e^-$ for ORR in different electrocatalysts. The heteroatom-doped graphenes Gl300G-900 and GSP 900 as the synthesized samples using grape leaves and sulfur trioxide pyridine complex show reasonable selectivity to the 4 electron reaction pathway and improved onset potential in an alkaline electrolyte, respectively.

LSV curves for electrocatalysts in the O_2 saturated 0.1 M KOH electrolyte at a scan rate of 5 mv/s and a rotation rate of 1500 compared to Pt/C 20 wt % and PG are shown in Figure 4.

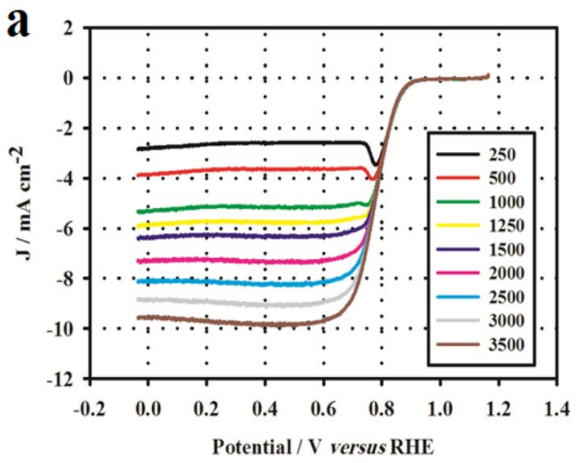

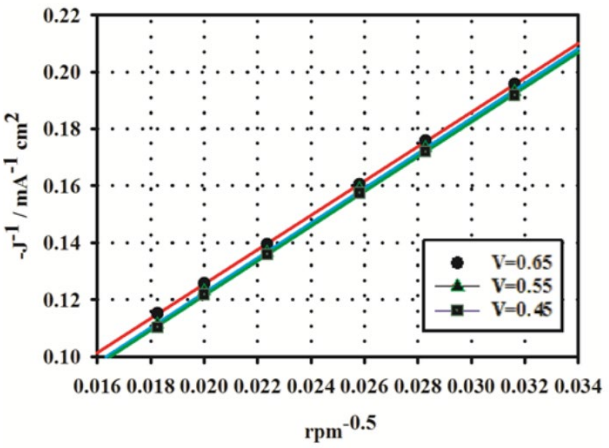

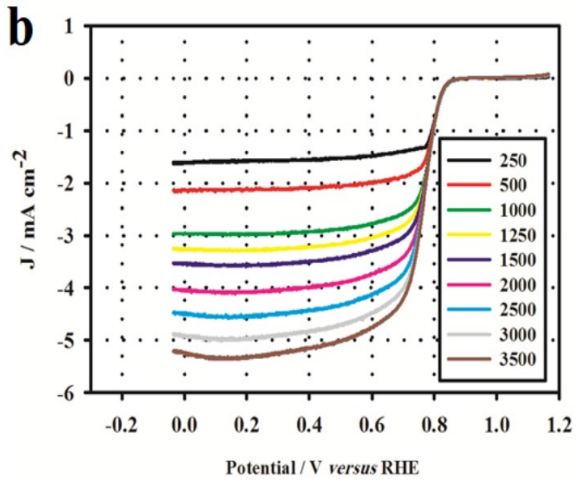

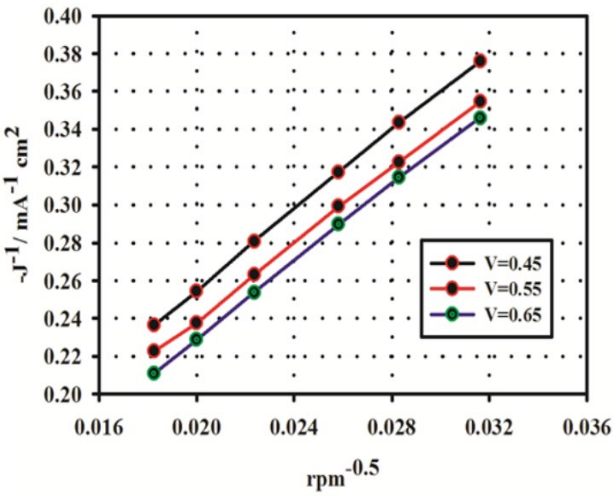

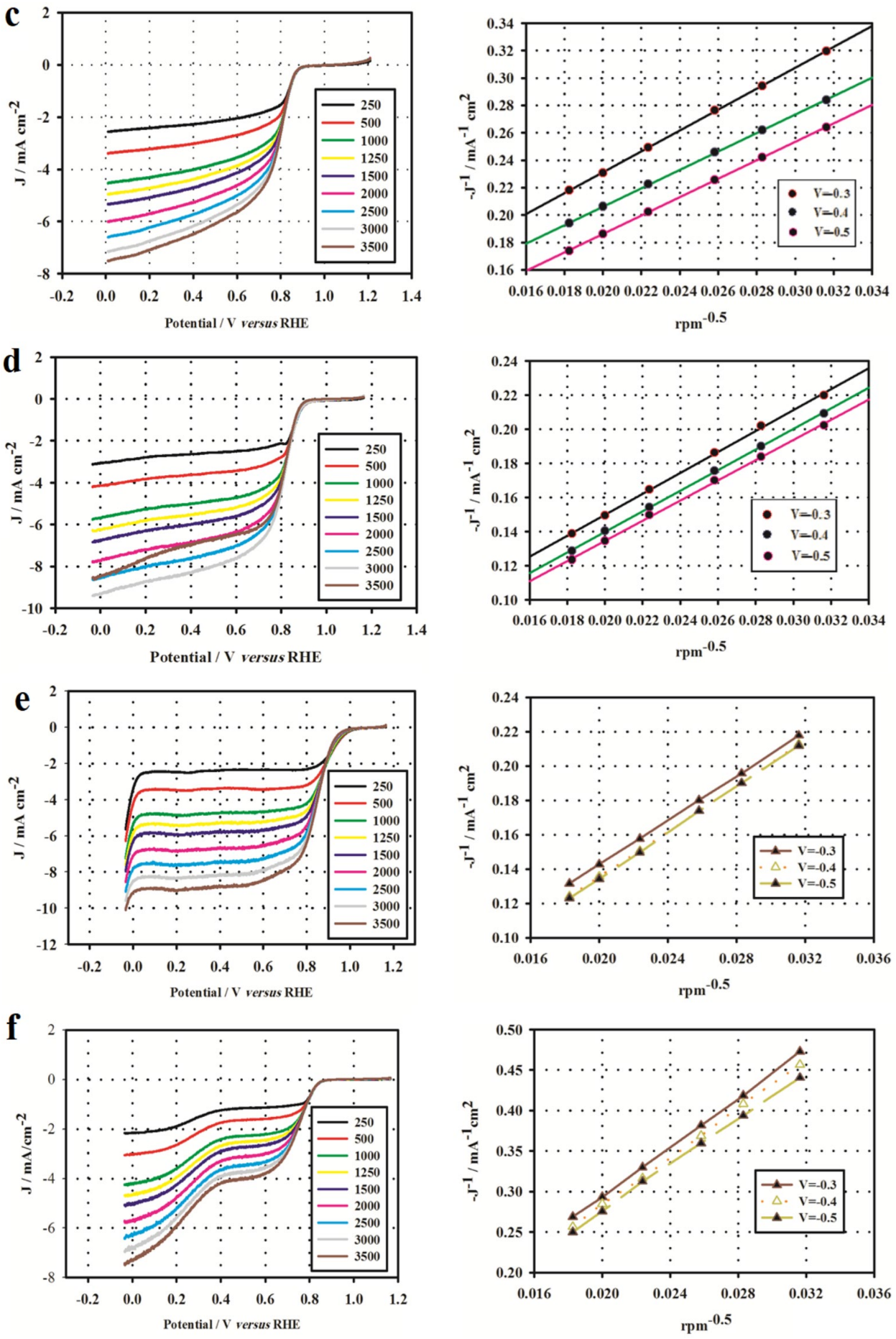

Figure 3. LSV at different rpm in KOH 0.1 M (scan rate 5 mV/s) and their Koutecky–Levich plots at different potentials for: GSP 900 (a), J300G-900 (b), S300G-900 (c), GI300G-900 (d), Pt/C 20 wt % (e), and PG (f)

Table 1. The current density, onset potential, and electron transfer number of electrocatalysts

Electrocatalysts	Electron transfer Number (n)	Onset potential (V vs RHE)	Steady state current density (mA/cm^2)
S300G-900	4.0	0.90	-5.4
Gl300G-900	4.0	0.93	-6.81
J300G-900	2.9	0.89	-3.52
GSP 900	4.1	0.93	-6.39
PG	2.2	0.85	-2. 70
Pt/C 20 wt %	4.0	0.99	-5.88

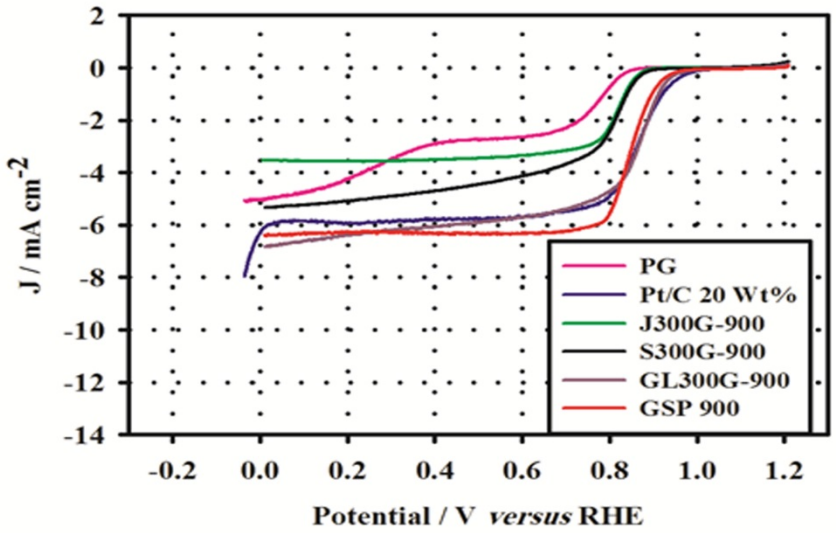

Figure 4. The LSV of electrocatalysts at 1500 rpm in O_2 saturated 0.1 M KOH

The PG electrode exhibited an ORR onset potential of almost 0.85 V (RHE). However, the onset potential of Gl300G-900, S300G-900 and J300G-900 electrodes was approximately 0.93, 0.93, and 0.89 V, which are more positive than PG. It can be suggested that due to the probability of heteroatom doping, the active sites of the synthesized electrocatalysts are enhanced and ORR is conducted in 4 electron pathways. The current density, onset potential, and electron transfer numbers of the synthesized electrocatalysts and Pt/C 20 wt % are compared in Table 1.

The electron transfer number of Gl300G-900, S300G-900, J300G-900, and GSP 900 samples in the ORR process was 4, 4, 2.9, and 4.1, respectively. The onset potential of Gl300G-900 and GSP 900 electrocatalysts is close to the Pt/C 20 wt %, and oxygen reduction is conducted via 4e$^-$ pathway, too. The improved ORR electrocatalytic performance of heteroatom-doped samples can be explained by charge polarization according to quantum mechanics calculations. The changes in bond length, electronegativity, and one more extra electron (in the nitrogen atom) make in the carbon atom surface asymmetrical and cause more defects for the structures, which act as the active sites for the ORR. It should be mentioned that through multiple doping and by introducing more heteroatoms in the carbon structure, it is quite important to locate heteroatoms in specific (unique) positions and form suitable bonds such as the B-C–N in the Gl300-G900 sample in addition to individual effects [11].

4.1.3. Stability in the methanol solution

Morover, the catalytic current of the synthesized electrocatalyst (Gl300G-900, S300G-900, J300G-900 and GSP 900), Pt/C 20 wt %, and PG before and after methanol (1 M) addition in the ORR test were investigated, as shown in Figure 5.

The results represented that after methanol addition, the ORR peaks of PG and Pt/C 20 wt % electrocatalysts are reduced and disappeared, respectively. However, the CV measurements showed the stable and relatively unchanged hydrogen reduction peaks of the prepared doped electocatalysts after several CV cycles upon methanol addition, which represents good tolerance against crossover effects and remarkable stability in the doped electrocatalysts.

4.2. Structural characterization

The Gl300G-900 and GSP 900 heteroatom-doped samples were selected for structural analysis due to their improved electrochemical properties. The heteroatom doping level and defects in the graphene frameworke could be recognized using Raman spectroscopy.

Graphene displays three main peaks in Raman spectrum: G band (~1580 cm^{-1}) related to sp^2 carbon atoms vibrations as well as D (~1350 cm^{-1}) and 2D (~2680 cm^{-1}) bands corresponded to disordered sp^2 carbon atoms and defects due to introduced heteroatoms into its structure [24, 25]. The diordering and defects of the graphene structure could be defined as higher value of I_D/I_G (ratio of D to G band intensities).

The I_D/I_G values of PG, Gl300G-900, and GSP 900 samples are shown in Table 2. The higher values of I_D/I_G for Gl300G-900 (1.17) and GSP 900 (1.17) than PG (0.96) imply high disordering or defects level in the structure of the doped samples, leading to greater oxygen adsorption [25-27].

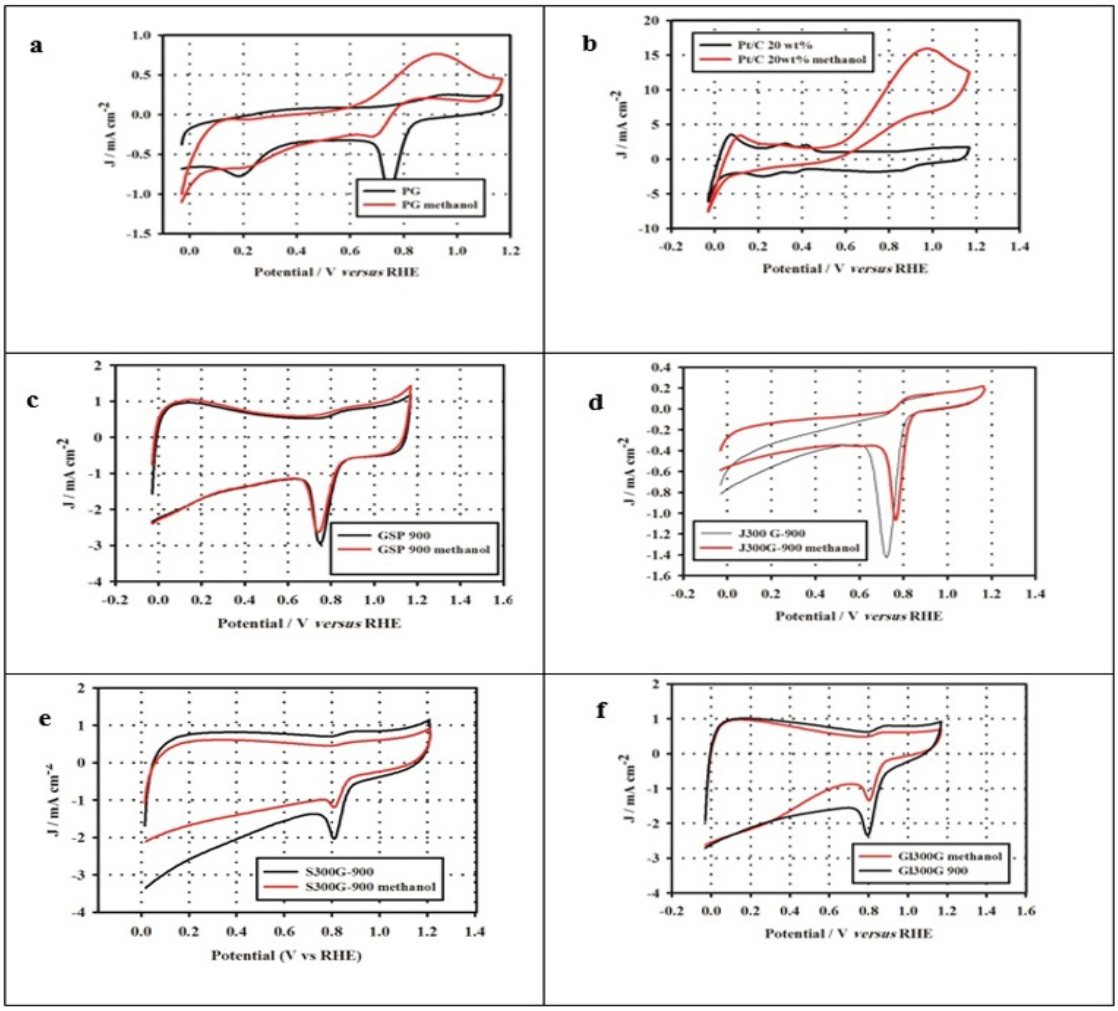

Figure 5. Cyclic voltammetry of (a) PG, (b) Pt/C 20 wt%, (c) GSP 900, (d) J300G-900, (e) S300-900, and (f) Gl300G-900 in KOH 0.1 M (scan rate: 50 mV/sec) by adding methanol

Table 2. Raman specification of the PG and heteroatom co-doped graphene

Sample	G band (cm^{-1})	D band (cm^{-1})	2D band (cm^{-1})	I_D/I_G
PG	1577.2	1341.85	2681.17	0.96
GSP 900	1577.12	1343.99	2679.13	1.17
Gl300G-900	1577.12	1343.99	2679.13	1.17

Fig. 6-a shows N_2 adsorption isotherms of PG and doped samples including Gl300G-900 and GSP 900. Typical type-IV isotherms with a loop beginning at the relative pressure approximately 0.4 were obtained, demonstrating that these materials have slit-shaped mesopores on the graphene structure [28]. Moreover, the average pore size distributions of the prepared electrocatalysts are given in Fig. 6-b. Also, the textural properties of the Gl300G-900 and GSP 900 electrocatalysts are shown in Table 3 and then, are compared to that of PG.

Moreover, the surface morphology and EDX image mapping analysis of the natural and chemical heteroatom doped samples (Gl300G-900 and GSP 900) were observed by FESEM (Fig. 7). The morphology of the prepared sample are similar to that of the graphene base. The elemental mapping distribution supports nitrogen, sulfur, boron, and phosphorous uniform dispersions in the pyrolyzed grape leaves sample, and the sample prepared using sulfur trioxide pyridine complex showed the presence of sulfur and nitrogen in the carbon structure.

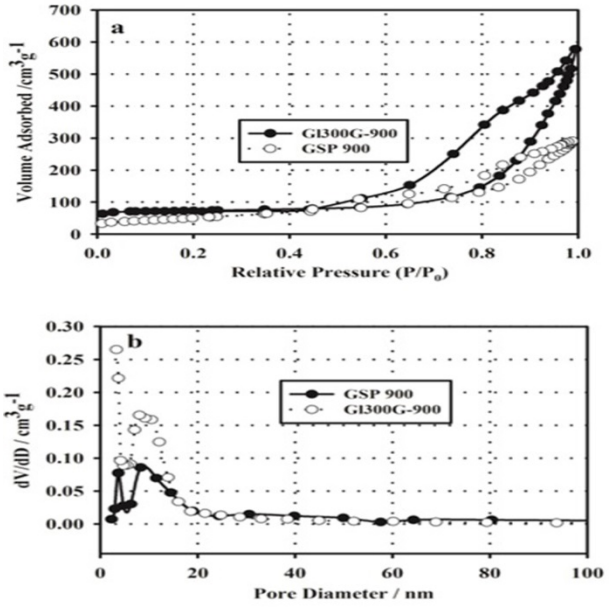

Figure 6. N_2 adsorption isotherms of PG and doped graphene (a), Pore size distribution of samples (b)

Table 3. Physical properties of PG and doped graphene

Electrocatalysts	BET surface area (m^2g^{-1})	Pore volume (cm^3g^{-1})	Mean pore size (nm)
PG	629.3	2.03	12.9
Gl300G-900	243.4	0.8	12.5
GSP 900	187.7`	0.44	9.7

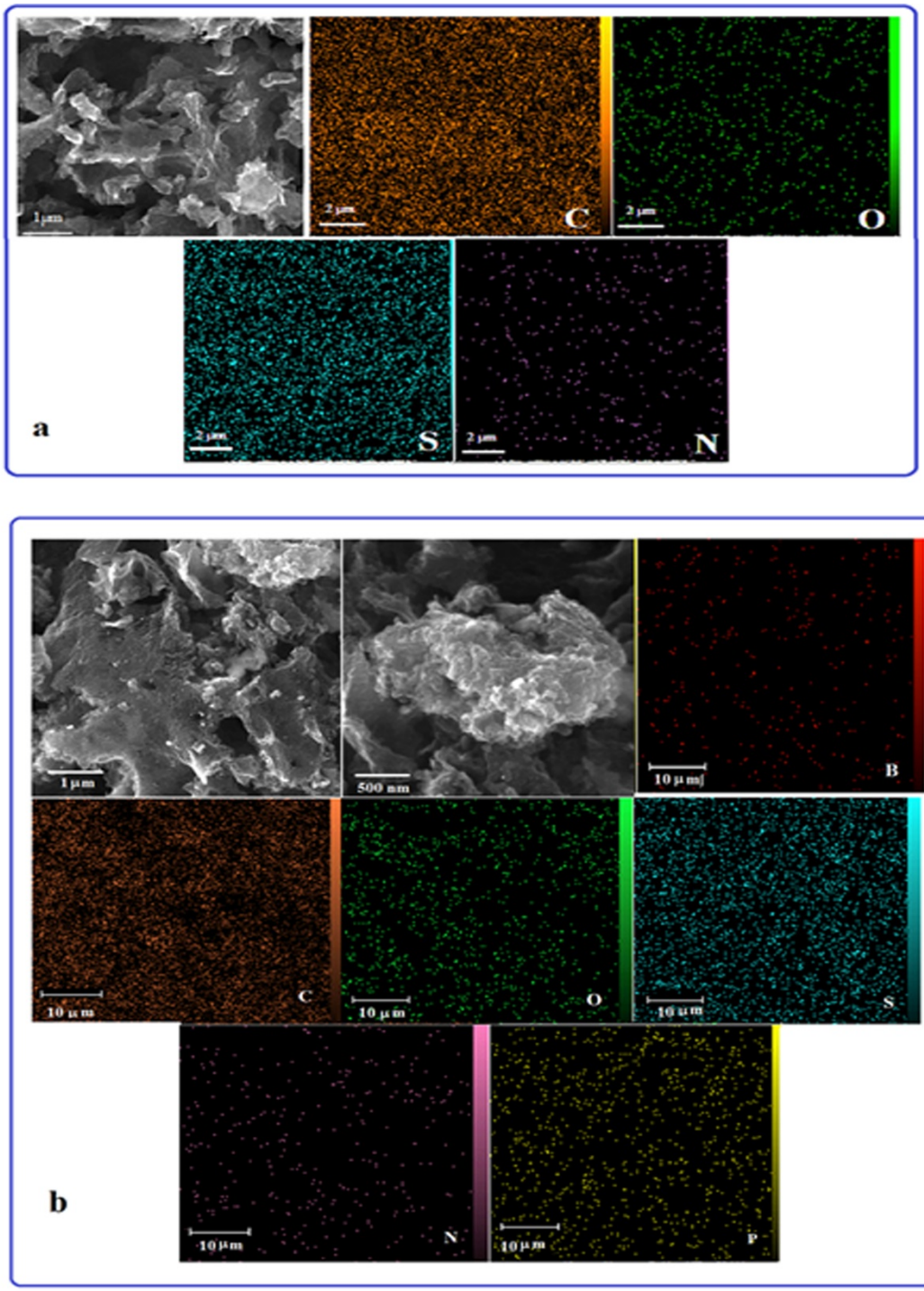

Figure7. FESEM micrographs of prepared samples in two magnification and EDX mapping analysis of Carbon, Oxygen, sulfur, nitrogen, Boron, and Phosphorus in (a) the GSP 900, (b) the Gl300G-900 samples

In addition, the XPS analysis was applied to investigate the chemical bonding of the prepared samples, Gl300G-900 and GSP 900. Figure 8 shows that all the samples were included with a predominant narrow graphitic C 1s peak at approximately 284.4 eV.

Also, the adsorbed oxygen was seen in the samples as an O 1s peak at ~530 eV due to the physical incorporation of O_2 in the graphene framework. Moreover, the Gl300G-900 sample represents N 1s, S 2p, P 2p, and B1s peaks at ~400 eV, ~165 eV, ~133 eV, and ~190 eV, respectively. However, the GSP 900 sample shows only N 1s and S 2p peaks at approximately ~400 eV and ~165 eV, respectively.

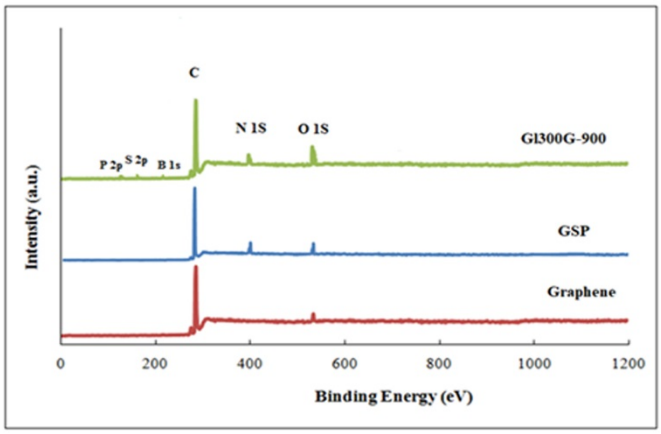

Figure 8. XPS survey for PG and as-synthesized samples

In addition, the high resolution XPS spectra for all the doped elements in GSP 900 and Gl300G900 samples are shown in Fig. 9 (a-b).

The pyridinic (~398.5 eV) and pyrrolic (~400.6 eV) species as the important phases with a nitrogen level of 2 % (at a ratio of 60 and 35 %, respectively) can be deconvluted from the high resolution N 1s XPS spectra in GSP 900 sample. Moreover, 5 % of the total N is present as oxidized forms (~403.2 eV) [1, 24, 29].

This result is important because pyridinic and graphitic species are suggested as the main ORR active sites due to allocation of one extra electron to the aromatic ring [29].

Also, three different peaks at approximately 163.8 (85 %), 165.0 (10 %), and 168.8 (5 %) were observed in the high-resolution S 2p spectra, which are related to C-S_n-C, C=S, sulfoxide specieses in the graphene framework [29-31]. In the high resolution spectrum of Gl300G-900, a strong S 2p peak (Fig. 9-b) shows a significant number of S doped atoms. Besides, the deconvolution analysis represents similar peaks of GSP 900 sample; however, at different intensities, around 46 % of sulfur in the Gl300G-900 sample appears in the sulfoxide forms in the graphene framework [29].

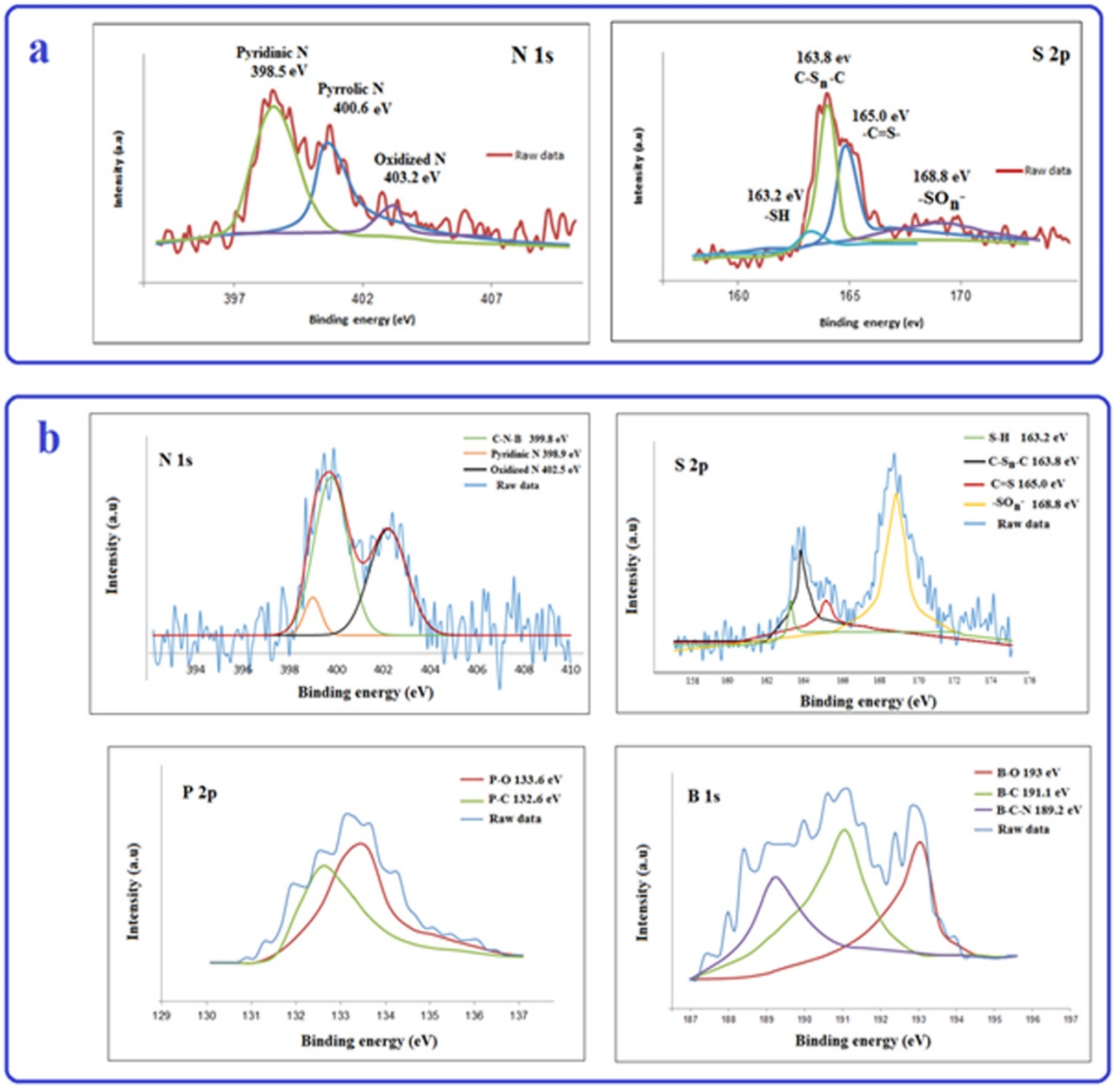

Figure 9. The HR-XPS spectra of prepared doped sample a:GSP 900, b:Gl300G-900

The HR-XPS of N 1s spectra of the Gl300G-900 sample can be resolved into three main peaks (Figure 9-b), related to pyridinic N (398.9 eV), nitrogrn in the N–B–C configuration (399.8 eV), and pyridinic N-oxide (402.5 eV) species [32-35].

The high resolution of B1s at approximately 193 eV (Fig. 9-b) is attributed to boron oxide. Also, the peak of 191 eV represents successful incorporation of boron atoms into the graphene framework. In this regard, the deconvolution

analysis of B1s shows three sub-peaks: B-C-N (189.2 eV), B-C (191.1 eV), and B-O (193 eV) bonds [32]. The XPS results confirm that N and B are covalently bound to the carbon in graphene structure, and N and B are covalently bound to each other (B–N bond) according to the peak of approximately 189.2 eV.

Moreover, deconvolution analysis of P 2p of Gl300G-900 (Fig. 9-b) represents the P-O and P-C binding energy peaks at approximately 133.6 eV and 132.6 eV, respectively, showing the P-doping feature [10]. The XPS results of element concentration, peaks position, and chemical state in the Gl300G-900 and GSP 900 samples are shown in Table 4.

Table 4. The XPS results of element concentration, peaks position, and chemical states in Gl300G-900 and GSP samples

Electrocatalyst	Element	%	Binding energy (eV)	Chemical state (%)
Gl300G-900	C	88.8		
	N	2.0	398.2 399.8 402.5	~10 % ~50 % ~40 %
	S	1.5	163.2 163.67 165.00 168.53	~7 % ~34 % ~13 % ~46 %
	B	1.2	191.1 193 189.2	~42 ~30 ~28
	P	0.7	133.6 132.6	~64 ~36
	O	5.8		
GSP 900	C	93.1	284.4	
	N	2.0	398.5 400.6 403.2	~60 % ~35 % ~5 %
	O	4.0		
	S	0.9	163.8 165.0 168.8	~85 % ~10 % ~5 %

The XPS results indicate that sulfur, nitrogen, phosphorus, and boron are incorporated into the graphene framework. Therefore, heteroatoms have been successfully quaternary doped in the graphene framework and bound to carbon using high-temperature pyrolysis method [36].

4.3. Evaluation using microbial fuel cell

Furthermore, the optimal natural and chemical synthesized electrocatalysts (Gl300G-900 and GSP 900) were evaluated in the Microbial Fuel cell. In this regard, by changing external resistance from OCP to 4700, 3900, 3300, 2700, 2200, 1500, 1000, 910, 680, 510, 390 Ω, the polarization curves were obtained and the related voltages were recorded.

Figure 10 shows power density and steady state polarization curves for the Gl300G-900 and GSP 900 electrocatalysts in the MFC and the results are compared with the Pt /C 20 wt % and bare PG and electrocatalysts. The obtained results showed that the OCPs of the fuel cell with Gl300G-900, GSP 900, PG, and Pt/C 20 wt % electrocatalysts were 522 mV, 545 mV, 515 mV, and 647 mV, respectively. The Gl300G-900 and GSP 900 as the optimal synthesized cathodes in the MFC test showed high power density peaks of 31.5 mW m^{-2} and 30.9 mW m^{-2}, respectively, with much higher power density than the PG (18.0 mV m^{-2}) and close to the Pt/C 20 wt % (38.6 mW m^{-2}) cathodes, confirming the improved efficiency of these electrodes.

The increased power density of the prepared electrocatalysts using grape leaves as a natural source (Gl300G-900) compared to the PG could be explained because of simultaneous doping of S, N, P, and B into the carbon framework and their synergetic effects. Also, the improved power density of the prepared sample using chemical source (GSP) compared to the PG was acheived due to the doping of S and N into the graphene framework.

Therefore, it is proposed that co heteroatom doping to the graphene structure leads to increase in the number of active sites and the electrocatalysts with improved performance as cathod catalysts could be obtained using natural and chemical sources.

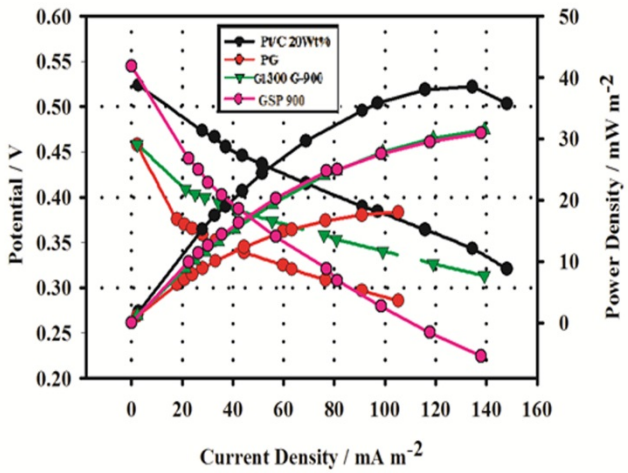

Figure 10. Power density and polarization and curves of MFC of the Gl300G-900 and GSP 900 samples at 25 ºC compared to the Pt/C 20 wt % and PG

5. CONCLUSIONS

This paper represents the preparation and characterization of heteroatoms-codoped porous graphene using garlic, grape leaves, microalgae Synechococcus elangatus, and sulfur trioxide pyridine complex. The optimal prepared electrocatalysts (Gl300G-900 and GSP 900) showed tolerance against methanol addition and long-term stability compared to the Pt/C 20 wt % and PG, with the onset potential and electron transfer number (0.93 vs RHE and 4.0) and (0.93 vs RHE and 4.1), respectively.

The electrochemical performance of the heteroatoms co-doped graphene (i.e., Gl300G-900 and GSP 900) represented high homogeneity of heteroatoms dispersion in the graphene framework, as well as a comparatively ORR performance versus Pt/C 20 wt %. The onset potential rates of the optimized electrocatalysts prepared using grape leaves (biomass resource) and sulfur trioxide pyridine complex (chemical source) were approximately 0.93 V vs RHE, being almost equal to Pt/C 20 wt % (0.99 V vs RHE). Furthermore, these electrocatalysts with excellent resistance towards methanol crossover effects conducted alkaline ORR in $4e^-$ electron transfer pathway. Thus, the prepared electrocatalysts using grape leaves and sulfur trioxide pyridine complex are good candidates for ORR at low-temperature fuel cells instead of precious metal-based electrocatalysts due to its low cost and good performance. Moreover, grape leaves as an economic, safe, and environment-friendly precursor that include suitable heteroatoms with capability to introduce graphene structure seem to be valuable biomass materials for replacing Pt-based catalyst in large-scale commercialization.

6. ACKNOWLEDGEMENT

We would like to acknowledge the support made available by the Research Institute of Petroleum Industries (RIPI).

REFERENCES

1. Zhang, H., Wang, Y., Wang, D., Li, Y., Liu, X., Liu, P., Yang, H., An, T., Tang, Z. and Zhao, H., "Hydrothermal transformation of dried grass into graphitic carbon based high performance electrocatalyst for oxygen reduction reaction", ***Small***, Vol. 10, (2014), 3371-3378. (https://doi.org/10.1002/smll.201400781).
2. Li, Y., Zhou, W., Wang, H., Xie, L., Liang, Y., Wei, F., Pennycook, S.J. and Dai, H., "An oxygen reduction electrocatalyst based on carbon nanotube-graphene complexes", ***Nature Nanotechnology***, Vol. 7, (2012), 394-400. (https://doi.org/10.1038/nnano.2012.72).
3. Sui, S., Wang, X., Zhou, X., Su ,Y., Riffat, S. and Liu, C.J., "A comprehensive review of Pt electrocatalysts for the oxygen reduction reaction: Nanostructure, activity, mechanism and carbon support in PEM fuel cells", ***Journal of Material Chemistry A***, Vol. 5, (2017), 1808-1825. (https://doi.org/10.1039/C6TA08580F).
4. Gupta, C., Maheshwari, P.H. and Dhakate, S.R., "Development of multiwalled carbon nanotubes platinum nanocomposite as efficient PEM fuel cell catalyst", ***Materials for Renewable and Sustainable Energy***, Vol. 5, (2016), 1-11. (https://doi.org/10.1007/s40243-015-0066-5).
5. Workman, M.J., Dzara, M., Ngo, C., Pylypenko, S., Serov, A., McKinney, S., Gordon, J., Atanassov, P. and Artyushkov, K., "Platinum group metal-free electrocatalysts: Effects of synthesis on structure and performance in proton-exchange membrane fuel cell cathodes", ***Journal of Power Sources***, Vol. 384, (2017), 30-39. (https://doi.org/10.1016/j.jpowsour.2017.02.067).
6. Venkateswara Rao, C., Cabrera, C.R. and Ishikawa, Y., "In search of the active site in nitrogen-doped carbon nanotube electrodes for the oxygen reduction reaction", ***Journal of Physical Chemistry Letters***, Vol. 1, (2010), 2622-2627. (https://doi.org/10.1021/jz100971v).
7. Cheon, J.Y., Ahn, C., You, D.J., Pak, C., Hur, S.H., Kim, J. and Joo, S.H., "Ordered mesoporous carbon–carbon nanotube nanocomposites as highly conductive and durable cathode catalyst supports for polymer electrolyte fuel cells", ***Journal of Material Chemistry A***, Vol. 1, No. 4, (2012), 1270-1283. (https://doi.org/10.1039/C2TA00076H).
8. Jafri, R.I., Rajalakshmi, N. and Ramaprabhu, S., "Nitrogen-doped multi-walled carbon nanocoils as catalyst support for oxygen reduction reaction in proton exchange membrane fuel cell", ***Journal of Power Sources***, Vol. 195, (2010), 8080-8083. (https://doi.org/10.1016/j.jpowsour.2010.06.109).
9. Zhang, H., Chen, J., Li, Y., Liu, P., Wang, Y., An, T. and Zhao, H., "Nitrogen-doped carbon nanodots@nanospheres as an efficient electrocatalyst for oxygen reduction reaction", ***Electrochimica Acta***, Vol. 65, (2015), 7-13. (https://doi.org/10.1016/j.electacta.2015.02.240).
10. Qiao, X., Liao, S., You, C. and Chen, R., "Phosphorus and nitrogen dual doped and simultaneously reduced graphene oxide with high surface area as efficient metal-free electrocatalyst for oxygen reduction", ***Catalysts***, Vol. 5, (2015), 981-991. (https://doi.org/10.3390/catal5020981).
11. Sadegh Hassani, S. and Samiee, L., Carbon nanostructured catalysts as high efficient materials for low temperature fuel cells, Hanbook of ecomaterials, Springer International Publishing, (2018). (https://doi.org/10.1007/978-3-319-48281-1_79-1)..
12. Arjmandi-Tash, H., Belyaeva, L.A. and Schneider, G.F., "Single molecule detection with graphene and other two-dimensional materials: nanopores and beyond", ***Chemical Society Reviews***, Vol. 45, (2015), 476-493. (https://doi.org/10.1039/C5CS00512D).
13. Palaniselvam, T., Valappil, M.O., Illathvalappil, R. and Kurungot, S., "Nanoporous graphene by quantum dots removal from graphene and its conversion to a potential oxygen reduction electrocatalyst via nitrogen doping", ***Energy & Environmental Sciences***, Vol. 7, No. 3, (2014), 1059-1067. (https://doi.org/10.1039/c3ee43648a).
14. Rivera, L.M., Fajardo, S., Arévalo, M.D.C., García, G. and Pastor, E., "S and N-doped graphene nanomaterials for the oxygen reduction reaction", ***Catalysts***, Vol. 7, No. 9, (2017), 278-290. (https://doi.org/10.3390/catal7090278).
15. Wang, X., Sun, G., Routh, P., Kim, D.H., Huang, W. and Chen, P., "Heteroatom-doped graphene materials: Syntheses, properties and applications", ***Chemical Society Reviews***, Vol. 43, (2014), 7067-7098. (https://doi.org/10.1039/C4CS00141A).
16. Daems, N., Sheng, X., Vankelecom Ivo, F.J. and Pescarmona, P.P., "Metal-free doped carbon materials as electrocatalysts for the oxygen reduction reaction", ***Journal of Material Chemistry A***, Vol. 2, (2014), 4085-4110. (https://doi.org/10.1039/C3TA14043A).
17. Guo, C., Liao, W., Li, Z., Sun, L. and Chen, C., "Easy conversion of protein-rich enoki mushroom biomass to nitrogen-doped carbon nanomaterial as a promising metal-free catalyst for oxygen reduction reaction", ***Nanoscale***, Vol. 7, No. 38, (2015), 15990-15998. (https://doi.org/10.1039/C5NR03828F).
18. Guo, C., Sun, L., Liao, W. and Li, Z., "The use of an edible mushroom-derived renewable carbon material as a highly stable electrocatalyst towards four-electron oxygen reduction", ***Materials***, Vol. 9, No. 1, (2016), 1-11. (https://doi.org: 10.3390/ma9010001).
19. Sadegh Hassani, S., Ziaedini, A., Samiee, L., Dehghani, M., Mashyekhi, M. and Faramarzi, M.A., "One step synthesis of tertiary co-doped graphene electrocatalyst using microalgae synechococcus elangatus for applying in microbial fuel cell", ***Fuel Cells***, Vol. 19, No. 5, (2019), 623-634. (https://doi.org/10.1002/fuce.201800167).
20. Sadegh Hassani, S., Ganjali, M.R., Samiee, L., Rashidi, A.M., Tasharrofi, S., Yadegari, A., Shoghi, F. and Martel, R., "Comparative study of various types of metal free N and S co-doped porous graphene for high performance oxygen reduction reaction in alkaline solution", ***Journal of Nanoscience and Nanotechnology***, Vol. 18, (2018), 4565-4579. (https://doi.org/10.1166/jnn.2018.15316).
21. Pourmand, S., Abdouss, M. and Rashidi, A.M., "Preparation of via nanoporous zinc oxide and its application as a nano adsorbent for benzene, toluene and xylenes removal", ***International Journal of Environmental Research***, Vol. 9, (2015), 1269-1276. (https://doi.org/10.22059/IJER.2015.1018).
22. Qu, L.T., Liu, Y., Baek, J.B. and Dai, L.M., "Nitrogen-doped graphene as efficient metal-free electrocatalyst for oxygen reduction in fuel cells", ***ACS Nano***, Vol. 4, (2010), 1321-1326. (https://doi.org/10.1021/nn901850u).
23. Lin, Z., Waller, G., Liu, Y. and Wong, C.P., "3D nitrogen-doped graphene prepared by pyrolysis of graphene oxide with polypyrrole for electrocatalysis of oxygen reduction reaction", ***Nano Energy***, Vol. 2. (2013), 241-248. (https://doi.org/10.1016/j.nanoen.2012.09.002).

24. Xing, Z., Ju, Z., Zhao, Y., Wan, J., Zhu, Y., Qiang, Y. and Qian, Y., "One-pot hydrothermal synthesis of nitrogen-doped graphene as high-performance anode materials for lithium ion batteries", ***Scientific Reports***, Vol. 6, (2016), 26146-26158. (https://doi.org/10.1038/srep26146).
25. Ai, W., Luo, Z., Jiang, J., Zhu, J., Du, Z., Fan, Z., Xie, L., Zhang, H., Huang, W. and Yu, T., "Nitrogen and sulfur codoped graphene: multifunctional electrode materials for high performance Li ion batteries and oxygen reduction reaction", ***Advanced Materials***, Vol. 26, (2014), 6186-6192. (https://doi.org/10.1002/adma.201401427).
26. Sun, Z., Masa, J., Weide, P., Fairclough, S.M., Robertson, A.W., Ebbinghaus, P., Warner, F.H., Tsang, S.C.E., Muhlerb, M. and Schuhmann, W., "High-quality functionalized few-layer graphene: facile fabrication and doping with nitrogen as a metal-free catalyst for the oxygen reduction reaction", ***Journal of Material Chemistry A***, Vol. 3, (2015), 15444-15450. (https://doi.org/10.1039/C5TA02248G).
27. Brunauer, S., Deming, L.S., Deming ,W.E. and Teller, E., "On a theory of the van der Waals adsorption of gases", ***Journal of the American Chemical Society***, Vol. 62, No. 7, (1940), 1723-1732. (https://doi.org/10.1021/ja01864a025).
28. Ma, C.B., Zhu, Z.T., Wang, H.X., Huang, X., Zhang, X., Qi, X., Zhang, H.L., Zhu, Y., Deng, X., Peng, Y., Hand, Y., Zhang, H. and Lu, L., "Covalent entrapment of cobalt–iron sulfides in N-doped mesoporous carbon: Extraordinary bifunctional electrocatalysts for oxygen reduction and evolution reactions", ***ACS Applied Materials & Interfaces***, Vol. 7, (2015), 1207-1218. (https://doi.org/10.1021/am507033x).
29. Wu, Z.S., Yang, S., Sun, Y., Parvez, K., Feng, X. and Mullen, K., "3D nitrogen-doped graphene aerogel-supported Fe_3O_4 nanoparticles as efficient electrocatalysts for the oxygen reduction reaction", ***Journal of the American Chemical Society***, Vol. 134, (2012), 9082-9085. (https://doi.org/10.1021/ja3030565).
30. Bag, S., Mondal, B., Das, A.K. and Raj, C.R., "Nitrogen and sulfur dual-doped reduced graphene oxide: Synergistic effect of dopants towards oxygen reduction reaction", ***Electrochimica Acta***, Vol. 163, (2015), 16-23. (https://doi.org/10.1016/j.electacta.2015.02.130).
31. Su, Y., Zhang, Y., Zhuang, X., Li, S., Wu, D., Zhang, F. and Feng, X., "Low-temperature synthesis of nitrogen/sulfur co-doped three-dimensional graphene frameworks as efficient metal-free electrocatalyst for oxygen reduction reaction", ***Carbon***, Vol. 62, (2013), 296-301. (https://doi.org/10.1016/j.carbon.2013.05.067).
32. Dou, S., Huang, X., Ma, Z., Wu, J. and Wang, S., "A simple approach to the synthesis of BCN graphene with high capacitance", ***Nanotechnology***, Vol. 26, (2015), 045402. (https://doi.org/10.1088/0957-4484/26/4/045402).
33. Chen, X., Chen, X., Xu, X., Yang, Z., Liu, Z., Zhang, L., Xu, X., Chen, Y. and Huang, S., "Sulfur doped porous reduced graphene oxide hollow nanosphere frameworks as metal free electrocatalysts for oxygen reduction reaction and as supercapacitor electrode materials", ***Nanoscale***, Vol. 6, No. 22, (2014), 13740-13747. (https://doi.org/10.1039/C4NR04783D).
34. Dong, Y., Pang, H., Yang, H.B., Guo, C., Shao, J., Chi, Y., Li, C.M. and Yu, T., "Carbon based dots co-doped with nitrogen and sulfur for high quantum yield and excitation independent emission", ***Angewandte Chemie International Edition***, Vol. 52, (2013), 7800-7804. (https://doi.org/10.1002/anie.201301114).
35. Wang, Y., Zhang, B., Xu, M. and He, X., "Tunable ternary (P,S,N) – doped graphene as an efficient electrocatalyst for oxygen reduction reaction in an alkaline medium", ***RSC Advances***, Vol. 5, No. 105, (2015), 86746-86753. (https://doi.org/10.1039/C5RA18251D).
36. Lin, H., Chu, L., Wang, X., Yao, Z., Liu, F., Ai, Y., Zhuang, X. and Han, S., "Boron, nitrogen and phosphorous ternary doped graphene aerogel with hierarchically porous structures as highly efficient electrocatalysts for oxygen reduction reaction", ***New Journal of Chemistry***, Vol. 40, (2016), 6022-6029. (https://doi.org/10.1039/C5NJ03390J).

Journal of Renewable Energy and Environment

Research Article

Journal Homepage: www.jree.ir

Reuse of Wood-Based Industrial Wastewater through Optimization of Electrocoagulation Process Using Aluminum and Iron Electrodes

Abotaleb Bay [a], Payam Ghorbannezhad [b*], Javad Yazdan-Moghadam [c], Rahim Aali [d]

[a] *Environmental Health Research Center, Golestan University of Medical Sciences, Gorgan, Golestan, Iran.*
[b] *Department of Biorefinery Engineering, Faculty of New Technologies Engineering, Shahid Beheshti University, Tehran, Tehran, Iran.*
[c] *Center of Research and Development at Golestan Cellulose Group, Kimia Choob Golestan Inc. Company, Gorgan, Golestan, Iran.*
[d] *Research Center for Environmental Pollutants, Qom University of Medical Sciences, Qom, Qom, Iran.*

PAPER INFO

Paper history:
Received 06 November 2020
Accepted in revised form 06 July 2021

Keywords:
Electrocoagulation,
Iron,
Aluminum,
Medium Density Fiberboard,
Reuse Water

ABSTRACT

The wastewater treatment of Medium Density Fiberboard (MDF) is a harsh process because of its contents of high suspended solids, chemical oxygen demand, high molecular weight of lignin, and fatty acids. Electrocoagulation (EC) process was used for efficient removal of pollutants and reusing the water. The impact of aluminum and iron as sacrificial anodes on removal of Chemical Oxygen Demand (COD), Total Suspended Solid (TSS), turbidity, and Total Solid (TS) were investigated. A full quadratic model was deployed to optimize the EC process variables for pretreatment of MDF effluent through response surface methodology. The model results confirmed that the COD and TSS removal efficiency was enhanced upon increasing voltage and residence time; hence, other pollutants initially increased and then, decreased at higher levels. The comparison between aluminum and iron electrodes indicated that the polluted removal efficiencies of aluminum were higher than the iron electrode for MDF wastewater. The optimum values of voltage and residence time for electrocoagulation of MDF wastewater with aluminum were 33 V and 25 min, which resulted in 93 %, 89 %, 67 %, and 76 % for COD, TSS, turbidity, and TS removal, respectively. The implementation of electrocoagulation provided a possibility for reusing water and reducing water consumption in the MDF manufacturing process.

https://doi.org/10.30501/jree.2021.256108.1159

1. INTRODUCTION

The Medium Density Fiberboard (MDF) industry is a promising industrial sector in Iranian wood-based industries. It may be susceptible to high capital energy, raw materials, and water demanding in the environment. The wood-based manufacturing may cause an increase in forming different kinds of pollutants. Therefore, it is of significance to be attentive to establishing pollution preventive facilities for formaldehyde emissions and wastewater treatment. The elevated pollutants of MDF wastewater emerging from suspended solids, Chemical Oxygen Demand (COD), Biochemical Oxygen Demand (BOD), fatty acids, and other soluble substances result in sludge thickening, dye problem, and environmental concerns [1, 2] Therefore, noticeable concerns may arise in case of the release of the above untreated materials to the environment. The high fiber content derived from inefficient separation systems remains a problem for reuse of MDF wastewater [3, 4]. In general, the biological and chemical processes as well as their combination are the most common wastewater treatment processes. Biological treatment is sensitive to micro-organism, spaces, and high residence time. Although chemical treatments tend to be low consumable, they remarkably expand the capacity of downstream mechanical plants. Chemical treatments have a low degree of robustness because the utilization of chemicals can be an expensive and inefficient attempt. The amendment of pretreatment allows for the reuse of treated water which will reduce water consumption in the MDF industry and facilitate an economical and efficient separation of solid from liquid. Wastewater is a valuable resource of liquid in the MDF industry and its efficient recycling brings about a number of economic and environmental advantages: minimizing the cost of waste consumption; mitigating the volume of generated wastewater, and resolving water crisis limitation.

Electrocoagulation (EC) is identified as new technology and an efficient industrial system for removing organic contaminants. EC involves in-situ generation of coagulants through dissolution of ions from metal-electrolyte (such as iron and aluminum) [5]. Thus, the mechanism of electrolytic oxidation forms coagulant during the pre-treatment of wood-based wastewater. Further, the aggregation of destabilized colloids results in flocs formation which makes purification system productive in this manufacturing. Therefore, appropriate selection of electrode materials is very important. Mechanisms that were proposed for the production of aluminum anode are as follows :

*Corresponding Author's Email: p_ghorbannezhad@sbu.ac.ir (P. Ghorbannezhad)
URL: http://www.jree.ir/article_133114.html

Please cite this article as: Bay, A., Ghorbannezhad, P., Yazdan-Moghadam, J. and Aali, H., "Reuse of wood-based industrial wastewater through optimization of electrocoagulation process using aluminum and iron electrodes", ***Journal of Renewable Energy and Environment (JREE)***, Vol. 8, No. 4, (2021), 12-18. (https://doi.org/10.30501/jree.2021.256108.1159).

Anode reaction: $Al_{(s)} \rightarrow Al^{3+} + 3e^{-}$ (1)

Cathode reaction: $H_2O + 2e^{-} \rightarrow H_{2\,(g)} + 2\,OH$ (2)

In the solution: $Al^{+3}_{(aq)} + 3H_2O \rightarrow Al\,(OH)_3 + 3H^{+}$ (3)

A number of parameters with significant effect on the EC process include type of electrodes, electrolysis time, voltage, and wastewater characteristics. EC variables had different effects on the types of wastewater [6, 7]. In addition, a few studies have been explored to investigate the potential of reusing water through EC-treated effluent from industrial wastewater [8]. On the other hand, optimization of EC variables is an essential technique for high efficiency of wastewater treatment and minimizing power consumption and operation costs. Response Surface Methodology (RSM) is a useful statistical technique for optimization studies in several industrial processes [9-11]. RSM is an effective method for reducing the number of experimentals and assessing the importance of relative variable and their interaction with designing models. Optimization of wastewater process parameters by applying RSM methodology has been studied in the literature [12-14]. Thus, the aim of this study was to investigate the applicability of EC for pre-treatment and reusing water through EC process optimization to achieve maximum pollutant removal and minimum energy consumption. Removal efficiencies of COD, TSS, turbidity, and TS were measured and compared to the control group (i.e., sedimentation). Then, the possibility of reusing treated wastewater in MDF manufacturing process was analyzed.

2. EXPERIMENTAL

2.1. Electrocoagulation experiment by aluminum and iron electrodes

The samples were obtained from the plug screw feeder outlet that includes a chip converter machine, tapered compression zone, and chip/drain outlet from MDF manufacturing (Golestan Cellulose Group; Gorgan). Iran products 1.5 million m^3 of MDF per year through 8 large mills by consuming around 5 million m^3 of water and discharging 3 million m^3 of wastewater [15, 16]. The samples conducted in 20 l plastic containers were transferred immediately to the Environmental Health Engineering Laboratory (EHEL) of Medical Science, Gorgan, Iran and were preserved at 5 °C. According to standard methods, the characterization of wastewater samples was examined [17]. The properties of MDF wastewater are shown in Table 1.

Table 1. The typical medium density fiberboard wastewater

Component	Amount
COD (mg/l)	6400
BOD (mg/l)	2150
TSS (mg/l)	5360
Turbidity (NTU)	6170
TS (mg/l)	8000
pH	4.9

Figure 1 demonstrates the implementation of the EC process in WWTP. The primary influent from MDF wastewater was subjected to electrocoagulation with aluminum (Al-Al) and iron (Fe-Fe) in a batch reactor by optimizing two important process variables: voltage and residence time. The electrocoagulation experiment was conducted in an electrochemical reactor with four electrodes connected in parallel to a digital DC power supply (0-60 V, 5 A). A space of 4 cm between the electrodes and the 10 cm gap was maintained at the bottom of the reactor for the movement of magnetic stirrer. The dimension of the treated emulsion was 10 × 20 × 20 cm (the volume of 4 l) and the total effective electrode area was 150 cm^2. The experiments were performed at pH of 5.5 based on the characterization of wastewater effluent. The runs were performed at room temperature (20-25 °C).

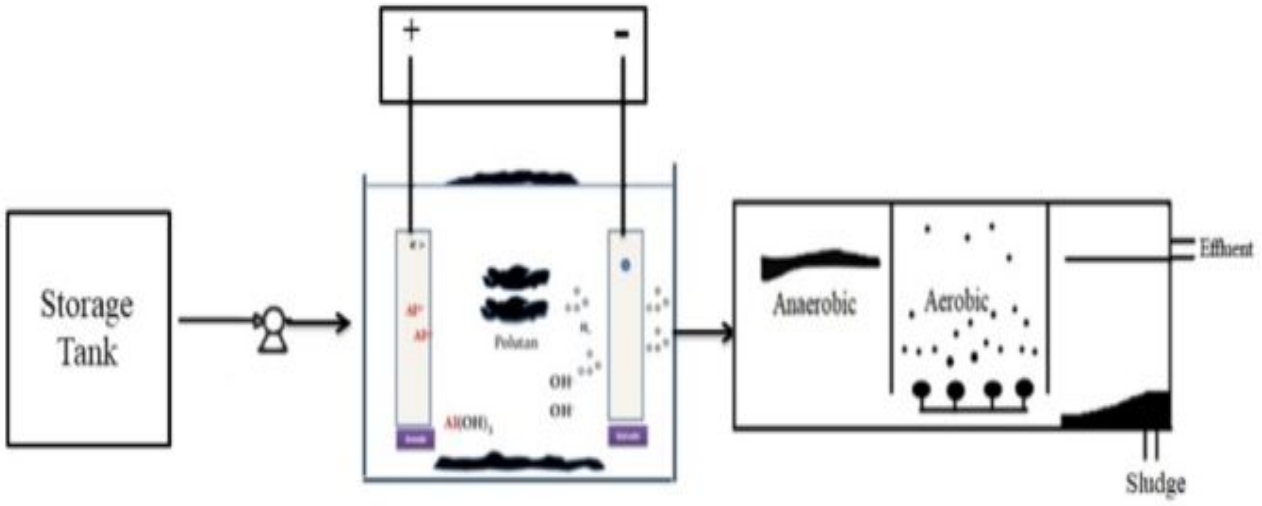

Figure 1. The overview of EC process implementation in MDF wastewater plant

2.2. Analytical measurement of COD and Turbidity

The turbidity was determined using a turbidimeter HANNA HI-98703 with a measurement range of 0 to 1000 NTU using the USEPA 180.1 procedure according to the EPA standards. The COD was measured using a Merk Spectroquant NOVA 60 with a measurement range of 25 to 1500 mgO_2L^{-1} using the EPA 410.4 procedure with a standard method 5220 according to the ISO 15,705 standard.

2.3. The design of experiment

The central composite design was applied in order to investigate the significance of variables in the response manner. Two following important reactions are identified as independent variables: voltage with a range of 20-40 V and residence time (10-30 min). The initial experiments were performed to choose the ranges of variables. Based on the response surface method, the CCRD was selected to fit the number of experimental runs with RSM second-order model. Furthermore, the CCRD, as an intellectual technique, was employed to select the prominent model based on the lack of fit test [18, 19]. The CCRD in the experimental design consisted of 8 factorial points, four axial points, and two blocks (aluminum and Iron electrodes). Five iterations at the center of the design were performed to predict the error sum of squares. The yield of response function helped predict the correlation between dependent and independent variables with a center point value. After measuring the response function, the second-order equation expressed the optimal point based on the full quadratic model as follows [20, 21].

$$Y = \beta_{k0} + \sum_{i=1}^{i=4} \beta_{ki} x_i + \sum_{i=1}^{i=4} \beta_{kii} x_i^2 + \sum_{i<j=2}^{i=4} \beta_{kij} x_i x_j \quad (4)$$

where Y is the predicted response (LA); β_{k0}, β_{ki}, β_{kii} and β_{kij} represent regression coefficients; x_i x_j are the coded independent factors. The quality of models was assessed by coefficient of determination (R^2), adjusted coefficient of determination (R^2-adj), and predicted coefficient of determination (R^2-pred). Moreover, the Root Mean Square Error of Prediction (RMSEP) and Absolute Average Deviation (AAD) were employed to minimize the relationship of responses with actual experimental values [2]. The analysis of variance (ANOVA) was accomplished to analyze the importance of response based on the accurate model.

$$\text{RMSEP} = \sqrt{\frac{\sum_{i=1}^{N}(y_{pre}-y_{exp})^2}{N}} \quad (5)$$

$$\text{ADD} = \left\{ \sum_{i=1}^{N} \left(\left| y_{exp} - y_{pre} \right| / y_{exp} \right) / N \right\} \times 100 \quad (6)$$

where y_{pre}, y_{exp}, and N are the predicted data, observed data, and number of treatments, respectively.

Optimization of multiple responses was simultaneously performed through numerical and graphical optimization execution of Design-Expert software. The optimum conditions were considered all independent variables within the studied ranges and the COD removal, the TSS removal, the turbidity removal, and TS removal were maximized. The range of 0-1 as desirability values from responses determined the reliability of optimum conditions. The most desirable optimum point was closer to 1. In order to ensure the overall process improvement, the desirability function was used as one of the most useful techniques for the optimization of multi-responses processes through independent variables series (Eq. 6).

$$D(x) = (d_1 \times d_2 \times \ldots \times d_n)^{\frac{1}{n}} \quad (6)$$

where n (1, 2, …, n) represents the number of independent variables. If any of the dependent variables is out of the desirable range, the function becomes zero. In this situation, the numerical optimization identifies a point that maximizes this function. The regression equation of the accurate model confirmed that the predicated values were in close agreement with actual values. The distribution of the predicted and actual values is illustrated in Figure 2, whose data mainly align. Thus, the underlying assumption of normality in this study was appropriate and therefore, the developed models were validated.

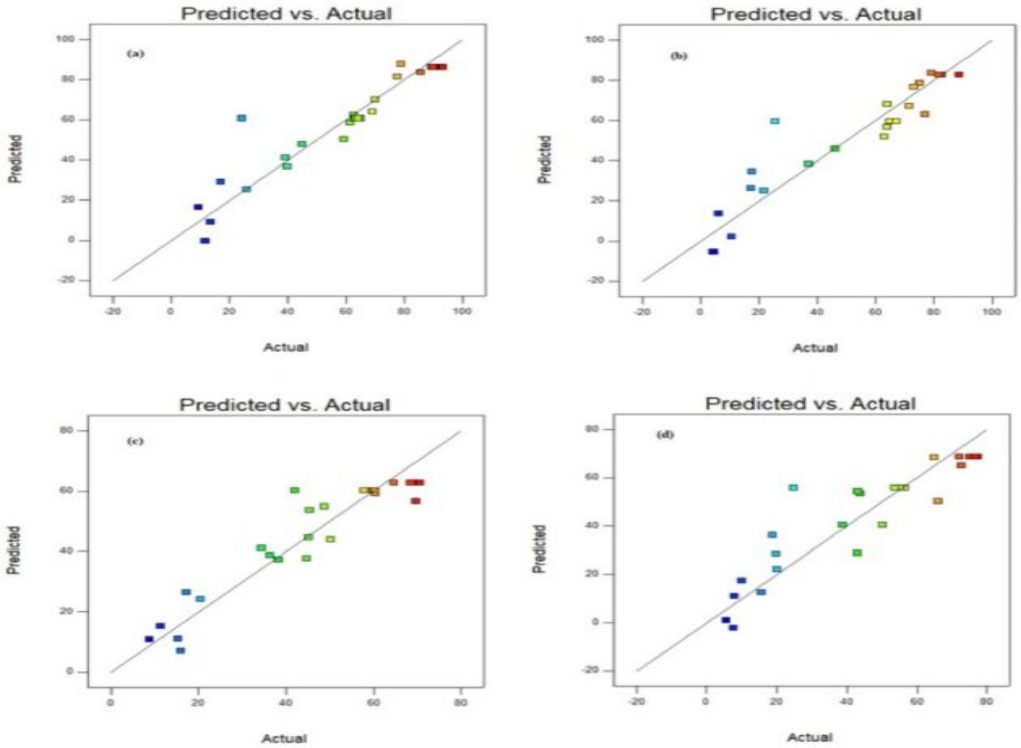

Figure 2. Predicted vs. actual values: (a) COD removal, (b) TSS removal, (c) Turbidity removal, and (d) TS removal

3. RESULTS AND DISCUSSION

3.1. The importance of electrodes on pretreatment of MDF wastewater

The variation in the pollutant removal efficiency using aluminum and iron electrodes is shown in Figure 3. The maximum COD removal efficiency rates experienced for aluminum and iron electrodes at around 30 V and 25 min were 93 % and 65 %, respectively. However, the maximum turbidity removal efficiency was around 70 % for aluminum and 60 % for iron. The results demonstrated that there were strong differences in the electrocoagulation of iron and aluminum electrodes. In [22], it was indicated that the COD and color removal by aluminum electrode was more efficient than that for the electrode at high voltage in the textile-industry wastewater. Amorphous hydroxides are the primary species in both cases. However, aluminum electrode dissolution yields significant concentrations of monomeric and even polymeric ionic species.

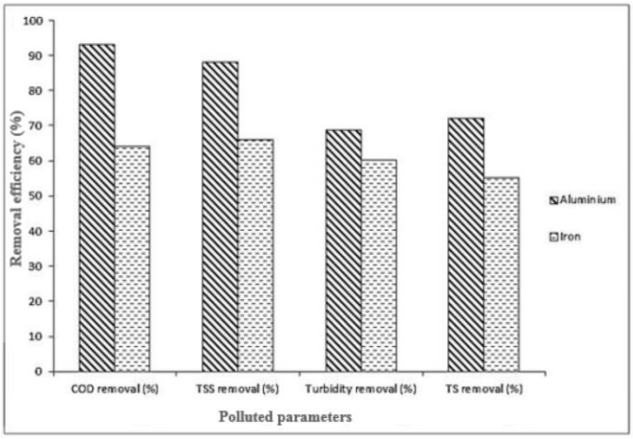

Figure 3. The effects of type of electrode on removal efficiency at voltage 30 V and time 20 min

3.2. The independent effects of voltage in electrocoagulation process

The independent influence of voltage was assessed to obtain the initial optimum condition of electrocoagulation variables (COD, TSS, Turbidity, and TS removal). Effect of voltage was investigated, ranging from 10 to 40 mA and the initial pH was kept at 5.5 in this study (Figure 4). The COD removal was found as the most significant variable when the aluminum electrode was used, while the Iron electrode exhibited remarkable responses to TSS removal. The maximum COD removal efficiency was obtained at nearly 93 % at voltage of 33 mA using aluminum electrode, whereas the COD removal of 69 % was detected by only Iran electrode in the same condition. On the other hand, the higher desirability for pretreatment of MDF wastewater through electrocoagulation process was considered with aluminum electrode when the voltage of 33 mA was relatively used in this process.

The variations in removal efficiencies for COD, TSS, turbidity, and TS removal are shown in Figure 5. The interaction between the voltage and residence time on the COD removal when pH was kept at 5.5 indicated that the COD removal gently increased upon increasing voltage. On the basis of Faraday's law, the electrolytic cell at a specific time directly corresponds to the number of coagulants at dissolved anodic metal. Therefore, the amounts of aluminum and iron hydroxide flocs increase by increasing the voltage, which results in the enhancement of colloidal particles removal [23]. The enhancement of hydroxide ion led to increase in the pH which results in decrease in the TSS, TS, and turbidity removal, as can be seen below.

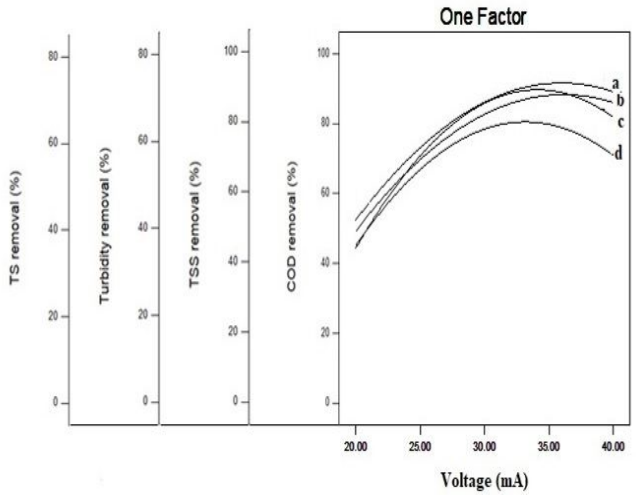

Figure 4. The independent effect of voltage on a) COD, b) TSS, c) TS, and d) turbidity removal

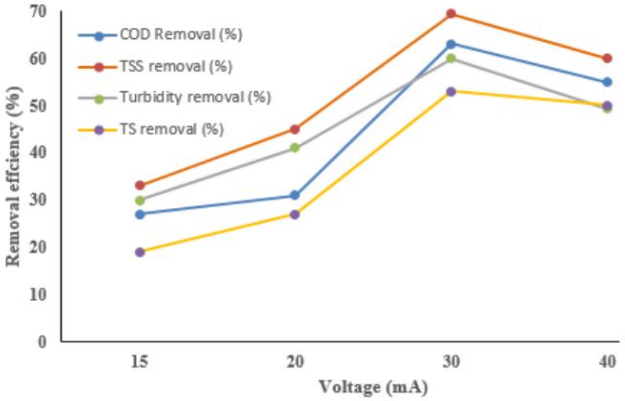

Figure 5. The effect of voltage on removal efficiency (%), Iron electrode, time 20 min

3.3. The independent correlation between residence time and the response variables

The effect of residence time on electrocoagulation is presented in Figure 6. All pollutant removal efficiencies increase with respect to the residence time. The TS removal was preliminarily enhanced by extending the time; notwithstanding, it decreased in the case of longer residence time. This evidence is presumably due to the great content of hydroxide ion from aluminum electrode at cathode, which results in the final pH rise. Mouldi-Mostafa et al. determined that the optimum reaction time for treatment was approximately 20 min [6].

In comparison of residence times, voltage has noticeably significant impact on the pollutant removal in the electrocoagulation of MDF manufacturing wastewater (Figures 4 and 7). For instance, the maximum TS removal was observed at nearly 75 % when the voltage was increased, while up to 60 % TS removal was obtained at maximum time. The optimal electrocoagulation time was found among 20 to 26 min when the maximum COD, TSS, turbidity, and TS removal was obtained at around 94 %, 89 %, 67 %, and 75 %,

respectively (Figure 7). The response variables experienced a decline at refining time of 30 min. The reduction of removal efficiency found here can be explained by the high concentration of color and colloidal particles in the samples after the treatment. The independent relationship for residence time ascertained that the COD and TSS underwent the most significant pollution reduction rather than turbidity and TS.

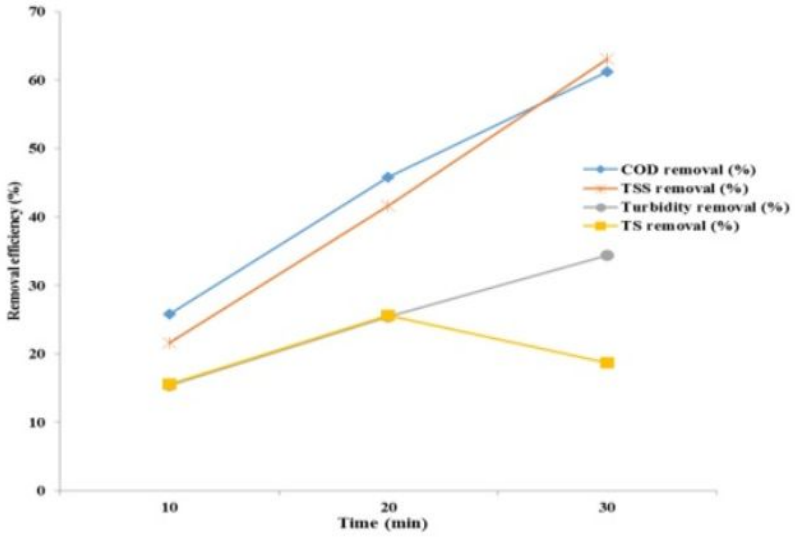

Figure 6. The effect of residence time on removal efficiency (%), aluminum electrode, voltage 20 V

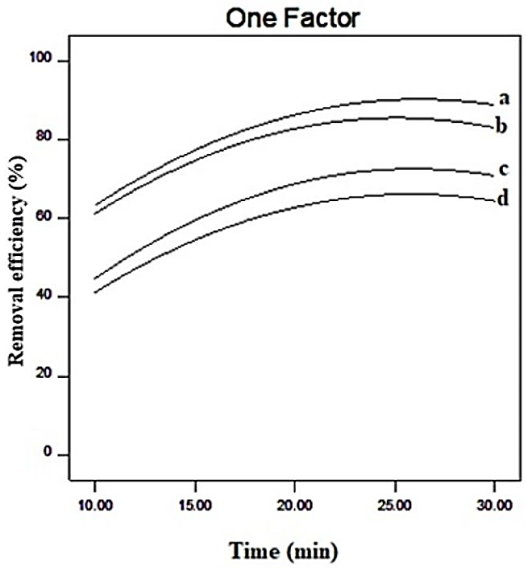

Figure 7. The independent effect of Time on a) COD removal, b) TSS removal, c) TS removal, and d) Turbidity removal

3.4. Optimization of EC variables as pre-treatment of MDF wastewater

The optimum experimental design was created and it comprised 52 sets of coagulation experiments. The full quadratic regression model was satisfied for all tests. The significance of full quadratic models to confirm the validity of models based on the ANOVA analyses is illustrated in Table 2. The importance and significance of each variable shows a large F-value and a small p-value for the responses. The values of the adjusted R^2 respectively measured at 0.88 and 0.83 for COD removal and turbidity removal are large enough to supported the significance of the model. The RSM plots derived from quadratic models for the variables are shown in Figure 8.

Of note, the COD and TSS removal efficiencies increased upon increasing current voltage and residence time; however, the turbidity and TS removal efficacies initially increased with increasing voltage and residence time, followed by a decrease at higher levels. The colloidal particles present in MDF wastewater had mostly a negative superficial charge and they were destabilized by the hydroxides generated during EC. Notwithstanding this evidence, the COD and TSS removal occurred easily due to efficient destabilization of charge [24, 25]. There was a remarkable difference between COD and TS removal efficiency rates for aluminum and Iron. Aluminum electrode was found to be more efficient than Iron electrode due to its higher charge as well as high solubility during EC process. Moreover, use of iron electrodes often results in the formation of very fine brown particles which are less prone to settling than the gel floc formed with aluminium [26]. The optimum amounts of voltage and residence time for electrocoagulation of MDF wastewater with aluminum were 33 V and 25 min, respectively. The maximum COD, TSS, turbidity, and TS removal rates were acquired 93 %, 89 %, 67 %, and 76 %, respectively.

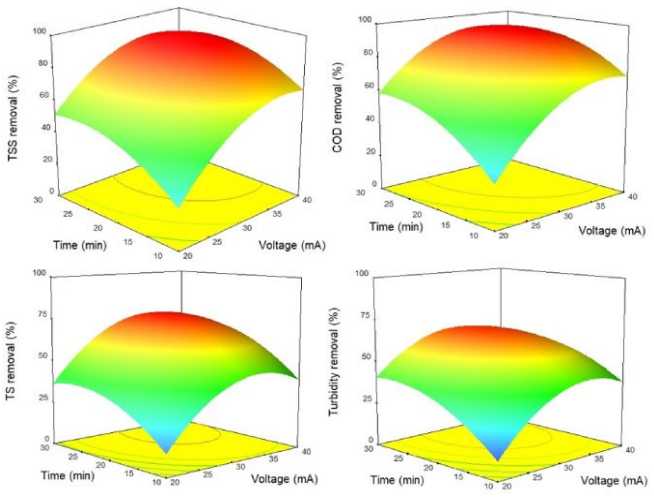

Figure 8. The interaction of voltage and residence time on removal efficacies (%)

Table 2. ANOVA for the models for COD removal

Source	Sum of squares	df	Mean of square	F value	P-value	Prob>F
Model	16567.20	8	2070.90	16.79	0.0001	Significant
A (voltage)	4335.83	1	4335.83	35.15	0.0001	Significant
B (time)	3476.60	1	3476.60	28.18	0.0001	Significant
C (electrode)	4229.43	1	4229.43	34.28	0.0001	Significant
AB	121.99	1	212.99	0.99	0.3340	
AC	61.12	1	61.12	0.50	0.4910	
BC	65.92	1	65.92	0.53	0.4747	
A2	3320.94	1	3320.94	26.92	0.0001	Significant
B2	1456.31	1	1456.31	11.81	0.0032	Significant
Residue	2097.16	17	123.36			
Lack of fit	825.97	9	91.77	0.58	0.7849	Not significant
Pure error	1271.19	8	158.90			
Total	18664.36	25				

3.5. Reuse of MDF wastewater

In this study, treatment of MDF wastewater through optimization of the EC process is essential to reusing the water. EC aimed to make the reusing of the water possible for MDF industrial process by removing the pollutants. The results point to the considerable difference between the turbidity and TSS removal efficiency rates for common design with and without the EC process for MDF wastewater treatment plant. The high concentration of suspended solid and turbidity inevitably led to prevention of reusing the water in common conventional systems of MDF wastewater. It is anticipated that high concentration of iron ionic allowing to oxidize the functional group of cellulosic fibers would result in negative impact on flocculation of solid wastes, while the aluminum ionic was not observed. Otherwise, the aluminum electrode was confirmed to have significant impact on pollutant removal, even at a low level of concentration. The high level of pollutant removal helps reuse the water for MDF manufacturing process, which has not been feasible in previous systems.

4. CONCLUSIONS

This study was carried out with aim of reusing the water through Electrocoagulation Process (EC) in manufacturing MDF wastewater. The colloidal particles were a major problem associated with the MDF wastewater. EC coupled with wastewater treatment plant helped compensate the sludge generation and reduce the cost of operations. The effects of two important independent variables, namely voltage and residence time, with iron and aluminum electrodes on responses including the COD, TSS, turbidity, and TS were evaluated. It was anticipated that the amounts of aluminum hydroxide flocs would increase upon increasing the voltage, which led to the enhancement of colloidal particle removal. The aluminum electrode was more efficient because of better electrolysis which generated higher charge and was easily soluble to destabilize the colloidal particle in MDF wastewater. RSM was successfully used for optimizing the EC process variables. The optimum values of voltage and residence time were determined at 33 V and 25 min. Under optimum values of process variables, 93 % removal COD, 89 % removal TSS, 67 % removal turbidity, and 76 % removal TS were obtained.

Therefore, the pretreatment of MDF wastewater through electrocoagulation confirmed that the EC system could perform biological treatment better than the current conventional physio-chemical treatments. The effluent of EC represented a significant difference in quality of water for reusing the water. In addition, it reduced energy consumption as well as process residence time. Removal of the chemical additives and low sludge production characterized a cost-effective approach of industrial wastewater management. It was also demonstrated that the EC process managed to reuse the water in the MDF manufacturing process.

5. ACKNOWLEDGEMENT

The authors would like to appreciate the support made for this study by Environmental Health Research Center, Golstan University of Medical Sciences (Code: 1395/74320, Date: 2017/02/25).

REFERENCES

1. Galehdar, M., Younesi, H., Hadavifar, M. and Zinatizadeh, A.A., "Optimization of a photo-assisted fenton oxidation process: A statistical model for MDF effluent treatment", ***CLEAN-Soil, Air, Water***, Vol. 37, No. 8, (2009), 629-637. (https://doi.org/10.1002/clen.200900052).
2. Song, L. -H., Zhu, C. -Y. and Wang, Q. -Q., "Study on medium/high density fiberboard wastewater treatment technology [J]", ***China Wood-Based Panels***, Vol. 10, (2008), 7. (caod.oriprobe.com/article/15003660).
3. Li, J. and Pang, S., "Modelling of energy demand in an MDF plant", ***Proceedings of CHEMECA 2006: Knowledge and Innovation***, Auckland, New Zealand, Auckland, (2006), 941-946. (http://hdl.handle.net/10092/408).
4. Ghorbannezhad, P., Bay, A., Yolmeh, M., Yadollahi, R. and Moghadam, J.Y., "Optimization of coagulation–flocculation process for medium density fiberboard (MDF) wastewater through response surface methodology", ***Desalination and Water Treatment***, Vol. 57, No. 56, (2016), 26916-26931. (https://doi.org/10.1080/19443994.2016.1170636).
5. İrdemez, Ş., Demircioğlu, N., Yıldız, Y.Ş. and Bingül, Z., "The effects of current density and phosphate concentration on phosphate removal from wastewater by electrocoagulation using aluminum and iron plate electrodes", ***Separation and Purification Technology***, Vol. 52, No. 2, (2006), 218-223. (https://doi.org/10.1016/j.seppur.2006.04.008).
6. Merzouk, B., Gourich, B., Sekki, A., Madani, K., Vial, C. and Barkaoui, M., "Studies on the decolorization of textile dye wastewater by continuous electrocoagulation process", ***Chemical Engineering Journal***, Vol. 149, No. 1, (2009), 207-214. (https://doi.org/10.1016/j.cej.2008.10.018).
7. Yetilmezsoy, K., Ilhan, F., Sapci-Zengin, Z., Sakar, S. and Gonullu, M.T., "Decolorization and COD reduction of UASB pretreated poultry manure wastewater by electrocoagulation process: A post-treatment study", ***Journal of Hazardous Materials***, Vol. 162, No. 1, (2009), 120-132. (https://doi.org/10.1016/j.jhazmat.2008.05.015).

8. Abdulla, H.M., El-Shatoury, S.A., El-Shahawy, A.A., Ghorab, S.A., Nasr, M. and Trujillo, M.E., "An integrated bioaugmentation/electrocoagulation concept for olive mill wastewater management and the reuse in irrigation of biofuel plants: A pilot study", ***Environmental Science and Pollution Research***, Vol. 26, No. 16, (2019), 15803-15815. (https://doi.org/10.1007/s11356-019-04893-w).
9. Irfan, M., Butt, T., Imtiaz, N., Abbas, N., Khan, R.A. and Shafique, A., "The removal of COD, TSS and colour of black liquor by coagulation–flocculation process at optimized pH, settling and dosing rate", ***Arabian Journal of Chemistry***, Vol. 10, (2013), 2307-2318. (https://doi.org/10.1016/j.arabjc.2013.08.007).
10. Bernalte, E., Salmanighabeshi, S., Rueda-Holgado, F., Palomo-Marín, M., Marín-Sánchez, C., Cereceda-Balic, F. and Pinilla-Gil, E., "Mercury pollution assessment in soils affected by industrial emissions using miniaturized ultrasonic probe extraction and ICP-MS", ***International Journal of Environmental Science and Technology***, Vol. 12, No. 3, (2015), 817-826. (https://doi.org/10.1007/s13762-013-0461-3).
11. Kanmani, P., Kumaresan, K. and Aravind, J., "Utilization of coconut oil mill waste as a substrate for optimized lipase production, oil biodegradation and enzyme purification studies in Staphylococcus pasteuri", ***Electronic Journal of Biotechnology***, Vol. 18, No. 1, (2015), 20-28. (https://doi.org/10.1016/j.ejbt.2014.11.003).
12. Körbahti, B.K. and Tanyolaç, A., "Electrochemical treatment of simulated textile wastewater with industrial components and Levafix Blue CA reactive dye: Optimization through response surface methodology", ***Journal of Hazardous Materials***, Vol. 151, No. 2, (2008), 422-431. (https://doi.org/10.1016/j.jhazmat.2007.06.010).
13. Kushwaha, J.P., Srivastava, V.C. and Mall, I.D., "Organics removal from dairy wastewater by electrochemical treatment and residue disposal", ***Separation and Purification Technology***, Vol. 76, No. 2, (2010), 198-205. (https://doi.org/10.1016/j.seppur.2010.10.008).
14. Suárez-Escobar, A., Pataquiva-Mateus, A. and López-Vasquez, A., "Electrocoagulation-photocatalytic process for the treatment of lithographic wastewater. Optimization using response surface methodology (RSM) and kinetic study", ***Catalysis Today***, Vol. 266, (2016), 120-125. (https://doi.org/10.1016/j.cattod.2015.09.016).
15. Dehghani Firouzabadi, M. and Ghorbannezhad, P., "Investigation on MDF market demand in Iran", ***International Journal of Lignocellulosic Products***, Vol. 1, No. 1, (2014), 72-81. (https://doi.org/10.22069/IJLP.2014.1925).
16. Azizi, M., Ghorbannezhad, P. and Hatefnia, H., "Estimation of demand for wood panels in Iran by the year of 2012", ***Journal of Forestry Research***, Vol. 20, No. 2, (2009), 179-182. (https://doi.org/10.1007/s11676-009-0033-z).
17. Rice, E.W., Baird, R.B., Eaton, A.D. and Clesceri, L.S., Standard methods for the examination of water and wastewater, 22nd Edition, American Public Health Association, American Water Works, Water Environment Federation, Washington DC., (2012). (https://books.google.com/books/about/Standard_Methods_for_the_Examination_of.html?id=dd2juAAACAAJ).
18. Subramonian, W., Wu, T.Y. and Chai, S.-P., "An application of response surface methodology for optimizing coagulation process of raw industrial effluent using Cassia obtusifolia seed gum together with alum", ***Industrial Crops and Products***, Vol. 70, (2015), 107-115. (https://doi.org/10.1016/j.indcrop.2015.02.026).
19. Esmaeili, M., Yolmeh, M., Shakerardakani, A. and Golivari, H., "A central composite design for the optimizing lipase and protease production from Bacillus subtilis PTCC 1720", ***Biocatalysis and Agricultural Biotechnology***, Vol. 4, No. 3, (2015), 349-354. (https://doi.org/10.1016/j.bcab.2015.05.002).
20. Xiao, A., Huang, Y., Ni, H., Cai, H. and Yang, Q., "Statistical optimization for tannase production by *Aspergillus tubingensis* in solid-state fermentation using tea stalks", ***Electronic Journal of Biotechnology***, Vol. 18, No. 3, (2015), 143-147. (https://doi.org/10.1016/j.ejbt.2015.02.001).
21. Hay, J.X.W., Wu, T.Y., Teh, C.Y. and Jahim, J.M., "Optimized growth of Rhodobacter sphaeroides OU 001 using response surface methodology (RSM)", ***Journal of Scientific & Industerial Research***, Vol. 71, (2012),149-154. (http://hdl.handle.net/123456789/13493).
22. Roopashree, G. and Lokesh, K., "Comparative study of electrode material (iron, aluminium and stainless steel) for treatment of textile industry wastewater", ***International Journal of Environmental Sciences***, Vol. 4, No. 4, (2014), 519. (https://doi.org/10.6088/ijes.2014040400008).
23. Paulista, L.O., Presumido, P.H., Theodoro, J.D.P. and Pinheiro, A.L.N., "Efficiency analysis of the electrocoagulation and electroflotation treatment of poultry slaughterhouse wastewater using aluminum and graphite anodes", ***Environmental Science and Pollution Research***, Vol. 25, No. 20, (2018), 19790-19800. (https://doi.org/10.1007/s11356-018-2184-y).
24. Camcioglu, S., Ozyurt, B. and Hapoglu, H., "Effect of process control on optimization of pulp and paper mill wastewater treatment by electrocoagulation", ***Process Safety and Environmental Protection***, Vol. 111, (2017), 300-319. (https://doi.org/10.1016/j.psep.2017.07.014).
25. Hansson, H., Marques, M., Laohaprapanon, S. and Hogland, W., "Electrocoagulation coupled to activated carbon sorption/filtration for treatment of cleaning wastewaters from wood-based industry", ***Desalination and Water Treatment***, Vol. 52, No. 28-30, (2014), 5243-5251. (https://doi.org/10.1080/19443994.2013.808582).
26. Islam, S.D.-U., "Electrocoagulation (EC) technology for wastewater treatment and pollutants removal", ***Sustainable Water Resources Management***, Vol. 5, No. 1, (2019), 359-380. (https://doi.org/10.1007/s40899-017-0152-1).

Journal of Renewable Energy and Environment

Research Article

Journal Homepage: www.jree.ir

Production of Hydrogen via Renewable Energy and Investigation of Water Molecular Changes During Electrolysis Process

Iessa Sabbe Moosa [a], Hussein A. Kazem [b*], Laila Masoud Rashid Al-Iessi [c]

[a] *Research Cooperator with Public Authority for Water, Al-Buraimi Province, P. C.: 512, Oman.*
[b] *Faculty of Engineering, Sohar University, Sohar, P. C.: 311, Oman.*
[c] *Public Authority for Water, Al-Buraimi Province, P. C.: 512, Oman.*

PAPER INFO

Paper history:
Received 01 December 2020
Accepted in revised form 03 August 2021

Keywords:
Electrolysis,
Hydrogen,
Chemical-Physical Actions,
Eclectic Dipoles,
Dielectric Strength,
Transpiration

ABSTRACT

Studies on renewable energy are essential topics that help find new energy sources to replace fossil sources and promote environment friendliness. Hydrogen is the most practical alternative energy carrier source that meets the mentioned purposes. The mass of hydrogen element in the Earth's water was calculated and found to be about 2.1×10^{20} kg, which is greater than the mass of the world oil reserves by about 9×10^{5} times. In addition, essential details of water molecular arrangement were investigated in order to better understand the electrolysis of water. Also, the energy of covalent and hydrogen bonds per molecule of water was theoretically calculated and found to be about 8.17×10^{-19} J/molecule and 3.87×10^{-20} J/molecule, respectively. In the electrolysis process, two stages should be undertaken: the first stage was to break hydrogen bonds between water molecules, in which all water eclectic dipoles would align in the direction of the Applied Electric Field across the electrolysis unit. The second stage was to break water covalent bonds to generate H_2 and O_2 gases. Moreover, the lowest cost to generate one kg of hydrogen (0.4 $/kg) by electrolysis method using solar energy was about 0.4 $, which has already been proven, while this value was about 2.8 $/kg upon considering the average price of electricity of Oman in comparison.

https://doi.org/10.30501/jree.2021.260034.1167

1. INTRODUCTION

Environmental challenges, availability of energy, and its sustainable development are the most vital issues that are faced by any nation. Most conventional energy sources and continuous environmental deterioration result from inadequate global cooperation. The population of the world will probably be about 9 billion in 2050 and the required power to run this huge population is around 30 TW; about 85 % of this power will be provided from fossil sources at that time [1]. In addition, fossil sources will be depleted with the passage of time. Therefore, in order to bridge this gap in energy sources in the future and to mitigate the environmental risks, the world has started to think seriously in green renewable energy sources such as solar, wind, geothermal, nuclear fusion, magnetic energy, and hydrogen as reliable energy carriers.

After the oil crisis of 1973 [2, 3], the search to find alternatives to fossil sources has exponentially increased and most Western and European countries have begun to invest massive capital in renewable energy sources. Furthermore, transformation to renewable energy will rely on the pace of development in this sensational field and its competitive price to meet the energy demand instead of fossil sources in the future as required. A general vision of the energy supply sustainability until 2050 for global transformation of the renewable energy sector has been propounded by the International Renewable Energy Agency (IRENA) [4].

In 2019, Zhai reported that within the last decade, the world began to show its concern and fear about the global environment changes because of the greenhouse effect due to fossil fuels combustion and now, they are trying to become a low-carbon world [5]. According to this report, hydrogen has received substantial attention because of its capability to produce water as a byproduct when burning with oxygen, hence eliminating harmful gases and replacing fossil fuels. He also anticipated that the percentage of hydrogen fuel might reach about 18 % of total world energy demand in 2050. Essential details of renewable energy sources, one of which was hydrogen, were investigated by Moosa and Kazem [6]. Globally, around 95 % of hydrogen gas is produced from fossil sources such as natural gas CH_4, oil, and coal and just about 4 % is produced by water electrolysis method [7]. The serious drawback to using fossil fuels to produce hydrogen gas is environmental pollution with a high percentage of carbon dioxide CO_2, which then exacerbates the problem of global warming. During 2019, Johan Martens and his co-researchers at KU Leuven in Belgium stated that hydrogen gas could be produced from air moisture using solar panels [8]. Very significant details of hydrogen production in different ways such as electrolysis, hot steam of natural gas CH_4, photo electrolysis process, plasma cracking, pyrolysis,

*Corresponding Author's Email: h.kazem@su.edu.om (H.A. Kazem)
URL: https://www.jree.ir/article_134571.html

Please cite this article as: Moosa, I.S., Kazem, H.A. and Al-Iessi, L.M.R., "Production of hydrogen via renewable energy and investigation of water molecular changes during electrolysis process", ***Journal of Renewable Energy and Environment (JREE)***, Vol. 8, No. 4, (2021), 19-28. (https://doi.org/10.30501/jree.2021.260034.1167).

copyrolysis, and thermochemical water splitting routes at a temperature of about 650 °C have been published [9-14]. A comprehensive review of biohydrogen production was reported by Sarvanan et al. in 2020 [15]. They emphasized that biohydrogen and biofuel could be used instead of fossil fuels to resolve their depletion problem over time and with no greenhouse effect. This review includes remarkable details about Microbial Fuel Cells (MFC) and Microbial Electrolysis Cells (MEC). Also, Samsudeen et al. demonstrated that hydrogen could be generated from the distilling of wastewater [16]. They contracted their own compact design of MEC for this purpose. Their results achieved higher efficiency than the conventional route of hydrogen production employing the Microbial electrolysis technique.

To the best of our knowledge and information, the total mass of hydrogen element in the Earth's water as an energy carrier has not been estimated and compared with the world reserve oil so far. In addition, there is a lack of available detail about water molecular structure changes that happen during water electrolysis to produce hydrogen and oxygen gases. The production cost of one kilogram of hydrogen by electrolysis route by utilizing recent solar energy price will be included in the planning of the present work, and it will be compared to the cost of production using the price of electricity in Oman. Furthermore, the authors will focus on using the released byproduct drain-water from air-cooling systems in humid areas to feed the electrolysis cells instead of the water produced by conventional ways to reduce the production cost of hydrogen, which is a new idea in this field.

Depending upon the previous review, the aims and objectives of this article are: (i) Calculating how much the amount of hydrogen is available in the Earth compared with the mass of proven world oil reserves; (ii) devoting very significant attention to hydrogen which is produced using water electrolysis in correlation with some renewable energy sources to generate the required electricity such as solar and wind energy; (iii) comparing the hydrogen production cost when using the present price of electricity in Oman, with the recent price of solar electricity; and (iv) meanwhile, studying the changes that occur for water molecular arrangement during the electrolysis process under the effect of a direct current circuit.

2. HYDROGEN MASS AS EARTH COMPONENT

The hydrogen mass in the Earth can be calculated in proportion to the Earth's water. Table 1 includes different estimated water reservoirs in the Earth. It is very difficult to access mantle water which can be found at the depth ranges of about 400-600 km [17]. Therefore, other amounts of water will be counted to calculate approximately the mass of hydrogen in the Earth: (1.37×10^{21} kg + 5×10^{20} kg = 1.87×10^{21} kg). From Table 1, the volume of the Earth's water (V_{water}) is approximately 5.87×10^{18} m^3 after using the pure water density of 1×10^3 kg/m^3 at 1 Atm. pressure and 25 °C to calculate the volume of the water (V_{water} = $m/\rho_{water,}$). The volume of the Earth is about 1.1×10^{21} m^3 (V_{Earth}= $4/3\pi\ r^3$, r = 6.37×10^6 m); therefore, the volume of the Earth's water is around 0.53 % of Earth's volume.

The mass of hydrogen in the water contained in the Earth without mantle water can be calculated as follows:

The molar mass of the water H_2O is ~ 18 g/mol and the total number of moles of H_2O in Earth's water is:

$$\frac{\text{No. of mole}}{1\ \text{mol}\ H_2O} \quad \frac{\text{Mass}}{18\ \text{g}}$$

$$\text{x} \qquad 1.87\times10^{24}\ \text{g} \quad \rightarrow \quad \text{x} = \frac{(1\ \text{mol}\ H_2O)(1.87\times10^{24}\ \text{g})}{18\ \text{g}} = 10.39\times10^{22}\ \text{mol} \approx 10.4\times10^{22}\ \text{mol}$$

Each mole of H_2O contains 2 moles of H element so that the total mass of the H element in the water is:

Mass of the H element = (No. of mol H_2O)(2)(molar mass of H) = $(10.4\times10^{22}\ \text{mol})(2)(1.008\ \text{g/mol}) \approx 2.1\times10^{23}\ \text{g} \approx 2.1\times10^{20}\ \text{kg}$ (1)

Similarly, the number of H_2O moles in one kg of water is:

$$\frac{\text{No. of mole}}{1\ \text{mol}\ H_2O} \quad \frac{\text{Mass}}{18\ \text{g}}$$

$$\text{x} \qquad 1000\ \text{g} \quad \rightarrow \quad \text{x} = \frac{(1\ \text{mol}\ H_2O)(1000\ \text{g})}{18\ \text{g}} = 55.55\ \text{mol}$$

Therefore, the mass of the H element in one kg of H_2O is:

Mass of the H element = (No. of mol H_2O)(2)(molar mass of H) = (1 kg)(55.55 mol)(2)(1.008 g/mol) ≈ 112 g

Table 1. Different reservoirs of the Earth's water [17]

Type of reservoir	~ Mass (kg) [17]	~ Volume m^3 $V= m/\rho_{water}$	of Earth's volume %
Oceans	1.37×10^{21}	1.37×10^{18}	0.1245 %
Ice and snow, Atmospheric moisture, Rivers, Groundwater, Sedimentary rocks, Lakes, Soils	5×10^{20}	5×10^{17}	0.0454 %
Mantle water	4×10^{21}	4×10^{18}	0.3636 %
Total	**5.87×10^{21}**	**5.87×10^{18}**	**~ 0.53 %**

Another approach to determining the hydrogen and oxygen amount per kilogram of water is as follows:

$$\%\ \text{elem. in a comp.} = \frac{\text{n(molar mass of the elem.)}}{\text{molar mass of the comp.}} \times 100 \qquad (2)$$

where n is the number of atoms of the counted element in the compound. Afterwards, the mass of the element can be calculated at a certain amount of any compound as follows:

Mass of elem. in a comp. = mass of the elem. in the comp. × percent of the elem. in the comp. (3)

Hence, the % H and % O in one kg of water:

$$\%\ \text{H} = \frac{2(\text{molar mass of H})}{\text{molar mass of}\ H_2O} \times 100\ \% = \frac{2(1.008\ \text{g/mol})}{18\ \text{g/mol}} \times 100\ \% = 11.2\ \%$$

$$\%\ \text{O} = \frac{1(\text{molar mass of O})}{\text{molar mass of}\ H_2O} \times 100\ \% = \frac{1(16\ \text{g/mol})}{18\ \text{g/mol}} \times 100\ \% = 88.88\ \%$$

Thus, the masses of H and O in one kg of water are:

Mass of H in 1 kg of water = watermass × percent of H
= (1 kg)(0.112) = (1000 g)(0.112) = 112 g

Mass of O in 1 kg of water = watermass × percent of O
= (1 kg)(0.8888) = (1000 g)(0.8888) = 888.8 g

The total mass of H and O is 100.8 g; the slight difference results from the rounding process of the molar masses of H, O, and H_2O. From these calculations, it can be concluded that the generated mass of O is much higher than that of H by about 8 times. This result should be considered environmentally and economically for a massive quantity of oxygen mass as a byproduct of the electrolysis process. Fortunately, this byproduct oxygen gas can be used in many industrial and health sectors. Furthermore, it is expected that the mentioned gas will reduce the level of carbon dioxide CO_2 in the atmosphere to a greater extent upon turning to global-scale renewable energy rather than fossil fuels. This matter must be considered in advance by environment specialist scientists to guess the environmental changes that will result from the use of many renewable energy sources instead of fossil fuels.

The total world oil reserve on 31st December 2018 was about 1,663,331 million barrels, around 50 % of which is produced in the Middle East countries. The top 10 reserves holders range from Venezuela (302,809 million) all the way to Libya (48,363 million) [18]. The volume of the oil barrel is approximately 42 gallons and the volume of one gallon is about 0.003785 m^3 so that the volume of one barrel of oil is around 0.159 m^3. The average of crude oil density is about 900 kg/m^3 which is dependent on the production zone [19] and so, the mass of crude oil barrel is about 143 kg ($m = \rho V$). The whole mass of the world oil reserves ($M_{res.oil}$ = no. barrels × 143 kg) is around 2.38×10^{14} kg. Therefore, the mass of the hydrogen element (M_H) in the Earth as calculated above (~2.1×10^{20} kg) is much greater than the mass of the world crude oil reserves by about 9×10^5 times:

$$\frac{M_H}{M_{res.oil}} = \frac{2.1\times10^{20}\ kg}{2.38\times10^{14}\ kg} = 8.8\times10^5 \approx 9\times10^5$$

3. ENERGY STORED IN HYDROGEN FUEL

The stored energy in hydrogen fuel is in the range of 120-143 MJ/kg, while it is much less in the case of fossil fuels, e.g., is around 54 MJ/kg and 46 MJ/kg in the liquefied natural gas and automotive diesel, respectively [1, 14]. Also, fossil fuels will surely come to an end in the coming future, even if the Earth is entirely turned into fossil fuels. Therefore, researchers and policy-makers should seriously consider hydrogen as a promising energy carrier and other renewable energy sources to replace fossil fuels in many energy sectors. Table 2 includes the energy density (MJ/kg) for different types of fossil fuels and hydrogen.

4. SIGNIFICANCE OF HYDROGEN

- Representing the future source of energy carrier that can replace fossil fuels.
- Being the source of solar energy, as the Sun is almost a plasma of hydrogen ions and electrons confined by a very strong magnetic field to keep the Sun in its present form and activity [6]. Therefore, the hydrogen element is the basis of life on the Earth because the Sun is the main source of energy.
- Generally, there is no water on the Earth without the existence of hydrogen element [20]. The water is the main component of the human body (around ¾ of the human body consists of water on average), plants, and other organisms. Hydrogen is one of the elements that forms the water molecules and the water is the basic substance to maintain life on our planet beside the Sun.
- Petroleum materials mainly consist of carbon and hydrogen, which are extremely important sources of energy that ensure the continuity of life on the Earth, in addition to the renewable energy contribution by a small proportion, nowadays, and in the near future.
- It has been very successfully used in the production of very strong Rare Earth Permanent Magnets (REPM) worldwide since 1978 employing the Hydrogen Decrepitation (HD) process. In this process, hydrogen could be fragmented to cast Rare Earth ingots of Sm-Co and Nd-Fe-B when exposed to hydrogen gas to get very friable hydride, which is easy to mill to the required particle size prior to magnets production [21].

Table 2. Energy density of different fuels in [1] and [14]

Fuel	Energy density (MJ/kg), [14]	Energy density (MJ/kg), [1]	Av. energy density (MJ/kg)
Hydrogen	120	143	131.5
Liquefied natural gas	54.4	54	54.2
Propane	49.6	-	-
Aviation gasoline	46.8	-	-
Automotive gasoline	46.4	44	44.8
Automotive diesel	45.6	46	45.8
Ethanol	29.6	-	-
Methanol	19.6	20	19.8
Coke	27	24	25.5
Wood (dry)	16.2	16	16.1
Biogases	9.6	-	-

5. WATER FOR ELECTROLYSIS PROCESS

Freshwater is the main substance in the electrolysis of water to produce hydrogen gas. Production of freshwater from rivers, groundwater, and desalination of seawater is very costly according to the world standard level. Producing water for electrolysis at a low cost is one of the significant factors in reducing hydrogen production expenditure. Consequently, encouraging the world to use it as an alternative source of energy carrier instead of fossil fuels.

All sources of natural freshwater come to being with the formation of atmospheric moisture as water vapor by solar energy everywhere in the world. Subsequently, the hydrologic cycle (water cycle) starts to circulate itself as a natural system between the atmosphere and the Earth until the end of the Sun's epoch because the Sun is not an endless source of energy [6]. Generally, about 97.5 % of the Earth's water is briny. Around 2.5 % is freshwater, 70 % of it is ice at the polar caps, and about 30 % is atmospheric moisture. Thus, only < 1 % of the water is ready for direct use [22]. In fact, even the main cause of the natural freshwater formation on the Earth is hydrogen ions in the Sun, which consists of plasma of hydrogen ions and electrons as mentioned above. All-natural freshwater is formed by the condensation of water vapor in the

atmosphere as rainwater. Generally, the cheapest freshwater provided by electrolysis or any other methods involves a process in which water generates hydrogen, which can be summarized as follows:

- Direct rainwater collection and storage.
- Collection of drain water out of cooling air-conditioning units given that this water is a byproduct in humid areas [23]. It was found to be almost distilled water with a pH of about 7, very low electrical conductivity, and low TDS [24]. Table 3 reveals some chemical and physical parameters of the drain water released from Air Cooling systems in three Provinces of Oman, even though the TDS can be greatly reduced by filtration.
- Condensation and precipitation of water vapor take place in coastal and agricultural places worldwide, which are characterized by relatively high humidity zones, through any cooling system technique in correlation with solar or wind energy [25, 26]. Figure 1 shows monthly mean values of Relative Humidity (RH %) in the year 2019 in Sohar, which is one of the coastal cities in Oman. The trend of the curves is almost the same; the maximum value of the three curves is in July which represents the peak of summer in Oman. Also, there is a valley shape in the spring season from March to May in Oman. The mean value of the RH % in the year 2019 is about 67 %, which is too high to exploit to produce freshwater for various uses.

Table 3. Some physical and chemical analysis of drain-water released from air cooling unit in three provinces in Oman [24]

Parameters	Results: mean value of 3 samples of collecting drain-water		
	Muscat	**Sohar**	**Al-Buraimi**
Temperature (°C)	20.7	22	19.1
Turbidity (NTU)	0.57	0.94	2.1
pH	**7.01**	**6.9**	**7.01**
Electrical Conductivity, EC (µS/cm)	25.29	40.44	45.68
TDS (Total Dissolved Solids) (mg/L)	16.44	25.29	29.69
Chloride Cl^- (mg/L)	6.17	3.7	4.68
Total alkalinity (mg/L)	12.6	17	20.33
Calcium hardness (mg/L)	2.8	2.46	7.53
Total Hardness (mg/L)	4.13	3.33	7.8
NO^{-3} (mg/L)	1.03	0.39	1.42
SO_4^{-2} (mg/L)	2.47	1.73	5.82

6. PRODUCTION OF HYDRODEN BY ELECTROLYSIS USING RENEWABLE SOURCES

6.1. Production process

One of the objectives of this research is to focus on the production of hydrogen via water electrolysis as the easiest method and using renewable energy sources for electricity generation to feed the electrolysis cells. In countries where high solar intensity is abundant such as all Middle East countries, in which 90 % of the days are sunny per year. Accordingly, solar energy is the best and cheapest option for long-term plans to provide the required electricity for hydrogen production. This idea has been strongly recommended by the authors of the current article [6, 24].

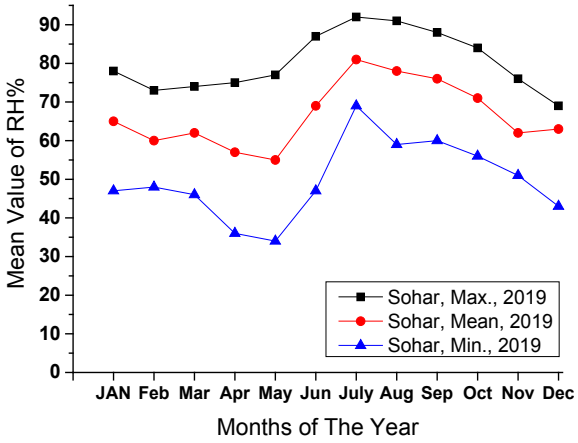

Figure 1. Monthly mean values of RH % vs. the months of 2019, Sohar, Oman

The electrolysis process of water can be defined as chemical-physical actions to split the water molecule into its hydrogen and oxygen elements by applying a direct current through the electrolysis unit. It is a chemical process because the water molecule decomposes into H and O elements and it is also a physical process because electrical energy must be provided to the electrolysis unit to generate H_2 and O_2 gases at its electrodes (cathode and anode) at room temperature. Commonly, electrodes are made of Platinum, Nickel, or Stainless Steel to avoid corrosion.

Electrolysis of water is a very practical method to produce hydrogen in correlation with the most available renewable energy sources such as PV solar panels and wind turbines. The production of hydrogen utilizing renewable energy was reported by Levene et al., Badea et al., and Bca´kova´et al. [27-29]. Historically, the electrolysis of water method to generate hydrogen gas has been known for 223 years, with its first discovery dating back to 1797 by Troostwijk and Deiman [30].

The advantages of using electrolysis route for hydrogen production over other adopted production methods include (i) being the easiest approach which can be run at room temperature, (ii) non-requirement for highly sophisticated technology, (iii) higher efficiency, and (iv) zero greenhouse gas byproduct in the case of using solar or wind energy. Figure 2 illustrates the electrolysis unit together with solar panels and wind power mill setting to provide the required electricity. The efficiency of hydrogen gas production reaches about 75 % through electrolysis [31].

According to Figure 2, the pressure of H_2 gas is twice O_2 gas pressure, because each molecule of water contains two atoms of hydrogen and one atom of oxygen and the volume of H_2 is twice the O_2 volume according to the ideal gas law:

$$P_H V_H = n_H RT \rightarrow P = \frac{n_H RT}{V_H} \quad (4)$$

where n is the number of moles and in the case of the water electrolysis, the produced moles of H_2 are twice that of O_2.

The production equation for hydrogen and oxygen gases by electrolysis route is given below:

$$2H_2O\ (aq) \xrightarrow{\text{Electrical Energy}} 2H_2\ (g) + O_2\ (g) \quad (5)$$

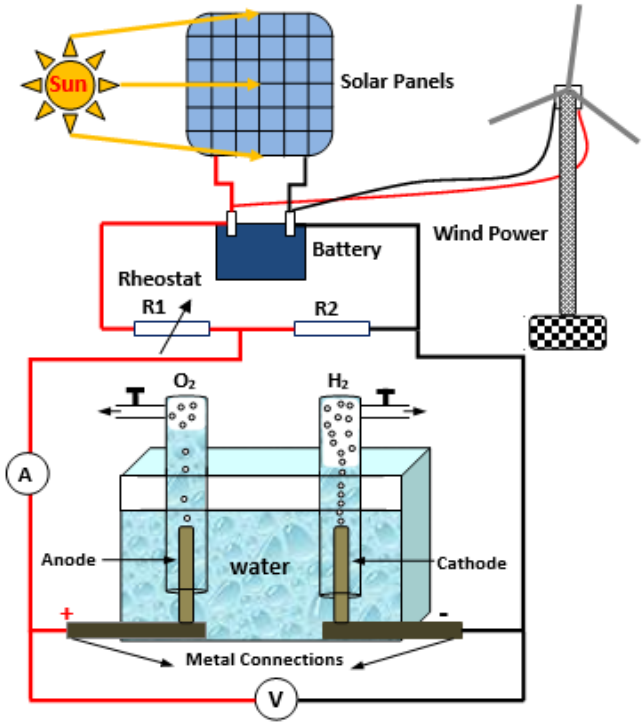

Figure 2. General proposed schematic setting of electrolysis unit of water using solar and wind power

Electricity provided by some renewable energy sources could help to provide vast amounts of hydrogen for different uses with no harmful environmental impact [32], particularly in countries that receive high solar intensity, as in the Middle East and African countries. Most territories of these countries are unused Sahara areas with very high solar intensity. As a logical consequence, such countries will likely be exporters of electricity from solar fields and of hydrogen produced by solar energy.

In Europe and other countries that have wide agricultural areas as well as those with long coastal lines, wind energy is the dominated option for hydrogen production, because different regions in such countries are characterized by pressure differences (ΔPs) and high relative humidity RH % because of water evaporation and plants transpiration process. The ΔPs will cause the formation of wind which can be utilized for electricity generation. The higher RH % value helps collect an immense quantity of water by condensation process, thus augmenting the production of green hydrogen using renewable energy. Germany in Europe is the best example of widely using wind energy on a large scale [33], and Oman in the GCC countries has a very long coastline with a length of about 3160 km and high RH % and also receives a very high solar intensity [6]. The most important factor in the production of hydrogen is electricity price, which has significant influence on the hydrogen sale price.

To understand what happens over the electrolysis process, much meditation must be given to changes to the water molecular structure. The water molecule is polar and consists of 2 H atoms and O atom, forming two electric dipoles with an angle of about 105º, as shown in Figure 3.

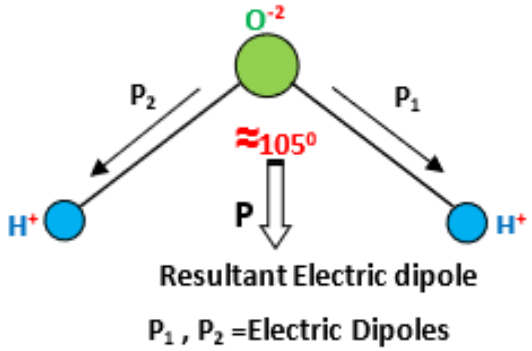

Figure 3. Ionic structure of water molecule with 2 electric dipoles P_1 and P_2

The bonds between H and O atoms in the water molecule are covalent, because the first orbit of H atom is saturated by 2 electrons and the second orbit of O atom is saturated by 8 electrons. These bonds are weak and can be broken by slight energy, of about 492 kJ/mol [34]. Meanwhile, this sort of water molecular structure will lead to formation of another type of bonds, called hydrogen bonds, due to the electrostatic reaction between the positively charged hydrogen and the negatively charged oxygen of the water molecules. These bonds are very weak within the range of 23.3 kJ/mol [34]. By using these values of energy densities and after dividing them on the Avogadro's number (~ 6.022×10^{23} atom or molecule/mole), the energy per molecule of covalent and hydrogen bonds is about 8.17×10^{-19} J/molecule and 3.87×10^{-20} J/molecule, respectively.

To generate hydrogen by electrolysis of water; covalent and hydrogen bonds of the water molecules must be broken by applying enough external electric field across the electrolysis cell. This process will occur in two stages:

Stage one

At this stage, the water dipoles will be aligned in the direction of the Applied Electric Field (**E**) due to the electrical effect between **E** and the electric charges of H^+ and O^{-2} of each dipole. As a result, electric force **F** is exerted on each charge of the electric dipoles (**F**=q **E**), **F** and **E** are written as bold letters because they are vector quantities. Consequently, the dipoles will orient according to the direction of **E**, as illustrated in Figure 4. The angle between the dipoles of H-O certainly will decrease because of the net forces exerting on H^+ and O^{-2} of each molecule. This stage represents the phase of the hydrogen bonds disjointing within a certain limit of **E**, which must be enough to align all water molecules, as shown in Figure 4. The magnitude of **E** across the electrolysis cell can be controlled by adjusting the distance d between the cathode and the anode of the cell, and the applied external potential difference V, (E=V/d), where **E** is directly proportional to V and inversely proportional to d.

Stage two

Stage two represents the rupture between water covalent bonds by increasing the applied external voltage gradually until bubbles of hydrogen and oxygen gases start to appear around the cathode and the anode of the electrolysis cell. In this period, the magnitude of **E** must be greater than the dielectric strength of the used water. Generally, the dielectric strength represents the maximum of **E** that the dielectric substance can withstand before its breakdown. The pure water is a dielectric substance with dielectric constant of 80.4 at

room temperature and dielectric strength of 6.5×10^7 V/m [35]. Figure 5 clarifies the idea of forming H_2 and O_2 gases through electrolysis route. Water with low electrical conductivity and TDS is preferred to be used in the electrolysis process to avoid the formation of some compounds on the cathode and the anode. Therefore, as noted in Table 4, the collected and released drain water from cooling air-conditioners as a byproduct is ready to be used in electrolysis cells for hydrogen production [24].

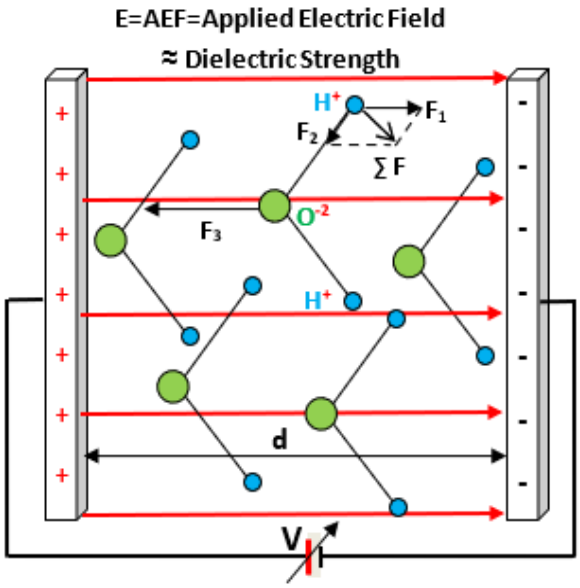

Figure 4. Full alignment of the water dipoles under the influence of **E**

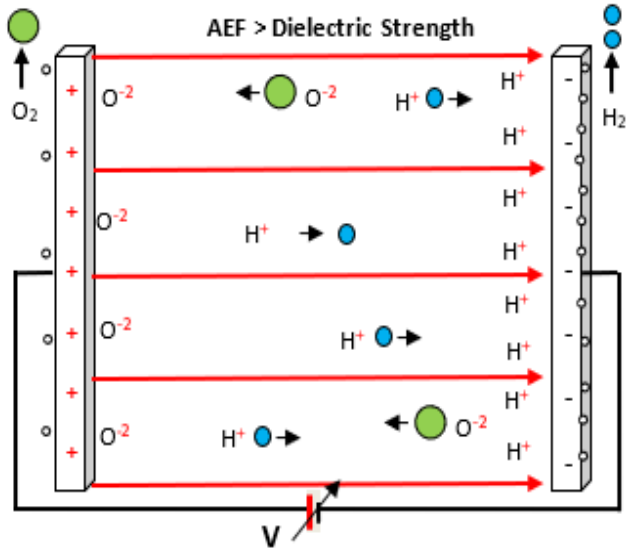

Figure 5. Splitting the molecules of the water into hydrogen and oxygen by electrolysis method

7. DETERMINING REQUIRED ENERGY TO DECOMPOSE ONE KILOGRAM OF WATER INTO OXYGEN AND HYDROGEN

7.1. Using domestic electricity

The required electricity to decompose one kilogram of H_2O can be calculated as follows:

- The total energy to break the covalent and hydrogen bonds of the water is:

E = 492 kJ/mol + 23.3 kJ/mol = 515.3 kJ/mol, as mentioned in the above information [34].

- Each kilogram of H_2O contains about 55.55 mole of water molecules; hence, the total required energy for electrolysis one kg of water is:

E = (515.3 kJ/mol)(55.55 mol) ≈ 28625 kJ

- Energy unit factor is converted as follows:

1 kWh = 3.6×10^3 kJ

- Therefore, the energy (kWh) for electrolysis of one kg of water is:

1 kWh = 3.6×10^3 kJ

$$x \qquad 28625\ \text{kJ} \quad \rightarrow \quad x = \frac{(1\ \text{kWh})(28625\ \text{kJ})}{3.6 \times 10^3\ \text{kJ}} \approx 8\ \text{kWh}$$

- Given that the energy price of one kWh in Oman is 15 Pisa on average in Oman, the cost of converting one kg of water into H_2 and O_2 gases is (8 kWh × 15 Pisa/kWh = 120 Pisa = 0.12 RO, RO = Rial Omani). Each kilogram of water contains about 112 g of hydrogen and about 888 g of oxygen; therefore, the cost of producing one kg of hydrogen by electrolysis route is as follows:

$$\frac{\text{Mass of H}}{112\ \text{g}} \quad \frac{\text{Cost in RO}}{0.12\ \text{RO}}$$

$$1000\ \text{g/kg} \qquad x \quad \rightarrow \quad x = \frac{(0.12\ \text{RO})(1000\ \text{g/kg})}{112\ \text{g}} \approx 1.07\ \text{RO/kg}$$

1 Rial Omani equal 2.6 US Dollar as an average of 2020; thus, the cost to produce one kg of hydrogen in the US Dollar is 1.07 RO/kg × 2.6 $/RO = 2.78 $/kg. These are theoretical calculations; however, in practice, the cost may be much more or less depending on the experimental work and electricity price during the production stage. Also, the almost pure byproduct oxygen gas that is generated during the electrolysis process will be definitely used in industrial and health sectors instead of the industrial one.

7.2. By using solar electricity

In Oman, the Authority for Electricity Regulation (AER) in March 2018 has approved the grid-connected PV incentives. Any surplus power exported back into the grid will be remunerated at prevailing Bulk Supply Tariffs (BST), which are higher than the electricity tariffs for residential customers − a feature designed to incentivize the rollout of rooftop solar capacity under the Authority's "Sahim" initiative.

The cost of energy is calculated based on the "Sahim" initiative. The costs of Grid-Connected Photovoltaic (GCPV) systems specified by the AER are as follows: 0.879, 0.805, and 0.776 USD for 1-10 kWp, 10-100 kWp, and 100-500 kWp, respectively. Table 4 shows the Cost of Energy (CoE) compared with studies in Oman. It is worth mentioning that the cost specified by the AER is relatively high.

From Table 4, the calculated revenue for grid-connected PV systems in different sites of Oman is promising for PV system installation due to the higher solar energy available than that in other sites. In addition, it is noted that the authors of [36-40] did not consider the production reduction due to system age. In other words, the CoE in these researches could be higher than the stated one in the case of considering this important issue.

Table 4. PV systems' cost of energy comparison

Ref.	Year	Location	PV power	Cost of generated kWh ($)	Cost of generated kWh (RO)
[36]	2011	Oman	10 kW	0.2100	0.081
[37]	2011	Oman	5 MW	0.3270	0.125
[38]	2012	Oman	50 kW	0.2060	0.079
[39]	2017	Oman	1 MW	0.2258	0.086
[40]	2019	Oman	1.4 kW	0.0450	0.017
AER CoE	2018	Oman	-	0.7760	0.298

Therefore, using solar energy, the production cost of hydrogen is calculated:

$$\frac{\text{Mass of H}}{112\text{ g}} \quad \frac{\text{Cost in RO}}{0.298\text{ RO}}$$

$$1000\text{ g/kg} \quad x \quad \rightarrow \quad x = \frac{(0.298\text{ RO})(1000\text{ g/kg})}{112\text{ g}} \approx 2.66\text{ RO/kg}$$

However, this cost is relatively high since it depends on the selling of electricity to the grid. If a standalone solar system is used and is dependent on the highest and lowest costs published by [37] and [40], respectively, the cost will be as follows:

$$\frac{\text{Mass of H}}{112\text{ g}} \quad \frac{\text{Cost in RO}}{0.125\text{ RO}}$$

$$1000\text{ g/kg} \quad x \quad \rightarrow \quad x = \frac{(0.125\text{ RO})(1000\text{ g/kg})}{112\text{ g}} \approx 1.11\text{ RO/kg}$$

This value in [37] is in good agreement with our calculation above when using the domestic electricity price.

$$\frac{\text{Mass of H}}{112\text{ g}} \quad \frac{\text{Cost in RO}}{0.017\text{ RO}}$$

$$1000\text{ g/kg} \quad x \quad \rightarrow \quad x = \frac{(0.017\text{ RO})(1000\text{ g/kg})}{112\text{ g}} \approx 0.151\text{ RO/kg}$$

The last value in [40] (0.151 RO/kg is about 0.4 $/kg) points to a very promising method to produce hydrogen using solar energy and is probably reduced over long-term use. This value represents the lowest cost of hydrogen production worldwide.

8. THE FUTURE VISUALIZATION OF USING HYDROGEN AS AN ENERGY CARRIER

The great advantage of using hydrogen as a future energy carrier fuel is two-fold: its high availability in the Earth's water and its burning with oxygen yields water as a byproduct. Also, the hydrogen fuel cell automobiles are classified by zero harmful greenhouse gases emission. It appears that hydrogen as an alternative energy carrier has the following advantages over the fossil fuels:

- It is very environment friendly as its combustion feedback is water byproduct.
- The byproduct water can be reused to generate hydrogen gas again and consequently; the hydrogen production cycle repeats itself using many renewable energy sources.
- Globally, more abundant than any other element can be used as an energy carrier fuel.
- Hydrogen energy density is greater than that of fossil fuels by about 2.4 times (Please see Table 2). It is characterized by the highest energy density among other energy sources.
- It can be produced using many methods and different energy sources, either renewable or ordinary.
- Hydrogen contributes to solving energy scarcity problems worldwide in intermediate- and long-term scenario plans, say 2040-2050.
- The production cost will decrease upon reducing renewable energy price with the passage of time such as solar and wind energy.
- It can be used as liquid or gas in many domestic sectors and industry such as power generation or fuel cells that convert chemical energy into electrical energy to run engines such as trucks, trains, cars, etc.

Figure 6 accentuates a general idea about hydrogen production by electrolysis route using condensed water from atmospheric moisture and electricity generated by solar or wind energy.

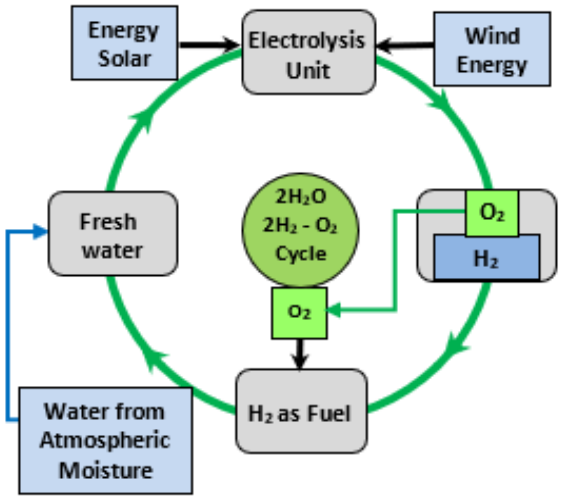

Figure 6. A general scheme of water-hydrogen-oxygen-fuel cycle by electrolysis together with solar and wind energy

In 2019, very essential details of production routes and the future of using hydrogen in many energy sectors were almost fully reported by the IEA (International Energy Agency) [41]. In April 2020, Bill Ireland urged the world seriously to adopt hydrogen as a future green fuel to overcome the global greenhouse effect [42]. According to the recent report of the International Renewable Energy Agency in September 2019, the production cost of hydrogen utilizing solar and wind energy will be very competitive to fossil fuels during the coming five years. The report also revealed that the cost of green hydrogen would be less than that produced from fossil fuels in the period of 2030-2040 [43]. Figure 7 projects the general view of hydrogen production cost via solar and wind energy up to 2050, from which it could be seen that the cost is always less upon using wind energy. Generally, the production cost decreases with time for the two cases because of technological development in these two important fields of renewable energy applications.

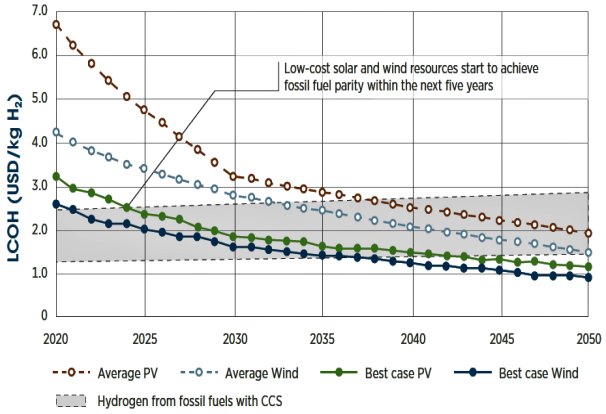

Figure 7. The production cost of hydrogen with years using solar and wind energy; LCOH: Levelized Cost of Hydrogen; CCS: Carbon Capture and Storage [43]

Very important visions about hydrogen as a renewable source of energy were proposed by Pareek et al. in 2020 [44]. They confirmed that hydrogen was the most attractive option of renewable source to replace fossil fuels, that are inevitably declining with time, in addition to no environmental harm when using green-hydrogen as a fuel.

9. RESULTS AND DISCUSSION

Hydrogen, as the most abundant Earth element, has been theoretically estimated depending on the whole water reserves in the Earth, excluding the mantle water, which is very deep into the Earth's crust. The obtained result showed that the quantity of hydrogen of the Earth was much greater than the world oil reserves by about 5×10^5 times. Economically, this finding is remarkable and it makes hydrogen ready as an energy carrier to ensure its adoption as the alternative to fossil fuels when required. In addition, some important features of hydrogen are summarized to highlight the research of this field.

It is proven that finding freshwater with low price, or free of charge, as a byproduct from any physical activities is very essential to reduce the production cost of hydrogen and oxygen gases by electrolysis technique. Therefore, using the byproduct-gained water from any air-cooling system in humid areas certainly will reduce the production cost of hydrogen in any way. Technically and comparatively, using almost distilled water, as shown in Table 3, is more reliable than wastewater, used in the biohydrogen method to generate hydrogen [15, 16].

A deeper study on the electrolysis of water to produce hydrogen and oxygen gases is still very necessary for researchers in this field to demonstrate the physical water structure variations via the influence of DC current. The energy to split water molecules into hydrogen and oxygen after breaking the covalent and hydrogen bonds of the water was theoretically calculated, which is a very important attempt to understand the electrolysis process better.

The cost of producing one kilogram of hydrogen by water electrolysis method through the proposed theoretical framework of ours and based on the present price of electricity in Oman was determined to be about 2.8 $/kg. This cost is quite reasonable compared with those in other relevant researches [27, 37, 40]. Furthermore, this study proved the lowest cost of hydrogen production so far by using recent solar energy price in Oman, which was about 0.4 $/kg as a very significant novel result.

The general conclusion is that hydrogen is a very encouraging energy carrier to replace the fossil fuels, which are already depleting with time. Meanwhile, using hydrogen in different sectors on a large scale will contribute to the reduction of greenhouse harm gases and global enhancement of the environmental quality.

10. CONCLUSIONS

The novelty of the article can be given as follows:

(i) The whole hydrogen mass of the Earth's water without mantle part was calculated and found to be much greater than the world oil reserves by about 9×10^5 times.
(ii) Much attention was given to the production of green hydrogen by water electrolysis and using solar and wind energy as a very promising energy carrier instead of fossil fuels.
(iii) The water molecular structure and its change were thoroughly investigated under the influence of the AEF during the water electrolysis process.
(iv) The production cost of hydrogen utilizing normal electricity of Oman and solar electricity was studied for comparison purposes. A production cost of one kg of hydrogen gas by electrolysis method was calculated and found to be about 0.4 $/kg, depending on recent information about price of solar energy. However, using the present electricity price of Oman showed a reasonable value of around 2.8 $/kg.

Also, the following general findings can be concluded:

- Hydrogen is a very reliable energy carrier as an alternative to fossil fuels presently and in the future.
- Solar and wind energy is recommended to be utilized to provide the required electricity to run the electrolysis cells to generate H_2 and O_2.
- The byproduct oxygen gas of the electrolysis method certainly will be used in industrial and health sectors.
- Production cost of hydrogen will be reasonable in long-term plans using renewable energy sources with much less greenhouse effect.
- The required water for electrolysis process could be produced from atmospheric moisture in different ways such as the byproduct drain water of air-conditioner units in humid places, leading to a decrease in the production cost of hydrogen.

11. ACKNOWLEDGEMENT

The authors gratefully thank the Public Authority for Water, Al-Buraimi Province, Oman for their kind support. The authors also would like to thank Mr. Shahjahan Bhatti of the Center of Foundation Study, University of Buraimi, Oman, for helpful proofreading and support.

REFERENCES

1. van de Karol, R. and Grätzel, M., Photoelectrochemical hydrogen production, Electronic Materials: Science & Technology, Springer, Boston, (2012). (https://doi.org/10.1007/978-1-4614-1380-6).
2. Horton, S., "The 1973 oil crisis". (http://www.docdatabase.net/more-the-1973-oil-crisis-by-sarah-horton-473476.html).
3. Rüdiger, M., "The 1973 oil crisis and the designing of a Danish energy policy", ***Historical Social Research***, Vol. 39, No. 4, (2014), 94-112. (https://doi.org/10.12759/hsr.39.2014.4.94-112).

4. The International Renewable Energy Agency (IRENA), "Global energy, transformation, A roadmap to 2025", Report, (2018). (https://www.irena.org//media/Files/IRENA/Agency/Publication/2018/Apr/IRENA_Report_GET_2018.pdf).
5. Zhai, Y., "It's clean, powerful and available: Are you ready for hydrogen energy?", ***Renewable Energy World***, (2019). (https://www.renewableenergyworld.com/2019/06/06/its-clean-powerful-and-available-are-you-ready-for-hydrogen-energy/#gref).
6. Moosa, I.S. and Kazem, H.A., "Review of basic renewable energy in GCC countries: Current status and future vision", ***International Journal of Computation and Applies Science***, Vol. 6, No. 1, (2019), 397-406. (https://www.researchgate.net/publication/331175791_Review_of_Basic_Renewable_Energy_in_GCC_Countries_Current_Status_and_Future_Vision).
7. The International Renewable Energy Agency (IRENA), "Hydrogen from renewable power technology outlook for the energy transition", Report, (2018). (https://www.irena.org//media/Files/IRENA/Agency/Publication/2018/Sep/IRENA_Hydrogen_from_renewable_power_2018.pdf).
8. Martens, J., "KU Leuven scientists crack the code for affordable, eco-friendly hydrogen gas", (2019). (https://nieuws.kuleuven.be/en/content/2019/belgian-scientists-crack-the-code-for-affordable-eco-friendly-hydrogen-gas), (Accessed: October 2020).
9. Holladay, J.D., Hu, J., King, D.L. and Wang, Y., "An overview of hydrogen production technologies", ***Catalysis Today***, Vol. 139, No. 4, (2009), 244-260. (https://doi.org/10.1016/j.cattod.2008.08.039).
10. Bičáková, O. and Straka, P., "The resources and methods of hydrogen production", ***Acta Geodynamica et Geomaterialia***, Vol. 7, No. 2, (158) (2010), 175-188. (https://www.researchgate.net/publication/269705182_The_resources_and_methods_of_hydrogen_production).
11. Abdol Rahim, A.H., Tijani, A., Wan Mohamed, W.A.N., Hanapi, S. and Sainan, I., "An overview of hydrogen production from renewable energy source for remote area application", ***Applied Mechanics and Materials***, Vol. 699, (2015), 474-479. (https://doi.org/10.4028/www.scientific.net/AMM.699.474).
12. Li, Z., Guo, P. and Sun, H., "Current status and development trend of wind power generation based on hydrogen production technology", ***Energy Exploration & Exploitation***, Vol. 35, No. 1, (2019), 5-25. (https://doi.org/10.1177/0144598718787294).
13. Kumar, S.S. and Himabindu, V., "Hydrogen production by REM water electrolysis–A review", ***Materials Science for Energy Technologies***, Vol. 2, No. 3, (2019), 442-454. (https://doi.org/10.1016/j.mset.2019.03.002).
14. El-Shafie, M., Kambara, S. and Hayakawa, Y., "Hydrogen production technologies overview", ***Journal of Power and Energy Engineering***, Vol. 7, (2019), 107-154. (https://doi.org/10.4236/jpee.2019.71007).
15. Saravanan, A., Karishma, S., Senthil Kumar, P., Yaashikaa, P.R., Jeevanantham, S. and Gayathri, B., "Microbial electrolysis cells and microbial fuel cells for biohydrogen production: Current advances and emerging challenges", ***Biomass Conversion and Biorefinery***, (2020), 1-21. (https://doi.org/10.1007/s13399-020-00973-x).
16. Samsudeen, N., Spurgeon, J., Matheswaran, M. and Satyavolu, J., "Simultaneous biohydrogen production with distillery wastewater treatment using modified microbial electrolysis cell", ***International Journal of Hydrogen Energy***, Vol. 45, No. 36, (2020), 18266-18274. (https://doi.org/10.1016/j.ijhydene.2019.06.134).
17. Genda, H., "Origin of Earth's oceans: An assessment of the total amount, history and supply of water", ***Geochemical Journal***, Vol. 50, (2016), 27-42. (http://doi.org/10.2343/geochemj.2.0398).
18. Descalzi, C., "World oil review", O & GR, Vol. 1, (2019). (https://www.eni.com/assets/documents/documents-en/WORLD-OIL-REVIEW-2019-Volume-1.pdf), (Accessed: Novmber 2020).
19. Alomair, O., Jumaa, M., Alkoriem, A. and Hamed, M., "Heavy oil viscosity and density prediction at normal and elevated temperatures", ***Journal of Petroleum Exploration and Production Technology***, Vol. 6, **(**2016), 253-263. (https://doi.org/10.1007/s13202-015-0184-8).
20. Wu, J., Desch, S.J., Schaefer L., Elkins-Tanton, L.T., Pahlevan, K. and Buseck, P.R., "Origin of Earth's water: Chondritic inheritance plus nebular in gassing and storage of hydrogen in the core", ***American Geophysical Research: Plants***, (2018), 1-22, (https://doi.org/10.1029/2018JE005698).
21. Moosa, I.S., "Hydrogen Decrepitation (HD), history and application in the production of permanent magnets", ***International Journal of Advanced Research in Engineering and Technology (IJARET)***, Vol. 7, No. 5, (2016), 37-44. (https://iaeme.com/MasterAdmin/Journal_uploads/IJARET/VOLUME_7_ISSUE_5/IJARET_07_05_005.pdf).
22. Eslami, M., Tajeddini, F. and Etaati, N., "Thermal analysis and optimization of a system for water harvesting from humid air using thermoelectric coolers", ***Energy Conversion and Management***, Vol. 174, (2018), 417-429. (https://doi.org/10.1016/j.enconman.2018.08.045).
23. Moosa I.S., Maqableh, B.B. and Alattar, N., "Production of fresh water from drain-water released from cooling air-conditioning systems: Experimental and analysis studies", ***International Journal of Computation and Applied Sciences (IJOCAAS)***, Vol. 5, No. 1, (2018), 350-355. (https://www.researchgate.net/publication/327845946_Production_of_fresh_water_from_drainwater_released_from_cooling_airconditioning_systems_experimental_and_analysis_studies).
24. Moosa I.S., Al-Iessi, L.M.R. and Kazem, H.A., "Freshwater production and solar disinfection of water released from the air-conditioning cooling system: an experimental investigation", ***Renewable Energy and Environmental Sustainability***, Vol. 5, No. 9, (2020), 1-10. (https://doi.org/10.1051/rees/2020004).
25. Ekad, A., Pawar, T., Yeole, N., Taksale, A. and Gajjar, A., "Solar powered atmospheric water generator and overview on AWG technologies", ***International Journal of Innovative Research in Science, Engineering and Technology***, Vol. 7, No. 1, (2018), 71-79. (https://doi.org/10.15680/IJIRSET.2018.0701006).
26. Mahal, S.K. and Alimin, A.J., "Experimental investigation on a novel integrated solar chimney and liquid desiccant system for simultaneous power and fresh water generation", ***International Energy Journal*** , Vol. 20, (2020), 67-86. (https://www.researchgate.net/publication/340525947).
27. Levene, J.I., Mann, M.K., Margolis, R. and Milbrandt, A., "An analysis of hydrogen production from renewable electricity sources", ***National Renewable Energy Laboratory, Proceedings of ISES 2005 Solar World Congress***, Orlando, Florida, *NREL*/CP-560-37612, (2005), 1-7. (https://www.nrel.gov/docs/fy05osti/37612.pdf).
28. Badea, G., Naghiu, G.S, Giurca, I., Aşchilean, I. and Megyesi, E., "Hydrogen production using solar energy-technical analysis", ***Energy Procedia***, Vol. 112, (2017), 418-425. (https://doi.org/10.1016/j.egypro.2017.03.1097).
29. Bičáková, O. and Straka, P., "Production of hydrogen from renewable resources and its Effectiveness", ***International Journal of Hydrogen Energy***, Vol. 37, (2012), 11563-11578. (http://doi.org/10.1016/j.ijhydene.2012.05.047).
30. de Levie, R., "The electrolysis of water", ***Journal of Electroanalytical Chemistry*** ,Vol. 476, (1999), 92-93. (https://hofstedesterreschans.nl/wp-content/uploads/2020/01/The-electrolysis-of-water.pdf).
31. Edwards, P.P., Kuznetsov, V.L. and David, W.I.F., "Hydrogen energy", ***Philosophical Transactions of the Royal Society A***, Vol. 365*,* (2007), 1043-1056. (https://doi.org/10.1098/rsta.2006.1965).
32. Bartels, J.R., Pate, M.B. and Olson, N.K., "An economic survey of hydrogen production from conventional and alternative energy sources", ***International Journal of Hydrogen Energy***, Vol. 35, (2010), 8371-8384. (https://doi.org/10.1016/j.ijhydene.2010.04.035).
33. Birol, F., "Germany 2020, Energy policy review", ***International Energy Agency***, Report, (2020). (https://www.bmwi.de/Redaktion/DE/Downloads/G/germany-2020-energy-policy-review.pdf?__blob=publicationFile&v=4).
34. Chaplin, M., "Water's hydrogen bond strength", Cornell University, (2007), 1-20. (https://arxiv.org/ftp/arxiv/papers/0706/0706.1355.pdf).
35. Bauer, W. and Westfall, G.D., University physics with modern physics, McGraw-Hill, New York, USA, (2011), 789.
36. Al-Ismaily, H.A. and Douglas P., "Photovoltaic electricity prospects in Oman", ***Applied. Energy***, Vol. 59, No. 2-3, (1998), 97-124. (https://doi.org/10.1016/S0306-2619(98)00007-5).
37. Al-Badi, A.H., Albadi, M.H., Al-Lawati, A.M. and Malik, A.S., "Economic perspective of PV electricity in Oman", ***Energy***, Vol. 36, No. 1, (2011), 226-232. (https://doi.org/10.1016/j.energy.2010.10.047).
38. Al-Badi, A.H., AL-Toobi, M., AL-Harthy, S., Al-Hosni, Z. and AL-Harthy, A., "Hybrid systems for decentralized power generation in

Oman", ***International Journal of Sustainable Energy***, Vol. 31, No. 6, (2012), 411-421. (https://doi.org/10.1080/14786451.2011.590898).

39. Humada, A.M., Aaref, A.M., Hamada H.M., Sulaiman, M.H., Amin, N. and Mekhilef, S., "Modeling and characterization of a grid-connected photovoltaic system under tropical climate conditions", ***Renewable Renewable and Sustainable Energy Reviews***, Vol. 82, Part 3, (2018), 2094-2105. (https://doi.org/10.1016/j.rser.2017.08.053).
40. Kazem, H.A., Yousif, J., Chaichan, M.T. and Al-Waeli, A.H.A., "Experimental and deep learning artificial neural network approach for evaluating grid-connected photovoltaic systems", ***International Journal of Energy Research***, Vol. 43, No. 14, (2019), 8572-8591. (https://doi.org/10.1002/er.4855).
41. "The future of hydrogen seizing today's opportunities", Report prepared by the IEA for the G20, Japan, (2019), 1-199. (http://ir.qibebt.ac.cn/bitstream/337004/10838/120/IEA%EF%BC%9AThe%20Future%20of%20Hydrogen%20Seizing%20Today%E2%80%99s%20Opportunities.pdf).
42. Ireland, B., "Green hydrogen: The clean fuel of our dreams?", ***Renewable Energy World***, (2020). (https://www.renewableenergyworld.com/hydrogen/green-hydrogen-the-clean-fuel-of-our-dreams/#gref), (Accessed: September 2020).
43. Gielen, D., Taibi, E. and Miranda R., "Hydrogen: A renewable energy prospective", ***The International Renewable Energy Agency (IRENA)***, Report prepared for the 2nd Hydrogen Energy Ministerial Meeting in Tokyo, Japan, (2019), 1-51. (https://www.researchgate.net/publication/339788120).
44. Pareek, A., Dom, R., Gupta, J., Chandran, J., Adepu, V. and Borse, P.H., "Insights into renewable hydrogen energy: Recent advances and prospects", ***Materials Science for Energy Technologies***, Vol. 3, (2020), 319-327. (https://doi.org/10.1016/j.mset.2019.12.002).

Journal of Renewable Energy and Environment

Research Article

Journal Homepage: www.jree.ir

Effect of Covering Aperture of Conical Cavity Receiver on Thermal Performance of Parabolic Dish Collector: Experimental and Numerical Investigations

Sina Eterafi [a], Shiva Gorjian [a*], Majid Amidpour [b]

[a] *Department of Biosystems Engineering, Factuly of Agriculture, Tarbiat Modares University (TMU), P. O. Box: 14115-111, Tehran, Tehran, Iran.*
[b] *Department of Energy System Engineering, Factuly of Mechanical Engineering, K. N. Toosi University of Technology, P. O. Box: 19395-1999, Tehran, Tehran, Iran.*

PAPER INFO

Paper history:
Received 06 April 2021
Accepted in revised form 10 August 2021

Keywords:
Experimental Analysis,
Conical Cavity Receiver,
Ultra-White Glass Cover,
Parabolic Dish Concentrator

ABSTRACT

In this study, the effect of covering the aperture area of a conical cavity receiver with an ultra-white glass on operational parameters of a Parabolic Dish Collector (PDC) was numerically and experimentally investigated under climate conditions of Tehran (35.44° N latitude and 51.10° longitude). The main components of the experimental setup include a dish reflector, a conical cavity receiver, Heat Transfer Fluid (HTF), hydraulic and cooling cycle, and a sun tracker. For this purpose, a conical cavity receiver with an ultra-white glass cover on its aperture was numerically modeled in Fortran software. During the evaluation, environmental parameters including ambient temperature, solar radiation, and wind speed were considered as inputs of the model. The results revealed fair agreement between the numerical and experimental data with the maximum error of approximately 4.63 % and 7.89 % for receivers with and without the glass cover on the aperture, respectively. For a steady-state analysis, the mean values of useful energy ($\dot{Q}_u$) absorbed by the receiver were calculated as 1,253.25 W and 987.68 W, while thermal efficiency (η_{th}) of the receiver was calculated as 52.61 % and 40.69 % for receivers with and without glass cover, respectively. The results revealed that both η_{th} and $\dot{Q}_u$ followed a similar trend of the variations in the HTF's temperature between the inlet and outlet of the receiver. Also, the overall heat loss coefficient (U_l) and the collector heat removal factor (F_r) were calculated as 420.76 W/m^2°C and 0.62 for the conical cavity receiver with the glass cover.

https://doi.org/10.30501/jree.2021.275871.1194

1. INTRODUCTION

Solar energy is the most abundant and freely available renewable energy source. In geographical regions with higher potential of solar energy, this renewable source can be considered as the best alternative to fossil fuels in distributed generation systems [1, 2]. Harnessing solar energy using thermal devices such as collectors and concentrators can be done in various applications including electric power generation systems, heating and cooling applications, cogeneration and direct thermal applications, desalination, and thermochemical operations [3-5]. Parabolic Dish Concentrators (PDCs) offer higher thermal performance than other solar collectors due to their high concentration ratio and employing two-axis tracking systems, causing them to achieve a high temperature range up to 1200 °C [6-8]. The most important component of PDCs which has been widely evaluated in the literature is the receiver. In a PDC, to achieve high temperature ranges, reducing the heat loss of the receiver is of particular importance. Also, among different types of receivers employed in PDCs including external, cavity, and flat, the efficiency of the cavity has been reported as the highest one with the lowest level of heat loss [9-11]. Different values of thermal efficiencies have been reported for cavity receivers due to their different geometries and shapes. According to the literature, cylindrical, conical, hemispherical, and cubical have been reported as the most common types of cavity receivers employed in PDCs [12]. In this regard, several studies have been conducted to improve the thermal performance of PDCs and their embedded components as a whole.

1.1. Literature review

Pavlovic et al. [13] conducted numerical and experimental investigations to evaluate the thermal performance of a flat spiral tube receiver. In this study, numerical results were compared with the experimental data obtained from a conical cavity receiver. They concluded that the heat loss rate from a flat spiral tube receiver was much higher than that of a cavity receiver with an efficiency of about 34 %. Li et al. [14] developed a numerical Computational Fluid Dynamic (CFD) model to investigate the thermal efficiency of a conical cavity receiver employed in a heliostat system. They reported that at the constant flow rate of Heat Transfer Fluid (HTF), changes in the temperature for the inlet and outlet of the receiver from 81 K to 181 K would lead in the thermal efficiency from 39 %

*Corresponding Author's Email: gorjian@modares.ac.ir (Sh. Gorjian)
URL: https://www.jree.ir/article_134895.html

Please cite this article as: Eterafi, S., Gorjian, Sh. and Amidpour, M., "Effect of covering aperture of conical cavity receiver on thermal performance of parabolic dish collector: Experimental and numerical investigations", ***Journal of Renewable Energy and Environment (JREE)***, Vol. 8, No. 4, (2021), 29-41. (https://doi.org/10.30501/jree.2021.275871.1194).

to 60 %. Alhsani and Al-Dulaimi [15] performed an experimental comparative study of three geometries of conical, oval, and cylindrical receivers. The study was performed at three levels of flow rate and five levels of the HTF's temperature at the inlet of the receiver. It was observed that the conical cavity receiver had the maximum energy and exergy efficiencies of 82.1 % and 23.76 %, respectively. Pavlovic et al. [16] performed both experimental and numerical studies for two cavity receivers with the shapes of flat, spiral and conical and the results were compared. They also optimized the location of the receiver at the focal point of the PDC. It was observed that the conical cavity receiver had an optical efficiency of 1.38 % at the surface temperature of 200 °C with energy and exergy efficiencies of 40.45 % and 42.06 %, respectively, which was higher than those of the flat spiral receiver. In different studies, Daabo et al. [17-19] investigated three cylindrical, spherical, and conical cavity receivers by performing a numerical study using the CFD method and compared the obtained results. These studies investigated the effects of the helical tube, covering the aperture of the receiver with clear glass, and environmental parameters on the performance of the receivers. Results indicated that the optical efficiency of the conical cavity receiver was 8 % and 13 % and thermal efficiency was 8 % and 15 % higher than those of the cylindrical and spherical receivers, respectively. They also reported about a 7 % increase in thermal efficiency when the receiver aperture was covered with glass.

Azzouzi et al. [20] performed experimental and numerical investigations of cylindrical cavity receivers with an outer concrete insulation layer considering zero thermal losses from the insulated surface. In this study, the effects of the inclination angle of the receiver and variations in the Nusselt number (Nu) of wind streams on the heat loss of the interior wall of the cavity were investigated. The numerical results pointed to good agreement with a maximum 12 % deviation from the results obtained from experimental investigations. Loni et al. [21] performed both experimental and numerical studies for two cubical cavity receivers and the obtained results were compared with those obtained from cylindrical and cubical receivers. They concluded that the cubical cavity receiver offered about 9 % more thermal performance than the cylindrical receiver. Singh and Kumar Natarajan [22] compared the results of numerical models of two modified conical and hemispherical receivers models using Comsol software. It was observed that with the modified shape of the receiver aperture, the highest efficiency of 84.7 % was obtained for the conical receiver. Yuan et al. [23] performed both numerical and experimental studies and compared a type of cavity receiver with a convex end surface with a simple type of receiver. It was observed that the thermal efficiency of the receiver with the convex end surface was 6.02 % higher than that of the simple type. Bopche et al. [24] conducted an experimental study and compared a semi-spherical modified hollow receiver with its simple type. In this study, conical blades were used on the inner surface of the cavity to absorb more heat. It was observed that the thermal efficiency of the modified receiver increased by 23.5 %.

Bellos et al. [25] performed a numerical comparative study using the CFD method to achieve optimal geometry and maximum thermal efficiency of cylindrical, conical, spherical, cubical, and cylindro-conical receivers. They considered the diameter, length, pitch, and thickness of the adsorbent tube as optimization parameters. According to the results, the cylindro-conical receiver indicated the maximum optical efficiency of 85.42 %, the thermal efficiency of 67.95 %, and the maximum exergy efficiency of 35.73 %. They also introduced the conical geometry as the one with the best performance and the least performance for the cubical geometry. Soltani et al. [26] performed an experimental and numerical study of a cylindrical cavity receiver by developing a thermo-optical model. In this study, the effects of environmental parameters, the focal length of the concentrator, and variations in temperature and flow rate of the HTF on the thermal performance of the receiver were evaluated. They concluded that the operation of the receiver under optimal conditions increased the thermal efficiency up to 65 %. Thirunavukkarasu and Cheralathan [27] conducted an experimental study on a flat spiral tube receiver employed in a PDC. This study was conducted in different radiation conditions and for different temperature and flowrate values of the HTF. From the results, the energy and exergy efficiencies of the receiver were calculated as 56.21 % and 5.45 % at the average direct radiation of 750 W/m^2, respectively. Wang et al. [28] conducted an experimental and numerical study of three different geometries of the cavity receiver used in a food-grade Fresnel lens system. In this study, to increase the optical efficiency and better distribution of radiant flux in three cylindrical, spherical, and conical geometries, a metal cone reflector was used at the end of all three cavity holes. This metal cone reflector eventually caused a less than 2 % and 4 % increase in the optical efficiency of conical and spherical receivers, respectively.

Al-Dulaimi [29] conducted an experimental study of a flat-tube receiver with two layers of the absorbent tube employed in a PDC. The results indicated that the energy and exergy efficiencies of the system were 78.8 % and 19.8 %, respectively. Loni et al. [30] conducted an experimental and numerical comparative study among three hemispherical, cylindrical, and cubical cavity receivers. They also reviewed different types of cavity receivers used in PDCs. They used three types of nanomaterials based on thermal oil as HTFs. The results indicated that the use of nanomaterials in HTFs increased the thermal efficiency of each type of cavity receiver. Also, approximately 12.9 %, 5.84 %, and 1.44 % increases in efficiency were observed for hemispherical, cubical, and cylindrical receivers, respectively.

According to the literature, it was observed that several experimental and numerical studies were conducted on the optimization of geometry, increasing the values of energy and exergy efficiency and reducing the optical and thermal losses of cavity receivers. However, the employment of a conical cavity receiver in a PDC using thermal oil as the HTF was not experimentally investigated. Also, the thermal performance of the receiver with and without ultra-white glass cover on the aperture was experimentally and numerically investigated and profoundly discussed. The results of the current study could be used as a guide for the improvement of PDCs employed in different solar thermal applications using conical cavity receivers.

2. MATERIAL AND METHODS

2.1. Experimental setup

The experimental tests were conducted at the Renewable Energy Research Institute (RERI) of Tarbiat Modares University (TMU) located in Tehran (at 35.44° N latitude and 51.10° longitude), Iran. The developed solar collector in this

study consists of the main structure, a parabolic dish reflector, a conical cavity receiver, a hydraulic circuit, and a tracker system. The PDC is made of small pieces of mirrors (4 cm × 4 cm) sticking to a parabolic dish made of fiberglass. The dimensional characteristics of the reflector are presented in Table 1.

Table 1. Geometric parameters of the PDC used in the current study [7]

Parameter	Value
Aperture diameter	1.9 m
Focal length	1.35 m
Rim angle	36°
Reflectivity	0.84
Tracking error	1°
Concentration ratio	184

The conical cavity receiver was constructed according to the optimal dimensions reported in Refs. [31] and [32]. The preparation of the conical receiver was performed in four steps. First, the copper tube as an absorber tube was made in the form of springy and helical to create a conical shape. The cone angle of the receiver was chosen according to the geometry reported in Ref. [32]. The surface of the copper tube was coated with carbon black and matte refractory black paint (Ambrosol brand) to increase the absorptivity and reduce the reflectivity of the inner wall of the cavity. In the next step, the outer surface of the conical cavity receiver was completely covered with rock wool thermal insulation to minimize heat losses. Finally, the aperture of the receiver was covered with ultra-white glass to separate the inside and outside spaces of the cavity and reduce convective losses from the aperture of the receiver. The geometric characteristics of the conical receiver are presented in Table 2. Also, the images of the experimental setup along with the main components are shown in Figure 1a.

Table 2. Specifications of the cavity receiver

Parameter	Data
Cavity aperture's diameter (D_{ap})	14 cm
Diameter of the receiver (D_{ca})	18 cm
Length of the receiver (l)	14 cm
Outer diameter of the absorber tube (D)	11 mm
Inner diameter of the absorber tube (D_i)	9 mm
Pitch of the spiral coil	12 mm
Cone angle of the receiver (θ)	40°

The optical and thermal characteristics of the glass cover, properties of the refractory paint layer, and thermal properties of the used insulation are also presented in Table 3. All steps required for fabricating and preparing the receiver are presented in Figure 1b. A hydraulic circuit was installed on the system according to ASHRAE 93-86 standard (Ref. [33]). The main components of the hydraulic circuit are a 20-liter storage tank, a circulating pump, heat exchangers, and a conical receiver (as shown in Figure 2a). The HTF stored in the tank is circulated using a pump and its temperature rises by passing through the path 1-2-3. Then, it goes through heat exchangers by passing through the path 3-4. In this way, the heat absorbed by the HTF in the receiver is transferred to the cooling water and then, it returns to the oil storage tank.

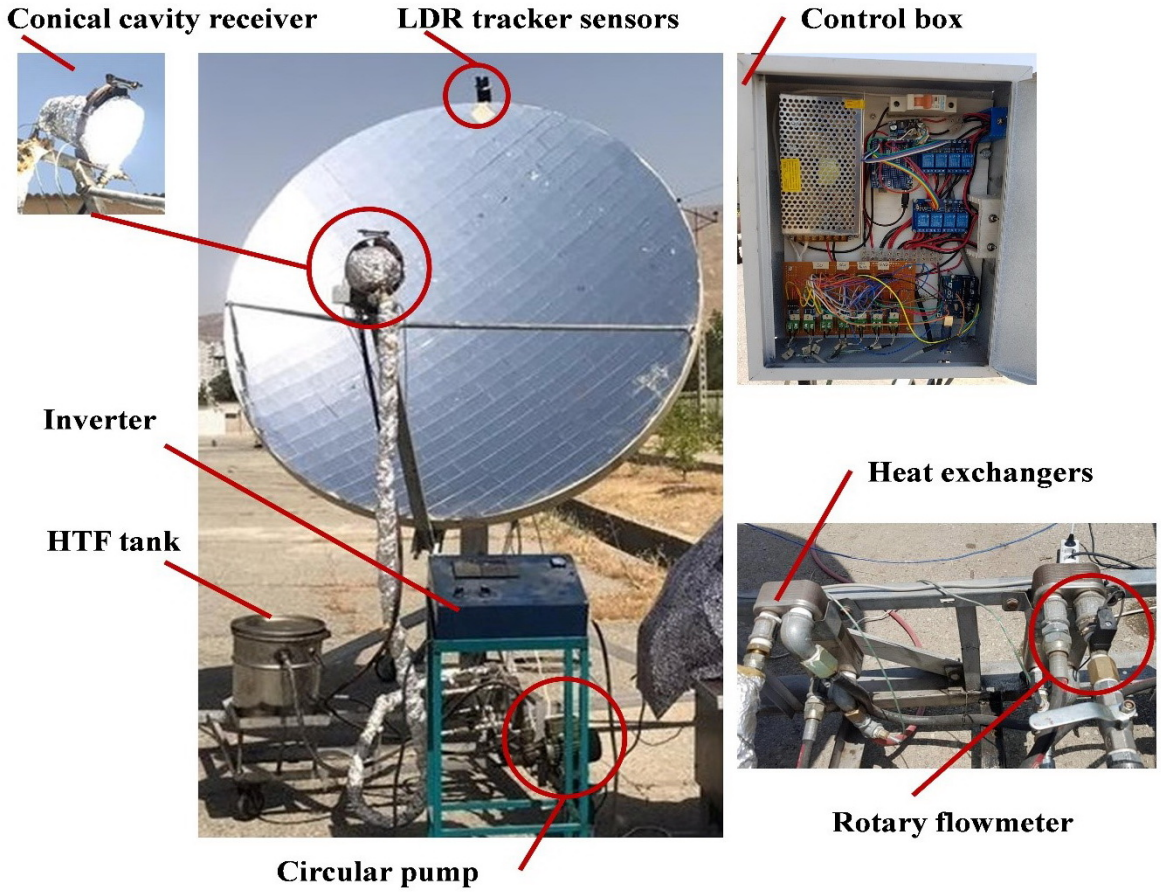

(a)

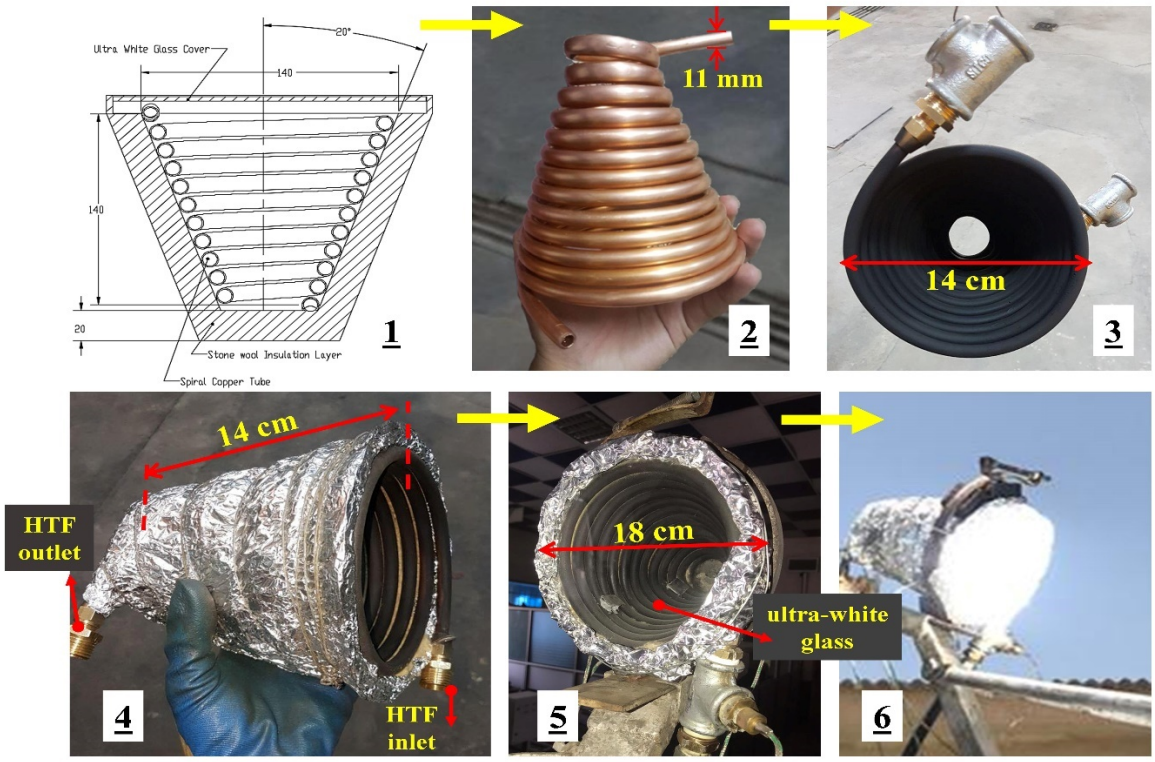

(b)

Figure 1. a) Photo of the experimental device and its main components, b) Different steps of fabricating the conical cavity receiver

Table 3. Properties of the materials used to construct the cavity receiver

Materials	Properties	Reason for use
Copper tube	• Thermal conductivity: 386 W/m.K • High melting point: 1000 °C [34]	Low thermal resistance
Black refractory coating	• Emissivity: 0.95 • Absorptivity: 0.9 • Stability: up to 700 °C	High absorptivity
Mineral wool insulation	• Thickness: 2 cm • Conductivity: 0.062 W/m.K [35]	Low thermal conductivity
Ultra-white glass cover	• Refractive index: 1.52 • Emissivity: 0.9	Low refraction

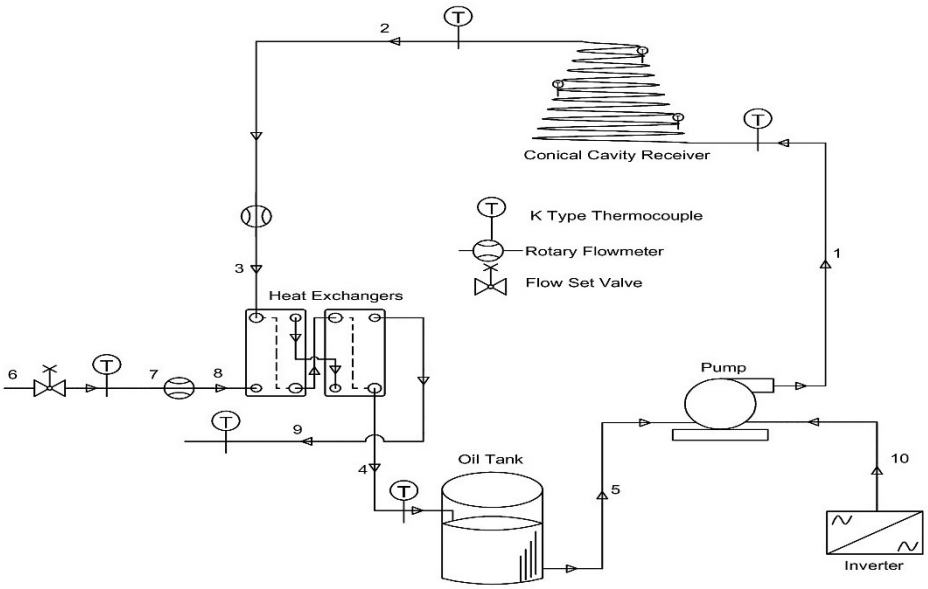

(a)

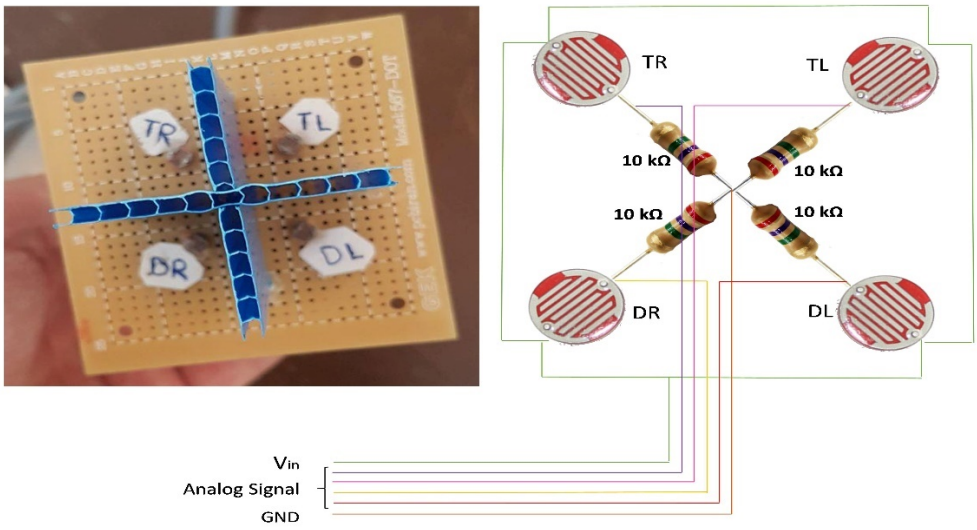

(b)

Figure 2. a) Schematic of the hydraulic circuit of the parabolic dish collector; b) The installation pattern of LDRs used to track the sun

In this study, a two-axis sun tracker composed of Light-Dependent Resistors (LDRs) was installed on the PDC system. The electronic circuit of the LDRs is presented in Figure 2b. The LDRs were installed on the upper part of the PDC and perpendicular to the reflector's surface. Due to variations in the angle of received solar radiation during the day, the internal resistance of LDRs related to each other varied and a signal was sent to the microcontroller such that the sun's path was processed and routed according to the defined algorithm of the microcontroller.

2.2. Uncertainty analysis

The measured parameters during the experiments were temperature, the HTF's volumetric flow rate, the amount of received solar radiation, wind speed, and air temperature. According to Figure 2a, the HTF's temperature at different locations including the inlet and outlet of the receiver and the exit of heat exchangers and the entrance of the tank, the temperature of the cooling water before and after entering the heat exchangers, and the temperature of the inner wall of the receiver were measured. Additionally, the volumetric flow rates of the HTF and cooling water (as shown in Figure 2a) were measured using turbine rotary flowmeters (Vision; type 2000). Also, K-type thermocouples (Chromel-Alumel) were employed to measure the temperature of different parts of the system. The data were then collected in a data logger for further analysis. The solar radiation was measured using the TES-1333 solar power meter and the wind speed was measured using the CT-AM 4220 anemometer. The calibration of K-type thermocouples and data logger was performed using TES-1307 thermometers along with a glass of ice and boiling water. Also, the flowmeters were calibrated by pouring water inside a scaled cylinder during a specific period. In this study, thermal efficiency uncertainty was calculated as 1.18 % using Eq. 1. [21]:

$$\frac{U\eta_{th}}{\eta_{th}}=\sqrt{\left(\frac{U\dot{Q}_{solar}}{\dot{Q}_{solar}}\right)^2+\left(\frac{U\Delta T}{\Delta T}\right)^2+\left(\frac{U\dot{m}}{\dot{m}}\right)^2} \quad (1)$$

The accuracy values for measuring instruments along with uncertainty values are presented in Table 4. Since only the measured temperature of the HTF is affected by other measured parameters, the standard uncertainty analysis of the HTF's temperature was performed using the Guide for Expression of Uncertainty in Measurement (GUM) method, as presented in Ref. [36]:

$$u=\sqrt{\frac{\sum_{i=1}^{n}(X_i-\bar{X})^2}{n(n-1)}} \quad (2)$$

where X and $\bar{X}$ are the measured and average temperature values of the HTF, respectively, n is the sample count, and u is the standard uncertainty. Using this formula, the maximum values of the standard uncertainty were calculated as 0.365 and 0.666 for the conical cavity receiver with and without a glass cover on the aperture, respectively.

Table 4. Accuracy values and ranges for measuring instruments

Instrument type	Resolution	Accuracy	Range of operation	Uncertainty (%)
K-type thermocouples	0.25 °C	± 0.56 °C	0-1000 °C	0.26
Solar power meter	0.1 W/m^2	± 0.11 W/m^2	0-2000 W/m^2	0.26
Anemometer	0.1 m/s	± 0.2 m/s	0.9-35 m/s	10
Rotary flowmeter	0.01 mA	± 0.05 mA	0-20 mA	

3. NUMERICAL INVESTIGATION

3.1. Boundary conditions

In this study, only the thermal model of the conical cavity receiver was evaluated. Boundary conditions and experimental test conditions for the numerical solution are negligible heat loss from the outer surface of the insulation, constant temperature of the oil tank, the HTF's temperature of 50 °C at the entrance of the receiver, equal pressure of separate air between the cavity and the glass cover with the

ambient air, oil pressure equal to ambient pressure due to the open circuit of the hydraulic cycle, and the constant oil flow rate of 0.7 l/min in the circuit.

3.2. Heat transfer analysis

The amount of heat loss from the cavity receiver depends on various factors such as the geometry of the concentrator and receiver, temperatures of the HTF at the inlet and outlet of the receiver, temperature of the inner wall of the cavity, ambient temperature, emissivity of the inner surface and glass cover of the cavity, etc. The schematic of the heat transfer model governing the receiver in this study is shown in Figure 3.

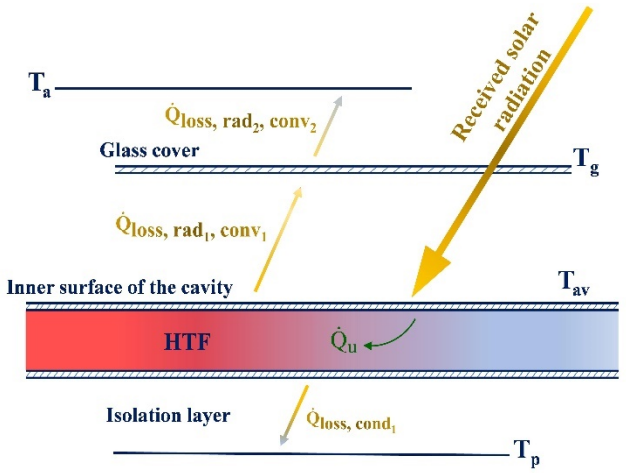

Figure 3. The schematic of the heat transfer model governing the receiver with ultra-white glass cover

The net heat transfer rate of the absorber tube was calculated as [34]:

$$\dot{Q}_u = \dot{Q}^* - \dot{Q}_{loss} \quad (3)$$

$$\dot{Q}_{loss} = \dot{Q}_{loss,cd} + \dot{Q}_{loss,cv} + \dot{Q}_{loss,r} \quad (4)$$

$$\dot{Q}^* = \eta_{optical} A_{ref} \dot{Q}_{solar} \quad (5)$$

According to Eq. 3, the rate of useful energy absorbed by the receiver is obtained by subtracting the heat loss rate from the amount of solar radiation received by the receiver ($\dot{Q}^*$). The receiver's total heat loss occurs through the main heat transfer mechanisms of conduction ($\dot{Q}_{loss,cd}$), convection ($\dot{Q}_{loss,cv}$), and radiation ($\dot{Q}_{loss,r}$), as presented in Eq. 4. Under the steady-state conditions, heat loss from the cavity receiver occurs when the aperture is covered with an ultra-white glass which can be calculated as follows [33]:

$$\dot{Q}_{loss} = \dot{Q}_{loss,\ cd1} + \dot{Q}_{loss,cv1} + \dot{Q}_{loss,r1} = \dot{Q}_{loss,cv2} + \dot{Q}_{loss,r2} \quad (6)$$

According to this equation, the rate of heat loss is equal to the losses that occur between the walls of the receiver and the inner surface of the glass cover, as well as the outer surface of the glass cover and the ambient. Herein, $\dot{Q}_{loss,\ cd1}$, $\dot{Q}_{loss,cv1}$, $\dot{Q}_{loss,r1}$, $\dot{Q}_{loss,cv2}$, and $\dot{Q}_{loss,r2}$ are the rates of conduction losses between the surface of the receiver and the glass cover, convection losses between the inner wall of the cavity and the glass cover, radiation losses between the inside walls of the cavity and the glass cover, convection losses from the outer surface of the glass cover to the ambient, and radiation losses from the outer surface of the glass cover to the air, respectively. The rates of heat loss from the inner wall of the receiver to the glass cover are calculated as follows [33]:

$$\dot{Q}_{loss,cd1} = \frac{\pi l \lambda (T_{av} - T_p)}{\ln(r_2/r_1)} \quad (7)$$

$$\dot{Q}_{loss,cv1} + \dot{Q}_{loss,rd1} = \pi r_1 l (h_{cv1} + h_{r1})(T_{av} - T_g) \quad (8)$$

where l, λ, r_2, r_1, T_{av}, T_p, and T_g are the effective length of the cavity receiver, the thermal conductivity of the insulation material, the radius of the cavity and the insulation layer, the average temperature of the inner wall of the cavity, the surface temperature of the insulation, and the temperature of the glass cover, respectively. h_{cv1} and h_{r1} are coefficients of convective and radiative heat losses and are calculated as follows [37]:

$$h_{cv1} = \frac{0.212 \lambda (Gr_\delta\ p_r)^{1/4}}{\delta} \quad (9)$$

$$h_{r1} = \frac{\sigma (T_{av}^2 + T_g^2)(T_{av} + T_g)}{\frac{1}{\varepsilon_{av}} + \frac{A_{av}}{A_g}\frac{1}{\varepsilon_g} - 1} \quad (10)$$

where δ is the average space between the inner wall of the cavity and the glass cover, Gr is the Grashof number, P_r is the Prandtl number, σ is the Stefan Boltzmann constant, and ε_{av} and ε_g are the inner wall emissivity of the cavity and the emissivity of the glass cover, respectively. A_{av} and A_g are the inner surfaces of the cavity and glass cover, respectively. Considering Eqs. 11 and 12, the rate and the overall coefficient of heat loss from the cavity are calculated as follows:

$$\dot{Q}_l = A_{av} U_l (T_{av} - T_a) \quad (11)$$

$$U_l = \frac{\frac{\lambda (T_{av} - T_p)}{r_1 \ln(r_2/r_1)} + \frac{0.212 \lambda (Gr_\delta\ p_r)^{1/4}}{\delta}(T_{av} - T_g) + \frac{\sigma (T_{av}^2 + T_g^2)(T_{av} + T_g)}{\frac{1}{\varepsilon_{av}} + \frac{A_{av}}{A_g}\frac{1}{\varepsilon_g} - 1}(T_{av} - T_g)}{T_{av} - T_a} \quad (12)$$

According to the rate of heat loss calculated by Eq. 11, the rate of useful gained heat considering the overall coefficient of heat loss from the receiver is calculated as follows:

$$\dot{Q}_u = A_r [S - U_l'(T_{av} - T_a)] \quad (13)$$

$$S = \eta_{optical} I C \sin\frac{\theta}{2} \quad (14)$$

$$U_l' = U_l C \sin\frac{\theta}{2} \quad (15)$$

where A_r, T_a, I, C, and θ are the cavity's aperture area, ambient temperature, received solar radiation, the geometrical concentration ratio of the concentrator, and conical receiver's cone angle, respectively. The useful gained energy which is transferred to the HTF can be calculated from Eq. 16:

$$\dot{Q}_u = \frac{L(T_{av} - T_i)}{\frac{1}{\pi D_i h_{fi}} + \frac{1}{2\pi\lambda}\ln\frac{D}{D_i}} \quad (16)$$

$$L = \frac{\pi w (D + w)}{4D \sin(\frac{\theta}{2})} \quad (17)$$

where T_i is the temperature of the HTF at the inlet of the cavity, D and D_i are outer and inner diameters of the absorber

tube, respectively, h_{fi} is the convective heat transfer coefficient of the HTF at the inlet of the receiver, and w and L are the aperture diameter of the cavity and the total length of the absorber tube, respectively. The rate of useful energy absorbed by the HTF can be obtained through Eq. 18 [33]:

$$\dot{Q}_u = A_r F_R C \sin\frac{\theta}{2}[\eta_{optical} I - U_l(T_i - T_a)] \quad (18)$$

$$F_R = \frac{4\dot{m}C_p}{\pi w^2 U_l C \sin\frac{\theta}{2}}\{1 - \exp[-\frac{\pi w^2 (D+w) U_l F'}{4D \sin\frac{\theta}{2}\dot{m}C_p}]\} \quad (19)$$

$$F' = \frac{1/w}{\frac{4}{C\pi w^2 \sin\frac{\theta}{2}} + \frac{4D\sin\frac{\theta}{2}}{\pi w(D+w)}(\frac{1}{\pi D_i h_{fi}} + \frac{1}{2\pi\lambda}\ln\frac{D}{D_i})U_l} \quad (20)$$

where F_R and F' are heat removal and efficiency factors of the collector, respectively. Also, the overall heat loss coefficient of the cavity receiver (U_l) without the glass cover on the aperture can be calculated as follows [38]:

$$U_l = \frac{Nu\, k}{D_{ap}} + \frac{\sigma(T_{av}^2 + T_a^2)(T_{av} + T_a)}{1 + (\frac{1-\varepsilon}{\varepsilon})\frac{A_{ap}}{A_{av}}} \quad (21)$$

$$Nu = 1.635\, Re^{0.38} Pr^{-1.2} (\frac{D_{ap}}{D_{ca}})^{0.892} (1 + \cos\emptyset)^{0.285} \quad (22)$$

In Eq. 21, U_l consists of the convection and radiative heat transfer coefficients, Nu is the non-dimensional Nusselt number of the wind flow near the receiver aperture which was experimentally calculated using Ref. [39] and used in Ref. [40] to validate the simulation and a correlation of over 83 %, k is the air's thermal conductivity, and D_{ap} is the diameter of the cavity's aperture. The Nu is calculated from Eq. 22, where $\emptyset$ is the inclination angle of the receiver. The thermal efficiency of PDCs can be calculated as follows [33]:

$$\eta_{th} = \frac{\dot{Q}_u}{\dot{Q}^*} = \frac{\dot{Q}^* - \dot{Q}_{loss}}{\eta_{optical} A_{ref} \dot{Q}_{solar}} \quad (23)$$

$$\eta_{opt} = \frac{\dot{Q}^*}{A_{ref}\dot{Q}_{solar}} \quad (24)$$

The thermal model of the cavity receiver with the aperture covered with a glass cover was solved by Newton-Raphson root-finding method in Fortran software with four equations and four unknowns. Using this method, four unknown temperature values of the ultra-white glass cover, the temperature of the cavity's inner wall, the rate of the useful gained heat ($\dot{Q}_u$) by the receiver and the HTF, and the rate of the heat loss ($\dot{Q}_{loss}$) from the receiver were obtained. Also, considering the cavity without the glass cover, two equations and two unknowns were solved. Finally, the two unknown temperature values of the inner wall of the cavity receiver and the rate of gained useful energy ($\dot{Q}_u$) were obtained.

4. RESULTS AND DISCUSSION

Experimental tests were performed continuously from 10:00 to 16:00. During the tests, the viscosity of the HTF varied by temperature variations. Therefore, to keep the volumetric flow rate of the oil constant, an inverter was used to control the speed of the oil pump (shown in Figure 1a). During the tests, the temperature of the oil before entering the receiver (temperature of the stored oil in the tank) was kept constant by continuously monitoring the HTF's temperature and variations in the flow rate of the cooling water flowing in heat exchangers.

4.1. Experimental results

4.1.1. Conical cavity receiver with ultra-white glass on the aperture

The conical cavity receiver of the PDC with an ultra-white glass cover on its aperture was evaluated on 4th July 2020 under climate conditions of Tehran, Iran. Figure 4a shows the variations in solar radiation and the air temperature, as well as the temperature difference between the HTF at the inlet and outlet of the receiver. During the test, the oil temperature at the inlet of the receiver was kept constant at 50 °C and its flow rate at 0.7 l/min. According to Figure 4a, the maximum amount of radiation was recorded as 965.6 W/m^2 at 13:00 and the minimum value was recorded as 917.8 W/m^2 at 10:00 (in the morning). As shown in this figure, differences in the temperature of the oil at the inlet and outlet of the receiver follow the same trend of variations in solar radiation with the maximum difference of 69 °C at 13:00 and the minimum difference of 63.25 °C at 10:00. Also, the air temperature in the middle of the day was recorded as 33 °C, which was higher than the initial and final hours with the recorded temperature value of 29 °C at 16:00.

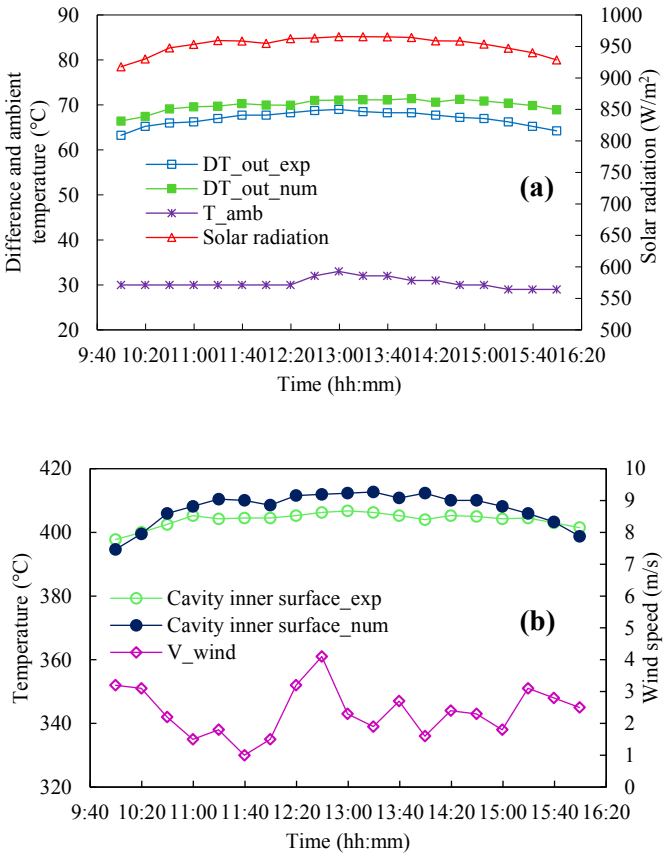

Figure 4. a) Variations of different environmental and operational parameters (on 4th July), b) Variations in the temperature of the inner wall of the receiver and wind speed (on 4th July)

The variations in the temperature of the inner wall of the receiver and the wind speed are shown in Figure 4b. According to this figure, it can be seen that the highest surface

temperature is 406.75 °C between 12:40 and 13:20. It can also be seen that the variation in the receiver's wall temperature approximately follows the trend of the solar radiation variation. This figure shows variations in the wind speed during the evaluation day, ranging from 1 m/s at 11:40 to 4.1 m/s at 12:40. According to the figure, it appears that due to the existence of the glass cover on the receiver aperture, variations in wind speed could not significantly affect the receiver's surface temperature.

The rate of heat absorbed by the HTF inside the receiver and also thermal efficiency of the receiver are shown in Figure 5. The figure shows that at 13:00, the maximum heat of 1,291.68 W was absorbed by the receiver, while the minimum values were recorded at 10:00 and 16:00 (initial and final hours of the evaluation day) as 1,184.04 W and 1,202.76 W, respectively. Also, the highest thermal efficiency of the PDC was reported as 53.51 % at 13:00. According to the numerical analyses, it was found that by increasing the temperature of the HTF at the inlet of the receiver, the temperature of the HTF at the outlet of the receiver and the temperature of the inner wall of the receiver increased, while the useful absorbed heat and the thermal efficiency of the system decreased. Similar results have been reported in Refs. [21] and [41].

4.1.2. Conical cavity receiver without ultra-white glass on its aperture

Experimental evaluations of the PDC collector with a conical cavity receiver without a glass cover on the aperture were performed on 7th July 2020. The evaluations were performed similarly to the experiments performed for the receiver with a glass cover. The flow rate and temperature of the HTF at the inlet of the receiver were constant at 0.7 l/min and 50 °C, respectively. According to Figure 6a, the solar radiation variation reaches the highest value of 967.5 W/m^2 at 13:00 and the lowest value of 935.9 W/m^2 at 10:00 on 7th July. Also, the highest temperature difference of the HTF at the inlet and outlet of the receiver was recorded as 56.25 °C from 12:40 to 13:20 with the air temperature variations in the range of 25-33 °C at 10:00 and 13:00, respectively.

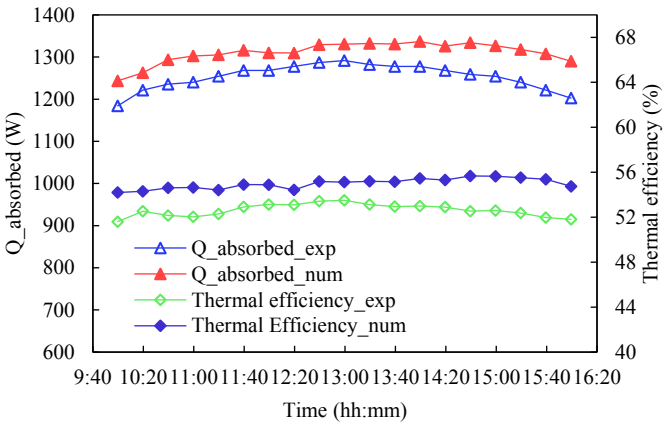

Figure 5. Variations in the absorbed energy and the thermal efficiency of the conical cavity receiver on 4th July

Figure 6b shows variations of the inner wall of the receiver and changes in the wind speed during experiment hours. The maximum temperature of the inner wall of the receiver was recorded as 382.5 °C at 13:20. According to this figure and considering that the aperture of the receiver is not covered (thus, it is exposed to the wind streams), a decline in the temperature of the inner surface of the receiver from its mean value of 377.3 °C in the previous hours (10:00 to 15:00) to 366.25 °C is observed at the final hours of the experiment. Likewise, the wind speed increased from its mean value of 2.6 m/s at the previous hours (10:00 to 15:00) to 5.3 m/s, while at the hour between 10:00-15:00, the wind speed showed steady fluctuations.

Figure 7 shows the variations in the amount of useful absorbed energy and the thermal efficiency of the system during evaluation hours. It can be seen that the most useful heat of 1,053 W was absorbed between 12:40-13:20. Also, the highest thermal efficiency ranging from 42.66 % to 43.03 % was recorded during the same period. It can be observed that the curves of the useful absorbed heat and thermal efficiency follow a similar trend of the temperature difference of the HTF at the inlet and outlet of the receiver.

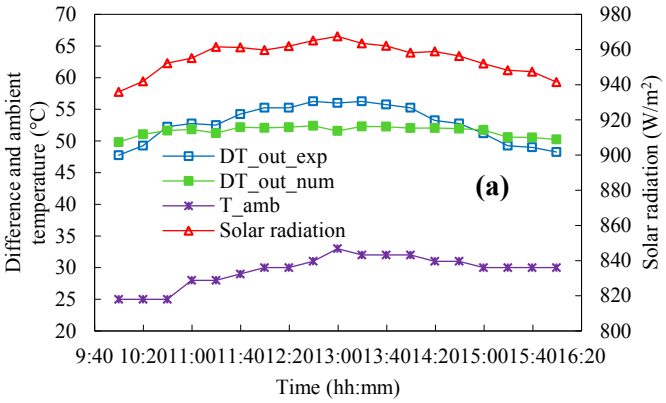

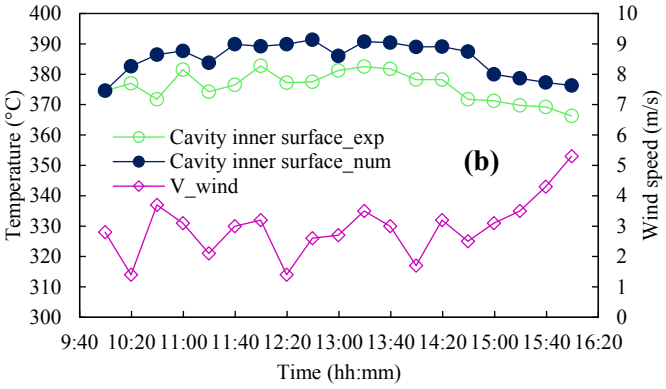

Figure 6. a) Variations of different parameters of the conical cavity receiver; b) Variations in the temperature of the cavity inner surface and wind speed on 7th July

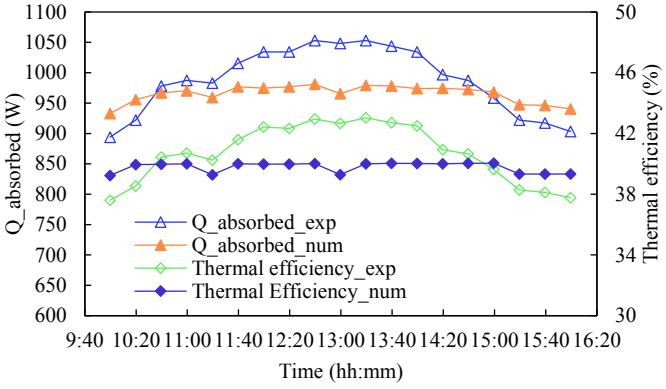

Figure 7. Variations in the absorbed energy and the thermal efficiency of the receiver on 7th July

4.2. Numerical modeling results and validation

In the numerical study, by solving the governing equations of the PDC and the receiver using Fortran software, the parameters of HTF temperature at the outlet of the receiver, the temperature of the inner wall of the receiver, and also the rate of the useful absorbed heat were calculated. Also, the value of the thermodynamic efficiency of the system was obtained. The results of the numerical simulation of the receiver with the aperture covered with an ultra-white glass and the aperture with no glass cover are presented in Figures 4 to 7.

The results of the numerical simulations do not differ much from the results of experimental tests. The reason could be the proper definition of the environmental, geometric, optical, and thermal parameters of the cavity receiver. Table 5 reports the values of the measured parameters including the temperature of the HTF at the inlet of the receiver, solar radiation, air temperature, and wind speed on 4th and 7th July. Also, according to Tables 6 and 7, it can be seen that in the case of the receiver with the glass cover, there are 2.05 %, 1.46 % and 3.56 % differences for the experimental and numerical data of the temperature of the HTF at the inlet and outlet of the receiver, the temperature of the inner wall of the receiver, and thermal efficiency, respectively. In the case of the receiver without a glass cover, the differences between numerical and experimental values of the mentioned parameters are 3.40 %, 2.45 % and 6.45 %, respectively.

Table 5. Measured parameters at the steady-state test times on 4th and 7th July

Time	Measured parameters on 4th July 2020				Measured parameters on 7th July 2020			
	T_{in} (°C)	I_{solar} (W/m^2)	T_{amb} (°C)	V_{wind} (m/s)	T_{in} (°C)	I_{solar} (W/m^2)	T_{amb} (°C)	V_{wind} (m/s)
11:40	-	-	-	-	50.50	961.2	29	3.0
12:00	50.25	959.7	30	1.5	50.25	959.7	30	3.2
12:20	51.00	961.9	30	3.2	49.75	961.9	30	1.4
12:40	49.75	965.1	31	4.1	50.25	965.1	31	2.6
13:00	49.5	967.5	33	2.3	50.00	967.5	33	2.7
13:20	50.00	963.5	32	1.9	50.50	963.5	32	3.5
13:40	50.25	962.1	32	2.7	49.75	962.1	32	3.0
14:00	50.00	958.2	32	1.6	50.25	958.2	32	1.7

Table 6. Comparison between experimental and numerical results for the receiver with an ultra-white glass cover on 4th July

Time	Experimental				Numerical				Derivation		
	T_{out} (°C)	T_{surf} (°C)	Q_{abs} (W)	η_{th} (%)	T_{out} (°C)	T_{surf} (°C)	Q_{abs} (W)	η_{th} (%)	D_{Tout} (%)	D_{Tsurf} (%)	$D_{\eta th}$ (%)
11:40	117.75	404.50	1268.28	52.92	120.29	410.06	1315	54.90	2.16	1.38	3.75
12:00	117.75	404.50	1268.28	53.14	119.98	408.5	1310	54.89	1.89	1.00	3.29
12:20	118.25	405.25	1277.64	53.10	119.96	411.5	1309	54.43	1.44	1.56	2.50
12:40	118.75	406.25	1287.00	53.43	121.01	411.9	1329	55.18	1.90	1.40	3.28
13:00	119.00	406.75	1291.68	53.51	121.09	412.3	1330	55.20	1.75	1.37	3.02
13:20	118.50	406.25	1382.32	53.13	121.16	412.7	1332	55.20	2.25	1.59	3.89
13:40	118.25	405.25	1277.64	52.95	121.10	410.8	1330	55.46	2.41	1.37	4.17
14:00	118.25	404.00	1277.64	52.99	121.41	412.3	1336	55.45	2.67	2.06	4.63

Table 7. Comparison between experimental and numerical results for the receiver without cover on 7th July

Time	Experimental				Numerical				Derivation		
	T_{out} (°C)	T_{surf} (°C)	Q_{abs} (W)	η_{th} (%)	T_{out} (°C)	T_{surf} (°C)	Q_{abs} (W)	η_{th} (%)	D_{Tout} (%)	D_{Tsurf} (%)	$D_{\eta th}$ (%)
12:00	105.25	382.75	1034.28	42.43	102.07	389.20	974.7	39.99	3.02	1.69	5.76
12:20	105.25	377.25	1034.28	42.33	102.18	389.90	976.7	39.98	2.95	3.35	5.56
12:40	106.25	377.50	1053.00	42.96	102.40	391.36	980.9	40.02	3.62	3.67	6.84
13:00	106.00	381.25	1048.32	42.66	101.58	386.01	965.5	39.29	4.17	1.25	7.89
13:20	106.25	382.50	1053.00	43.03	102.30	390.72	979.0	40.01	3.72	2.15	7.02
13:40	105.75	381.75	1043.64	42.71	102.26	390.42	978.2	40.03	3.30	2.27	6.27
14:00	105.25	378.25	1034.28	42.50	102.03	388.96	974.0	40.02	3.06	2.83	5.82

4.3. Comparison of performances

The thermal performance of a PDC with a conical cavity receiver with and without ultra-white glass cover on its aperture was numerically and experimentally investigated on 4th and 7th July 2020 with similar environmental conditions. Table 8 shows the mean values of solar radiation, air temperature, and wind speed with the measured values already reported in Table 5 for the same evaluation days. Observing average values of mentioned parameters shows similar amounts of these values for each day of the experiment. Also, the volume flow rate and the HTF's temperature at the inlet of the receiver were the same in both cases.

Figure 8a shows the experimental values of the HTF's temperature at the outlet of the receiver and the temperature of the inner wall of the cavity, while Figure 8b shows the

experimental values of the useful gained heat by the HTF and the thermal efficiency of the receiver with and without a glass cover on its aperture. Furthermore, Table 9 shows the maximum, minimum, and mean values of the mentioned parameters.

Table 8. Comparison between the mean values of measured parameters on 4th and 7th July

Conical cavity receiver	$I_{solar\text{-}ave}$ (W/m²)	$T_{amb\text{-}ave}$ (°C)	$V_{wind\text{-}ave}$ (m/s)
With glass cover (4th July 2020)	953.33	30.27	2.34
Without glass cover (7th July 2020)	955.26	29.57	2.95

Upon comparing the mean values of the parameters presented in Table 9, it is observed that by installing the glass cover on the receiver aperture, the HTF's temperature at the outlet of the receiver and the temperature of the inner wall of the receiver increase to 14.19 °C and 28.04 °C, respectively. Also, the increase of 11.94 % in the thermal efficiency of the receiver was observed. Similar results were reported in the numerical results reported in Ref. [18] with a 7 % increase in thermal efficiency in the case of the glass cover on the receiver aperture. Figure 9 shows the overall efficiency of the receiver versus the value of $(\frac{T_i - T_a}{I_b})$ with and without a glass cover on the receiver's aperture, respectively. Both diagrams presented in Figure 9 are plotted at the time interval when the system is in the steady state (the time interval is shown in Figure 8b). For the cavity with and without a glass cover, the predicted models according to the experimental results are described as:

$$\eta_{th} = 0.5581 - 1.4178(\frac{T_i - T_a}{I_b}) \quad (25)$$

$$\eta_{th} = 0.4411 - 0.755(\frac{T_i - T_a}{I_b}) \quad (26)$$

Based on Figure 9 and considering Eqs. 25 and 26, it is found that the slope and coordinate distance constant of the plotted graphs are equal to $\frac{F_R U_l}{C}$ and $F_R\eta_{opt}$, respectively.

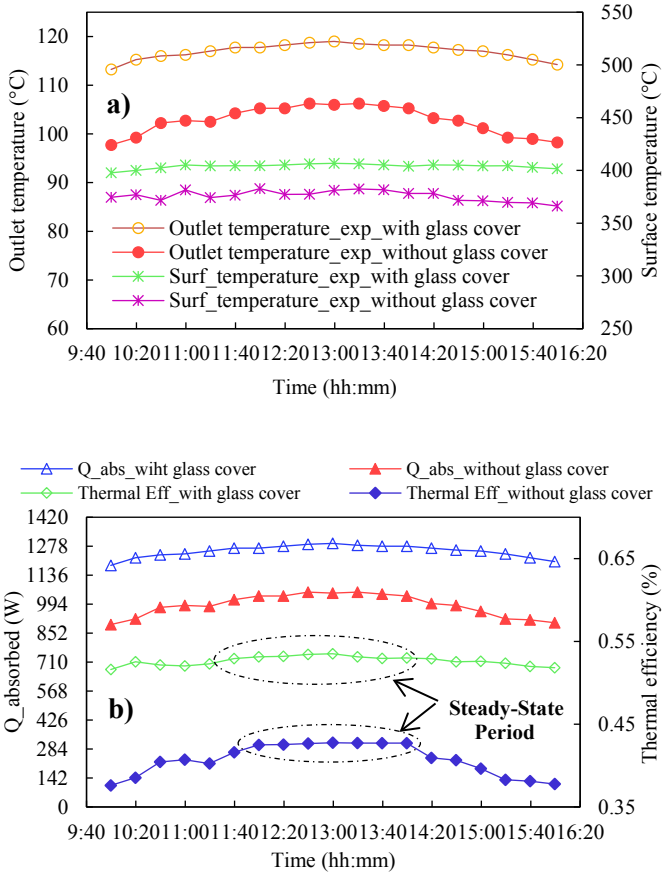

Figure 8. a) Temperature of the HTF at the outlet of the receiver and the temperature of the cavity's inner wall based on experimental results; b) Heat gained by the HTF and the receiver's thermal efficiency based on experimental results

Table 9. Comparison between the results for the conical cavity receiver with and without an ultra-white glass cover on its aperture based on experimental results

Conical cavity receiver	$T_{out\text{-}max}$ (°C)	$T_{out\text{-}min}$ (°C)	$T_{surf\text{-}max}$ (°C)	$T_{surf\text{-}min}$ (°C)	$Q_{abs\text{-}max}$ (w)	$Q_{abs\text{-}min}$ (w)	$\eta_{th\text{-}max}$ (%)	$\eta_{th\text{-}min}$ (%)
With ultra-white glass cover	119	113.2	406.75	397.75	1291.1	1184.4	53.51	51.60
Average values	116.95		404		1253.25		52.63	
Without ultra-white glass cover	106.25	97.75	382.75	366.25	1053	893.88	42.75	37.60
Average values	102.76		375.96		987.68		40.69	

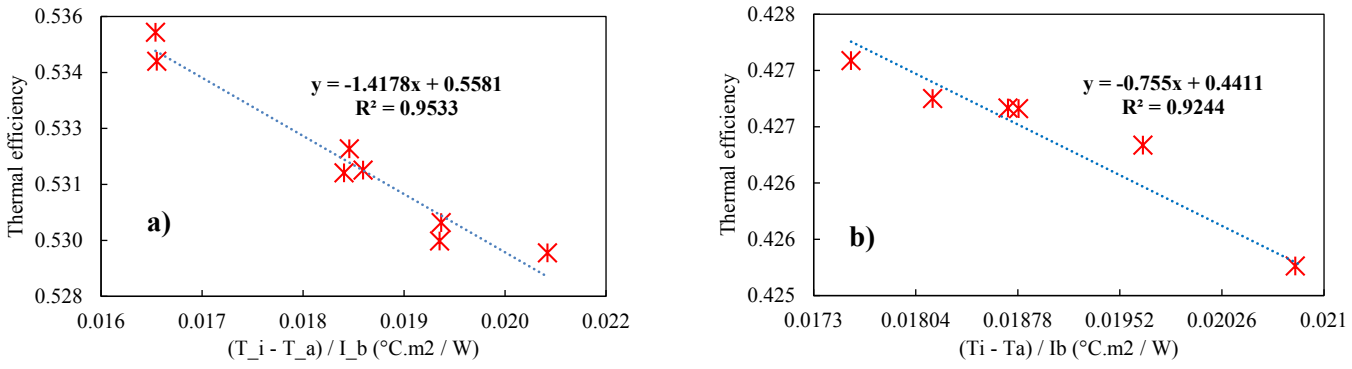

Figure 9. Overall thermal efficiency of the receiver versus $(\frac{T_i - T_a}{I_b})$ for the receiver: a) with the glass cover, b) without the glass cover

Table 10 shows the values of $F_R\eta_{opt}$, $\frac{F_R U_l}{C}$, F_R, U_l, and $\frac{U_l}{C}$. It can be found that the values of F_R (heat removal factor of the PDC) and U_l (overall heat loss coefficient) of the receiver with the glass cover are higher than those in the case without the glass cover. Upon comparing Eqs. 25 and 26 and considering the obtained results presented in Table 10, it is found that due to the higher efficiency achieved for the receiver with the glass cover, the higher temperature of the HTF at the outlet of the receiver, and the high value of the F_R for the conical cavity receiver, the value of U_l is less than that obtained for the receiver without the glass cover. Similar results were reported in Ref. [21] for two cylindrical and cubical cavity receivers, where a lower value of U_l and a larger value of F_R were obtained for the cubical receiver than those for the cylindrical type because of the higher performance of the cubical receiver. It should be mentioned that the optical efficiency of the parabolic concentrator was assumed as 90 % in all calculations.

It is concluded that for the conical cavity receiver with the glass cover on its aperture, by reaching high temperature values for the inner wall of the cavity, higher values of F_R and lower values of the overall heat loss from the receiver (U_l) are achievable for the receiver without the glass cover.

Table 10. Comparison between overall heat loss coefficient and heat removal factor of the PDC and the receiver with and without an ultra-white glass cover on the aperture

Conical cavity receiver	$F_R\eta_{opt}$	$\frac{F_R U_l}{C}$	F_R	C	U_l	$\frac{U_l}{C}$
With ultra-white glass cover	0.5581	1.4178	0.62	184	420.76	2.28
Without ultra-white glass cover	0.4411	0.755	0.49	184	283.51	1.54

Similar results for η_{opt} are reported in Ref. [33] for three conical, cubical, and cylindrical cavity receivers (with glass cover on their aperture) installed on a Fresnel lens system. Also, similar results for η_{th} were reported in Ref. [21] for two cubical and cylindrical cavity receivers used in a PDC. To calculate the divergence of the thermal efficiency of the conical cavity receivers with and without ultra-white glass cover, the Root-Mean-Square Error (RMSE) was used. Table 11 shows the estimated RSME values under the steady-state condition. The RMSE can be calculated as:

$$RMSE=\sqrt{\frac{\sum_{i=1}^{N}(\bar{Y}_i-Y_i)^2}{N}} \quad (27)$$

where N is the total number of the calculated parameters under the steady-state condition, Y_i is the calculated parameter, and $\bar{Y}_i$ is the average of the calculated parameter.

Table 11. Estimated RSME values for the thermal efficiency and heat gain of the cavity receiver

Conical cavity receiver	RMSE for cavity heat gain (W)	RMSE for thermal efficiency (%)
With glass cover	7.6722	0.57
Without glass cover	8.07	0.09

5. CONCLUSIONS

In this study, the thermal performance of a PDC employing a conical cavity receiver was numerically and experimentally investigated. The effect of the presence and absence of the ultra-white glass cover on the aperture of the receiver on the thermal performance of the PDC and receiver was investigated. In the experiments, environmental and operational parameters were measured, recorded, and analyzed. From this study, the following points are concluded:

- According to the experimental and numerical results, it was found that there was good agreement between the experimental and numerical results. For the receiver with glass cover on its aperture and without glass cover, 2.67 % and 3.06 % deviations in HTF's outlet temperature were observed. Also, 2.06 % and 2.83 % deviations in the cavity's inner surface temperature and 4.63 % and 5.82 % deviations in the useful heat gained by the HTF and thermal efficiency of the PDC were observed.
- It was found that by covering the aperture of the cavity, the average concentrating thermal efficiency increased from 11.92 % to 52.63 %.
- The useful heat absorbed by the HTF and the temperature of the HTF at the inlet of the receiver were obtained as 1253.25 W, 116.95 °C for the cavity with the glass cover and 987.68 W and 102.76 °C for the cavity without the glass cover.
- In the diagram representing thermal efficiency versus $\frac{T_i - T_a}{I_b}$, it was observed that due to the higher values of efficiency, the parameter F_R for the conical cavity receiver with the glass cover on its aperture was 0.62, being more than that of the cavity without the glass cover (0.49).
- The value of U_l for the receiver with the glass cover on its aperture was 420.76 W/m^2°C. The reason for its high value compared to the case of no glass cover on the aperture is the high value of the useful absorbed heat and the high temperature of the inner surface of the cavity, as well as the high amount of heat loss.

Considering that the present study is a thermal investigation of a CSP system and due to the appropriate thermal performance of the conical cavity receiver with the glass cover on its aperture, this system can be used as a study to build a PDC on a larger scale in a CSP power plant to generate electricity employing thermodynamics cycles. For further studies, it is also recommended that different types of nanofluids with the oil-based fluid used as the HTF in this study be compared, and also, steam generator power cycles working based on PDCs be studied.

6. ACKNOWLEDGEMENT

The authors would like to thank the advisory support received from the Renewable Energy Research Institute, an affiliation of Tarbiat Modares University (TMU) (http://www.modares.ac.ir) and the received financial support (grant number IG/39705) for the 'Renewable Energies Research Group'.

NOMENCLATURE

$\dot{Q}^*$	Rate of available solar heat for concentrator (W)
$\dot{Q}_u$	Net heat transfer rate (W)
$\dot{Q}_{loss}$	Thermal heat losses (W)
I	Solar radiation (W/m^2)
h	Convection heat transfer coefficient (W/m^2°C)
T	Temperature (°C)
r	Radiation (m)
l	Length (m)
L	Length of the absorber tube (m)
A	Area (m^2)
δ	Average space between cavity and glass cover (m)
U_l	Overall heat loss coefficient (W/m^2°C)
F_r	Collector heat removal factor
C	Concentration ratio
u	Uncertainty
n	Sample count
$\eta_{optical}$	Optical efficiency (%)
η_{th}	Thermal efficiency (%)
$\bar{X}$	Average value of the measured HTF temperature (°C)
X	Measured HTF's temperature (°C)
Pr	Prandtl number
Gr	Grashof number
Nu	Nusselt number
Greek letters	
ε	Emissivity
λ	Thermal conductivity (W/m. K)
θ	Cone angle of the receiver (°)
Ø	Inclination angle of the receiver (°)
k	Conduction heat transfer coefficient (W/m^{2}k)
σ	Stefan-Boltzmann constant
Subscripts	
ap	Aperture
av	Average
cv	Convection
cd	Conduction
ra	Radiation
a	Ambient
g	Glass
fi	Inlet fluid
i	Inlet

REFERENCES

1. Gorjian, Sh., Nemat-Zadeh, B., Eltrop, R.R. Shamshiri, L. and Amanlou, Y., "Solar photovoltaic power generation in Iran: Development, policies, and barriers", ***Renewable and Sustainable Energy Reviews***, Vol. 106, (2019), 110-123. (https://doi.org/10.1016/j.rser.2019.02.025).
2. Gorjian, Sh. and Ghobadian, B., "Solar desalination: A sustainable solution to water crisis in Iran", ***Renewable and Sustainable Energy Reviews***, Vol. 48, (2015), 571-584. (https://doi.org/10.1016/j.rser.2015.04.009).
3. Gorjian, Sh., Ghobadian, B., Ebadi, H., Ketabchi, F. and Khanmohammadi, S., "Applications of solar PV systems in desalination technologies", Photovoltaic solar energy conversion, Elsevier, Iran, (2020), 237-274. (https://doi.org/10.1016/B978-0-12-819610-6.00008-9).
4. Sharon, H., Reddy, K.S. and Gorjian, Sh., "Parametric investigation and year round performance of a novel passive multi-chamber vertical solar diffusion still: Energy, exergy and enviro-economic aspects", ***Solar Energy***, Vol. 211, (2020), 831-846. (https://doi.org/10.1016/j.solener.2020.10.016).
5. Hosseini, A., Banakar, A. and Gorjian, Sh., "Development and performance evaluation of an active solar distillation system integrated with a vacuum-type heat exchanger", ***Desalination***, Vol. 435, (2017), 45-59. (https://doi.org/10.1016/j.desal.2017.12.031).
6. Gorjian, Sh., Ebadi, H., Calise, F., Shukla, A. and Ingrao, C., "A review on recent advancements in performance enhancement techniques for low-temperature solar collectors", ***Energy Conversion Management***, Vol. 222, (2020a), 113246. (https://doi.org/10.1016/j.enconman.2020.113246).
7. Gorjian, Sh., Ghobadian, B., Tavakkoli-Hashjin, T. and Banakar, A., "Experimental performance evaluation of a stand-alone point-focus parabolic solar still", ***Desalination***, Vol. 352, (2014), 1-17. (https://doi.org/10.1016/j.desal.2014.08.005).
8. Gorjian, Sh. and Ghobadian, B., "Solar thermal power plants: Progress and prospects in Iran", ***Energy Procedia***, Vol. 75, (2015), 533-539. (https://doi.org/10.1016/j.egypro.2015.07.447).
9. Madadi, V., Tavakoli, T. and Rahimi, A., "Estimation of heat loss from a cylindrical cavity receiver based on simultaneous energy and exergy analyses", ***Journal of Non-Equilibrium Thermodynamics***, Vol. 40, No. 1, (2015), 49-61. (https://doi.org/10.1515/jnet-2014-0029).
10. Gorjian, Sh., Tavakkoli-Hashjin, T., Ghobadian, B. and Banakar, A., "A thermal performance evaluation of a medium-temperature point-focus solar collector using local weather data and artificial neural networks", ***International Journal of Green Energy***, Vol. 12, No. 5, (2015), 493-505. (https://doi.org/10.1080/15435075.2013.848405).
11. Arkian, A.H., Najafi, G.H., Gorjian, Sh., Loni, R., Bellos, E. and Yusaf, T., "Performance assessment of a solar dryer system using small parabolic dish and alumina/oil nanofluid: Simulation and experimental study", ***Energies***, Vol. 12, No. 24, (2019), 4747. (https://doi.org/10.3390/en12244747).
12. Loni, R., Askari-Asli-Ardeh, E., Ghobadian, B., Kasaeian, A.B. and Gorjian, Sh., "Thermodynamic analysis of a solar dish receiver using different nanofluids", ***Energy***, Vol. 133, (2017), 749-760. (https://doi.org/10.1016/j.energy.2017.05.016).
13. Pavlovic, S., Daabo, A.M., Bellos, E., Stefanovic, V., Mahmoud, S. and Al-Dadah, R.K., "Experimental and numerical investigation on the optical and thermal performance of solar parabolic dish and corrugated spiral cavity receiver", ***Journal of Cleaner Production***, Vol. 150, (2017), 75-92. (https://doi.org/10.1016/j.jclepro.2017.02.201).
14. Li, X., Dai, Y.J. and Wang, R.Z., "Performance investigation on solar thermal conversion of a conical cavity receiver employing a beam-down solar tower concentrator", ***Solar Energy***, Vol. 114, (2015), 134-151. (https://doi.org/10.1016/j.solener.2015.01.033).
15. Abdulrazzaq Alhsani, Z.I. and Al-Dulaimi, R.K.M., "Experimental analysis of solar dish concentrators with cylindrical, oval, and conical cavity receivers", ***International Journal of Renewable Energy Research***, Vol. 10, (2020), 591-600.
16. Pavlovic, S., Loni, R., Bellos, E., Vasiljević, D., Najafi, G. and Kasaeian, A., "Comparative study of spiral and conical cavity receivers for a solar dish collector", ***Energy Conversion and Management***, Vol. 178, (2018), 111-122. (https://doi.org/10.1016/j.enconman.2018.10.030).
17. Daabo, A.M., Mahmoud, S. and Al-Dadah, R.K., "The optical efficiency of three different geometries of a small scale cavity receiver for concentrated solar applications", ***Applied Energy***, Vol. 179, (2016), 1081-1096. (https://doi.org/10.1016/j.apenergy.2016.07.064).
18. Daabo, A.M., Mahmoud, S., Al-Dadah, R.K. and Ahmad, A., "Numerical investigation of pitch value on thermal performance of solar receiver for solar powered Brayton cycle application", ***Energy***, Vol. 119, (2017), 523-539. (https://doi.org/10.1016/j.energy.2016.12.085).
19. Daabo, A.M., Ahmad, A., Mahmoud, S. and Al-Dadah, R.K., "Parametric analysis of small scale cavity receiver with optimum shape for solar powered closed Brayton cycle applications", ***Applied Thermal Engineering***, Vol. 122, (2017), 626-641. (https://doi.org/10.1016/j.applthermaleng.2017.03.093).
20. Azzouzi, D., Boumeddane, B. and Abene, A., "Experimental and analytical thermal analysis of cylindrical cavity receiver for solar dish", ***Renewable Energy***, Vol. 106, (2017), 111-121. (https://doi.org/10.1016/j.renene.2016.12.102).
21. Loni, R., Kasaeian, A.B., Askari-Asli-Ardeh, E., Ghobadian, B. and Gorjian, Sh., "Experimental and numerical study on dish concentrator with cubical and cylindrical cavity receivers using thermal oil", ***Energy***, Vol. 154, (2018), 168-181. (https://doi.org/10.1016/j.energy.2018.04.102).
22. Singh, A.K. and Natarajan, S.K., "Comparative study of modified conical cavity receiver with other receivers for solar paraboloidal dish collector system", ***Research Square***, (2021). (https://doi.org/10.21203/rs.3.rs-237950/v1).
23. Yuan, Y., Xiaojie, L., Ziming, C., Fuqiang, W., Yong, S. and Heping, T., "Experimental investigation of thermal performance enhancement of cavity receiver with bottom surface interior convex", ***Applied Thermal Engineering***, Vol. 168, (2020). (https://doi.org/10.1016/j.applthermaleng.2019.114847).
24. Bopche, S., Rana, K. and Kumar, V., "Performance improvement of a modified cavity receiver for parabolic dish concentrator at medium and

high heat concentration", ***Solar Energy***, Vol. 209, (2020), 57-78. (https://doi.org/10.1016/j.solener.2020.08.089).

25. Bellos, E., Bousi, E., Tzivanidis, C. and Pavlovic, S., "Optical and thermal analysis of different cavity receiver designs for solar dish concentrators", ***Energy Conversion and Management: X***, Vol. 2, (2019), 100013. (https://doi.org/10.1016/j.ecmx.2019.100013).
26. Soltani, S., Bonyadi, M. and Madadi-Avargani, V., "A novel optical-thermal modeling of a parabolic dish collector with a helically baffled cylindrical cavity receiver", ***Energy***, Vol. 168, (2019), 88-98. (https://doi.org/10.1016/j.energy.2018.11.097).
27. Thirunavukkarasu, V. and Cheralathan, M., "An experimental study on energy and exergy performance of a spiral tube receiver for solar parabolic dish concentrator", ***Energy***, Vol. 192, (2020), 116635. (https://doi.org/10.1016/j.energy.2019.116635).
28. Wang, H., Huang, J., Song, M. and Yan, J., "Effects of receiver parameters on the optical performance of a fixed-focus Fresnel lens solar concentrator/cavity receiver system in solar cooker", ***Applied Energy***, Vol. 237, (2019), 70-82. (https://doi.org/10.1016/j.apenergy.2018.12.092).
29. Al-Dulaimi, R.K.M., "Experimental investigation of the receiver of a solar thermal dish collector with a dual layer, staggered tube arrangement, and multiscale diameter", ***Energy Exploration and Exploitation***, Vol. 38, No. 4, (2020), 1212-1227. (https://doi.org/10.1177/0144598719900658).
30. Loni, R., Askari-Asli-Ardeh, E., Ghobadian, B., Kasaeian, A.B., Gorjian, Sh, Najafi, G. and Evangelos, B., "Research and review study of solar dish concentrators with different nanofluids and different shapes of cavity receiver: Experimental tests", ***Renewable Energy***, Vol. 145, (2020), 783-804. (https://doi.org/10.1016/j.renene.2019.06.056).
31. Gavagnin, G., Sánchez, D., Martínez, G.S., Rodríguez, J.M. and Muñoz, A., "Cost analysis of solar thermal power generators based on parabolic dish and micro gas turbine: Manufacturing, transportation and installation", ***Applied Energy***, Vol. 194, (2017), 108-122. (https://doi.org/10.1016/j.apenergy.2017.02.052).
32. Pathak, A., Deshpande, K., Kurhe, N., Baste, P. and Jadkar, S., "Comfort cooling application using fixed focus solar parabolic dish concentrator integrated with double effect vapor absorption Machine", ***International Research Journal of Engineering and Technology***, Vol. 5, No. 3, (2018), 1875-1880. (https://www.irjet.net/archives/V5/i3/IRJET-V5I3424.pdf).
33. Xie, W.T., Dai, Y.J. and Wang, R.Z., "Numerical and experimental analysis of a point focus solar collector using high concentration imaging PMMA Fresnel lens", ***Energy Conversion and Management***, Vol. 52, No. 6, (2011), 2417-2426. (https://doi.org/10.1016/j.enconman.2010.12.048).
34. Çengel, Y.A. and Ghajar, A.J., Heat and mass transfer: Fundamentals and applications, McGraw Hill, Turkey, (2007), 432-522. (https://www.mheducation.com).
35. ROCKWOOL stone wool insulation. (https://www.rockwool.com/group/).
36. Kirkup, L. and Frenkel, B., An introduction to unceratinty measurement using the GUM, Calculation of unceratinty, Cambridge University Press, Sydney, (2006), 97-125. (https://doi.org/10.1017/CBO9780511755538).
37. Yang S.M. and Tao, W.Q.B.Z., Heat transfer, Higher Education Press, (2000). (https://www.amazon.com/Transfer-third-Higher-Education-Chinese/dp/7040066939).
38. Jilte, R.D., Kedare, S.B. and Nayak, J.K., "Investigation on convective heat losses from solar cavities under wind conditions", ***Energy Procedia***, Vol. 57, (2014), 437-446. (https://doi.org/10.1016/j.egypro.2014.10.197).
39. Prakash, M., Kedare, S.B. and Nayak, J.K., "Investigations on heat losses from a solar cavity receiver", ***Solar Energy***, Vol. 83, No. 2, (2009), 150-170. (https://doi.org/10.1016/j.solener.2008.07.011).
40. Jilte, R.D., Kedare, S.B. and Nayak, J.K., "Natural convection and radiation heat loss from open cavities of different shapes and sizes used with dish concentrator", ***Mechanical Engineering Research***, Vol. 3, No. 1, (2013), 25-43. (https://doi.org/10.5539/mer.v3n1p25).
41. Mawire, A. and Taole, S.H., "Experimental energy and exergy performance of a solar receiver for a domestic parabolic dish concentrator for teaching purposes", ***Energy for Sustainable Development***, Vol. 19, (2014), 162-169. (https://doi.org/10.1016/j.esd.2014.01.004).

JREE: Vol. 8, No. 4, (Autumn 2021) 42-51

Journal of Renewable Energy and Environment

Research Article

Journal Homepage: www.jree.ir

Effect of Nano Fluids on the Thermal Performance and Efficiency of Linear Fresnel Collector in Hot Summer Months

Najmeh Salehi [a], Arash Mirabdolah Lavasani [a*], Ramin Mehdipour [b], Mohammad Eftekhari Yazdi [a]

[a] *Department of Mechanical Engineering, School of Engineering, Central Tehran Branch, Islamic Azad University, Tehran, Iran.*
[b] *Department of Mechanical Engineering, Faculty of Engineering, Tafresh University, Tafresh, Markazi, Iran.*

PAPER INFO

Paper history:
Received 12 September 2020
Accepted in revised form 15 August 2021

Keywords:
Linear Fresnel Collectors,
Direct Steam Generation,
Critical Heat Flux,
Thermal Efficiency,
Nanofluid,
Look Up Table

ABSTRACT

One of the best and most important types of concentrating solar power plants is the linear Fresnel collector. The thermal performance and application of absorber in a solar power plant can be enhanced using direct steam generation technology. A particular discrepancy between the present study and others lies in our attempt at applying a new method for calculating critical heat flux based on Look-up Table. In the current study, effects of nanofluid on the length of the critical heat flux and convection heat transfer coefficient were investigated. The nanoparticles considered in this study were aluminum, silver, nickel, and titanium dioxide at concentrations of 0.01, 0.1, 0.3, 0.5, 1 and 2 %. Modeling results revealed that the heat transfer coefficient increased upon enhancing the volumetric concentration of nanoparticles, thereby improving this coefficient at 2 vol. % nickel nanoparticles, which was 10.6 % above the value of pure water. On the other hand, thermal efficiency was enhanced when nickel nanoparticles were dispersed in pure water such that increase rates of thermal efficiency equaled 11.2, 10.8 and 11.3 % in the months of June, July, and August, respectively, when the volume concentration of nanoparticles was 0.5 %.

https://doi.org/10.30501/jree.2020.243043.1141

1. INTRODUCTION

Solar energy is a clean renewable energy resource and it is quite advantageous in preventing serious environmental problems attributed to fossil fuel. The concentrated solar power plant technology that converts sun irradiation to electricity is a promising approach in most industries. One of the best important types of this technology is Linear Fresnel Collector (LFC) and it is considered an economical choice for electricity production at moderate temperatures. In these concentrators, sun irradiation is absorbed by flat mirrors, which rely on sun direction [1].

So far, many researchers have modeled and investigated the performance of linear Fresnel collectors, e.g., the study of Guadamud et al. for further reference [2]. In a study, the advanced method was used for heat transfer modeling and dynamic discussion based on the details of linear Fresnel collectors. Also, Benyakhlef et al. conducted a numerical analysis so that the curvature effect of mirrors could be studied on optical efficiency and flux density on absorber of linear Fresnel collector installed in solar fields in Morocco [3].

Many studies have targeted the application of nanoparticles to heat transfer in recent years. Bellos et al. investigated the quality enhancement of the linear Fresnel collector using nanofluids. The used nanofluid included Syltherm/CuO at volume concentrations of 2, 4, and 6 % and thermal efficiency enhancement was 0.82 % with a volumetric concentration of 4 % and finned absorber [4]. Also, in another research, Bellos and Tzivanidis proposed an innovative way for improving the thermal quality of linear Fresnel collectors, particularly at high temperatures. CuO used nanoparticles with Syltherm 800 as the base fluid. According to the obtained results, the highest enhancement of the thermal efficiency was near 0.8 %, while it increased up to 50 % with the existing pump [5].

Further, to ensure better results for heat transfer with nanofluid, Zamzamian and Mansouri executed an experimental investigation regarding the enhancement of the thermal performance of Vacuum Tube Soalr Collectors (VTSC) by using alumina nanofluid as heat transfer fluid [6]. Rezazadeh et al. [7] carried out a numerical analysis of a proton exchange membrane fuel cell based on a three-dimensional CFD model. The numerical simulation revealed that some important parameters in their research were highly dependent on each other and the fuel cell efficiency was affected by the kind of species distribution. In another study regarding the energy and entropy generation rate in linear Fresnel reflector, Nunez et al. [8] have been carried out a numerical analysis so that they have been obtained the first law, second law and optical efficiencies of the LFR. Eventually, their results has revealed the 97.4 % of the total entropy generation is due to conduction. Ardekani et al. [9] did an experimental study on the heat transfer enhancement in the nanofluid flow on the helically coiled tubes while flow type was considered to be of turbulence and nanoparticles

*Corresponding Author's Email: arashlavasani@iauctb.ac.ir (A. Mirabdolah Lavasani)
URL: https://www.jree.ir/article_135113.html

Please cite this article as: Salehi, N., Mirabdolah Lavasani, A., Ramin Mehdipour, R. and Eftekhari Yazdi, M., "Effect of nano fluids on the thermal performance and efficiency of linear fresnel collector in hot summer months", ***Journal of Renewable Energy and Environment (JREE)***, Vol. 8, No. 4, (2021), 42-51. (https://doi.org/10.30501/jree.2020.243043.1141).

silver and SiO_2 were applied inside pure water as the base fluid. Bellos and Tzivanidis [10] pointed to the most effective enhancement methods for the concentrating solar collectors based on a review of the recent tendency for the solar concentrating collectors considering the performance improvement methods. Ghodbane et al. [11] performed a performance evaluation regarding using Multi-walled carbon nanotube nanoparticles in distilled water in linear Fresnel collector to obtain its influence on thermal efficiency. According to their results, the nanofluid used by Ghodbane et al. with 0.3 vol. % attained thermal efficiency of 33.81 %. On the other hand, Bellos and Tzivanidis [12] scrutinized the thermal efficiency increasing of nanofluid-based parabolic trough collectors. In fact, they have used nanoparticles with thermal oil as heat transfer fluid so that thermal efficiency improvement could be obtained at 0.31, 0.54, and 0.74 % for Cu nanoparticles with 2, 4, and 6 vol. %, respectively.

In a similar research, Razeghi et al. investigated the effect of Al_2O_3–Water nanofluid flow on Nusselt number and pressure drop enhancement in a rectangular curved micro-channel [13]. Razmmand and Mehdipour [14, 15] investigated the effect of different coatings on the thermal performance and tube thermal stress for the parabolic trough collectors. On the other hand, Razmmand et al. [16] conducted a numerical investigation into the effect of adding nanoparticles to the pure water about the solar parabolic trough collector. Boiling heat transfer has been enormously used in many industries including boiler tubes, cooling, and evaporating reactors at nuclear power plants, recently. Kamel et al. carried out some experimental studies and investigated the augmentation of the heat transfer coefficient and Critical Heat Flux (CHF) [17].

In the current study, the effect of nanofluid on the length of the CHF and heat transfer coefficient was examined. For the sake of accuracy and specificity, the location of Mahallat in Iran was a case study. The considered irradiations in this research involved 336, 380 and 341 (W/m^2) in the months of June, July, and August, respectively. Also, the mass flux equaled 500 (Kg/m^2s). The used nanoparticles included aluminum, silver, nickel, and titanium dioxide with the volumetric concentrators of 0.01, 0.1, 0.3, 0.5, 1 and 2 %. In fact, the critical heat flux was calculated by LUT method [18] and the main distinguishing feature of the current study from others is its choice of calculation method. The convective heat flux entering fluid was obtained by performing code calculation for thermal analysis. The critical heat flux was determined by the comparison between the consequent convection heat fluxes in each element from results of performing code calculation and facts on LUT. However, convective heat flux in the boiling section does not exist in the LUT; hence, the convective heat flux related to last element was determined as critical heat flux. In the following, other parameters including internal surface temperature of tube, vapor quality, and critical heat flux location in the CHF point were obtained upon determining the elements related to critical heat flux.

According to the obtained results, the heat transfer coefficient that is the desired parameter in current study was increased following the dispersion of nanoparticles. This coefficient was enhanced at nanoparticles Ag, Ni, TiO_2, and Al at a volumetric concentration of 2 % than the obtained values for the pure water so that it equaled 11.65, 10.6, 5.65 and 4.94 %, respectively, in August. There is no doubt that our priority to reap the economical fruit of choosing the best type of nanoparticles. As a result, the nanoparticle nickel had the best results for heat transfer coefficient parameter. Also, the best and most important point is the increasing and decreasing values of the length of the CHF in consecutive months. For the hottest three months of the year, it was observed that the length of the CHF point decreased upon increasing sun irradiation from June to July and it equaled 1.2 %. However, the mentioned length was enhanced by decreasing sun irradiation in August which was equal to 3.6 %.

2. THE GOVERNING EQUATIONS AND MODELING

In fact, the thermo-physical characteristics of the heat transfer fluid were determined upon considering the nanoparticles dispersed in the base fluid. In this section, some equations and the corresponding fluid thermo-physical parameters are explained. In this study, the modeling is based on the energy balance for the thermal collector element. In the linear Fresnel collector, this balance generally involves sun irradiation, radiation losses from flat mirrors and absorber complex, thermal losses from thermal collector, and existing fluxes in heat transfer fluid. Calculating the CHF has been executed by the LUT method with approach of the iteration technique. The Gauss-Seidel, which is an iteration technique, was employed in the current study for solving a linear system of equations. The relevant items are given in Figures 1 and 2.

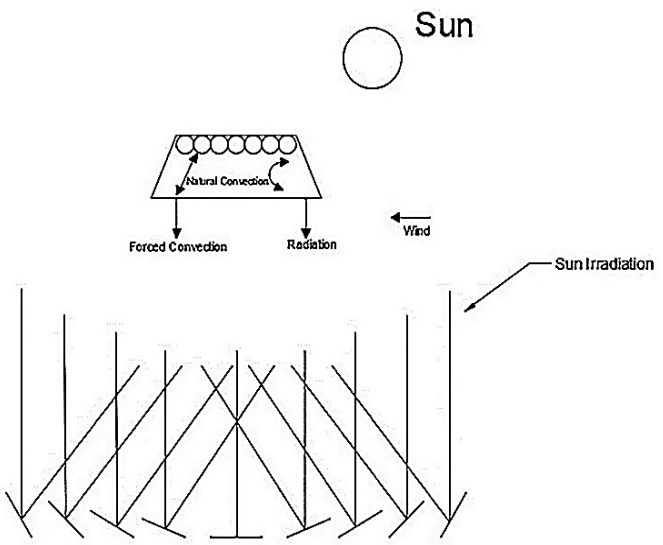

Figure 1. Cross-section of the Fresnel power plant

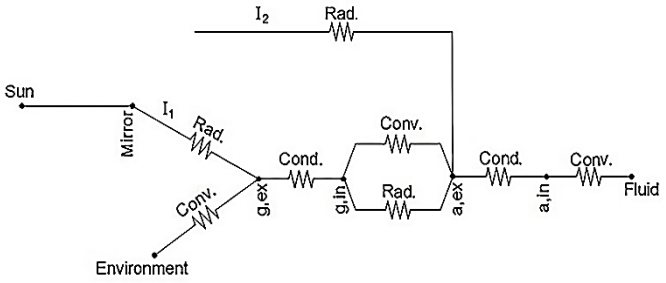

Figure 2. The heat transfer circuit

According to Figure 2, the first radiation heat flux is reflected from the mirror to the external surface of the glass equals "I_1". Therefore, part of the mentioned flux was transferred through the glass thickness by the conduction type of heat flux and the remaining part entered the circumference by the convection heat flux.

In the following, the transmitted radiation heat flux, "I_2", entered the external surface of the tubes and it was shared among the entire tubes equally. In fact, the mentioned heat flux was divided into "N", if there was the amount "N" for the tubes. In this section, part of radiation heat flux was reflected onto the cavity due to the transmission coefficient of the absorber and another part entered the heat transfer fluid. A significant point is that these types of the existing heat fluxes inside the cavity include convection and radiation heat flux. Due to the small quantity of the existing radiation heat flux inside the cavity, it can be neglected in the calculations.

2.1. Energy balance inside of heat transfer fluid

Due to some modifications made to the approach in the two-phase flow section [22], the balance correlation changed based on enthalpy and vapor quality [19].

Since the vapor quality equals zero in the entire single-phase fluid flow and sub-cooled boiling flow sections, the most important items in these sections include specific heat capacity and mass flow rate. Eq. 1 shows the energy balance inside the heat transfer fluid in the two mentioned sections [20].

$$\dot{q}_{a-f,conv} = \frac{\dot{m}C_p(T_{out}-T_{in})}{l} \quad (1)$$

In the two-phase flow section, the heat transfer fluid was divided into liquid and vapor modes. Since the fluid temperature was constant and phase variations occurred in the entire two-phase fluid flow section, there was the latent heat of the vaporization characteristic. The heat transfer fluid lost its heat in order to produce the vapor phase and in fact, the latent heat of vaporization was defined [22].

$$\dot{q}_{a-f,conv} = \frac{m_p h_{fg}}{l} \quad (2)$$

In the above correlation, the parameter "m_p" is fluid mass that is converted from liquid to vapor in every element and it is calculated by the following equation [22].

$$m_p = m_{total}(x_{out} - x_{in}) \quad (3)$$

Also, parameter "m_{total}" is the total mass of fluid in a long flow.

2.2. Energy balance associated with absorber complex

The first law of thermodynamics was applied to some of the heat transfer problems. At first, control volume was specified to elaborate this law and the two control volumes were called in the current model such as control volumes related to the absorber and glass. In the following, the correlations related to the energy balance on glass and absorber wall are given respectively as follows [20]:

$$\dot{q}_{g,s.rad} + (N.\dot{q}_{a-g,conv}) - \dot{q}_{g-e,conv} = 0 \quad (4)$$

$$\dot{q}_{a,s.rad} - \dot{q}_{a-f,conv} - \dot{q}_{a-g,conv} = 0 \quad (5)$$

Also, there are two energy balances on the surface of the absorber and glass, as separately shown in Eqs. 6 and 7, [20].

$$\dot{q}_{g,cond} + \dot{q}_{a-g,conv} = 0 \quad (6)$$

$$\dot{q}_{a,cond} - \dot{q}_{a-f,conv} = 0 \quad (7)$$

2.3. Convection heat flux between tube and heat transfer fluid

Heat was transferred to the fluid through the convection heat flux "$\dot{q}_{a-f,conv}$"; therefore, transmission from the wall and the increase in the fluid temperature occurred. In the following, the convection heat flux equations were for all sections of the fluid flow including single-phase fluid flow, sub-cooled boiling flow, and eventually two-phase fluid flow. The convection heat flux from the absorber to the fluid is given in Eq. 1 [19, 20].

$$\dot{q}_{a-f,conv} = h_f \pi D_{a,in}(T_{a,in} - T_m) \quad (8)$$

The parameter T_m can be determined through $T_m = \frac{T_{in}+T_{out}}{2}$ and Nusselt number in the single-phase fluid flow is calculated through the following equation [20]. As a matter of fact, this formula has been set due to the existing turbulent flow in the circular tube and the heating process in the long flow.

$$Nu_f = 0.023(Re_f)^{0.8}(Pr_f)^{0.4} \quad (9)$$

In the sub-cooled boiling section, the tube temperature on its internal surface reached the saturated temperature immediately. The heat transfer coefficient has been calculated by the correlation of Forster-Zuber that it has come in Eq. 11 [21].

$$\dot{q}_{nb} = h_{nb}\pi D_{a,in}(T_{a,in} - T_{out}) \quad (10)$$

$$h_{nb} = 0.00122\frac{k_l^{0.79}C_{p,l}^{0.45}\rho_l^{0.49}}{\sigma^{0.5}\mu_l^{0.29}h_{fg}^{0.24}\rho_v^{0.24}}(T_{a,in} - T_{out})^{0.24}\Delta P_{sat}^{0.75} \quad (11)$$

Subsequently, the heat transfer fluid was conveyed from the sub-cooled flow to the two-phase flow section when the fluid temperature reached the saturated temperature. Thus, from now on, the fluid temperature remains constant and equals the saturated temperature; however, the tube temperature on its internal surface and the vapor quality were enhanced step by step up to the CHF [22].

$$\dot{q}_{nb} = h_{tp}\pi D_{a,in}(T_{a,in} - T_s) \quad (12)$$

$$h_{tp} = h_L[(1-x)^{0.8} + \frac{3.8\,x^{0.76}(1-x)^{0.04}}{pr^{0.38}}] \quad (13)$$

$$h_L = 0.023 Re_l^{0.8} Pr_l^{0.4}\frac{k_l}{D_{a,in}} \quad (14)$$

2.4. Nanofluid equations and thermo-physical characteristics of based fluid

In the current analysis, the effective parameters of heat flux from the absorber to the fluid in considering nanofluid are based on the correlations of nanoparticles.

According to this approach, such parameters as density, dynamic viscosity, and coefficient of thermal conductivity, specific heat capacity, and enthalpy have modified the outcome of the calculations [23]. Massimo Corcione [24] proposed two empirical correlations for predicting density and dynamic viscosity of nanofluids and it was revealed that the ratio between the thermal conductivity of the nanofluid and the pure base liquid as well as the ratio between the dynamic viscosity of the nanofluid and the pure base liquid increased following an increase in the nanoparticle volume concentration.

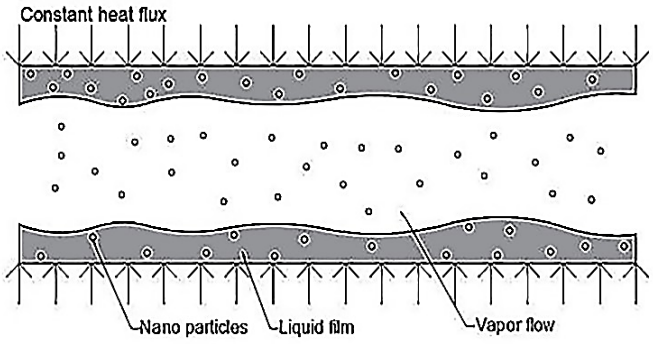

Figure 3. Schematic of nanoparticles mixing inside heat transfer fluid [16]

$$\rho_{nf} = \rho_p \phi + \rho_l (1 - \phi) \quad (15)$$

$$\mu_{nf} = \frac{\mu_l}{\left(1-34.87\left(\frac{d_p}{d_l}\right)^{-0.3} \phi^{1.03}\right)} \quad (16)$$

$$d_l = 0.1\left(\frac{6M}{N\pi\rho_{l,ref}}\right) \quad (17)$$

$$k_{nf} = k_l\left[\frac{k_p+(n-1)k_l-(n-1)\phi(k_l-k_p)}{k_p+(n-1)k_l+\phi(k_l-k_p)}\right] \quad (18)$$

$$C_{p,nf} = \frac{(\phi\rho_p C_{p,p}+(1-\phi)\rho_l C_{p,l})}{\rho_{nf}} \quad (19)$$

In Equation (17), d_l is the equivalent diameter of a base fluid molecule, M is the molecular weight of the base fluid, N is the Avogadro number, and $\rho_{l,ref}$ is the mass density of the base fluid which varies with fluid temperature [23, 24]. The enthalpy for nanofluids was calculated through the experimental Eq. 20. Coefficients (C1) and (C2) were calculated through the experimental Eqs. 21 and 22 such that they were only dependent on volumetric concentrations. Of note, the used coefficients in Eqs. 21 and 22 are exclusive for every nanoparticle, as given in Table 1.

$$h_{lv} = C_1 P^{C_2} \quad (20)$$

$$C_1 = A\phi^5 + B\phi^4 + C\phi^3 + D\phi^2 + E\phi + F \quad (21)$$

$$C_2 = \alpha\phi^5 + \beta\phi^4 + \gamma\phi^3 + \sigma\phi^2 + \varepsilon\phi + \omega \quad (22)$$

Table 1. Data of the coefficients in enthalpy equation [25]

Coefficients	Nanoparticles			
	Ag	**Al**	**Ni**	**TiO_2**
A	190.6	-13.6	529.1	-244.9
B	-1342.6	267.6	-4081.7	2096.2
C	3297.4	-1550.5	11357.9	-6687.7
D	-3279.4	3342.7	-13995.7	9633.9
E	973.5	-2417.6	7231.3	-5563.7
F	2271.3	3225	2235.1	2368.3
α	-0.01	0.00	-0.03	0.01
β	0.1	-0.03	0.3	-0.2
γ	-0.3	0.1	-0.7	0.6
σ	0.3	-0.2	0.9	-0.9
ε	-0.1	0.2	-0.4	0.6
ω	0	-0.1	-0.01	-0.01

Thermo-physical characteristics of the base fluid are dependent on the fluid temperature and are modified by altering temperature in the whole fluid flow so that the following equations reveal this important point [26].

$$\mu(T_{fluid}) = (2.1897e^{-11})T_{fluid}^{\ 4} - (3.055e^{-8})T_{fluid}^{\ 3} + (1.6028e^{-5})T_{fluid}^{\ 2} - 0.0037524T_{fluid} + 0.33158 \quad (23)$$

$$\rho(T_{fluid}) = (-1.5629e^{-5})T_{fluid}^{\ 3} + (0.011778)T_{fluid}^{\ 2} - (3.0726)T_{fluid} + 1227.8 \quad (24)$$

$$k(T_{fluid}) = (1.5362e^{-8})T_{fluid}^{\ 3} - (2.261e^{-5})T_{fluid}^{\ 2} + (0.010879)T_{fluid} - 1.0294 \quad (25)$$

$$C_p(T_{fluid}) = (1.1105e^{-5})T_{fluid}^{\ 3} - (0.0031078)T_{fluid}^{\ 2} - (1.478)T_{fluid} + 4631.9 \quad (26)$$

Bellos and Tzivanidis [12] presented a formula to calculate thermal efficiency, as shown in the following correlation.

$$\eta_{th} = Q_u/Q_s \quad (27)$$

In the above equation, Q_u is the useful heat obtained from energy balance in the fluid volume (Eq. 8) and Q_s is the solar radiation obtained from Eq. 28 [20].

$$\dot{q}_{a,s.rad} = \frac{1}{N} I_{sun}.\beta.\gamma.\alpha_a.W \quad (28)$$

In the above equations, W, N, I_{sun}, α_a, α_g, β, and γ denote the width of total of mirrors, number of tubes, the amount of sun irradiation, absorption coefficient of tube, absorption coefficient of glass, reflection, and transient coefficient of glass, respectively.

3. SOLUTION ALGORITHM

At first, the convection heat flux was computed by performing code calculations and so, the obtained results were compared with the existing heat fluxes on LUT. Ultimately, the CHF was acquired by the interpolation between the resulting convection heat flux and vapor quality from the code calculation and LUT data. For this reason, current research was distinguished against other executed works. The solution flowchart is accessible in [27]. In addition, the model geometry and thermo-physical characteristics of the base fluid and the used nanoparticles are given in Tables 2 and 3.

Table 2. Geometrical and thermo-physical characteristics

Parameters	Value
Length of pipe	600 m
$D_{a,in}$	0.064 m
$D_{a,ex}$	0.078 m
Height of cavity	0.1 m
Width of glass	0.6 m
Thickness of glass	0.01 m
Surface width for bottom of pipes	0.49 m
Width of mirrors	31.58, 35.2, 35.7 m
Thermal conductivity of glass	1.4
Absorptivity coefficient of glass	0.05
Thermal conductivity of absorber	126.7
Density	957.85
Thermal conductivity	0.680
Viscosity	0.000279
Heat capacity	4217

Table 3. Thermo-physical properties of the mentioned nanoparticles [17]

Nano fluid	Ag	Al	Ni	TiO_2
Specific heat	235	903	444	690
Thermal conductivity	419	237	90.7	8.5
Density	10500	2702	8900	4230

The effect of nanofluid on the length of the CHF and heat transfer coefficient was investigated based on the climate condition of Mahallat city. Mahallat is a city in Markazi province, Iran. It has a cold climate in the winter and in this study, thermal analysis was conducted for the three hottest months including June, July, and August. In Table 4, the sun irradiation levels of the entire months were obtained.

Table 4. The sun irradiation of Mahallat, Iran

Months	Sun irradiation (W/m^2)	Time of sun irradiation (h)
January	143	200
February	188	205
March	218	218
April	267	240
May	278	260
June	336	343
July	380	332
August	341	346
September	296	327
October	228	286
November	155	206
December	156	198

4. VALIDATION

4.1. Single-phase validation

To ensure the validation of our research, a study counterpart of Ruben Abbas et al. was employed [29]. In this research, the results for different states with various tubes were obtained. Also, the dimensions of the vacuum chamber were considered fixed, and finally, the diameter of the tubes was modified while some changes in the number of tubes were observed. A common point of these analyses was the large-to-small diameter ratio of the tubes, equal to 1.167 for all states. In Table 5, the exterior and internal diameters of different tubes are given.

Table 5. The exterior and internal diameters of different tubes [29]

Number of pipes	External diameter (cm)	Internal diameter (cm)
1	28.4	24.4
3	16.3	14
5	9.8	8.4
7	7	6
9	5.4	4.7
11	4.5	3.8
19	2.2	1.9
25	2	1.7
31	1.6	1.4
33	1.5	1.3
35	1.4	1.2

According to the referenced study [29], the length of the tube was 300 meters and Therminol VP1 oil was considered as the heat carrier fluid in this validation. Furthermore, the fluid inlet temperature to linear Fresnel collector was assumed 290 °C. In Table 6, the thermo-physical properties of this fluid can be revealed. By applying the Fresnel system properties according to [29] and the fluid properties to simulated software, the temperatures were calculated. In this section, the validation testing of the fluid temperature at the end of the tube was conducted for 3 tubes, 5 tubes and 7 tubes at velocities of 0.1, 0.3, 0.5, 0.8, 1, 3 and 6 m/s, which can be observed in Figures 4 to 6. In Tables 7 to 9, the numerical results of these diagrams are also obtained.

Table 6. Thermo-physical characteristics of Therminol VP1 at 290 °C [29]

Parameter	Quantity	Unit
Density	828	$\frac{kg}{m^3}$
Thermal conductivity	0.098	$\frac{W}{m.K}$
Viscosity	0.281	$\frac{m^2}{s}$
Heat capacity	2287	$\frac{j}{kg.K}$

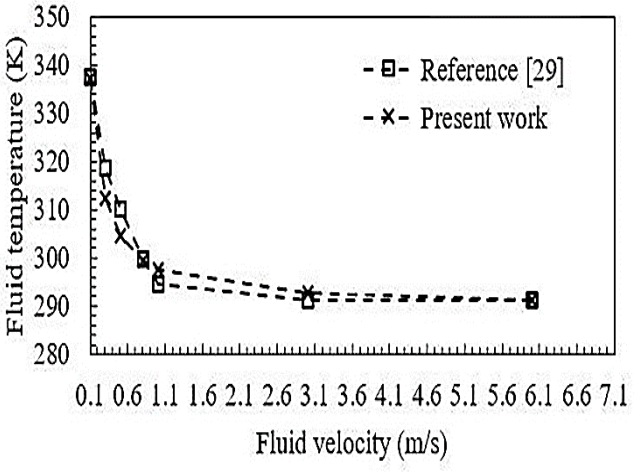

Figure 4. Comparison between the fluid temperature at the end of tube and the fluid velocity measured in [29] for three absorber tubes

Table 7. Numerical values of diagram in Figure 4

Fluid velocity (m/s)	Reference [29] (K)	Present work (K)	Deviation (%)
0.1	337.571	337.29	0.083
0.3	318.714	312.36	2.034
0.5	310.143	304.48	1.860
0.8	299.857	299.45	0.136
1	294.714	297.67	0.993
3	291.286	292.66	0.469
6	291.286	291.34	0.019

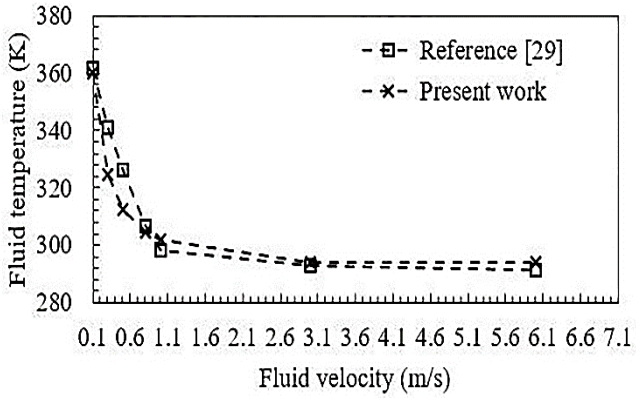

Figure 5. Comparison between the fluid temperature at the end of tube and the fluid velocity measured in [29] for five absorber tubes

Table 8. Numerical values of the diagram in Figure 5

Fluid velocity(m/s)	Reference [29] (K)	Present work (K)	Deviation (%)
0.1	361.571	360.23	0.372
0.3	341	324.43	5.107
0.5	326.429	312.47	4.467
0.8	306.714	304.74	0.648
1	298.143	301.99	1.274
3	293	294.18	0.401
6	291.286	294.18	0.984

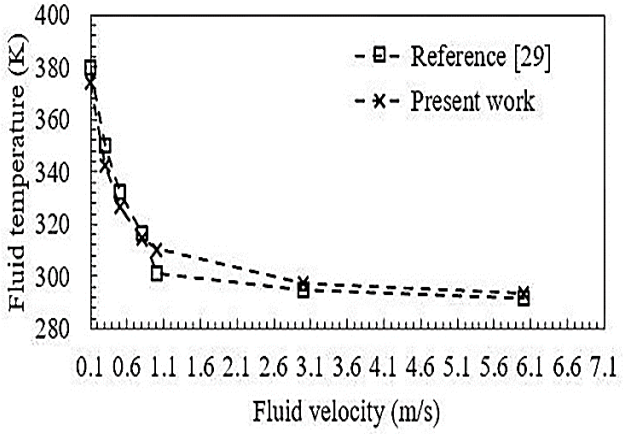

Figure 6. Comparison between the fluid temperature at the end of tube and the fluid velocity measured in [29] for seven absorber tubes

Table 9. Numerical values of the diagram in Figure 6

Fluid velocity (m/s)	Reference [29] (K)	Present work (K)	Deviation (%)
0.1	379.595	374.1	1.469
0.3	350.209	342.14	2.358
0.5	332.211	326.3	1.812
0.8	316.622	314.75	0.595
1	300.949	310.4	3.045
3	295.031	297.37	0.787
6	291.529	293.76	0.759

4.2. Nanofluid validation

Nanofluid validation is significantly important for the present analysis because the investigation of the nanofluid effect on thermal properties is the objective of this research. Razmmand et al. [16] investigated the effect of nanofluids on the heat transfer from the solar parabolic trough collectors, and in the current study, validation was done in accordance with Razmmand's findings about the length of CHF versus the volumetric concentration for the gold nanoparticles. Also, the volumetric concentrations were considered 0, 0.1, 0.3, 0.5, 1 and 2 % where the difference of results between the current finding and Razmmand's result was ultimately obtained at about 7.8 %. The result of this validation is illustrated in Figure 7 and Table 10.

Table 10. Numerical result of the nanofluid validation about the length of CHF in Au-H_2O nanofluid

Volumetric concentration (%)	Reference [16] (m)	Present work (m)	Deviation (%)
0	49.69	53.56	7.226
0.1	99.67	105.95	5.927
0.3	103.05	111.81	7.835
0.5	106.28	113.72	6.542
1	116.85	126.20	7.409
2	133.52	145.80	8.422

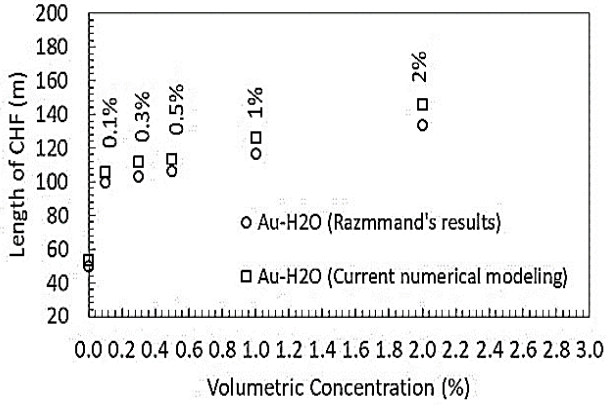

Figure 7. Comparison between the results of the length of the CHF point and those in [16]

5. RESULTS AND DISCUSSION

CHF is an upper limit of heat flux for nucleate boiling. Enhancing CHF or postponing the dryout condition offers the potential for improving the performance of many practical applications that use boiling as their heat transfer mode. Different techniques have been proposed to achieve this objective and one of the most important and practical of them is using nanofluids [30]. As mentioned above, the environmental condition specific to Mahallat in Iran was considered for analysis such that the sun irradiation rates in the hottest three months of the year including June, July, and August were 336, 380 and 341 (W/m^2), respectively. Also, in this study, the amount of mass flux equaled 500 kg/m^2s.

In this research, a comparison was made between the results obtained from pure water and nanofluid in order to investigate the effectiveness of nanoparticles in the thermal performance. In the following, diagrams of the fluid temperature in August for nickel nanoparticles are shown in Figure 4. As a result,

enhancing the length of the CHF for nanofluid nickel-pure water than pure water in the entire month is considered with volume concentrations of 28.89, 29.84, 31.93, 34.05, 39.34 and 50.10. In fact, delay in the occurrence of CHF in nanofluids is greater than that in pure water.

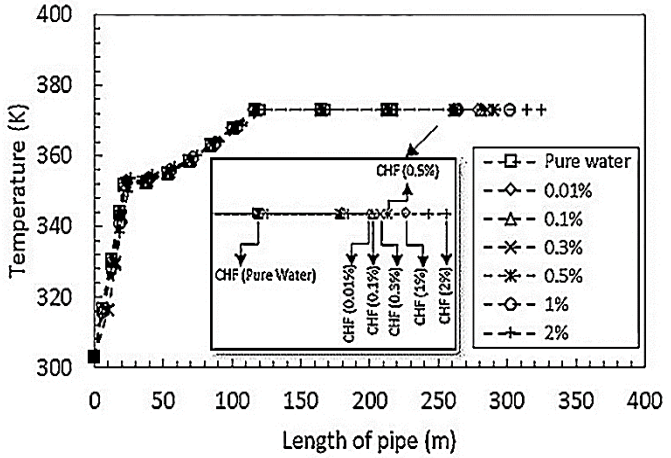

Figure 8. Distribution of fluid temperature for nickel nanoparticles in August

Thermal performance for all the nanoparticles is observable in Figures 9 and 10. One of the characteristics of using the nanoparticles is improving the length of the CHF obtained by increasing the volumetric concentration of nanoparticles. Figure 9 exhibits this improvement for nickel and aluminum nanoparticles. As a result, the greatest length of CHF among the entire nanoparticles compared to pure water equaled 64.30 %, which was related to aluminum. In Figure 7, the heat transfer coefficient and temperature difference for fluid and wall in CHF point versus volumetric concentration were determined for Aluminum and Nickel nanoparticles at volume concentrations of 0.001, 0.01, 0.03, 0.05, 1 and 2 % in August. As observed earlier, the heat transfer coefficient was enhanced upon increase in the volume concentration and a decrease in the temperature difference for the fluid and wall. Since fluid temperature is constant and equals the saturated temperature, the tube temperature on its internal surface decreases in the long flow, according to Table 11. As a matter of fact, the length of the CHF was taken as a case in point to pinpoint the importance of CHF postponement that occurred following the dispersion of the nanoparticles in pure water.

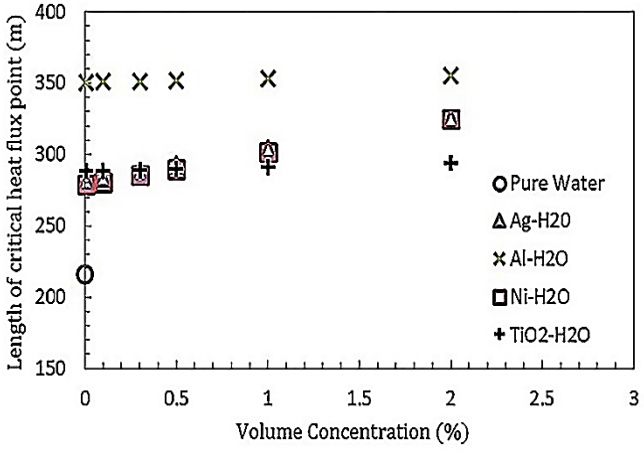

Figure 9. Diagram of the length of the CHF point versus volumetric concentration for pure water and all the nanofluids

Table 11. Tube temperature on its internal surface for nanoparticles in all the considered volumetric concentrations

Volumetric concentration (%)	Nano particles			
	Ag	Ni	TiO_2	Al
0 (pure water)	379	379	379	379
0.01	379	379	379	378.99
0.1	378.97	378.97	378.98	378.98
0.3	378.91	378.91	378.96	378.96
0.5	378.84	378.86	378.92	378.93
1	378.7	378.72	378.85	378.86
2	378.43	378.47	378.7	378.73

The following figure illustrates the linear enhancement, reduced heat transfer coefficient, and temperature difference. Also, enhancement of the heat transfer coefficient was the obvious result at high volumetric concentrations of the nanoparticles. In this respect, enhancement of the heat transfer coefficients equaled 10.6 and 4.94 % in nickel and aluminum nanoparticles at a volumetric concentration of 2 %, compared to pure water. Tables 12 and 13 show the numerical results of heat transfer coefficient and the length of the CHF point for all the nanoparticles.

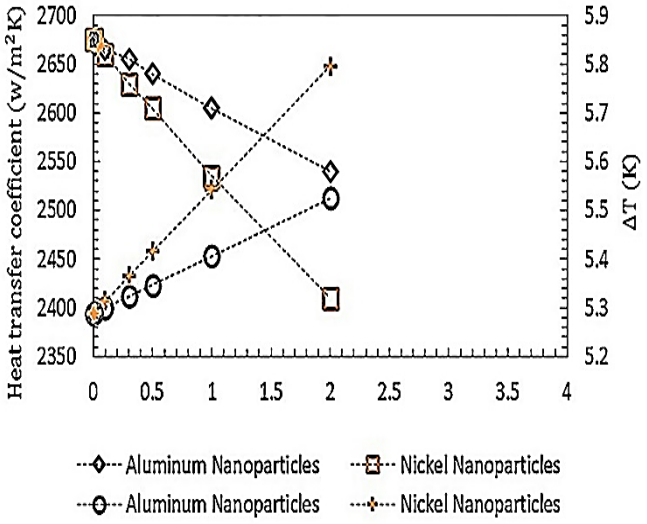

Figure 10. Heat transfer coefficient and temperature difference for fluid and wall versus volumetric concentration

Table 12. Heat transfer coefficient at the CHF point for all the nanoparticles used in August

Volumetric concentration (%)	Nano particles			
	Ag	Ni	TiO_2	Al
0 (pure water)	2394.12	2394.12	2394.12	2394.12
0.01	2395.64	2395.52	2394.94	2395.1
0.1	2408.43	2406.97	2401.03	2400.31
0.3	2436.65	2432.47	2414.48	2412.02
0.5	2464.82	2457.92	2427.98	2423.74
1	2534.33	2521.40	2461.67	2453.09
2	2672.98	2647.86	2529.45	2512.41

Table 13. Length of the CHF point for all the nanoparticles used in August

Volumetric concentration (%)	Nano particles			
	Ag	Ni	TiO_2	Al
0 (pure water)	216.39	216.39	216.39	216.39
0.01	281.53	278.9	288.41	350.77
0.1	283.52	280.95	288.67	350.99
0.3	287.97	285.48	289.26	351.45
0.5	292.4	290.06	289.83	351.95
1	303.61	301.51	291.28	353.15
2	325.4	324.8	294.01	355.52

One of the most important results is thermal efficiency that helps choose available nanoparticles. The thermal efficiency was obtained for nickel nanoparticle with vol. 0.5 % in this study. The obtained results are given in Table 14.

Table 14. Thermal efficiency for nickel nanoparticles

Months	Qs	0% (Pure water)		Nickel 0.5 %	
		Qu	η	Qu	η
June	5209.3	3316.45	0.64	3688.08	0.71
July	5211.6	3386.9	0.64	3754	0.71
August	5212.8	3324.33	0.65	3698.76	0.72

In fact, thermal efficiency was enhanced following the dispersion of the nanoparticles in pure water and therefore, increase rates of thermal efficiency in Ni-pure water nanofluid, compared to pure water, were equal to 11.3, 11.2 and 10.8 % in June, July and August, respectively, when nickel nanoparticles were used with vol. 0.5 %. Also, in comparison with the results obtained by Bellos et al. [11], our findings regarding thermal efficiency showed the rates of 0.71, 0.71 and 0.72 % in June, July and August, respectively, while Bellos et al. determined the rates of thermal efficiency equal 0.31 % for vol. 2 % of Cu nanoparticles.

In fact, cost-effectiveness is a significant parameter in nanoparticle selection, especially due to the oscillations of dollar price. Heat transfer coefficients were equal to 2464.82, 2457.92, 2427.98 and 2423.74 w/mK in nanoparticles Ag, Ni, TiO_2, and Al, respectively, when volumetric concentration was equal to 0.5 %. Following the enhancement of volumetric concentration of nanoparticles, Al nanoparticle was found an optimum choice economically at a volumetric concentration of 2 % and its heat transfer coefficient was equal to 2512.41 w/mK. For instance, Ag nanoparticle price is about 168 $ per 25 gr, while Al nanoparticles price is 75 $ per 30 gr in global markets.

6. CONCLUSIONS

The solar power plant employing linear Fresnel collector based on Direct Steam Generation (DSG) can be considered to be using an advanced technology. It has drawn noticeable attention in different industries. This technology was considered as an effective choice economically with a moderate temperature. In this study, the effect of nanoparticles on the thermal performance of the linear Fresnel collector for Mahalat in Iran was investigated. The considered volumetric concentrations included 0.01, 0.1, 0.3, 0.5, 1 and 2 % in the current research in the hottest three months of the year involving June, July and August. Attempt was made to consider different possible aspects to obtain the available nanoparticles, particularly their most economical ones.

By studying the heat transfer coefficient at the CHF point, the obtained result illustrated that the heat transfer coefficient was enhanced by increasing the volumetric concentration of nanoparticles. Thus, the mentioned coefficient was improved and it equaled 11.65, 10.6, 5.65 and 4.94 % in Silver, Nickel, Titanium Dioxide, and Aluminum, respectively, compared to pure water. It was found that silver was not economically advantageous. In the current study, the remarkable point was the effectiveness of increasing or decreasing sun irradiation in the length of the CHF point. As a result, this investigation targeted nickel nanoparticles for the three hottest months of the year and it was observed that the length of the CHF point decreased by increasing sun irradiation from June to July and equaled 1.2 %. Furthermore, the mentioned length was enhanced upon decrease in sun irradiation in August and equaled 3.6 %. On the other hand, the obtained results of thermal efficiency in pure water and nickel-pure water nanofluids revealed that the thermal efficiency increased after dispersing the nanoparticles and the thermal efficiency increased to 11.3, 11.2 and 10.8 in June, July and August, respectively. In terms of cost effectiveness, Ag, Ni, TiO_2 and Al nanoparticles with a volume concentration of 0.5 % are the available choices. However, by enhancing the volumetric concentration, e.g., 2 %, Al can be the best nanoparticle.

7. ACKNOWLEDGEMENT

The current study is an academic research and no assistance has not been received from any organization.

NOMENCLATURE

c_p	Specific heat at constant pressure (J/kg.K)
d	Equivalent diameter of a base fluid molecule
D	Diameter, Height of cavity (m)
F_{rad}	Fraction of blackbody radiation in a wavelength band
h	Convective heat transfer coefficient ($W/m^2.K$)
h_L	heat transfer coefficient on single-phase section ($W/m^2.K$)
h_{lv}	Latent heat of vaporization (j/kg)
k	Thermal conductivity (W/m.K)
l	Length of each element (m)
m	Mass (kg)
$\dot{m}$	Mass flow rate (kg/s)
N	Number of pipes
Nu	Nusselt number
p	Pressure (N/m^2)
Pr	Prandtl number
pr	Rate between saturate pressure and critical pressure
Q_s	Available solar irradiation (W)
Q_u	Useful heat (W)
q	Heat transfer rate (W)
$\dot{q}$	Heat transfer rate per unit length (W/m)
Ra	Rayleigh number
Re	Reynolds number
T	Temperature (K)
t	Thickness (m)
V	Volume (m^3)
w_c	Length of bottom trapezoidal base (m)
x	Vapor quality
Greek letters	
μ	Viscosity (kg/s.m)
η	Thermal efficiency (%)
π	Pi number, 3.14
ρ	Density (kg/m^3)
σ	Stefan-Boltzmann constant

Δ	Different
ϕ	volume fraction of nanoparticles
Subscripts and superscripts	
a	Absorber
c	Cavity
cond	Conduction
conv	Convective
crit	Critical
e	Environment
eff	Effective
ex	External
f	Fluid
g	Glass
in	Internal, Inlet
l	Liquid
m	Middle
nb	Nucleate boiling
nf	Nano fluid
out	Outlet
p	Particle
rad	Radiation
s	Sun
Sat	Saturation
tp	Two-Phase
v	Vapor
Abbreviation	
LFC	Linear Fresnel Collector
CHF	Critical Heat Flux
LUT	Look-up Table

REFERENCES

1. Qiu, Y., He, Y.L., Wu, M. and Zheng, Z.J., "A comprehensive model for optical and thermal characterization of a linear Fresnel solar reflector with a trapezoidal cavity receiver", ***Renewable Energy***, Vol. 97, (2016), 129-144. (https://doi.org/10.1016/j.renene.2016.05.065).
2. Guadamud, E., Olivia, A., Lehmkuhl, O., Rodriguez, I. and Gonzalez, I., "Thermal analysis of a receiver for linear Fresnel reflectors", ***Energy Procedia***, Vol. 69, (2015), 405-414. (https://doi.org/10.1016/j.egypro.2015.03.047).
3. Benyakhlef, S., Al Mers, A., Merroun, O., Bouatem, A., Boutammachte, N., El Alj, S., Ajdad, H., Erregueragui, Z. and Zemmouri, E., "Impact of heliostat curvature on optical performance of linear Fresnel solar concentrators", ***Renewable Energy***, Vol. 89, (2016), 463-474. (https://doi.org/10.1016/j.renene.2015.12.018).
4. Bellos, E., Tzivanidis, C. and Papadopoulos, A., "Enhancing the performance of a linear Fresnel reflector using nanofluids and internal finned absorber", ***Journal of Thermal Analysis and Calorimetry***, Vol. 135, (2019), 237-255. (https://doi.org/10.1007/s10973-018-6989-1).
5. Bellos, E. and Tzivanidis, C., "Multi-criteria evaluation of a nanofluid-based linear Fresnel solar collector", ***Solar Energy***, Vol. 163, (2018), 200-214. (https://doi.org/10.1016/j.solener.2018.02.007).
6. Zamzamian, S.A.H. and Mansouri, M., "Experimental investigation of the thermal performance of vacuum tube solar collectors (VTSC) using alumina nanofluids", ***Journal of Renewable Energy and Environment (JREE)***, Vol. 5, (2018), 52-60. (https://doi.org/10.30501/jree.2018.88634).
7. Alah Rezazadeh, S., Mirzaie, I., Pourmahmoud, N. and Ahmadi, N., "Three dimensional computational fluid dynamics analysis of a proton exchange membrane fuel cell", ***Journal of Renewable Energy and Environment (JREE)***, Vol. 1, No. 1, (2014), 30-42. (https://doi.org/10.30501/jree.2015.70069).
8. Lopez-Nunez, O.A., Arturo Alfaro-Ayala, J., Jaramillo, O.A., Ramirez-Minguela, J.J., Carlos Castro, J., Damian-Ascencio, C.E. and Cano-Andrade, S., "A numerical analysis of the energy and entropy generation rate in a linear Fresnel reflector using computational fluid dynamic", ***Renewable Energy***, Vol. 146, (2020), 1083-1100. (https://doi.org/10.1016/j.renene.2019.06.144).
9. Mokhtari Ardekani, A., Kalantar, V. and Heyhat, M.M., "Experimental study on heat transfer enhancement of nanofluid flow through helical tubes", ***Advanced Powder Technology***, Vol. 30, (2019), 1815-1822. (https://doi.org/10.1016/j.apt.2019.05.026).
10. Bellos, E. and Tzivanidis, C., "A review of concentrating solar thermal collectors with and without nanofluids", ***Journal of Thermal Analysis and Calorimetry***, Vol. 135, (2019), 763-786. (https://doi.org/10.1007/s10973-018-7183-1).
11. Ghodbane, M., Said, Z., Hachicha, A.A. and Boumeddane, B., "Performance assessment of linear Fresnel solar reflector using MWCNTs/DW nanofluids", ***Renewable Energy***, Vol. 151, (2020), 43-56. (https://doi.org/10.1016/j.renene.2019.10.137).
12. Bellos, E. and Tzivanidis, C., "Thermal efficiency enhancement of nanofluid-based parabolic trough collectors", ***Journal of Thermal Analysis and Calorimetry***, Vol. 135, (2019), 597-608. (https://doi.org/10.1007/s10973-018-7056-7).
13. Razeghi, A., Mirzaee, I., Abbasalizadeh, M. and Soltanipour, H., "Al_2O_3/water nano-fluid forced convective flow in a rectangular curved micro-channel: First and second law analysis, single-phase and multi-phase approach", ***Journal of the Brazilian Society of Mechanical Sciences and Engineering***, Vol. 39, (2017), 2307-2318. (https://doi.org/10.1007/s40430-016-0686-4).
14. Razmmand, F. and Mehdipour, R., "Effects of different coatings on thermal stress of solar parabolic trough collector absorber in direct steam generation systems", ***Thermal Science***, Vol. 23, (2019), 727-738. (https://doi.org/10.2298/TSCI161019177R).
15. Razmmand, F. and Mehdipour, R., "Studying thermal stresses of a solar absorber in single and two-phase regimes and effects of various coatings on the absorber", ***Heat and Mass Transfer***, Vol. 55, (2019), 1693-1703. (https://doi.org/10.1007/s00231-018-2525-x).
16. Razmmand, F., Mehdipour, R. and Mousavi, S.M., "A numerical investigation on the effect of nanofluids on heat transfer of the solar parabolic trough collectors", ***Applied Thermal Engineering***, Vol. 152, (2019), 624-633. (https://doi.org/10.1016/j.applthermaleng.2019.02.118).
17. Saad Kamel, M., Lezsovits, F. and Kadhim Hussein, A., "Experimental studies of flow boiling heat transfer by using nanofluids", ***Journal of Thermal Analysis and Calorimetry***, Vol. 138, (2019), 4019-4043. (https://doi.org/ 10.1007/s10973-019-08333-2).
18. Tanase, A., Cheng, S.C., Groeneveld, D.C. and Shan, J.Q., "Diameter effect on critical heat flux", ***Nuclear Engineering and Design***, Vol. 239, (2009), 289-294. (https://doi.org/10.1016/j.nucengdes.2008.10.008).
19. Fang, X., Chen, Y., Zhang, H., Chen, W., Dong, A. and Wang, R., "Heat transfer and critical heat flux of nanofluid boiling: A comprehensive review", ***Renewable and Sustainable Energy Reviews***, Vol. 62, (2016), 924-940. (https://doi.org/10.1016/j.rser.2016.05.047).
20. Bergman, T.L., Lavine, A.S., Incropera, F.P. and Dewitt, D.P., Fundamentals of heat and mass transfer, 8th edition, John Wiley & Sons Inc., (2018), New York, USA. (https://www.wiley.com/en-us/Fundamentals+of+Heat+and+Mass+Transfer%2C+8th+Edition-p-9781119353881).
21. Sarma, P.K., Srinivas, V., Sharma, K.V., Subrahmanyam, T. and Kakac, S., "A correlation to predict heat transfer coefficient in nucleate boiling on cylindrical heating elements", ***International Journal of Thermal Sciences***, Vol. 47, (2008), 347-354. (https://doi.org/10.1016/j.ijthermalsci.2007.03.003).
22. Shah, M.M., "A general correlation for heat transfer during film condensation inside pipe", ***International Journal of Heat and Mass Transfer***, Vol. 29, (1979), 547-556. (https://doi.org/10.1016/0017-9310(79)90058-9).
23. Baniamerian, Z., "Analytical modeling of boiling nanofluids", ***Journal of Thermophysics and Heat Transfer***, Vol. 31, (2017), 136-144. (https://doi.org/10.2514/1.T4910).
24. Corcione, M., "Empirical correlation equations for predicting the effective thermal conductivity and dynamic viscosity of nanofluids", ***Journal of Thermal Analysis and Calorimetry***, Vol. 52, (2011), 789-793. (https://doi.org/10.1016/j.enconman.2010.06.072).
25. Baniamerian, Z. and Mashayekhi, M., "Experimental assessment of saturation behavior of boiling nanofluids: pressure and temperature", ***Journal of Thermophysics and Heat Transfer***, Vol. 31, (2017), 732-738. (https://doi.org/10.2514/1.T5081).
26. Jayakumar, J.S., Mahajani, S.M., Mandal, J.C., Vijayan, P.K. and Bhoi, R., "Experimental and CFD estimation of heat transfer in helically coiled heat exchangers", ***Chemical Engineering Research and Design***, Vol. 86, (2008), 221-232. (https://doi.org/10.1016/j.cherd.2007.10.021).
27. Salehi, N., Lavasani, A.M. and Mehdipour, R., "Effect of tube number on critical heat flux and thermal performance in linear Fresnel collector based on direct steam generation", ***International Journal of Heat and Technology***, Vol. 38, No. 1, (2020), 223-230. (https://doi.org/10.18280/ijht.380124).

28. Salehi, N., Lavasani, A.M., Mehdipour, R. and Yazdi, M.E., "Investigation the increased heat performance of direct steam generation of Fresnel power plant using nanoparticles", ***Environmental Progress and Sustainable Energy***, Vol. 40, No. 1, (2020), 1-11. (https://doi.org/10.1002/ep.13480).

29. Abbas, R., Munoz, J. and Martinez-Val, J.M., "Steady-state thermal analysis of an innovative receiver for linear Fresnel reflectors", ***Applied Energy***, Vol. 92, (2012), 503-515. (https://doi.org/10.1016/j.apenergy.2011.11.070).

30. Borzuei, M. and Baniamerian, Z., "Role of nanoparticles on critical heat flux in convective boiling of nanofluids: Nanoparticle sedimentation and Brownian motion", ***International Journal of Heat and Mass Transfer***, Vol. 150, (2020), 119299. (https://doi.org/10.1016/j.ijheatmasstransfer.2019.119299).

Journal of Renewable Energy and Environment

Research Article

Journal Homepage: www.jree.ir

An Experimental and Analytical Study of Influential Parameters of Parabolic trough Solar Collector

Daryoosh Borzuei, Seyed Farhan Moosavian, Abolfazl Ahmadi *, Rouhollah Ahmadi *, Kourosh Bagherzadeh

School of New Technologies, Department of Energy Systems Engineering, Iran University of Science & Technology, Tehran, Tehran, Iran.

PAPER INFO

Paper history:
Received 14 December 2020
Accepted in revised form 17 August 2021

Keywords:
Solar Collector,
PTC,
Heat Transfer Fluid,
Vacuum Tube,
Analytical Study

ABSTRACT

Energy plays a vital role in all human life activities. Due to the problems caused by fossil fuels in recent decades such as global warming, greenhouse gas emissions, ozone depletion, etc., the use of renewable and clean energy has been considered. An experimental facility for the acquisition of reliable data from Parabolic Trough Solar Collectors (PTCs) was established to develop a robust analytical model. A wide range of Heat Transfer Fluid (HTF) flow rates (0.0372-0.1072 kg/s) and solar radiation (400-900 W/m^2) were used to determine PTC parameters such as the outlet temperature of HTF loss and temperature distribution. Vacuum conditions in the receiver were considered effective in terms of thermal efficiency. Also, three types of HTF including two oil fluids (Syltherm 800 and S2) and water were examined. The temperature distribution showed that when Syltherm 800 or S2 passed through the absorber tube, the outlet temperature was higher than water: 2.84 % for Syltherm 800 and 3.72 % for S2. Since the absorber tube temperature was much higher than water, the heat loss in this condition was considered for oil HTF. Of note, the results demonstrated that use of the vacuum tube could diminish heat loss for the oil HTF. The effect of solar intensity increases from 600 W/m^2 to 900 W/m^2 on the maximum temperature of the receiver tube indicated that when Syltherm 800 was used as an HTF, this temperature increased by 35.1 % (from 167 °C to 219 °C), while this percentage was 32.7 % and 6.8 % for S2 and water, respectively.

https://doi.org/10.30501/jree.2021.261647.1172

1. INTRODUCTION

In current years, the development of energy consumption and the growing trend of using fossil fuels have led to widespread adverse environmental damage such as greenhouse gas emissions and global warming [1]. In order to overcome these problems, the use of renewable energy as a viable alternative to fossil fuels has led to the development of energy harvesting technologies from solar, wind, geothermal, hydroelectric, and biomass sources [2]. Meanwhile, due to the advantages of solar energy such as cleanliness, easy access, and greater sustainability, this energy has found a special place among renewable energy sources which have paid a great deal of attention to this area of research [3]. Solar radiation can be used for a variety of purposes such as generating power, providing heating and cooling loads, preparing fresh water for residential and industrial use, and air conditioning [4, 5]. In solar thermal collectors, generally, the temperature of the working fluid is raised through absorption of solar radiation and then, this heat is transferred to operating fluid [6].

In general, thermal solar collectors are segmented into two categories: flat and concentrated solar collectors [7]. In decentralized solar collectors, the output temperature range is less than centralized solar collectors. Therefore, the concentrated solar collectors such as solar dishes and linear parabolic collectors (PTCs) are applicable since high temperatures are needed [8]. The temperature range for the PTC is in the range of 30 to 400 °C. This type of solar collector is capable of producing superheated steam for power generation in solar power plants [9-11]. Due to the role of solar collectors in supplying heat to residential and industrial places, many researches have been focused to increase the capacity factor, stability and efficiency [12]. These studies have been conducted in the form of numerical simulations and experimental tests to evaluate the effect of changing geometrical parameters of solar collectors, type of working fluid, geographic orientation and location, and other relevant parameters. The following is a review of some research in this area of study. Kalogirou [13] conducted a comprehensive overview of different kinds of solar collectors and their applications. In this regard, the performance of different types of solar collectors such as flat plate, compound parabolic, evacuated tube, parabolic lens, parabolic dish, and heliostat was examined from the thermal, optical, and thermodynamic points of view.

Some numerical studies have provided information related to the geometry and the use of linear parabolic collector tube feeders. In this regard, Bellos et al. [14] studied different arrangements of fins in the absorber tube of LS-2 linear parabolic collectors by numerical modeling. They examined

*Corresponding Author's Email: a_ahmadi@iust.ac.ir (A. Ahmadi) and ahmadi@iust.ac.ir (R. Ahmadi)
URL: https://www.jree.ir/article_135327.html

Please cite this article as: Borzuei, D., Moosavian, S.F., Ahmadi, A., Ahmadi, R. and Bagherzadeh, K., "An experimental and analytical study of influential parameters of parabolic trough solar collector", ***Journal of Renewable Energy and Environment (JREE)***, Vol. 8, No. 4, (2021), 52-66. (https://doi.org/10.30501/jree.2021.261647.1172).

twelve different fins with different lengths and thicknesses for linear parabolic collectors. The result showed that increasing the absorber length caused an increase in fluid temperature on the one side, and an increase in pressure drop, on the other side. Bellos et al. [15] did not consider this point of view, i.e., the examination of star fins on the absorber tube of the solar parabolic collector was carried out. Some researchers have studied the effect of fin geometry inside of the absorber tube of the solar collector from the numerical and experimental points of view. In this respect, Xiao et al. [16] analyzed the theoretical and empirical effects of using rectangular fins inside of the absorber tube of linear parabolic solar collectors. The results of this study showed that the rectangular shape of the inside absorber enhanced the performance of solar collectors.

Some studies have analyzed the effect of different types of working fluid inside the absorber tube on the performance of the PTC. Bellos and Tsivandis [17] investigated the effect of using hybrid nanofluid on the linear parabolic solar collectors. They modeled an LS-2 linear parabolic solar collector with Syltherm 800 oil as a working fluid in EES software. The results of this study showed that this hybrid nanofluid could enhance the thermal efficiency of the system by 1.8 %. Marefati et al. [7] analyzed the impact of different types of working fluid in the linear parabolic solar collector in different climates of Iran. The investigation of different types of working fluids on the performance of the thermal energy of solar collectors has also been the goal of some studies. Boukelia et al. [18] investigated the effect of two types of working fluids consisting of molten salt and thermal oils in solar collectors. The results demonstrated that the thermal efficiency of thermal oil as a working fluid in the solar collector was better than that of molten salt.

Studies on these topics have not been sufficient and there have been some numerical and experimental studies on the design and construction of linear parabolic collectors. In this regard, Dudley et al. [19] studied the efficiency and thermal loss of linear parabolic solar collector SEGS LS-2 by numerous experimental tests. They examined two different materials as an absorber tube in a linear parabolic solar collector. Reddy et al. [20] studied the effect of using porous plates in an absorber tube of the linear parabolic solar collector with an area of 15 m^2. They studied the application of six different configurations of porous plates inside the absorber tube and it concluded that the use of a porous plate enhanced the performance of linear parabolic solar collectors.

This paper represents a comprehensive investigation of the impact of variation of solar radiation intensity and mass flow rate of working fluid on temperature changes of HTF in the parabolic solar collector. The results of this investigation have been obtained with an experimental test and a numerical simulation of a linear PTC modeled in MATLAB software. The obtained results of simulation and experiments are validated with each other. Investigation of three types of heat transfer fluids with eight different mass flow rates for changing solar radiation intensity is analyzed. Besides, the effect of the presence or absence of the vacuum in the space between the absorber tube and the coating on the heat transfer fluid temperature at different radiations was also investigated. Also, the temperature distribution across the collector was obtained for three types of heat transfer fluid by numerical simulation. The novelty of this research is in expressing the results in a new and tangible way using temperature and parametric distribution diagrams as a comparison criterion.

2. Experimental Description

2.1. Typical parabolic trough collector

A test facility composed of a PTC is made, as shown in Figure 1 and a black-coated copper tube is enclosed in a Pyrex glass tube located at the focal line of the parabolic mirror as a solar collector receiver. Hence, by focusing solar irradiation on this receiver, Heat Transfer Fluid (HTF) temperature increases [9]. Since this system is rather smaller and lighter than the conventional PTC, the receiver is fixed and parabolic trough reflector rotates to track the sun. Hence, a single-axis solar tracker is provided to adjust the reflector so that the absorber tube is at the focal point of the mirror throughout the day.

Table 1 shows the general characteristics of the PTC and Table 2 shows the material properties of the PTC.

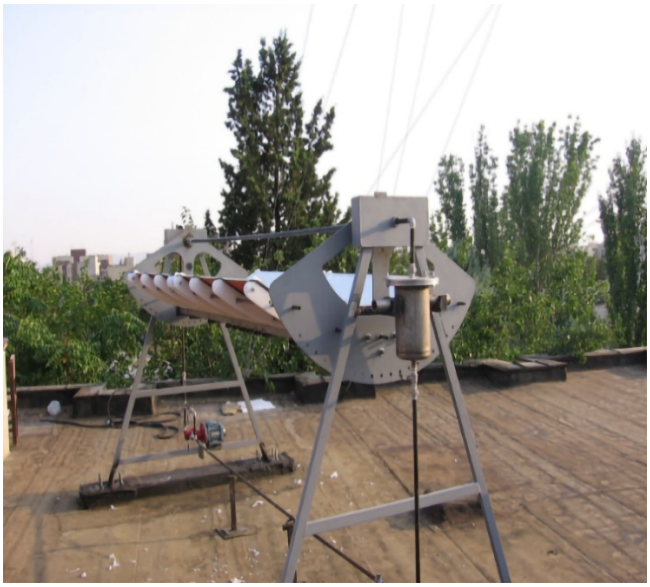

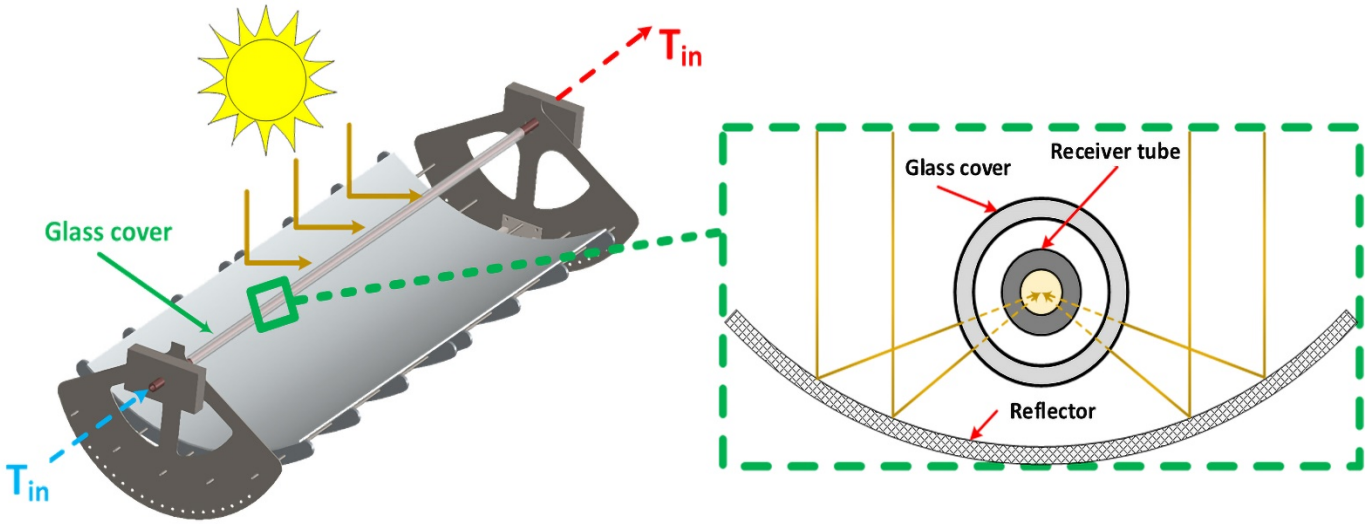

Figure 1. PTC experimental test facilities

Table 1. Characteristics of the PTC

Symbol	Parameter	Value	Unit
W	Width	1.2	m
L	Length	3	m
D_{ai}	Absorber inner diameter	25.4×10^{-3}	m
D_{ao}	Absorber outer diameter	28×10^{-3}	m
D_{gi}	Glass tube inner diameter	45×10^{-3}	m
D_{go}	Glass tube outer diameter	50×10^{-3}	m
F	Focal length	0.45	m
M	Weight	84.728	kg
T_{sun}	Sun's temperature	5780	K
ρ_{ref}	Collector reflectance	0.9	-
γ	Intercept factor	0.99	-
ε_r	Receiver emittance	0.23	-
ε_c	Cover emittance	0.9	-
σ	Stefan Boltzmann constant	5.6704×10^{-8}	W/m^2K^4
T	Cover transmittance	0.95	-
α	Absorber absorbance	0.967	-
V	Volumetric flow rate	50	L/min
K_r	Receiver thermal conductivity	401	W/mK
K_c	Cover thermal conductivity	1.14	W/mK
$\dot{m}$	Mass flow rate	0.06717	kg/s

Table 2. PTC's material properties

Parameter	Type
HTF	Shell Thermia B-S2
Collector	LS-2
Receiver tube	Copper
Cover material	Pyrex glass

Thermal oil (with brand Shell Thermia B) flows through the absorber tube as HTF with high heat transfer conductivity, excellent oxidation resistance, and resistance to a temperature range of 10 to 330 °C. Table 3 represents the technical specifications of this HTF at different temperatures.

Table 3. Technical specifications–Shell Thermia Oil B

Temperature	°C	0	20	40	100	150	200	250	300	340
Density	kg/m^3	876	863	850	811	778	746	713	681	655
Specific heat	J/kgK	1809	1882	1954	2173	2355	2538	2720	2902	3048
Thermal conductivity	W/mK	0.136	0.134	0.133	0.128	0.125	0.121	0.118	0.114	0.111
Prandtl	-	3375	919	375	69	32	20	14	11	9
Dynamic viscosity	kgm/s	0.2537	0.0654	0.0255	0.0041	0.0017	0.0010	0.0006	0.0004	0.0003

2.2. Data acquisition system

Data acquisition systems are one of the essential parts of empirical research. Accuracy of measurement, data verification, and control of conditions during the experiment are essential issues in data acquisition. This study measured inlet, outlet and ambient temperatures, HTF flow rate, wind speed, and solar radiation intensity. The schematic of the test loop and instrument location and measurement device is shown in Figure 2. Furthermore, Table 4 demonstrates the characteristics of instruments such as type and accuracy as well as the specification of data acquisition system.

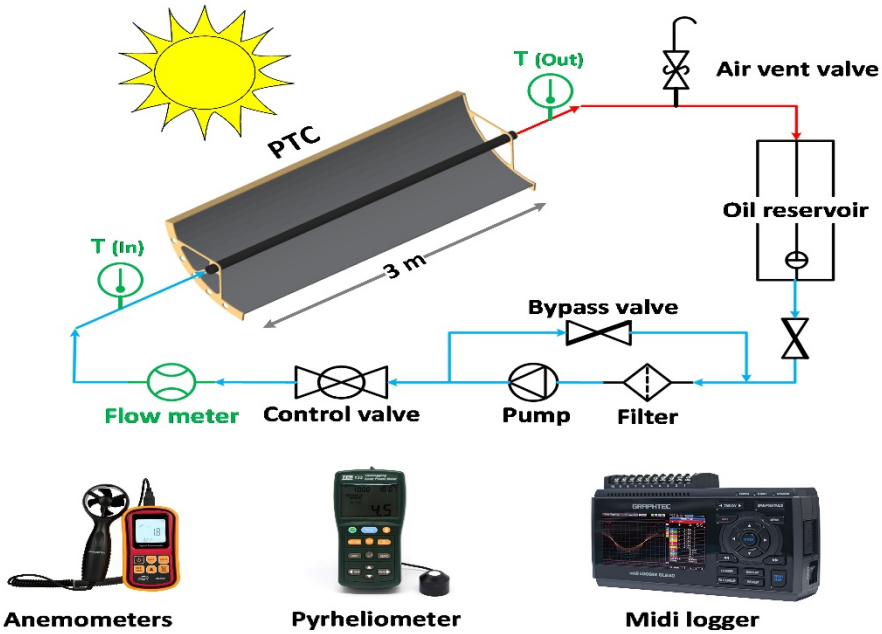

Figure 2. Schematic of the measurement system

Table 4. Characteristics of measuring instruments

Measuring instrument	Measurement parameter	Type	Range	Uncertainties
Midi-logger	Data acquisition-20 channel	Midi-840	Temperature, voltage, Ampere, Humidity	up to 10 Hz
Thermometer	Temperature	K-Type	$(-40)-1200$ K	± 0.5 ^{0}K
Flowmeter	Fluid flow rate	Rota Meter	$0-5$ L/min	± 0.1 L/min
Pyrheliometer	Direct normal irradiation	TES 132	$0-2000$ W/m^2	± 0.1 W/m^2
Anemometer	Wind velocity	GM89901	$0-45$ m/s	± 0.1 m/s

3. MODELING AND SIMULATION

Based on the experimental facilities and experimental design tests, this study presented a precise analytical model using MATLAB software to compare not only the analytical model with experimental results but also predict further conditions applying different input dates on PTC. Based on the environmental conditions, physical and geometrical parameters of the PTC, the fluid outlet temperature, Glass cover temperature, receiver tube temperature, optical efficiency, and thermal efficiency are obtained. Figure 3 depicts the flowchart of the modeling and simulation procedure. As was mentioned earlier, in order to validate the analytical model first, the experimental investigation was conducted and implemented in the Matlab code. The results of the validation are represented in the next section. Another essential aim of analytical modeling is to extract further result data, which is very time-consuming and costly with the experimental investigation approach. In the following, hence, the influence of fluid temperature parameter, HTF type, and its flow rate on PTC thermal efficiency is also objective of analytical modeling.

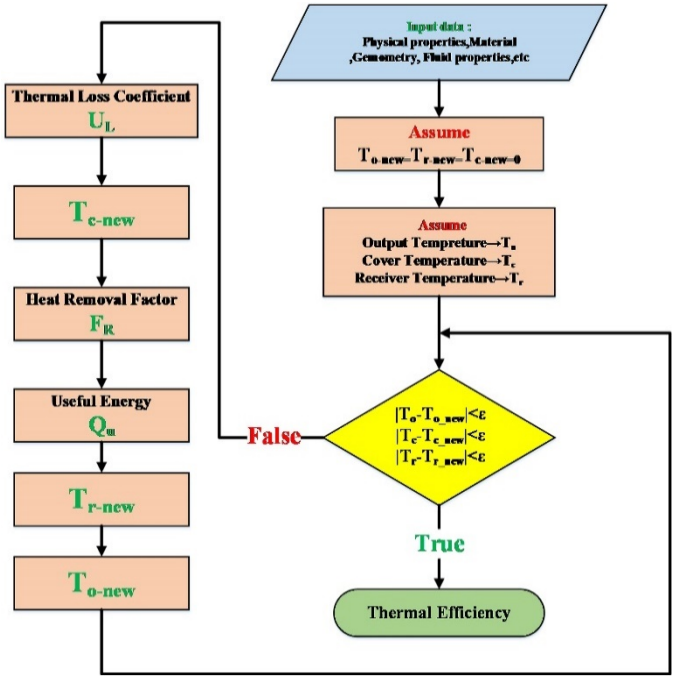

Figure 3. Modeling and simulation algorithm flow diagram

3.1. The governing equations

To obtain the part of solar radiation energy absorbed via the collector receiver and the heat dissipated to the environment, precise governing equations are implemented [21]. Thereby, using this data, the accurate thermal efficiency of the solar collector is achieved. Figure 4a demonstrates a schematic of the heat transfer model in the receiver of the PTC system. Furthermore, the detail of the thermal resistances network of the component from the HTF core to the environment is shown in Figure 4b.

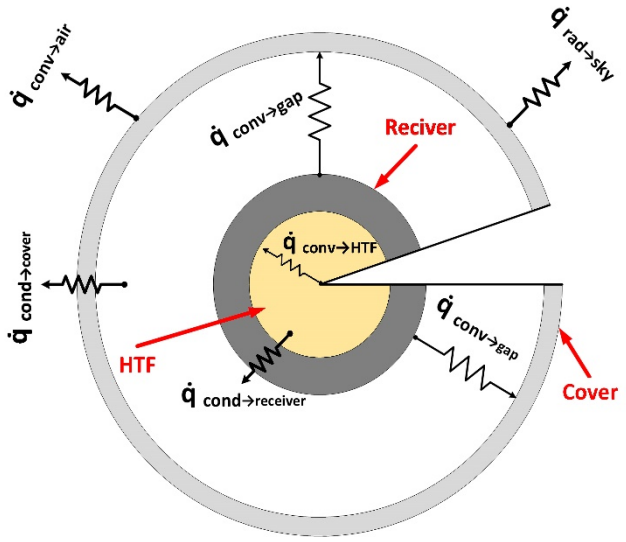

a) Receiver tube heat transfer

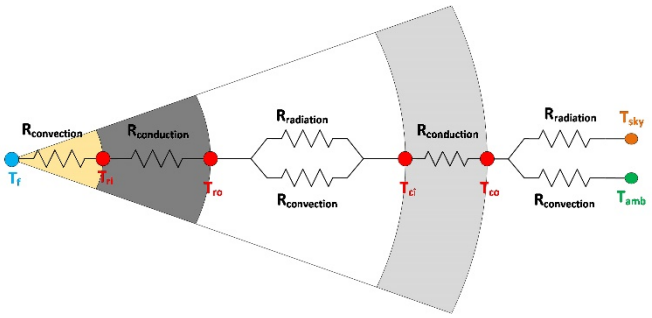

b) Receiver tube resistance network

Figure 4. 2D heat transfer modeling of receiver tube

To measure the useful heat transferred, appropriate relationships for the collector efficiency factor F', heat loss factor U_L, and the heat removal factor F_R must be derived. The heat removal coefficient in PTC, F_R, is calculated in the following [9].

$$F_R = \frac{M_f \times Cp_f}{A_r \times U_L}\left[1 - \exp\left(\frac{-A_r \times U_L \times F'}{M_f \times Cp_f}\right)\right] \quad (1)$$

A_r is the absorbent area (m^2) and F' is the efficiency factor obtained using Eq. 2 [22].

$$F' = \frac{\frac{1}{U_L}}{\left(\frac{1}{U_L} + \frac{D_{ro}}{h_{cf} \times D_{ri}} + D_{ro} \times \frac{\ln\left(\frac{D_{ro}}{D_{ri}}\right)}{2 \times K_r}\right)} \quad (2)$$

where D_{ri} and D_{ro} are the inner and outer diameters of the absorber tube, respectively, and h_{cf} is the heat transfer coefficient. The U_L, known as heat loss factor, can be calculated for two types of receivers: when the space between the absorber tube and the glass cover is vacuumed, U_L is calculated from Eq. 3; and when there is gas in this gap, U_L is calculated using Eq. 4 [9, 23].

$$U_L = \frac{1}{h_{r,r\to c} + \frac{A_r}{A_c} \times \left(h_{c,c\to am} + h_{r,c\to am}\right)} \quad (3)$$

$$U_L = \frac{1}{h_{r,r\to c} + \frac{2 \times k_{gas\_eff}}{D_{ci} \times \ln\left(\frac{D_{ci}}{D_{co}}\right)} + \frac{A_r}{A_c} \times \left(h_{c,c\to am} + h_{r,c\to am}\right)} \quad (4)$$

Here, A_c is the cover area, A_r is the area of absorber tube, $h_{c,c\to am}$ is the heat transfer coefficient between glass cover and environment, $h_{r,c\to am}$ is the radiative heat transfer coefficient between cover and environment, $h_{r,r\to c}$ is the radiant heat transfer coefficient between the adsorbent and the cover, and k_{gas_eff} is the effective heat transfer coefficient between the adsorbent and the glass cover.

Note, the heat transfer coefficient of displacement between the cover and the environment, $h_{c,c\to am}$, is obtained as follow:

$$h_{c,c\to am} = \frac{Nu_{air} \times K_{air}}{D_{co}} \quad (5)$$

where Nu_{air} is Nusselt number of air, which is calculated through the following equation [24].

$$Nu_{air} = C \times Re_{air}^{M} \times Pr_{air}^{N} \times \left(\frac{Pr_{air}}{Pr_W}\right)^{0.25} \quad (6)$$

The Prandtl number Pr_W was calculated at the outer surface temperature of the cover, and the other parameters of Relation 5 can be computed at the average temperature of the boundary layer between the cover and the air. The values of M, N, C are obtained from Table 5 [24].

Table 5. Constant for Eq. 6

Re	C	M	N	
$1-40$	0.75	0.4	Pr<10	Pr>10
$40-1000$	0.51	0.5	0.37	0.36
$1000-2\times10^5$	0.26	0.6		
$2\times10^5-10^7$	0.076	0.7		

The radiative heat transfer coefficient between the cover and the environment $h_{r,c\to am}$ is obtained from the following relation.

$$h_{r,c\to am} = \epsilon_c \times \sigma \times \left(T_c^2 + T_{sky}^2\right) \times \left(T_c + T_{sky}\right) \quad (7)$$

where σ is Stephen Boltzmann's constant (5.67×10^{-8} $\frac{W}{m^2 \times K^4}$), T_{sky} denotes the sky temperature, and T_C relates to the cover surface temperature with or without vacuum, which can be calculated through Relations 8 [25] and 9 [26], respectively.

$$T_{sky} = 0.05532 \times T_{amb}^{1.5} \quad (8)$$

$$T_{c_{vac}} = \frac{A_r h_{r,r\to c} \times T_r + A_c\left(h_{r,c\to am} + h_{c,c\to am}\right)T_{amb}}{A_r h_{r,r\to c} + A_c\left(h_{r,c\to am} + h_{c,c\to am}\right)}$$
$$T_{c_{no-Vac}} = \frac{A_r h_{r,r\to c} + \left(\frac{2 \times k_{gas_{eff}}}{D_{ci} \times \ln\left(\frac{D_{ci}}{D_{co}}\right)} T_r\right) + A_c\left(h_{r,c\to am} + h_{c,c\to am}\right)T_{amb}}{A_r h_{r,r\to c} + \frac{2 \times k_{gas\_eff}}{D_{ci} \times \ln\left(\frac{D_{ci}}{D_{co}}\right)} + A_c\left(h_{r,c\to am} + h_{c,c\to am}\right)} \quad (9)$$

The value of the radiant heat transfer coefficient between the absorber tube and the cover $h_{r,r\to c}$ is obtained from Equation 10 as follows:

$$h_{r,r\to c}=\frac{\sigma\times(T_r^2+T_c^2)\times(T_r+T_c)}{\frac{1}{\epsilon_r}+\left(\left(\frac{1}{\epsilon_c}-1\right)\times\left(\frac{A_r}{A_c}\right)\right)} \quad (10)$$

where T_r represents the surface temperature of the adsorbent tube which can be calculated using Equation 11 [26].

$$T_r=T_{in}+\frac{Q_u}{A_r\times U_L\times F_R}\times(1-F_R) \quad (11)$$

where Q_u is the useful heat transferred to the HTF. The effective heat transfer coefficient between the absorber tube and its cover, k_{gas_eff}, is as follows [23]:

$$k_{gas\_eff}=0.386\times k\times\left(\frac{Pr_{r\to c}}{0.861+Pr_{r\to c}}\right)^{0.25}\times Ra_{cy}^{0.25} \quad (12)$$

where k_{gas} is the conductivity heat transfer coefficient of the fluid between the absorber tube and the cover, and the Prandtl number $Pr_{r\to c}$ is obtained by considering the average temperature of the gas.

Further, the value of Ra_{cy} is obtained from Eq. 13 [23].

$$Ra_{cy}=\frac{\ln\left(\frac{D_{ci}}{D_{ro}}\right)^4\times Ra}{L_c^3\times\left(D_{ci}^{-0.6}+D_{ro}^{-0.6}\right)^5} \quad (13)$$

where L_c represents the effective length and Ra represents the Riley dimensionless number. The last parameter needed to calculate the F_R is the heat transfer coefficient of the fluid h_{cf} and it can be obtained from the following relation [27].

$$h_{cf}=\frac{Nu_f\times K_f}{D_{ri}} \quad (14)$$

The value of Nu_f can also be calculated from Eq. 15 [28].

$$Nu_f=3.66+\frac{0.0667\times Re_f\times Pr_f\times D_{ri}}{L\times\left(1+0.04\times\left(\frac{Re_f\times Pr_f\times D_{ri}}{L}\right)^{\frac{2}{3}}\right)} \quad (15)$$

$$Nu_f=0.023\times Re^{0.8}\times Pr^{0.4} \qquad Re<2300$$

In Equation 15, parameter L represents the collector tube length and Pr_f is the Prandtl number of the fluid in the tube. In consequence, after calculating the heat removal factor, F_R, the useful heat transferred to the HTF can be obtained in the following [29]:

$$Q_u=F_R\left[\left(G\times\eta_{opt}\times A_a\right)-\left(A_rU_L(T_i-T_{amb})\right)\right] \quad (16)$$

where the parameter G is the solar radiation intensity, A_a is area, and η_{opt} is the optical efficiency of the collector. Assuming that the solar radiation is perpendicular to the reflector span at any moment, the optical efficiency can be computed as follows:

$$\eta_{opt}=\rho_{ref}\times\tau\times\alpha\times\Upsilon \quad (17)$$

where α, τ, Υ and ρ_{ref} are the absorption coefficient, the cover transmittance, the intercept factor, and the collector reflectance, respectively. Meanwhile, the thermal efficiency is obtained from Equation 18 [9].

$$\eta_{th}=\frac{Q_u}{G\times A_a}\times 100 \quad (18)$$

where Q_u is the transferred useful heat to the HTF. Consequently, the HTF temperature difference is obtained from Eq. 18 below:

$$\Delta T=\left(\frac{A_a\times\eta_{th}}{\dot{m}\times c_p}\right)\times G \quad (19)$$

3.2. Validation

To show the robustness of the simulation, the validation process is a mandatory step. For this purpose, the obtained results from the experimental investigation should be compared with the analytical simulation. The experimental results obtained for a wide range of inlet temperatures and velocities are presented in Table 6. The fluid output temperature of the collector and its thermal efficiency in the experimental and numerical modeling are compared to confirm the accuracy of the modeling performance.

Table 6. Comparison between experimental result and numerical model

HTF flow rate = 0.06717 kg/s										
Date	G_b (W/m^2)	T_{amb} (^oC)	T_{in} (^oC)	V_{wind} (m/s)	T_{out} (^oC)			η_{th} (%)		
					EXP	**Model**	**Eror** (%)	**EXP**	**Model**	**Eror** (%)
2018/10/21	667	21.6	47.80	1.7	59.86	60.39	0.89	70.55	73.69	4.45
2018/10/21	676	22.9	54.50	2	66.81	67.03	0.33	71.91	73.21	1.82
2018/10/21	685	24.5	45.39	1.4	58.10	58.43	0.56	72.17	74.04	2.60
2018/10/21	767	25.5	42.73	0.9	58.29	57.43	1.47	76.67	74.29	-5.58
2018/10/21	882	25.6	46.62	1.4	62.99	63.23	0.39	72.56	73.67	1.53
2018/10/22	450	23.7	54.35	0.7	62.81	62.78	0.05	74.01	73.73	-0.37
2018/10/22	557	24.3	50.79	2.2	60.84	61.25	0.66	70.69	73.56	4.06
2018/10/22	414	24.15	44.88	0.5	53.09	52.87	0.41	76.72	74.67	-2.67
2018/10/22	587	24.15	45.74	2.3	56.89	56.91	0.03	73.77	73.89	0.16
2018/10/22	617	24.5	38.29	1.9	50.11	50.27	0.32	73.48	74.47	1.35
2018/10/23	613	17.5	39.84	0.9	51.65	51.70	0.09	74.08	74.39	0.42
2018/10/23	674	21.75	52.10	1.3	64.93	64.70	0.36	74.93	73.54	-1.85
2018/10/23	663	24.05	47.07	0.8	59.36	59.68	0.54	72.28	74.18	2.63
2018/10/23	715	24.45	48.59	1.2	62.42	62.08	0.54	75.71	73.86	-2.45

2018/10/23	874	23.75	49.10	1.6	65.79	65.44	0.53	75.02	73.43	-2.12
2018/10/24	758	22.70	39.67	1.9	53.95	54.23	0.52	72.63	74.06	1.97
2018/10/24	717	23.00	48.79	1.5	62.10	62.28	0.30	72.67	73.69	1.41
2018/10/24	790	24.55	49.02	0.5	64.51	63.94	0.88	76.92	74.07	-3.71
2018/10/24	852	25.20	50.36	1	66.73	66.31	0.63	75.62	73.65	-2.60
2018/10/24	888	24.90	47.75	0.8	64.68	64.47	0.32	74.75	73.81	-1.26

According to the results of Table 6, the maximum error associated with the fluid outlet temperature in analytical modeling is 1.47 % and the maximum error of thermal efficiency is 5.58. The analytical and experimental results are compared in Figures 5 and 6 the error interval in each case is determined.

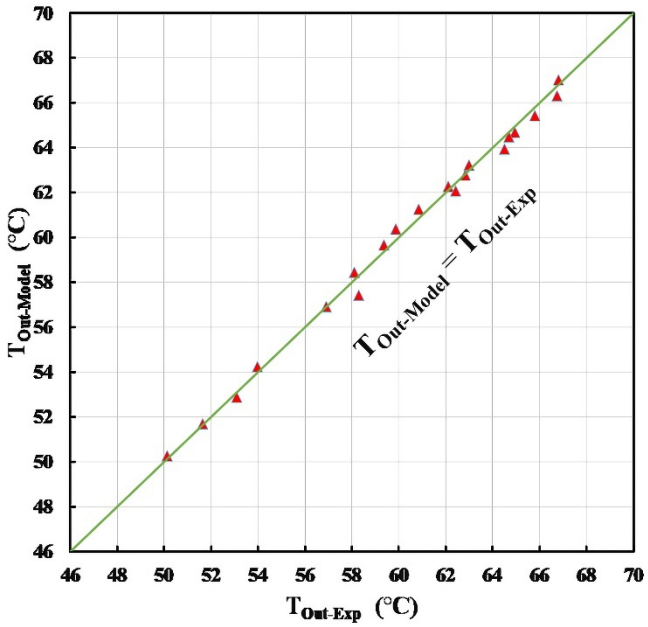

Figure 5. Comparison of the outlet temperature in analytical and experimental results

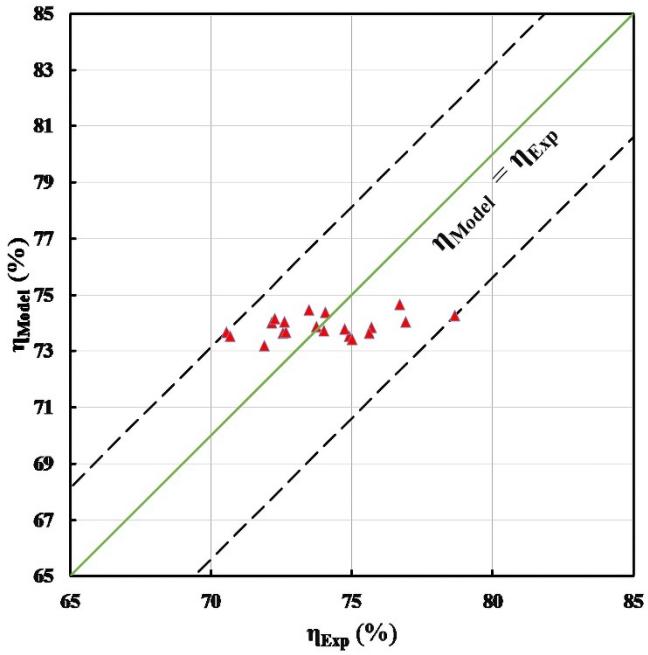

Figure 6. Comparison of the efficiency in analytical and experimental results

Accordingly, the right consistency is obtained between analytical and experimental results. Moreover, to make a better comparison between the experimental and analytical data, Figure 7 shows the temperature difference between inlet and outlet temperatures against solar radiation in both analytical and experimental cases.

The linear trend equation for both analytical and experimental investigations is demonstrated in this figure. Upon comparing the slope values of the experimental and analytical data in Figure 7, there is only 0.53 % error which shows the good accuracy of the analytical modeling approach.

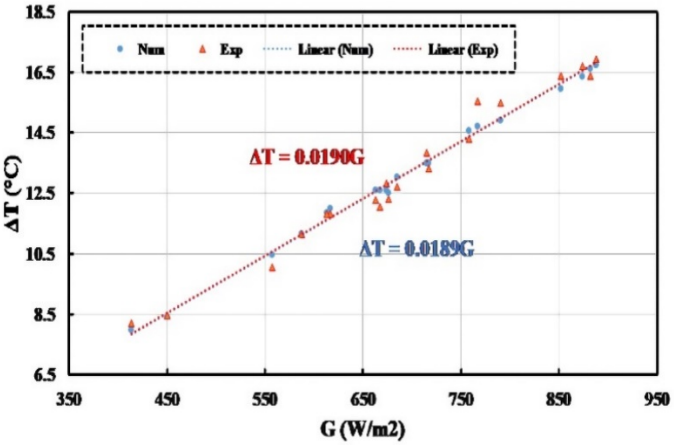

Figure 7. Comparison of HTF temperature difference between experimental and analytical results

4. RESULTS AND DISCUSSION

4.1. Mass Flow Rate Effect

The operating conditions of PTC influence thermal efficiency. Solar radiation, wind speed, and ambient temperature are the major affected factors. Calculation is carried out at a specified time interval, presuming that the wind speed and ambient temperature are constant. Figure 8 depicts the difference between the inlet and outlet HTF temperatures (ΔT) versus solar irradiation. According to Eq. 19, since ΔT is a function of PTC efficiency and HTF specific heat capacity, the slope of the fluid temperature diagram is fairly constant. Therefore, linear behavior for any HTF flow rate can be expected. In Figure 8, 8 different discharge flow rates are plotted.

According to Figure 8, as the HTF flow rate increased with the same solar irradiation ranges, the slope of the graph and, hence, the HTF temperature difference decrease. Furthermore, according to Figure 8, at specific solar irradiation, ΔT of HTF is more influential in the HTF flow rate. In other words, if more ΔT is targeted, the decrease of HTF flow rate is appreciated. For more clarity, Table 7 demonstrates the HTF mass flow rate with respect to the slope of the graphs in Figure 8. According to Eq. 19, the line slope is $(\frac{A_a \times \eta_{th}}{\dot{m} \times C_p})$, called capacity factor.

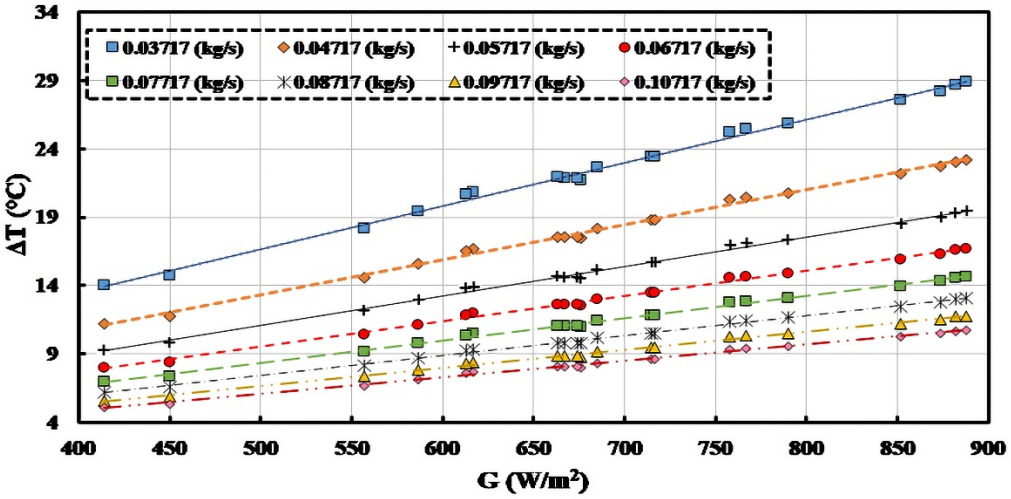

Figure 8. Effect of mass flow rate on the temperature difference for S2

Table 7. Capacity factor values for different mass flow rates

#	Mass flow rate ($\mathbf{kg/s}$)	$(\frac{A_a \times \eta_{th}}{\dot{m} \times C_p})$
1	0.03717	0.0328
2	0.04717	0.0263
3	0.05717	0.0220
4	0.06717	0.0189
5	0.07717	0.0166
6	0.08717	0.0148
7	0.09717	0.0133
8	0.10717	0.0121

According to the data illustrated in Table 7, the increase of mass flow rate is consistent with the decreasing of the capacity factor values. Furthermore, according to Eq. 19, the slope of the linear trends in Figure 8 corresponds with the inverse of mass flow rate $(\frac{1}{\dot{m}})$. Therefore, for clarity, if capacity factor is plotted against the reverse of mass flow rate, Figure 9 is formed. According to Figure 9, an excellent linear approximation can be obtained. It is inferred that the line slope is in fact related to PTC thermal efficiency and HTF heat capacity $(\frac{\eta_{th}}{C_p})$.

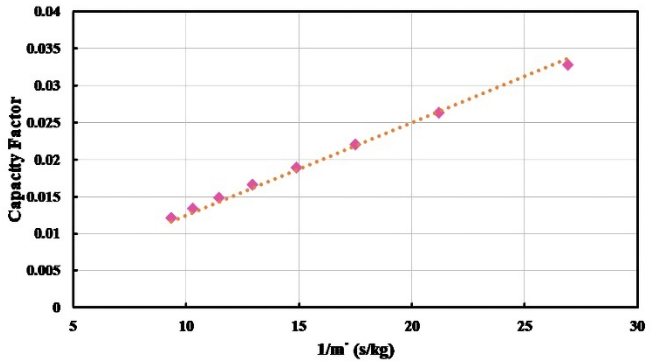

Figure 9. Variation in capacity factor against the inverse of mass flow rate

4.2. Influence of HTF type

To examine the influence of HTF type, a similar investigation is performed for two other fluids: Syltherm 800 and water. The results are obtained and illustrated in Figure 10. The HTF temperature difference at different solar irradiation and mass flow rates is depicted in this figure for two HTF types.

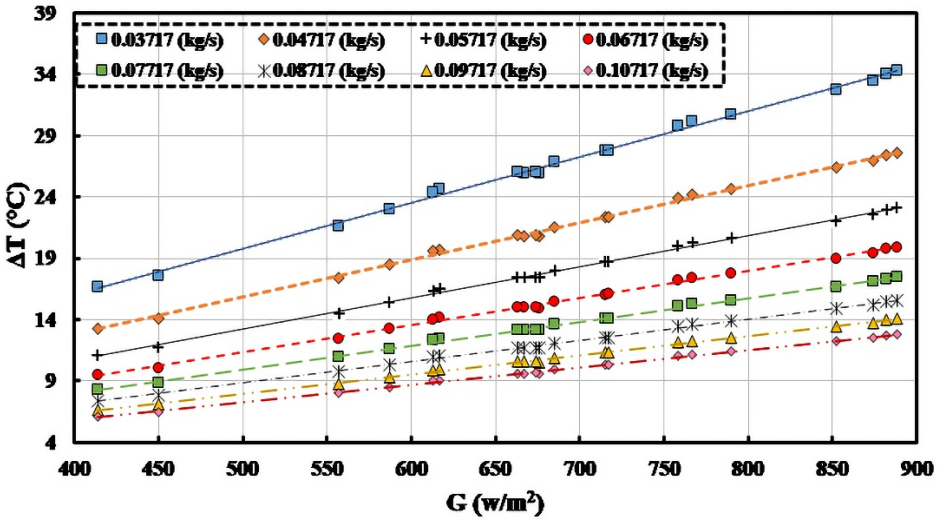

a) Syltherm 800

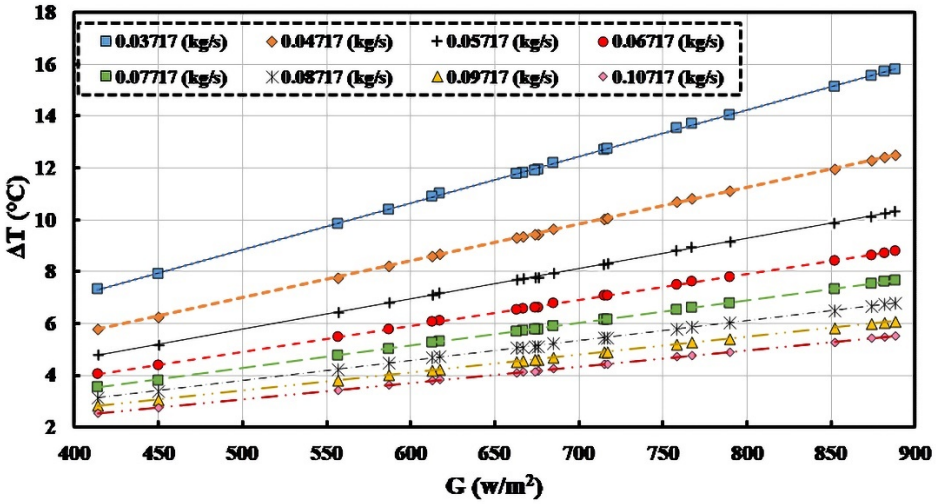

b) water

Figure 10. Effect of mass flow rate on the temperature difference

Figure 10 reveals that in the same condition, the HTF temperature difference in Syltherm 800 oil is higher than water, which can be attributed to its lower thermal capacity than water. Meanwhile, the reduction of the capacity factor due to an increase in the HTF flow rate is shown for the three HTF types of S2 oil, Syltherm 800 oil, and water (Figure 11) to better elucidate the effect of the HTF types. According to Figue 12, the term capacity factor for the Syltherm 800 oil is more responsive to the reduction of the HTF flow rate (increasing $1/\dot{m}$) compared to S2 and water. It is shown that to reach a higher temperature at a constant flow rate and solar irradiation, Syltherm 800 oil is better than S2 oil and S2 oil is better than water.

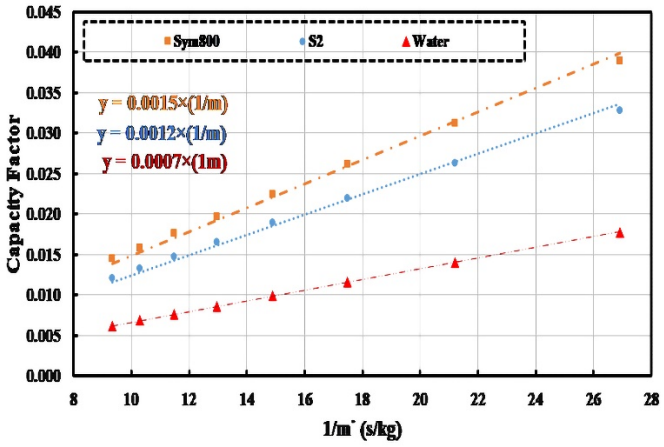

Figure 11. Variation in capacity factor against the inverse of mass flow rate for three different HTFs

4.3. The effect of vacuum

The effect of the vacuum in the gap between the glass cover and the absorber tube on the thermal performance is investigated. Thereby, the governing equations of the solar vacuum tube are implemented in the analytical model for different HTFs to obtain thermal factors. The results are depicted in Figure 12 for three HTF. As expected, implementing a vacuum tube will enhance the capacity factor more than the non-vacuumed tube (see Figure 11). This graph shows that the rates of the effectiveness of the evacuated tube in capacity factor for Syltherm 800 oil and S2 oil are 6.66 %, and 8.33 %, respectively, but it is negligible for the water. It can be attributed to the higher heat capacity of the water than other HTFs considered in this study. The high heat capacity of water causes a decrease in the absorber surface temperature, which has a high impact on the receiver heat loss. This outstanding result is discussed in the following.

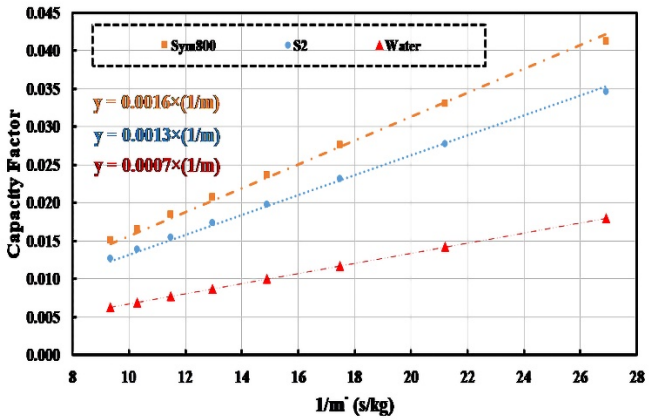

Figure 12. Effect of the vacuum on the variation of capacity factor with respect to the inverse of mass flow rate for three different HTF types

4.4. Temperature distribution of PTC

Furthermore, in the PTC system, another factor affecting the heat transfer rate and outlet HTF temperatures is the surrounding conditions of PTC such as the intensity of solar radiation, wind speed, and ambient and sky temperatures. These factors influence the temperature of various points of the receiver of PTC, such as the glass cover temperature as well as the surface temperature of the absorber tube, which affect the rate of heat transfer to the HTF. According to the model illustrated in Figure 5, the temperature distribution of the receiver can elucidate the heat transfer mechanism. In a specific surrounding condition listed in Table 8, use of 2D numerical model and simulation in the radial direction of the receiver is considered for three different HTF types for the receiver with & without vacuum. Accordingly, the temperature distribution in the radial direction is obtained and plotted in Figure 13 for three HTFs of Syltherm 800 oil, S2 oil and water.

Table 8. Governing condition of Figure 13

Flow rate (kg/s)	Ambient temperature (°C)	Wind speed (m/s)	Solar irradiance (W/m^2)	HTF inlet temperature (°C)
0.06717	21.6	1.7	667	47.8

As can be seen in Figure 13, the highest temperature for the receiver in the PTC is the outer surface temperature of the absorber tube and the lowest temperature is the outer surface temperature of the glass cover. The smallest temperature difference between the absorber tube and the HTF occurs for the water, and the biggest one is in Syltherm 800 oil, which is owing to the HTF thermo-physical properties, especially the specific heat capacity. Furthermore, the impact of the vacuum on the temperature is demonstrated in Figure 13. As can be seen, the overall temperature in the vacuumed tube is higher than that in the unvacuumed tube. However, the level of temperature for the vacuumed tube is higher for the Sym800 and S2 than that for the water.

4.5. Thermal efficiency effect

In consequence, this study calculated the thermal efficiency of the PTC for three different HTFs, flow rate ranging from 0.0372 to 0.1072 kg/s, and solar radiation from 400 to 900 W/m^2.

To obtain the thermal efficiency, the environmental conditions demonstrated in Table 8 are applied for 8 different HTF flow rates and wide ranges of solar irradiations. The results are depicted in Figure 14 for three HTFs used in this study.

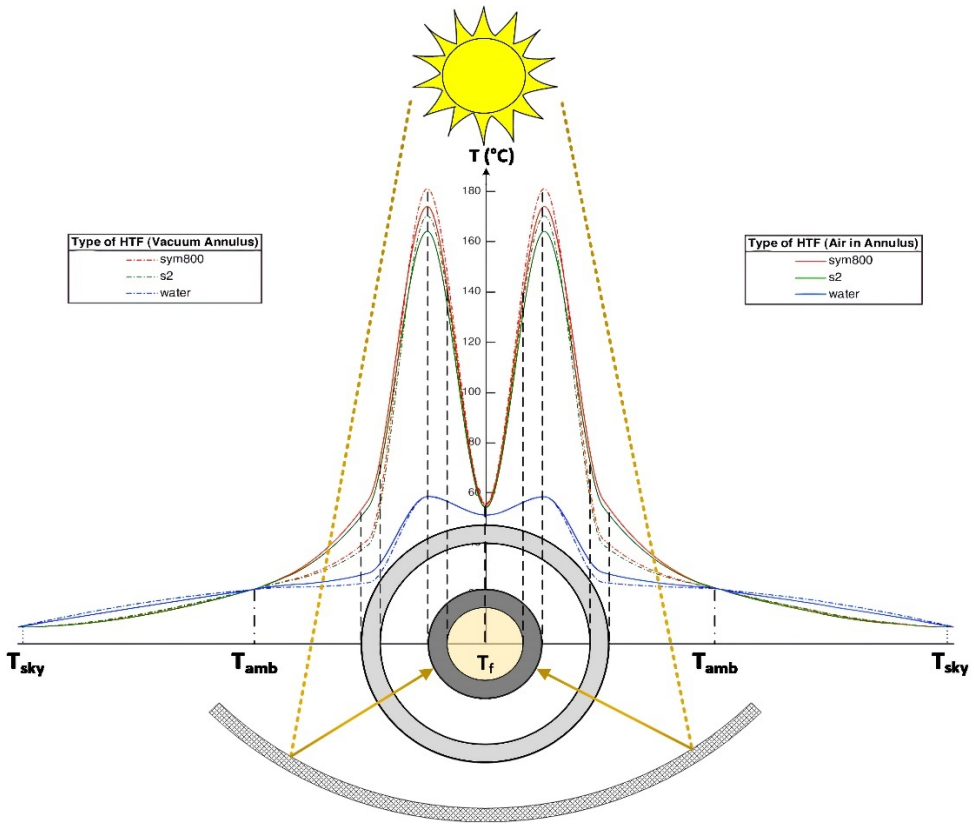

Figure 13. Temperature profile of PTC for vacuumed & unvacuumed tubes and three HTF types

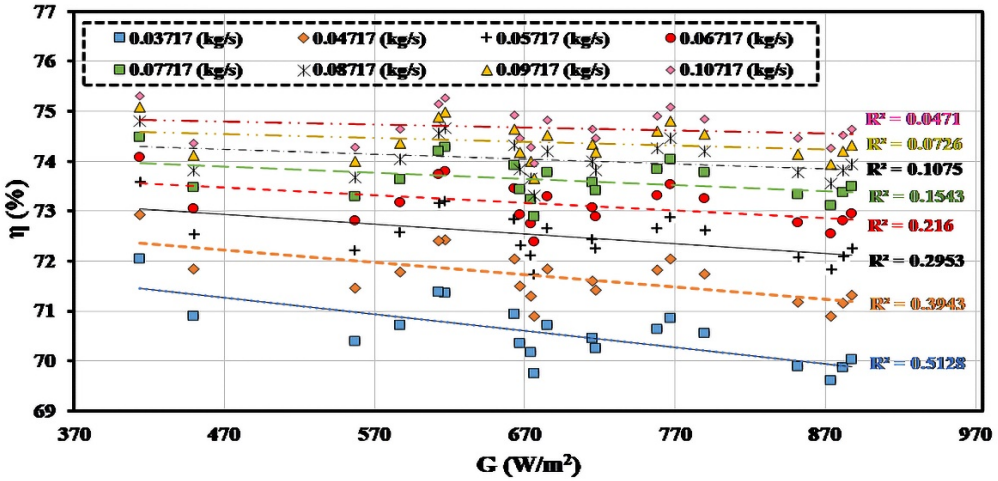

a) Syltherm 800

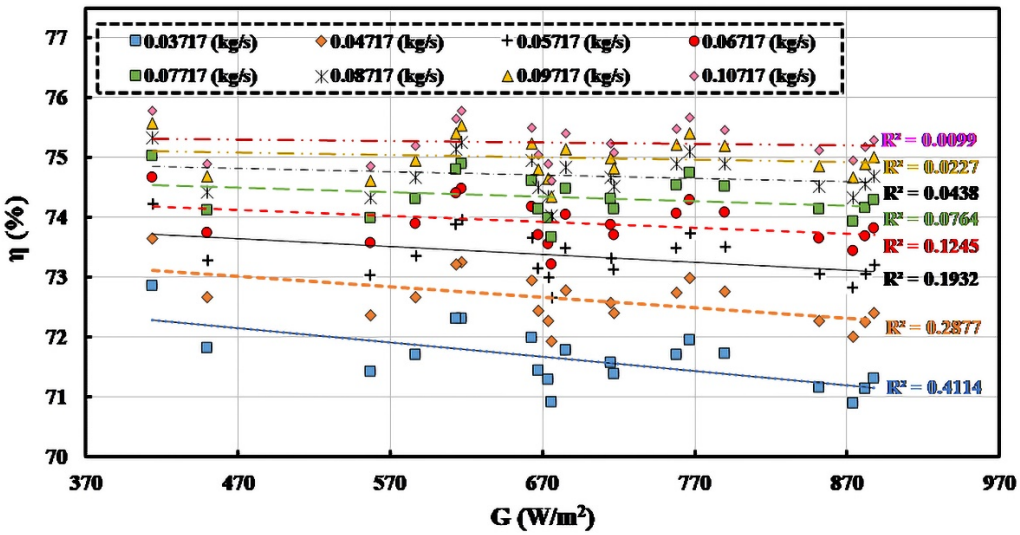

b) S2

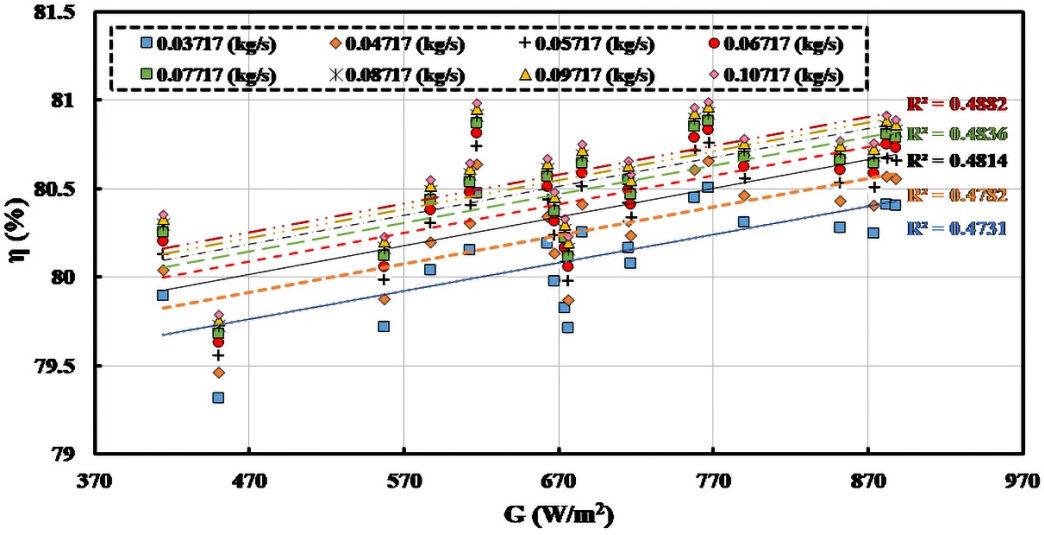

c) Water

Figure 14. Effect of mass flow rate and solar irradiation on thermal efficiency for three HTF types

According to Figure 14, the thermal efficiency raises with an increase in the HTF flow rate and decreases following the growth of solar radiation for Syltherm 800 and S2. The opposite behavior is seen for water, which is explicitly discussed in the paragraph below. Further, with the increment of the HTF flow rate, the Reynold number increases in the absorber tube. Therefore, it leads to an increase in the heat transfer coefficient, which consequently results in thermal efficiency rise at a higher HTF flow rate. Moreover, according to Figure 14, the thermal efficiencies obtained for the lower HTF are more scattered around the fitted line than the higher flow rate. The R-square is given in Figure 14 for all trend lines. It can be confirmed that the model is excellent consistent with the high flow rate.

The behavior of decrement of thermal efficiency with the solar radiation for Syltherm 800 and S2 is attributed to the heat loss from the receiver to the environment due to the hot surface of the receiver at higher solar irradiation. According to Figure 15c, the behavior of water differs from the other two HTFs. To assess this behavior, heat loss is calculated based on the analytical model shown in Figure 4 for three different HTFs. The results are depicted in Figure 15. Accordingly, the heat loss for Syltherm 800 and S2 is much higher than that for the water. It can be attributed to the high temperature of the absorber tube of Syltherm 800 and S2, compared to water. Compared to the two other HTFs, water with higher specific thermal heat and heat transfer conductivity would diminish absorber tube temperature. The impact of solar intensity variations on the temperature distribution across the horizontal cross-section of the PTC is shown in Figure 16 for the three HTFs. This figure confirms that the same value of solar intensity could produce maximum temperature on the absorbent tube for Syltherm 800 as a working fluid compared to S2 and water as a working fluid. Therefore, based on the conditions examined in this study, it can be concluded that water can cool down the absorber to gain more solar heat than the two other HTFs. However, the HTF temperature is lower for the water.

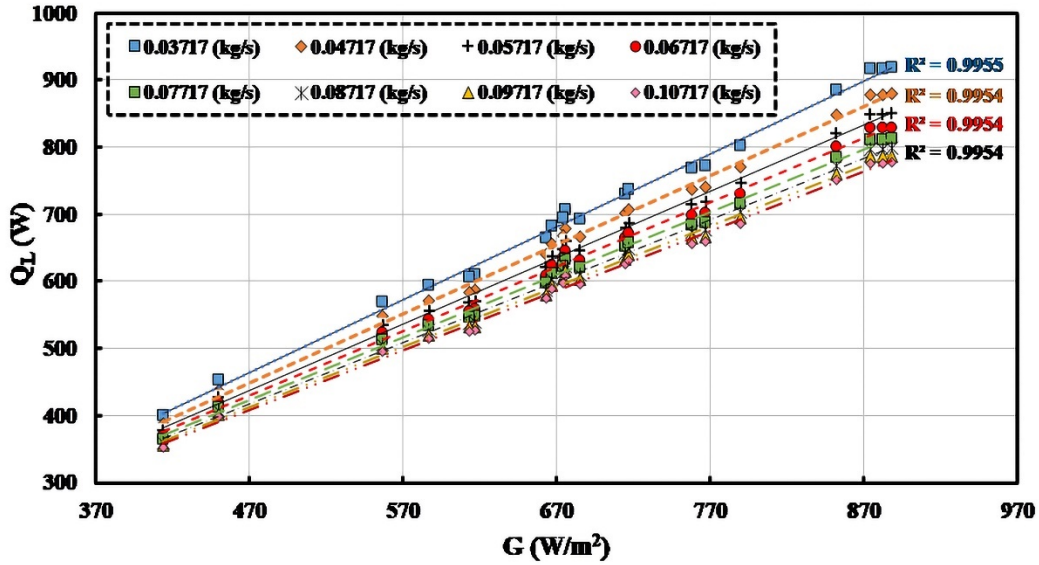

a) Syltherm 800

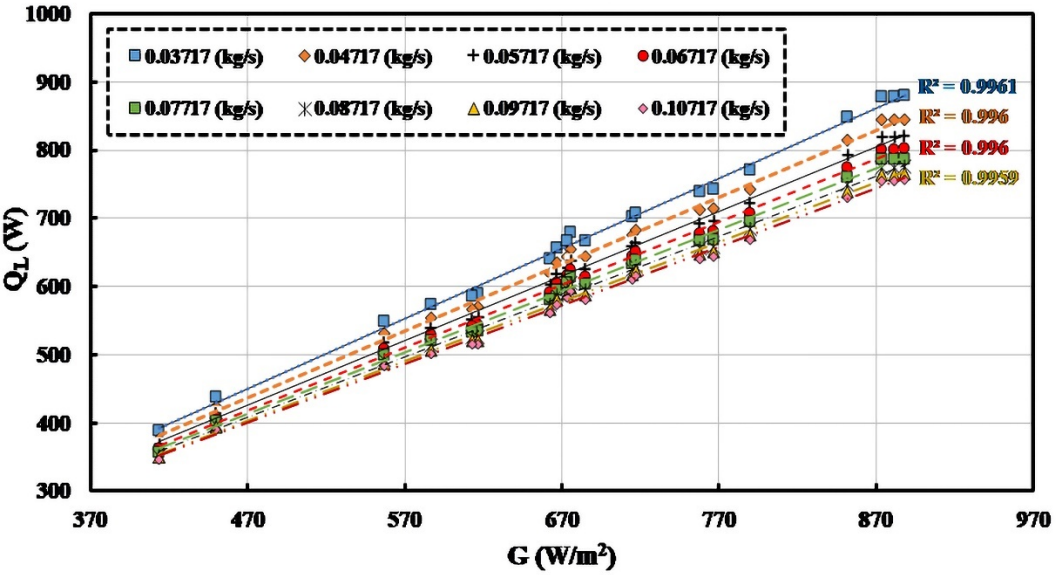

b) S2

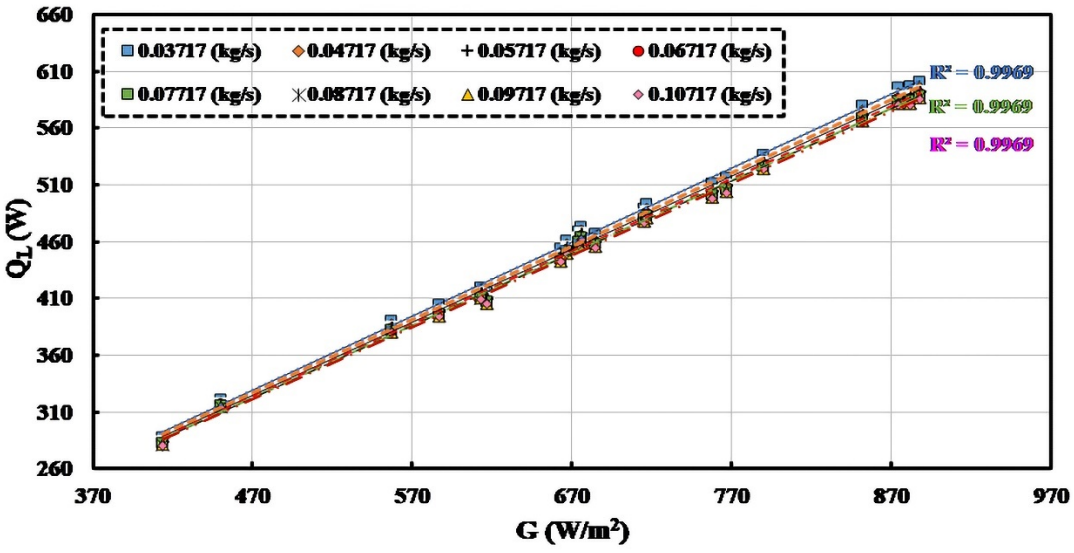

c) Water

Figure 15. Heat loss in three HTFs with different flow rates and solar irradiations

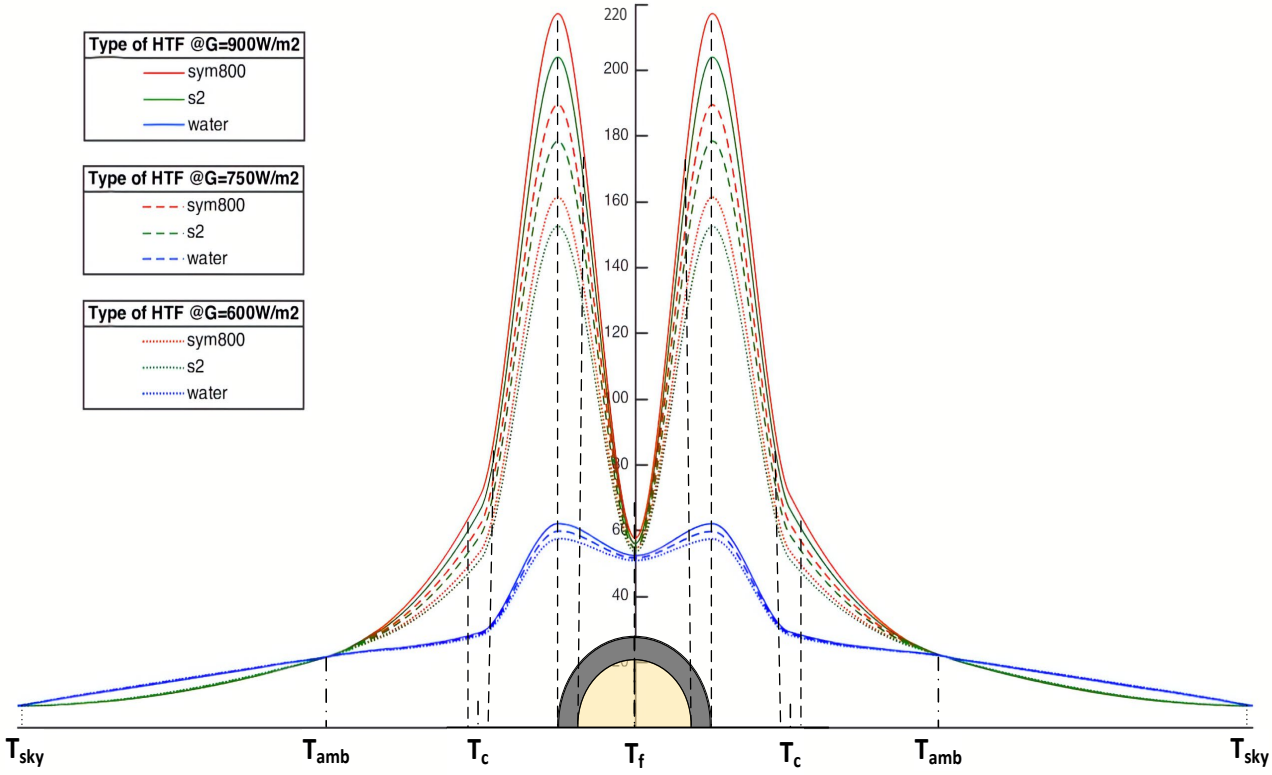

Figure 16. Temperature distribution for three HTFs and three irradiations

5. CONCLUSIONS

This study managed to carry out an experiment with the aim of investigating different rates of thermal efficiency, temperature distribution of a PTC for varying mass flow rates, and solar intensities for three Heat Transfer Fluid (HTF) types. In addition, the results were validated using a developed numerical model. In this regard, the PTC was employed and an experimental rig was built to perform the experimental study. Moreover, the effect of the vacuum in the space among the glass cover and the adsorbent tube was examined for these three HTFs. The following results can be concluded through this research:

-There was a linear relationship between the temperature change across the PTC and the variation of the HTF flow rate for constant solar radiation. The slope of these changes represents the sensitivity of these three HTFs. The results showed that the Syltherm 800 oil was more sensitive to the variation of the HTF flow rates than S2 oil and ordinary water. In other words, a higher temperature was available for a lower mass flow rate with a PTC and Syltherm 800.

-The linear relationship between the capacity factor and the inverse of mass flow rate demonstrated that the PTC with Syltherm 800 had a greater degree of thermal efficiency than the other two HFTs with PTC.

-The results for the presence of the vacuum between the glass cover and the adsorbent tube indicated that the existence of vacuum raised the thermal efficiency of PTC with Syltherm 800 oil by about 6.7 %, about 8.3 % with S2 oil, and a negligible amount for ordinary water.

-The temperature profile across the horizontal cross-section of the PTC with three working fluids (constant solar intensity and HTF mass flow rate) showed that maximum temperature was reached on the receiver tube and this maximum temperature for Syltherm 800 oil was 176 ^{o}C and for S2 oil and water were 161 ^{o}C and 61 ^{o}C, respectively.

-The presence of the vacuum between the glass cover and the adsorbent tube changed the maximum temperature of the receiver tube with Syltherm 800 oil by about 2.84 % from 176 ^{o}C to 181 ^{o}C, for S2 oil by about 3.72 % from 161 ^{o}C to 167 ^{o}C, and by negligible amount for water.

-The results for of the effects of solar intensity variation on the temperature profile across the horizontal cross-section of the PTC with three working fluids revealed that the maximum temperature still occurs on the receiver tube. However, the maximum temperature of the receiver tube with Syltherm 800 oil working fluid increased by 35.1 % from 167 ^{o}C to 219 ^{o}C, since the solar intensity changed from 600 W/m^2 to 900 W/m^2. This increase in the case of the same level of solar intensity variation for S2 working fluid was 32.7 % from 153 ^{o}C to 203 ^{o}C. Again, this temperature rise for water as a working fluid was about 6.8 %, which is almost negligible in compassion with that for these two oils as working fluids.

In the end, it should be noted that despite the proof of the existing modeling, it is better to evaluate the results with experimental research in future research, for which special facilities and equipment are required that make these studies limited and difficult.

6. ACKNOWLEDGEMENT

The authors acknowledge the support of renewable energy systems laboratory of Iran University of Science and Technology.

NOMENCLATURE

A	Area (m^2)
C	Concentration
Cp	Specific heat at constant pressure ($kJK^{-1}kg^{-1}$)
D	Diameter (m)
F	Focal distance (m)
F_R	Heat removal factor
h	Heat transfer coefficient ($Wm^{-2}K$)
G	Solar radiation (Wm^{-2})
K	Thermal conductivity ($WK^{-1}m^{-1}$)
Nu	Nusselt number
T	Temperature (C)
Pr	Prandtl number
Q_u	Useful energy (W)
Re	Reynolds number
U_L	Collector loss coefficient ($Wm^{-2}K^{-1}$)
V_{air}	Air velocity (ms^{-1})
W	Width (m)
L	Tube length (m)
Ra	Rayleigh number
Greek letters	
α	Absorber absorbance
ρ_{ref}	Collector reflectance
γ	Intercept factor
μ	Dynamic viscosity ($kgm^{-1}s^{-1}$)
ϵ	Emittance
η	PTC efficiency
η_{opt}	Optical efficiency
ρ	Density (kgm^{-3})
σ	Stefan-Boltzmann constant ($Wm^{-2}K^{-4}$)
τ	Cover transmittance
Subscripts	
sky	Sky condition
f	Fluid inlet
out	Outlet
in	Inlet
opt	Optical
c	Cover
r	Receiver
a	Aperture
i	Inner
o	Outer
amb	Ambient
L	Loss
Abbreviation	
CSP	Concentrating Solar Power
DNI	Direct Normal Irradiance
LS-2	Lus System 2 End Gen
SNL	Sandia National Laboratory
PTC	Parabolic Trough Collector
SNL	Sandia National Laboratory

REFERENCES

1. Borzuei, D., Moosavian, S.F. and Farajollahi, M., "On the performance enhancement of the three-blade savonius wind turbine implementing opening valve", ***Journal of Energy Resources Technology***, Vol. 143, No. 5, (2021). (https://doi.org/10.1115/1.4049460).
2. Zahedi, R., Ahmadi, A. and Sadeh, M., "Investigation of the load management and environmental impact of the hybrid cogeneration of the wind power plant and fuel cell", ***Energy Reports***, Vol. 7, (2021), 2930-2939. (https://doi.org/10.1016/j.egyr.2021.05.008).
3. Kizilkan, O., Kabul, A. and Dincer, I., "Development and performance assessment of a parabolic trough solar collector-based integrated system for an ice-cream factory", ***Energy,*** Vol. 100, (2016), 167-176. (https://doi.org/10.1016/j.energy.2016.01.098).
4. Jamar, A., Majid, Z., Azmi, W., Norhafana, M. and Razak, A., "A review of water heating system for solar energy applications", ***International Communications in Heat and Mass Transfer,*** Vol. 76, (2016), 178-187. (https://doi.org/10.1016/j.icheatmasstransfer.2016.05.028).
5. Chahine, K., Murr, R., Ramadan, M., Hage, H.E. and Khaled, M., "Use of parabolic troughs in HVAC applications–Design calculations and analysis", ***Case Studies in Thermal Engineering,*** Vol. 12, (2018), 285-291. (https://doi.org/10.1016/j.csite.2018.04.016).
6. Ahmadi, A., Ehyaei, M.A., Doustgani, A., El Haj Assad, M., Hmida, A., Jamali, D.H., Kumar, R., Li, Z.X. and Razmjoo, A., "Recent residential applications of low-temperature solar collector", ***Journal of Cleaner Production,*** (2020), 123549. (https://doi.org/10.1016/j.jclepro.2020.123549).
7. Marefati, M., Mehrpooya, M. and Shafii, M.B., "Optical and thermal analysis of a parabolic trough solar collector for production of thermal energy in different climates in Iran with comparison between the conventional nanofluids", ***Journal of Cleaner Production,*** Vol. 175, (2018), 294-313. (https://doi.org/10.1016/j.jclepro.2017.12.080).
8. Abid, M., Ratlamwala, T. and Atikol, U., "Performance assessment of parabolic dish and parabolic trough solar thermal power plant using nanofluids and molten salts", ***International Journal of Energy Research,*** Vol. 40, No. 4, (2016), 550-563. (http://doi.org/10.1002/er.3479).
9. Kalogirou, S.A., Solar energy engineering: Processes and systems, Academic Press, (2013). (https://www.google.com/books/edition/Solar_Energy_Engineering/wYRqAAAAQBAJ?hl=en&gbpv=1&dq=Kalogirou,+S.A.,+Solar+energy+engineering:+Processes+and+systems,+Academic+Press,+(2013)&pg=PP1&printsec=frontcover).
10. Ghodbane, M. and Boumeddane, B., "A numerical analysis of the energy behavior of a parabolic trough concentrator", ***Journal of Fundamental and Applied Sciences,*** Vol. 8, No. 3, (2016), 671-691. (http://doi.org/10.4314/jfas.v8i3.2).
11. Yaghoubi, M., Ahmadi, F. and Bandehee, M., "Analysis of heat losses of absorber tubes of parabolic through collector of Shiraz (Iran) solar power plant", ***Journal of Clean Energy Technologies,*** Vol. 1, No. 1, (2013), 33-37. (http://10.7763/JOCET.2013.V1.8).
12. Ibrar Hussain, M., Mokheimer, E. and Ahmed, S., "Optimal design of a solar collector for required flux distribution on a tubular receiver", ***Journal of Energy Resources Technology,*** Vol. 139, No. 1, (2017). (http://doi.org/10.1115/1.4035361).
13. Kalogirou, S.A., "Solar thermal collectors and applications", ***Progress in Energy and Combustion Science,*** Vol. 30, No. 3, (2004), 231-295. (https://doi.org/10.1016/j.pecs.2004.02.001).
14. Bellos, E., Tzivanidis, C. and Tsimpoukis, D., "Multi-criteria evaluation of parabolic trough collector with internally finned absorbers", ***Applied Energy,*** Vol. 205, (2017), 540-561. (https://doi.org/10.1016/j.apenergy.2017.07.141).
15. Bellos, E. and Tzivanidis, C., "Investigation of a star flow insert in a parabolic trough solar collector", ***Applied Energy,*** Vol. 224, (2018), 86-102. (https://doi.org/10.1016/j.apenergy.2018.04.099).
16. Xiao, X., Zhang, P., Shao, D. and Li, M., "Experimental and numerical heat transfer analysis of a V-cavity absorber for linear parabolic trough solar collector", ***Energy Conversion and Management,*** Vol. 86, (2014), 49-59. (https://doi.org/10.1016/j.enconman.2014.05.001).
17. Bellos, E. and Tzivanidis, C., "Thermal analysis of parabolic trough collector operating with mono and hybrid nanofluids", ***Sustainable Energy Technologies and Assessments,*** Vol. 26, (2018), 105-115. (https://doi.org/10.1016/j.seta.2017.10.005).
18. Boukelia, T., Mecibah, M. and Laouafi, A., "Performance simulation of parabolic trough solar collector using two fluids (thermic oil and molten salt)", ***Journal of Fundamental and Applied Sciences,*** Vol. 8, No. 2, (2016), 600-626. (https://doi.org/10.4314/jfas.v8i2.28).
19. Dudley, V.E., Kolb, G.J., Mahoney, A.R., Mancini, T.R., Matthews, C.W., Sloan, M. and Kearney, D., "Test results: SEGS LS-2 solar collector", Nasa STI/Recon Technical Report N, Vol. 96, (1994), 11437. (https://doi.org/10.2172/70756).
20. Reddy, K., Kumar, K.R. and Ajay, C., "Experimental investigation of porous disc enhanced receiver for solar parabolic trough collector", ***Renewable Energy,*** Vol. 77, (2015), 308-319. (https://doi.org/10.1016/j.renene.2014.12.016).
21. Chowdhury, M. and Mokheimer, E., "Recent developments in solar and low-temperature heat sources assisted power and cooling systems: A design perspective", ***Journal of Energy Resources Technology,*** Vol. 142, No. 4, (2020). (https://doi.org/10.1115/1.4044562).
22. Moosavian, S.F., Borzuei, D. and Ahmadi, A., "Energy, exergy, environmental and economic analysis of the parabolic solar collector with life cycle assessment for different climate conditions", ***Renewable Energy,*** Vol. 165, (2021), 301-320. (https://doi.org/10.1016/j.renene.2020.11.036).
23. Behar, O., Khellaf, A. and Mohammedi, K., "A novel parabolic trough solar collector model–Validation with experimental data and comparison to Engineering Equation Solver (EES)", ***Energy Conversion***

and Management, Vol. 106, (2015), 268-281. (https://doi.org/10.1016/j.enconman.2015.09.045).

24. Tagle-Salazar, P.D., Nigam, K. and Rivera-Solorio, C.I., "Heat transfer model for thermal performance analysis of parabolic trough solar collectors using nanofluids", ***Renewable Energy***, Vol. 125, (2018), 334-343. (http://10.1016/j.renene.2018.02.069).
25. Swinbank, W.C., "Long-wave radiation from clear skies", ***Quarterly Journal of the Royal Meteorological Society***, Vol. 89, No. 381, (1963), 339-348. (https://doi.org/10.1002/qj.49708938105).
26. Duffie, J.A. and Beckman, W.A., Solar engineering of thermal processes, John Wiley & Sons, (2013). (https://doi.org/ 10.1002/9781118671603).
27. Tzivanidis, C. and Bellos, E., "The use of parabolic trough collectors for solar cooling–A case study for Athens climate", ***Case Studies in Thermal Engineering***, Vol. 8, (2016), 403-413. (https://doi.org/10.1016/j.csite.2016.10.003).
28. Bergman, T.L., Incropera, F.P., DeWitt, D.P. and Lavine, A.S., Fundamentals of heat and mass transfer, John Wiley & Sons, (2011). (https://www.google.com/books/edition/Fundamentals_of_Heat_and_Mass_Transfer/vvyIoXEywMoC?hl=en).
29. Ehyaei, M., Ahmadi, A., El Haj Assad, M., Hachicha, A. and Said, Z.J.S.E., "Energy, exergy and economic analyses for the selection of working fluid and metal oxide nanofluids in a parabolic trough collector", ***Solar Energy***, Vol. 187, (2019), 175-184. (https://doi.org/10.1016/j.solener.2019.05.046).

JREE: Vol. 8, No. 4, (Autumn 2021) 67-76

Journal of Renewable Energy and Environment

Research Article

Journal Homepage: www.jree.ir

Renewable Energy-Based Systems on a Residential Scale in Southern Coastal Areas of Iran: Trigeneration of Heat, Power, and Hydrogen

Mehdi Jahangiri [a*], Fatemeh Karimi Shahmarvandi [b], Reza Alayi [c]

[a] *Department of Mechanical Engineering, Shahrekord Branch, Islamic Azad University, Shahrekord, Iran.*
[b] *Department of Biomedical Engineering, Shahrekord Branch, Islamic Azad University, Shahrekord, Iran.*
[c] *Department of Mechanical Engineering, Germi Branch, Islamic Azad University, Germi, Iran.*

PAPER INFO

Paper history:
Received 14 December 2020
Accepted in revised form 21 August 2021

Keywords:
CO_2 Penalty,
Interest Rate,
Fuel Cell,
Gas Boiler

ABSTRACT

The use of small-scale Combined Heat and Power (CHP) to meet the electrical and thermal needs of buildings has grown exponentially and plans have been made in Iran to expand these systems. In view of the above, in the present work, for the first time, sensitivity analysis has been performed on the parameters of natural gas price, annual interest rate, and the price of pollutant penalties. The CHP system studied included fuel cell, biomass generator, solar cell, wind turbine, and gas boiler. The techno-econo-enviro simulations were performed by HOMER software and the study area was Abadan. The use of a dump load to convert excess electricity into heat and heat recovery in a biomass generator and fuel cell are other advantages presented by the present work. The minimum Cost of Energy (COE) is 1.16 $/kWh. The results also showed that the use of biomass generators was economical when the annual interest rate was 30 %. The significant effect of using dump load on the required heat supply and the lowest price per kg of hydrogen produced equal to $ 35.440 are other results of the present work. In general, the results point to the superiority of solar radiation potential over wind energy potential of the study area and the prominent role of dump load in providing heat on a residential scale is clearly seen. Also, for the current situation, using biomass is not cost-effective.

https://doi.org/10.30501/jree.2021.261980.1170

1. INTRODUCTION

All around the globe, humans consume much energy to generate heat and electricity in such sectors as industry, construction, and agriculture [1, 2]. To ensure a sustainable future, especially in the wake of global warming and lack of fossil resources, further research and development works are essential to creating more efficient and environmentally friendly energy production systems [3, 4]. In response to this, being one of the best methods of energy efficiency [5], CHP can be a viable solution because it is usually useful to generate heat and electricity at the same time and is obtained in a single process and also, from a single energy source [6, 7]. The CHP system can be defined as a set of components: heat converter (or heat engine), generator, heat recovery system, and electric converter [8].

CHP systems improve the efficiency of the whole system and cause heat recovery in the power generation process [9]. Centralized power generation systems cause heat loss in generation and transportation [10]. For example, only one-third of the primary energy derived from a nuclear power plant is converted into electricity. Thus, the total efficiency of classical energy production (electricity and heat) is about 60 %, while the total efficiency of CHP can reach 90 % (Figure 1) [11, 12]. Thus, CHP systems improve the use of primary energy and in addition, can help diversify the country's energy mix with local electricity and heat generation.

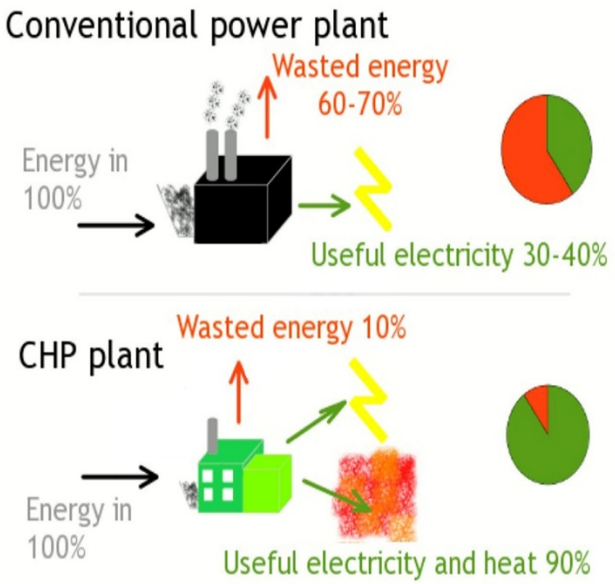

Figure 1. The energy efficiency schematic of a conventional system and CHP [13]

*Corresponding Author's Email: jahangiri.m@iaushk.ac.ir (M. Jahangiri)
URL: https://www.jree.ir/article_135328.html

Please cite this article as: Jahangiri, M., Karimi Shahmarvandi, F. and Alayi, R., "Renewable energy-based systems on a residential scale in southern coastal areas of Iran: Trigeneration of heat, power, and hydrogen", ***Journal of Renewable Energy and Environment (JREE)***, Vol. 8, No. 4, (2021), 67-76. (https://doi.org/10.30501/jree.2021.261980.1170).

Population growth in Iran has created a significant demand for electricity generation [14]. The population has doubled in the last 35 years, from 40.2 million in 1981 to 80.2 million in 2016 [15]. CO_2 emissions per capita increased from 2.8 tons in 1981 to 8.28 tons in 2014 [15]. Some of the challenges of Iran's electricity industry are increased electricity demand, low efficiency of centralized thermal power plants, and electrical losses in transmission and distribution lines [16, 17]. Centralized thermal power plants generate about 95 % of Iran's electricity [16]. The residential sector in Iran consumes about 33 % of electricity [16]. The average efficiency of Iran's thermal power plants is 37 %, and electricity losses in the transmission and distribution network are about 12.6 % [15, 16]. This statistic shows that there is an urgent need to upgrade Iran's electricity system using new technologies such as distributed generation systems and CHP. The type of CHP in each case study is determined by the availability of technology and fuel. In Iran, CHP technology is related to internal combustion engines. The price of natural gas is low and is widely available in most parts of the country. Therefore, gas-fired CHP systems are the most suitable technology options in Iran.

So far, few works have been done in the field of simultaneous generation of electricity and heat in the distributed generation scenario by HOMER software. Here are some of them.

Waqar et al. in 2017 [18] evaluated a CHP-based microgrid in the grid connection mode in 6 cities in Pakistan using HOMER software. The reason for the investigation was the frequent disturbances in natural gas and forced use of electricity to provide the required heat. The components used were solar cells, batteries, and diesel generators. The researchers' objectives were to reduce environmental pollution and minimize the cost of energy production. The results showed that Gilgit station had the lowest COE amount of 0.049 $/kWh, Lahore station had the lowest GHG emission amount about 1000 tons/y, Quetta station had the maximum waste heat recovery with an amount of 2040282 MWh/y, and Quetta station had the most electricity sales to the grid with a rate of 8322268 MWh/y.

Yuan et al. in 2017 [19] examined the use of a combined renewable energy system consisting of Photovoltaic Arrays (PV), wood-syngas CHP, and backup batteries in a typical semi-detached house in China. It was to meet home energy demand and reduce greenhouse gas emissions from fossil fuels. HOMER was used to simulate all operational configurations and to evaluate the system technically and economically. The results showed that the proposed optimum consisted of PV, wood gas generator, and the battery with the COE and NPC equal to 0.351 $/kWh and 3572 $, respectively.

Jahangiri et al. (2018) [20] in Zarrinshahr investigated the use of wind, solar, and biomass for simultaneous production of electricity and heat. The results showed that if the distance to the national grid in the study area was less than 2.58 km, receiving electricity from the national grid would be better than using biomass. Also, assuming a 15 % increase in electricity and gas prices annually and if 100 % of the energy required is provided by renewable energy sources over 25 years, the profit will be $ 20,310.

Jahangiri et al. in 2018 [21], for the first time, evaluated the effect of heat recovery factor on the simultaneous production of electricity and heat evaluated in distributed generation by solar cells. HOMER software was used for simulation and the place of study was Isfahan. Three different scenarios were considered for the fuel used by the generator and boiler, which were the diesel consumed by the generator and boiler, natural gas consumed by the generator and boiler, and the diesel consumed by the generator, and the natural gas consumed by the boiler. The results showed that by increasing the heat recovery factor, the consumption amount of fossil fuel reduced and as a result, the amount of CO_2 emissions and the cost per KWh hour of energy decreased. The results also indicated that the cheapest scenario was the natural gas use for both the generator and the boiler. Also, the scenario of using diesel for the generator and natural gas for the boiler was the most expensive scenario. The cheapest electricity produced was priced at 0.167 $/kWh.

Khormali and Niknam in 2019 [22] employed Homer software to minimize the cost of operating a grid-connected home-scale microgrid under usage time pricing. The study site was Gonbadkavoos Industrial Park in Iran and the evaluation criterion was Total NPC. The cost of diesel consumed was 0.16 $/L and the cost of consumed gas was 0.04 $/m^3. The results of studies of two different scenarios of electricity exchange price with the network showed that during the year, in the first scenario 94.7 % and in the second scenario 35.2 % of electricity were purchased from the network. The results also showed a much better potential of solar energy than the potential of wind energy in the study area.

Kalamaras et al. in 2019 [23] conducted a feasibility study on the CHP system of an island separate from the national electricity grid in Greece. HOMER software was used for the studies and their system included solar cell, wind turbine, fuel cell, battery, electrolyzer, and hydrogen tank. The results illustrated that the selected system with a COE of 1.2 €/kWh could meet the thermal and electrical needs throughout the year.

Gbadamosi et al. in 2020 [24] evaluated the optimal power and reliability analysis of the CHP-wind-solar hybrid system for agricultural applications. They used solver CPLEX to solve and their place of study was South Africa. The results showed that the CHP-wind-solar hybrid system would reduce costs by 48 % compared to the CHP system.

Masrur et al. in 2020 [25] conducted an energy-economic evaluation of a CHP-solar PV system for a camp in the United States using HOMER software. They chose two different scenarios to consider: one based on fossil fuels and one combined with solar PVs. The results showed that the solar PV-based system with 25,609 kWh/year energies generated by solar PVs had less LCOE (as much as 0.04 $/kWh).

Pelaez et al. in 2021 [26] conducted a feasibility study for a solar cell-fuel cell-based CHP system using hydrogen as the fuel source. HOMER software was used for the simulation and the study site was an off-grid station in Spain. The results showed that the optimal system had a net present cost of $ 1006293 and a cost per kWh of energy produced was $ 0.8399. They also stated that although the system under consideration was not currently economically viable, it was technically feasible.

Elkadeem et al. in 2021 [27] analyzed the feasibility and optimization of a renewable energy-based desalination system (wind turbine-solar cell-diesel generator-battery) for an airport in Egypt. They used HOMER software for simulation and considered heat supply. For the optimal system, the results showed that the LCOE was equal to 0.08 $/kWh and the payback time was 1.2 years. Also, compared to the traditional system of using a diesel generator, the optimal system produced 59.5% fewer pollutants.

According to studies, the effects of dump load and the use of heat recovery in a CHP system have not been studied so far. Also, due to the variability of the studied parameters, sensitivity analysis has rarely been done in the performed works. Therefore, in the present work, using a 20-year average climatic data and HOMER software, a technical-economic-environmental study has been performed. Finding the optimal system, the amount of electricity, heat, and hydrogen production for each scenario, assessing the number of pollutants produced, as well as assessing the amount of electricity and excess heat are among the items done in the present work. It should also be noted that although the results of the present work are specific to this station, the proposed method can be used to implement a biomass-based CHP system anywhere in the world. Also, performing sensitivity analysis for different parameters makes it possible to evaluate the behavior of the system for wider applications in an area.

2. THE LOCATION UNDER STUDY

In today's world, the protection of coastal areas and their habitats is very important. Coastal environmental management seeks to adapt human uses and activities to the potential of the region [28]. For this reason, the city of Abadan was selected on the coastline of 5000 km south of Iran for the present work, and its wind speed and solar radiation data, including 20-year average data [29], were extracted from the NASA site. The required climatic data are given in Table 1. The location of the study station is also shown in Figure 2.

Table 1. The climatic data for Abadan

Data	Jan.	Feb.	Mar.	Apr.	May	Jun.	Jul.	Aug.	Sept.	Oct.	Nov.	Dec.
Solar radition (kWh/m^2-day)	3.305	4.432	5.255	5.925	6.846	7.409	7.087	6.913	6.196	4.922	3.775	2.976
Wind speed (m/s)	2.100	2.800	3.000	3.300	3.400	4.500	4.400	3.600	3.300	2.200	2.200	2.100

Figure 2. The location of Abadan on the Iran map

3. METHODOLOGY

For the present studies, HOMER software was used, which performed technical-economic-environmental studies together [20, 30]. This software had the ability to supply electricity, heat, and hydrogen and was used for analysis connected to the grid and standalone [31, 32]. Software optimizations are economical and the selected system has the lowest current net total price [33]. HOMER simulates the performance of the system under study over a year in time steps from one minute to one hour [34]. A very important feature of HOMER software that distinguishes it from other software is the sensitivity analysis that considers the impact of variables that are beyond the user's control such as wind speed, fuel costs, etc. and helps determine how the optimal system changes because of the mentioned parametric variations [35, 36]. Table 2 presents the general advantages and limitations of HOMER software. Figure 3 also shows the flowchart of software performance to better understand the performed process.

Table 2. Advantages and disadvantages of HOMER software [37]

Advantages	Disadvantages
Providing a list of real technologies simulated based on available equipment.	Being time-consuming and slow for some solutions.
Quite accurate simulation results for analysis and evaluation.	Requiring for accurate input data.
Providing a list of possible configurations based on different technologies and different equipment sizes.	Requiring experience-based criteria to achieve a good solution.
Solving many configurations quickly.	High quality of input data (resources).
Utility of results in learning to optimize systems with different combinations.	Software's inability to guess key values or sizes in case of their absence.

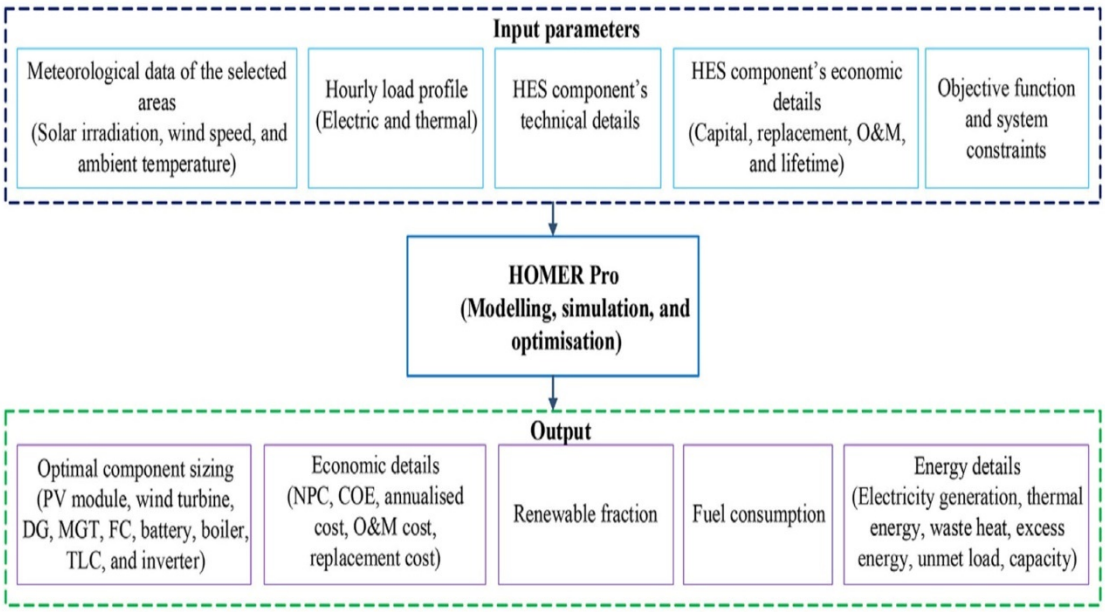

Figure 3. Flowchart of HOMER software performance [38]

By entering the average monthly radiation data, HOMER software calculates the air clearness index through the following equation [21, 39]:

$$k_t = \frac{H_{ave}}{H_{o,ave}} \quad (1)$$

where H_{ave} and $H_{o,ave}$ are the radiation that reaches the surface of the earth and above the atmosphere, respectively.

The power produced by solar cells (P_{PV}) in HOMER software is calculated using the following equation [40]:

$$P_{PV} = Y_{PV}\, f_{PV}\, \frac{\overline{G_T}}{\overline{G_{T,STC}}} \quad (2)$$

where Y_{pv} is the output power of the solar cell under standard conditions (kW), f_{PV} is the derating factor, $\overline{G_T}$ is the solar radiation to the collector surface (kW/m^2), and $\overline{G_{T,STC}}$ is the value of G under standard conditions (1 kW/m^2).

The angle of the solar cells is equal to the latitude of the studied station [41].

The output power of a wind turbine in real conditions depends on its location or, in other words, altitude [42, 43]. In HOMER software, the output power of wind turbines is calculated using the following equation [44]:

$$P_{WTG} = \frac{\rho}{\rho_0}\, P_{WTG,STP} \quad (3)$$

where ρ is the density of air in real conditions, ρ_0 is the density of air in standard conditions, and $P_{WTG,\ STP}$ is the output power of the turbine, which is obtained from the diagram of the turbine power curve.

The efficiency of the fuel cell and gas boiler in the present work is calculated by the following equation [45]:

$$\eta_{gen} = \frac{3.6\, P_{gen}}{\dot{m}_{fuel}\, LHV_{fuel}} \quad (4)$$

where P_{gen} is the total annual electricity produced (kWh/y) and $\dot{m}_{fuel}$ is the total annual fuel consumption (kg/y) and LHV_{fuel} is the low heating value of the fuel (MJ/kg).

HOMER displays a list of classified systems based on the total NPC as the main output which is given by [46]:

$$NPC = \frac{C_{ann,total}}{CRF(i, R_{proj})} \quad (5)$$

where $C_{ann,total}$ is the total annual cost ($), CRF is the factor of capital recovery, i is the real interest rate, and R_{proj} is the lifetime of the project. The CRF that represents the capital return in N years is calculated by [47]:

$$CRF = \frac{i(1+i)^N}{(1+i)^N - 1} \quad (6)$$

$$i = \frac{\acute{i} - f}{1+f} \quad (7)$$

The COE in kWh during the project useful lifetime is also calculated as follows [48]:

$$COE = \frac{C_{ann,total}}{E_{Load\ Served}} \quad (8)$$

where $E_{Load\ Served}$ is the actual electrical charge by the hybrid systems in kWh/y that is priced in dollars.

4. REQUIRED DATA

To use the solar cell, information on the average monthly radiation intensity (Table 1), geographical location (30° 40° N, 48° 30' E), and time zone of the studied station (GMT+03:30) is required. Also, the average wind speed (Table 1) and altitude (6 m) are the information required for wind turbines. Table 3 lists other information required for the simulation, including equipment price, equipment lifetime information, the available number of each equipment, etc.

The data used are natural gas price 0.015 and 0.03 $/m^3, average monthly biomass available for the study station equal to 0.788 ton/day, average animal biomass price in Iran 18 $/ton, biomass carbon content 5 %, gasification ratio 0.7 %, biomass low heating value 5.5 MJ/kg, annual interest rates 20 % and 30 %, project useful lifetime 20 years, grid extension cost 7600.6 $/km, grid maintenance cost 160 $/y-km, average price of grid electricity 0.01392 $/kWh, carbon dioxide emission penalty 0 and 150 $/ton, the efficiency of gas boiler 85 %, the content of carbon monoxide

and unburned hydrocarbons in natural gas 4.4 g/m^3 and 0.87 g/m^3, respectively.

The required power and heat diagrams are shown in Figures 4 and 5, in which the average annual power and heat requirements are 5.92 kWh/day and 15.6 kWh/day, respectively.

Table 3. The system information

Equipment	Cost ($)			Size to consider	Other information	Schematic
	Capital	Replacement	O & M			
PV [49]	1000	1000	5	1-5	Lifetime: 25 years Derating factor: 90 %	
Biogas generator [20]	800	700	0.001	1	Lifetime: 15000 h Heat recovery ratio: 25 %	
Converter [50]	200	200	10	1-3	Lifetime: 10 years Efficiency: 90 %	
BWC XL.1 wind turbine [51]	5725	3650	100	1	Lifetime: 20 years Hub height: 25 m	
Fuel cell [52]	400	400	0.01	1	Lifetime: 50000 h Heat recovery ratio: 25 %	
Electrolyzer [52]	100	100	5	1-5	Lifetime: 25 years Efficiency: 85 %	
Hydrogen tank [49]	200	150	10	1-6	Lifetime: 25 years	
Battery T-105 [36]	174	174	5	1-10	Lifetime: 845 kWh Nominal specs: 6V, 225 Ah	

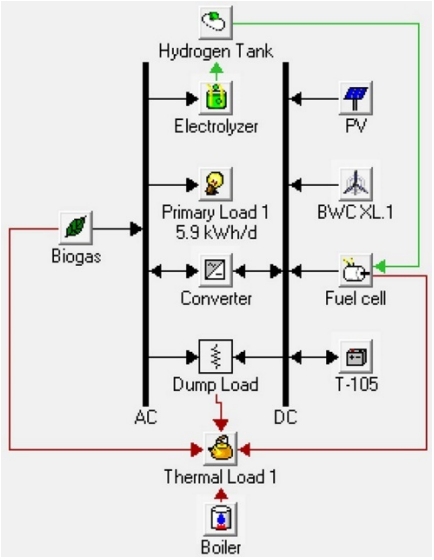

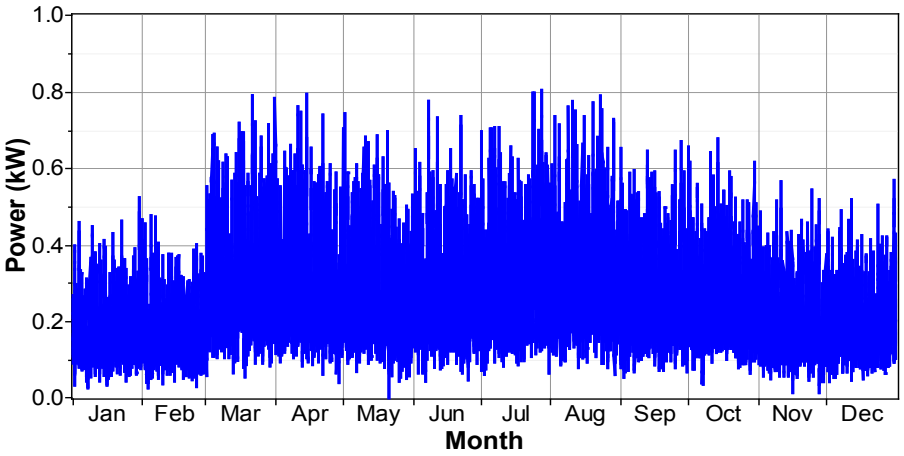

Figure 4. Daily electricity profile

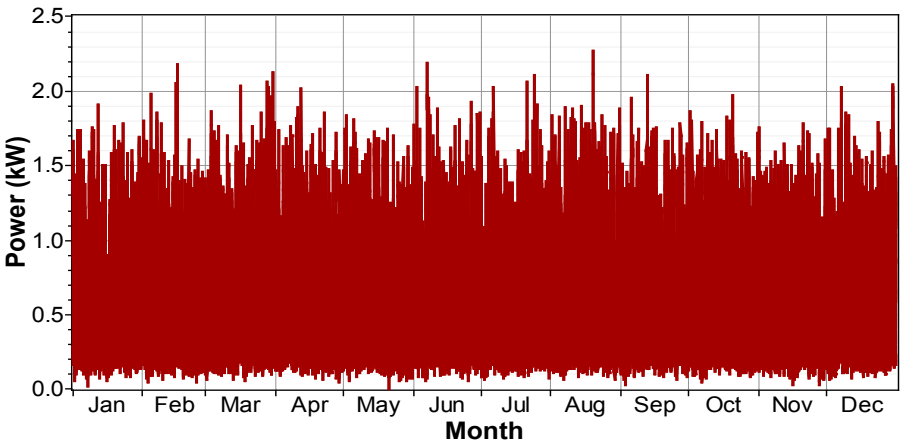

Figure 5. Daily thermal profile

5. RESULTS AND DISCUSSION

The results of the sensitivity analysis performed by the software for the system under consideration shown in Table 3, which includes an evaluation of 1419264 possible configurations, are given in Table 4.

From the results of Table 4, it can be seen that the optimal system under study includes 3 kW solar cells, 1 kW wind turbine, 1 kW biomass generator, 1 kW fuel cell, one battery, 2 kW electrolysis, and 2 kW electric converter. This system also includes a hydrogen storage tank. For the annual interest rates of 20 % and 30 %, 3 and 2 hydrogen storage tanks are used, respectively. The lowest total NPC with 12046 $ is for the second scenario, but the lowest COE with 1.160 $/kWh is for the seventh scenario. Due to the constant solar radiation and wind speed and the amount of biomass available, in all scenarios, 47 % of the required energy is provided by renewable energy. The minimum and maximum gas consumptions for gas boiler and required heat supply are 493 m^3 (second scenario) and 500 m^3 (third and seventh scenarios), respectively.

Table 4. Simulations results

Scenario	Natural gas price ($/m^3)	Interest rate (%)	CO_2 penalty ($/ton)	Optimal configuration	Electricity production (kWh/y)	Thermal production (kWh/y)
1	0.015	20	0	3 PV, 1 WT, 1 Biog.,1 FC, 2 Conv., 1 Batt., 2 Elec., 3 H_2 tank	PV: 5888 WT: 681 Biog.: 0 FC: 1307	Biog.:0 FC: 282 Boiler: 4169 Exc. Elec.: 1728
2	0.015	30	0	3 PV, 1 WT, 1 Biog.,1 FC, 2 Conv., 1 Batt., 2 Elec., 2 H_2 tank	PV: 5888 WT: 681 Biog.: 2 FC: 1303	Biog.:3 FC: 281 Boiler: 4142 Exc. Elec.: 1779
3	0.015	20	150	3 PV, 1 WT, 1 Biog.,1 FC, 2 Conv., 1 Batt., 2 Elec., 3 H_2 tank	PV: 5888 WT: 681 Biog.: 0 FC: 1339	Biog.:0 FC: 291 Boiler: 4199 Exc. Elec.: 1661
4	0.015	30	150	3 PV, 1 WT, 1 Biog.,1 FC, 2 Conv., 1 Batt., 2 Elec., 2 H_2 tank	PV: 5888 WT: 681 Biog.: 2 FC: 1336	Biog.:3 FC: 290 Boiler: 4170 Exc. Elec.: 1712
5	0.030	20	0	3 PV, 1 WT, 1 Biog.,1 FC, 2 Conv., 1 Batt., 2 Elec., 3 H_2 tank	PV: 5888 WT: 681 Biog.: 0 FC: 1308	Biog.:0 FC: 283 Boiler: 4171 Exc. Elec.: 1725
6	0.030	30	0	3 PV, 1 WT, 1 Biog.,1 FC, 2 Conv., 1 Batt., 2 Elec., 2 H_2 tank	PV: 5888 WT: 681 Biog.: 2 FC: 1305	Biog.:3 FC: 282 Boiler: 4143 Exc. Elec.: 1776
7	0.030	20	150	3 PV, 1 WT, 1 Biog.,1 FC, 2 Conv., 1 Batt., 2 Elec., 3 H_2 tank	PV: 5888 WT: 681 Biog.: 0 FC: 1340	Biog.:0 FC: 291 Boiler: 4199 Exc. Elec.: 1660
8	0.030	30	150	3 PV, 1 WT, 1 Biog.,1 FC, 2 Conv., 1 Batt., 2 Elec., 2 H_2 tank	PV: 5888 WT: 681 Biog.: 2 FC: 1337	Biog.:3 FC: 290 Boiler: 4170 Exc. Elec.: 1711

Table 4 (Continued)

Scenario	Total NPC ($)	COE ($/kWh)	Ren. fraction (%)	Nat. gas (m^3)	Biomass (t)	Excess electricity (kWh/y)	Excess thermal (kWh/y)	Breakeven grid extension distance (km)	LCOH ($/kg)	CO_2 emission (kh/y)
1	12507	1.184	47	497	0	1728	486	1.48	35.390	960
2	12046	1.667	47	493	3	1779	511	1.47	50.774	946
3	13223	1.161	47	500	0	1661	457	1.56	36.425	966
4	12554	1.657	47	497	3	1712	481	1.53	51.483	951
5	12544	1.183	47	497	0	1725	485	1.48	35.440	960
6	12100	1.679	47	494	3	1776	510	1.48	50.922	945
7	13260	1.160	47	500	0	1660	456	1.56	36.509	966
8	12579	1.655	47	497	3	1711	480	1.53	51.559	951

PV: Photovoltaic, WT: Wind turbine, Biog.: Biogas generator, FC: Fuel cell, Batt.: Battery, Elec.: Eletrolyzer, Exc. elec.: Excess electricity, Nat. gas: Natural gas, Ren. fraction: Renewable fraction

According to the results, another noteworthy point is that for every price of natural gas and every penalty for pollutants, the use of biomass generators is economically justified when the annual interest rate is 30 %. According to the results, solar cells with a production of 5888 kWh/y and wind turbine with a production of 681 kWh/y have a significant role in supplying the required electricity. Of course, after solar cells, the fuel cell is in the second place with the highest amount of electricity production. According to the results, the highest electricity generation by the fuel cell in the seventh scenario is 1340 kWh/y.

Given that dump load is used to convert excess electricity into heat in the present work, according to Table 3, the results show that much of the surplus electricity generated, which according to the results is completely cheaper than the heat generated by fossil fuels, with a value of 1779 kWh/y is in the second scenario.

According to the results, to provide the required heat in all the scenarios studied, the gas boiler had the largest share, followed by the excess electricity converted by the dump load and the fuel cell. It can also be seen that in all scenarios, some excess heat is generated that has no use, and if the system is connected to a district heating network, selling it can reduce costs slightly. The maximum excess heat with the amount of 511 kWh/y is in the second scenario, and the reason is that the dump load has generated more heat in this scenario.

To compare the standalone mode with the grid-connected mode, it can be seen that the minimum and maximum distances from the national power grid should be 1470 m and 1560 m, respectively, in order to use this system economically. Another important point is about the effect of interest rates on the cost per kg of hydrogen produced so that by increasing the interest rate from 20 % to 30 %, the cost per kilogram of hydrogen produced will be about $ 15 more. The lowest and highest costs per kilogram of hydrogen produced with amounts of 35.39 $ and 51.559 $ are for the first and eighth scenarios, respectively.

Due to the use of natural gas fuel in all scenarios, about 1 ton of CO_2 emissions are emitted each year in each scenario. Based on the results, as a general result, it can be said that with the increase of the annual interest rate, the price per kWh of energy increases, the consumption of natural gas decreases, the use of biomass increases, the emission of pollutants decreases, the price each kg of hydrogen produced increases sharply, and excess electricity increases. Also, according to the results, with the increase in the price of penalty for pollutants produced, the amount of COE decreases, the amount of natural gas consumption increases, biomass consumption remains unchanged, the amount of excess electricity decreases, pollutant emissions increase, and the price of each Kg of hydrogen produced also increases. In general, the effect of increasing interest rates is the opposite of the effect of increasing the penalty price of pollutants.

Given that the most economically appropriate system is the system that has the lowest total NPC value, the second scenario is selected as the most appropriate one. Figure 6 shows the monthly average electricity production for Scenario 2. It is observed that much of the electricity (about 75 %) is generated by solar cells; in May to October, the share of solar cells is higher than that in other months. This indicates a very high radiation potential of the study station. The fuel cell is also the second-largest producer of electricity, supplying 17 % of the electricity generated, mainly in the months of March and October to December. Wind energy is the third-largest producer of electricity, supplying about 9 % of the electricity generated, with the share of wind energy in June and July being more significant. The biomass generator also plays a negiligible role in the electricity generated in January.

Figure 7 shows the average monthly heat generation for the second scenario. It can be seen that gas boilers with the production of about 67 % of the thermal need, especially in the cold months of the year (October to April), have the largest share in the required heat production. The important point is the large share of surplus electricity in heat production, which is about 29 % and is more significant in the months of May to September. According to the results of Figure 7, the share of fuel cells in heat production in all months of the year is almost constant and is about 5 %. Also, the share of biomass generators in heat production is very low and is in January.

6. LIMITATIONS

As the number of sensitivity analysis modes or parameters involved in sensitivity analysis increases, the computation time increases exponentially, requiring very powerful computers. Also, due to the use of 20-year average data instead of one-year data, the results may be slightly different from the actual situation. Also, the cheap electricity of the national grid and fossil fuels and the absence of penalties for pollutants in Iran make the scenarios under study uneconomical in the current situation.

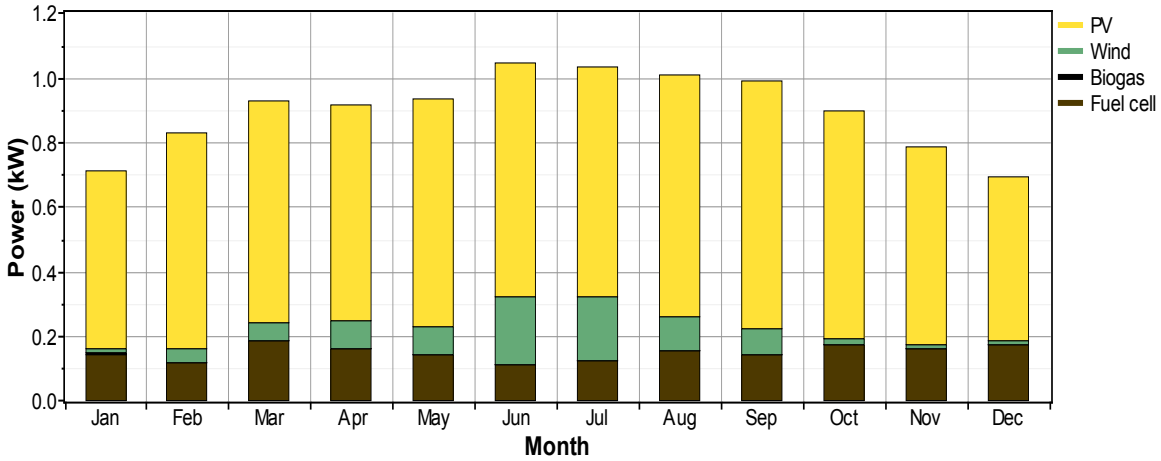

Figure 6. Monthly average electricity production

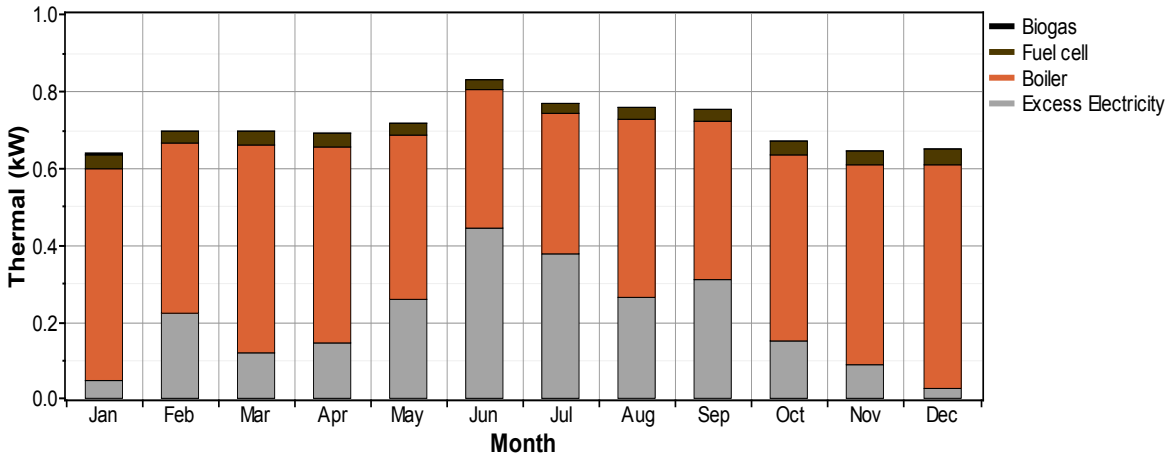

Figure 7. Monthly average thermal production

7. CONCLUSIONS

Despite the many advantages of CHP power plants, compared to other power and heat generation systems separately, including higher efficiency, reliability, stability and financial savings, environment, etc., these power plants have received slight attention in Iran. Therefore, in the present work, a CHP system on a residential scale including wind-solar-biomass-fuel cell-gas boiler-dump load components was investigated using HOMER software. Heat recovery was also performed in biomass generators and fuel cells. To look into the effect of variable parameters on the results, sensitivity analyses were performed on natural gas prices, annual interest rates, and emission penalties. Novelties and benefits of the present work included use of up-to-date prices for equipment used, annual interest rate and fossil fuel prices, use of heat recovery in the fuel cell and biogas generator, sensitivity analysis on the effective parameters, as well as investigating the role of dump load in the required heat supply. The important results of the present work are:

- The lowest COE price in the studied scenarios is 1.160 $/kWh.
- The supply of energy required by renewable energy is equal to 47 %.
- The use of biomass for an interest rate of 20 % is not economically justified.
- Much electricity is generated by solar cells, fuel cells, and wind turbines, in order.
- The highest heat produced by gas boiler, dump load, and fuel cell, in order.
- The minimum distance from the national electricity grid in order to be economical to use the standalone system is 1.47 km.
- The lowest cost per kilogram of hydrogen produced is 35.390 $/kg.
- The maximum annual surplus electricity production is equal to 1779 kWh.
- The maximum annual surplus heat production is equal to 511 kWh.
- About 1 ton of CO_2 emissions are emitted each year in each scenario.

To continue the present work, the following suggestions are provided along with the reason for reviewing them.

- For stations with different climates, the studied hybrid system should be implemented so that the effect of climate on system performance can be seen more clearly.
- Given that, the use of biomass is not economical in the current situation (20 % annual interest rate), other technologies for the use of biomass should be evaluated.
- Due to the surplus electricity generated, the system should also be evaluated when connected to the grid to see the effect of electricity exchange with the grid on the price of each kWh of electricity generated.
- The scale of the present work is domestic. The current renewable hybrid system can be used on a commercial or industrial scale to further determine the impact of such parameters as "dump load" and "heat recovery ratio".
- It is recommended to use other methods of hydrogen production, for example, using a reformer, because the price of hydrogen produced in the present work is very high.

8. ACKNOWLEDGEMENT

The authors would like to thank all the organizations that provided data for this work.

NOMENCLATURE

i	Annual interest rate (%)
f	Annual inflation rate (%)
i'	Nominal interest rate (%)
CRF	Capacity Recovery Factor
R_{proj}	Lifetime of project (year)
k_t	Clearness index
$H_{o,ave}$	Radiation on the horizontal surface above the atmosphere (kWh/m^2-day)
Y_{PV}	Output power of solar cell under standard conditions (kW)
f_{PV}	Derating factor (%)
$\overline{G_T}$	Incident radiation on the cell's surface on a monthly basis (kW/m^2)
H_{ave}	Monthly average radiation that reaches the surface of the earth (kWh/m^2-day)
$\overline{G_{T,STC}}$	Incident radiation on the cell's surface under standard conditions (1 kW/m^2)
P_{PV}	Output power of PV cells (kW)
$C_{ann,total}$	Total annual cost ($)
$E_{load\ served}$	Real electrical load by system (kWh/yr)
P_{gen}	Electricity produced by diesel generators (kW)
$\dot{m}_{fuel}$	Fuel consumption of generator (units/hr)
P_{WTG}	Power output of wind turbine (kW)
$P_{WTG,\ STP}$	Power output of wind turbine at standard pressure and temperature (kW)
y	Year
GMT	Greenwich Mean Time
O & M	Operations and Maintenance ($)
N	Useful life-time (year)
CHP	Combined Heat and Power
LCOH	Levelized Cost of Hydrogen ($/kg)
NPC	Net Present Cost ($)

COE	Levelized Cost of Energy ($/kWh)
LHV_{fuel}	Lower Heating Value of the fuel (MJ/kg)
Greek letters	
ρ_0	Air density at standard pressure and temperature equal to 1.225 kg/m^3
ρ	Actual air density (kg/m^3)
η_{gen}	Electrical efficiency of generator (%)

REFERENCES

1. Alidadi Shamsabadi, A., Jahangiri, M., Koohi Faegh, A. and Raeisi Dehkordi, A., "Biogas production in a dairy cow unit to provide a sustainable solution for reducing the environmental pollutions and pathogens", ***Proceedings of 11th International Energy Conference (IEC 2016)***, Tehran, Iran, (2016). (https://www.academia.edu/37642439/Biogas_production_in_a_dairy_cow_unit_to_provide_a_sustainable_solution_for_reducing_the_environmental_pollutions_and_pathogens).
2. Zaniani, J.R., Ghahfarokhi, S.T., Jahangiri, M. and Shamsabadi, A.A., "Design and optimization of heating, cooling and lightening systems for a residential villa at Saman city, Iran", ***Journal of Engineering, Design and Technology***, Vol. 17, (2019), 41-52. (https://doi.org/10.1108/JEDT-01-2018-0003).
3. Alamdari, P., Nematollahi, O. and Jahangiri, M., "Feasibility study of wind energy for generate electricity in Province of Sistan and Baluchistan, case study: Nosrat Abad", ***Proceedings of 3rd International Scientific Conference of Iranian Students in Belarus-Minsk***, (2012). (https://www.researchgate.net/publication/321623925_Feasibility_study_of_wind_energy_for_generate_electricity_in_Province_of_Sistan_and_Baluchistan_case_study_Nosrat_Abad).
4. Sorgulu, F. and Dincer, I., "Development and assessment of a biomass-based cogeneration system with desalination", ***Applied Thermal Engineering***, Vol. 185, (2021), 116432. (https://doi.org/10.1016/j.applthermaleng.2020.116432).
5. Fakhari, I., Behzadi, A., Gholamian, E., Ahmadi, P. and Arabkoohsar, A., "Comparative double and integer optimization of low-grade heat recovery from PEM fuel cells employing an organic Rankine cycle with zeotropic mixtures", ***Energy Conversion and Management***, Vol. 228, (2021), 13695. (https://doi.org/10.1016/j.enconman.2020.113695).
6. Ahmadi, A., Jamali, D.H., Ehyaei, M.A. and Assad, M.E.H., "Energy, exergy, economic and exergoenvironmental analyses of gas and air bottoming cycles for production of electricity and hydrogen with gas reformer", ***Journal of Cleaner Production***, Vol. 259, (2020), 120915. (https://doi.org/10.1016/j.jclepro.2020.120915).
7. Abu-Rayash, A. and Dincer, I., "A sustainable trigeneration system for residential applications", ***Journal of Energy Resources Technology***, Vol. 143, (2021), 012101. (https://doi.org/10.1115/1.4047599).
8. Shaygan, M., Ehyaei, M.A., Ahmadi, A., Assad, M.E.H. and Silveira, J.L., "Energy, exergy, advanced exergy and economic analyses of hybrid polymer electrolyte membrane (PEM) fuel cell and photovoltaic cells to produce hydrogen and electricity", ***Journal of Cleaner Production***, Vol. 234, (2019), 1082-1093. (https://doi.org/10.1016/j.jclepro.2019.06.298).
9. Ehyaei, M.A., Ahmadi, A., Assad, M.E.H. and Rosen, M.A., "Investigation of an integrated system combining an organic rankine cycle and absorption chiller driven by geothermal energy: Energy, exergy, and economic analyses and optimization", ***Journal of Cleaner Production***, Vol. 258, (2020), 120780. (https://doi.org/10.1016/j.jclepro.2020.120780).
10. Pahlavan, S., Jahangiri, M., Shamsabadi, A.A. and Baharizadeh, A., "Assessing the current status of renewable energies and their limitations in Iran", ***International Journal of Renewable Energy Development***, Vol. 9, (2020), 97-105. (https://doi.org/10.14710/ijred.9.1.97-105).
11. Rosen, M.A., Le, M.N. and Dincer, I., "Efficiency analysis of a cogeneration and district energy system", ***Applied Thermal Engineering***, Vol. 25, (2005), 147-159. (https://doi.org/10.1016/j.applthermaleng.2004.05.008).
12. Boudellal, M., "Cogénération et micro-cogénération-2e éd.: Solutions pour améliorer l'efficacité énergétique", ***Dunod***, (2013). (https://www.dunod.com/sciences-techniques/cogeneration-et-micro-cogeneration-solutions-pour-ameliorer-efficacite).
13. Combined heat and power (cogeneration)–making the most of energy, Green City Times, (2020). (https://www.greencitytimes.com/combined-heat-and-power), (Accessed: 04 Dec. 2020).
14. Mostafaeipour, A., Rezaei, M., Jahangiri, M. and Qolipour, M., "Feasibility analysis of a new tree-shaped wind turbine for urban application: A case study", ***Energy & Environment***, Vol. 31, (2020), 1230-1256. (https://doi.org/10.1177%2F0958305X19888878).
15. World Bank Statistics, Electric power transmission and distribution losses | World Bank Data, (2020). (https://data.worldbank.org/indicator/EG.ELC.LOSS.ZS?locations=IR), (Accessed: 04 Dec. 2020).
16. TAVANIR Publication, Statistics of Iran power generation, In: Iran power generation and transmission company statistics, Tavanir, (2008). (http://www.satba.gov.ir/suna_content/media/image/2017/02/5196_orig.pdf?t=636219021775330000).
17. Fakhari, I., Behzadi, A., Gholamian, E., Ahmadi, P. and Arabkoohsar, A., "Design and tri-objective optimization of a hybrid efficient energy system for tri-generation, based on PEM fuel cell and MED using syngas as a fuel", ***Journal of Cleaner Production***, Vol. 290, (2021), 125205. (https://doi.org/10.1016/j.jclepro.2020.125205).
18. Waqar, A., Shahbaz Tanveer, M., Ahmad, J., Aamir, M., Yaqoob, M. and Anwar, F., "Multi-objective analysis of a CHP plant integrated microgrid in Pakistan", ***Energies***, Vol. 10, (2017), 1625. (https://doi.org/10.3390/en10101625).
19. Yuan, J., Xu, J., Wang, Y. and Sutrisna, M., "Techno-economic study of a distributed hybrid renewable energy system supplying electrical power and heat for a rural house in China", ***Proceedings of International Conference on Renewable Energy and Environment (ICREE 2017)***, Toronto, Canada, (2018). (https://doi.org/10.1088/1755-1315/127/1/012001).
20. Jahangiri, M., Rizi, R.A. and Shamsabadi, A.A., "Feasibility study on simultaneous generation of electricity and heat using renewable energies in Zarrin Shahr, Iran", ***Sustainable Cities and Society***, Vol. 38, (2018), 647-661. (https://doi.org/10.1016/j.scs.2018.01.043).
21. Pahlavan, S., Jahangiri, M., Alidadi Shamsabadi, A. and Rahimi Ariae, A., "Assessment of PV-based CHP system: The effect of heat recovery factor and fuel type", ***Journal of Energy Management and Technology***, Vol. 3, (2019), 40-47. (https://doi.org/10.22109/jemt.2018.137207.1106).
22. Khormali, S. and Niknam, E., "Operation cost minimization of domestic microgrid under the time of use pricing using HOMER", ***Proceedings of 20th International Scientific Conference on Electric Power Engineering (EPE)***, (2019), 1-6. (https://doi.org/10.1109/EPE.2019.8778109).
23. Kalamaras, E., Belekoukia, M., Lin, Z., Xu, B., Wang, H. and Xuan, J., "Techno-economic assessment of a hybrid off-grid DC system for combined heat and power generation in remote islands", ***Energy Procedia***, Vol. 158, (2019), 6315-6320. (https://doi.org/10.1016/j.egypro.2019.01.406).
24. Gbadamosi, S.L. and Nwulu, N.I., "Optimal power dispatch and reliability analysis of hybrid CHP-PV-wind systems in farming applications", ***Sustainability***, Vol. 12, (2020), 8199. (http://doi.org/10.3390/su12198199).
25. Masrur, H., Khan, K.R., Abumelha, W. and Senjyu, T., "Efficient energy delivery system of the CHP-PV based microgrids with the economic feasibility study", ***International Journal of Emerging Electric Power Systems***, Vol. 21, (2020), 20190144. (https://doi.org/10.1515/ijeeps-2019-0144).
26. Pelaez-Pelaez, S., Colmenar-Santos, A., Pérez-Molina, C., Rosales, A.E. and Rosales-Asensio, E., "Techno-economic analysis of a heat and power combination system based on hybrid photovoltaic-fuel cell systems using hydrogen as an energy vector", ***Energy***, Vol. 224, (2021), 120110. (https://doi.org/10.1016/j.energy.2021.120110).
27. Elkadeem, M.R., Kotb, K.M., Elmaadawy, K., Ullah, Z., Elmolla, E., Liu, B., Wang, S., Dan, A. and Sharshir, S.W., "Feasibility analysis and optimization of an energy-water-heat nexus supplied by an autonomous hybrid renewable power generation system: An empirical study on airport facilities", ***Desalination***, Vol. 504, (2021), 114952. (https://doi.org/10.1016/j.desal.2021.114952).
28. Nematollahi, O., Alamdari, P., Jahangiri, M., Sedaghat, A. and Alemrajabi, A.A., "A techno-economical assessment of solar/wind resources and hydrogen production: A case study with GIS maps", ***Energy***, Vol. 175, (2019), 914-930. (https://doi.org/10.1016/j.energy.2019.03.125).
29. Jahangiri, M., Haghani, A., Heidarian, S., Alidadi Shamsabadi, A. and Pomares, L.M., "Electrification of a tourist village using hybrid renewable energy systems, Sarakhiyeh in Iran", ***Journal of Solar***

Energy Research, Vol. 3, (2018), 201-211. (https://journals.ut.ac.ir/article_68643.html).

30. Shamsabadi, A.A., Jahangiri, M., Bardei, F.K. and Raeisi, H.A., "Investigation of sensitivity analysis in the generation of renewable electricity for a hybrid system in Iran", ***Proceedings of 12th International Energy Conference (IEC 2018)***, Tehran, Iran, (2018). (https://en.civilica.com/doc/848589).
31. Jahangiri, M., Soulouknga, M.H., Bardei, F.K., Shamsabadi, A.A., Akinlabi, E.T., Sichilalu, S.M. and Mostafaeipour, A., "Techno-econo-environmental optimal operation of grid-wind-solar electricity generation with hydrogen storage system for domestic scale, case study in Chad", ***International Journal of Hydrogen Energy***, Vol. 44, (2019), 28613-28628. (https://doi.org/10.1016/j.ijhydene.2019.09.130).
32. Pahlavan, S., Jahangiri, M., Alidadi Shamsabadi, A. and Khechekhouche, A., "Feasibility study of solar water heaters in Algeria, a review", ***Journal of Solar Energy Research***, Vol. 3, (2018), 135-146. (https://jser.ut.ac.ir/article_67424.html).
33. Jahangiri, M., Shamsabadi, A.A., Mostafaeipour, A., Rezaei, M., Yousefi, Y. and Pomares, L.M., "Using fuzzy MCDM technique to find the best location in Qatar for exploiting wind and solar energy to generate hydrogen and electricity", ***International Journal of Hydrogen Energy***, Vol. 45, (2020), 13862-13875. (https://doi.org/10.1016/j.ijhydene.2020.03.101).
34. Jahangiri, M., Haghani, A., Mostafaeipour, A., Khosravi, A. and Raeisi, H.A., "Assessment of solar-wind power plants in Afghanistan: A review", ***Renewable and Sustainable Energy Reviews***, Vol. 99, (2019), 169-190. (https://doi.org/10.1016/j.rser.2018.10.003).
35. Jahangiri, M., Khosravi, A., Raiesi, H.A. and Mostafaeipour, A., "Analysis of standalone PV-based hybrid systems for power generation in Rural area", ***Proceedings of International Conference on Fundamental Research in Electrical Engineering***, Tehran, Iran, (2017). (https://en.civilica.com/doc/672922/).
36. Jahangiri, M., Haghani, A., Heidarian, S., Mostafaeipour, A., Raiesi, H.A. and Shamsabadi, A.A., "Sensitivity analysis of using solar cells in regional electricity power supply of off-grid power systems in Iran", ***Journal of Engineering, Design and Technology***, Vol. 18, (2020), 1849-1866. (https://doi.org/10.1108/JEDT-10-2019-0268).
37. Okedu, K.E. and Uhunmwangho, R., "Optimization of renewable energy efficiency using HOMER", ***International Journal of Renewable Energy Research (IJRER)***, Vol. 4, (2014), 421-427. (https://www.ijrer.org/ijrer/index.php/ijrer/article/view/1231).
38. Das, B.K., Tushar, M.S.H. and Zaman, F., "Techno-economic feasibility and size optimisation of an off-grid hybrid system for supplying electricity and thermal loads", ***Energy***, Vol. 215, (2021), 119141. (https://doi.org/10.1016/j.energy.2020.119141).
39. Ebrahimi, S., Jahangiri, M., Raiesi, H.A. and Ariae, A.R., "Optimal planning of on-grid hybrid microgrid for remote island using HOMER software, Kish in Iran", ***International Journal of Energetica***, Vol. 3, (2018), 13-21. (https://doi.org/10.47238/ijeca.v3i2.77).
40. Moein, M., Pahlavan, S., Jahangiri, M. and Alidadi Shamsabadi, A., "Finding the minimum distance from the national electricity grid for the cost-effective use of diesel generator-based hybrid renewable systems in Iran", ***Journal of Renewable Energy and Environment (JREE)***, Vol. 5, (2018), 8-22. (https://doi.org/10.30501/jree.2018.88377).
41. Jahangiri, M., Alidadi Shamsabadi, A. and Saghaei, H., "Comprehensive evaluation of using solar water heater on a household scale in Canada", ***Journal of Renewable Energy and Environment (JREE)***, Vol. 5, (2018), 35-42. (https://doi.org/10.30501/jree.2018.88491).
42. Alamdari, P., Nematollahi, O., Jahangiri, M. and Hajji Malayeri, A., "Feasibility study of wind energy potential in Alborz province for generate electricity, a case study: Eshtehard", ***Proceedings of 1st Specialty Conference of the Wind and Sun,*** Tehran, Iran, (2012). (https://en.civilica.com/doc/136593/).
43. Sedaghat, A., Mostafaeipour, A., Rezaei, M., Jahangiri, M. and Mehrabi, A., "A new semi-empirical wind turbine capacity factor for maximizing annual electricity and hydrogen production", ***International Journal of Hydrogen Energy***, Vol. 45, (2020), 15888-15903. (https://doi.org/10.1016/j.ijhydene.2020.04.028).
44. Jahangiri, M., Hajji Malayeri, A., Sedaghat, A. and Aghaei, E., "Investigating wind potential for clean energy production in Khorasan Razavi Province, case study: Jangal station", ***Proceedings of 1st Specialty Conference of the Wind and Sun***, Tehran, Iran, (2012). (https://en.civilica.com/doc/136596/).
45. Ariae, A.R., Jahangiri, M., Fakhr, M.H. and Shamsabadi, A.A., "Simulation of biogas utilization effect on the economic efficiency and greenhouse gas emission: A case study in Isfahan, Iran", ***International Journal of Renewable Energy Development***, Vol. 8, (2019), 149-160. (https://doi.org/10.14710/ijred.8.2.149-160).
46. Mostafaeipour, A., Jahangiri, M., Haghani, A., Dehshiri, S.J.H., Dehshiri, S.S.H., Sedaghat, A., Saghaei, H., Akinlabi, E.T., Sichilalu, S.M., Chowdhury, M.S. and Techato, K., "Statistical evaluation of using the new generation of wind turbines in South Africa", ***Energy Reports***, Vol. 6, (2020), 2816-2827. (https://doi.org/10.1016/j.egyr.2020.09.035).
47. Jahangiri, M., Shamsabadi, A.A., Riahi, R., Raeiszadeh, F. and Dehkordi, P.F., "Levelized cost of electricity for wind-solar power systems in Japan, a review", ***Journal of Power Technologies***, Vol. 100, (2020), 188-210. (https://papers.itc.pw.edu.pl/index.php/JPT/article/view/1359).
48. Jahangiri, M., Shamsabadi, A.A., Nematollahi, O. and Mostafaeipour, A., "Enviro-economic investigation of a new generation of wind turbines", ***International Journal of Strategic Energy and Environmental Planning***, Vol. 2, (2020), 43-59. (https://www.researchgate.net/publication/341670932_Enviro-economic_Investigation_of_a_New_Generation_of_Wind_Turbines_International_Journal_of_Strategic_Energy_Environmental_Planning_2_3_pp_43-59).
49. Rezk, H., Alghassab, M. and Ziedan, H.A., "An optimal sizing of stand-alone hybrid PV-fuel cell-battery to desalinate seawater at Saudi NEOM city", ***Processes***, Vol. 8, (2020), 382. (https://doi.org/10.3390/pr8040382).
50. Ghaderian, A., Jahangiri, M. and Saghaei, H., "Emergency power supply for NICU of a hospital by solar-wind-based system, a step towards sustainable development", ***Journal of Solar Energy Research***, Vol. 5, (2020), 506-515. (https://doi.org/10.22059/jser.2020.306423.1166).
51. Jahangiri, M., Nematollahi, O., Haghani, A., Raiesi, H.A. and Alidadi Shamsabadi, A., "An optimization of energy cost of clean hybrid solar-wind power plants in Iran", ***International Journal of Green Energy***, Vol. 16, (2019), 1422-1435. (https://doi.org/10.1080/15435075.2019.1671415).
52. Ghenai, C. and Bettayeb, M., "Grid-tied solar PV/fuel cell hybrid power system for university building", ***Energy Procedia***, Vol. 159, (2019), 96-103. (https://doi.org/10.1016/j.egypro.2018.12.025).
53. Zaniani, J.R., Dehkordi, R.H., Bibak, A., Bayat, P. and Jahangiri, M., "Examining the possibility of using solar energy to provide warm water using RETScreen4 software (Case study: Nasr primary school of pirbalut)", ***Current World Environment***, Vol. 10, (2015), 835-841. (https://doi.org/10.12944/CWE.10.Special-Issue1.101).

Journal of Renewable Energy and Environment

Research Article

Journal Homepage: www.jree.ir

Effect of Technological Mismatch on Photovoltaic Array: Analysis of Relative Power Loss

Stephen Ndubuisi Nnamchi [a*], Onyinyechi Adanma Nnamchi [b], Kevin Nnanye Nwaigwe [c], Zaid Oluwadurotimi Jagun [d], Johnson Ugochukwu Ezenwankwo [a]

[a] *Department of Mechanical Engineering, School of Engineering and Applied Sciences, Kampala International University, P. O. Box: 20000 Ggaba, Kansanga, Kampala, Uganda.*
[b] *Department of Agricultural Engineering and Bio Resources, Michael Okpara University of Agriculture, Umudike, Umuahia, Nigeria.*
[c] *Department of Mechanical Engineering, Faculty of Engineering and Technology, University of Botswana, Gaborone, Botswana.*
[d] *Department of Computer Engineering, Olabisi Onabanjo University, Ibogun, Nigeria.*

PAPER INFO

Paper history:
Received 13 February 2021
Accepted in revised form 20 September 2021

Keywords:
Configuration (S, P, SP),
Photovoltaic,
Mismatched Array,
Relative Power Loss,
Computational Scheme

ABSTRACT

This study conducts a comparative evaluation of the performance of modules and the arrays under standard test conditions. An equivalent circuit model was developed alongside a computational scheme. The model input data were obtained from the manufacturer's specification datasheets. They were used to analyse the maximum Fill Factor (FF) and Relative Power Losses (RPL) for Parallel (P), Series (S) and Series-Parallel (SP) configurations. For matching modules, the RPL was insignificant, but for mismatched modules, the parallel configuration (P) and series-parallel (SP) yielded RPL of 1.3 %, while the series configuration (S) produced RPL of 2.6 %. Thus, short circuit defects associated with the P and SP configuration were well below the open circuit defects associated with the series configuration (S). These results clearly show that the large photovoltaic plant needs to be configured with multiple blocks or strings of SP configuration in order to suppress RPL. In addition, the designer and installers of large solar power plants should adopt modules with uniform electrical and thermal properties in the construction of large solar power plants. The trivial RPL associated with the matched modules should be taken into consideration, as well.

https://doi.org/10.30501/jree.2021.272915.1189

1. INTRODUCTION

A paradigm shift from brown to green energy aims to preserve our environment and provide a cost-effective and sustainable energy supply to meet the domestic and industrial energy demands of our society. This quest fosters extensive research on the optimization of energy generated from different renewable energy sources, irrespective of natural constraints and adversities which pose challenges to the exploitation of energy from renewable resources, particularly in solar energy resources [1, 2]. The simplest device employed in the conversion of solar energy into electricity (by helio-photovoltaic process) is commonly known as photovoltaic device. Photovoltaic device consists of cells in the decreasing order of efficiency: monocrystalline, polycrystalline and amorphous silicon and thin film cells [3, 4]. These cells are the building blocks of the modules, while aggregating the module forms an array.

The factors militating against the conversion of solar energy into domestic and industrial power could be attributed to asymmetry in manufacturing, degradation of module blossoming surface, manufacturing defects, broken cells, snow, dirt (or soil) on the anterior part of the modules, aging of the materials used in encapsulation of the cells, uneven radiation of the modules, tilt, orientation, stringing configuration, and shading of modules and arrays [5, 6]. These challenges are responsible for power losses within modules and arrays. Losses may be attributed to an imbalance in the output power of the modules relative to the sum of the output power of the individual cells making up the modules. This phenomenon is commonly known as a mismatch effect of photovoltaic devices. This phenomenon is due to some cells not generating the expected optimum output power in the arrays [7]. The presence of the aforementioned challenges for the photovoltaic device engenders multiple peak powers, which make the probability of the photovoltaic system operating at global peak power null in the absence of Maximum Power Point Tracking (MPPT) or power electronics devices. Although shading solar cells do not have a significant effect on parallel configurations, recent works on optimization of the output power have suggested that parallel system configuration with a fully installed DC-DC converter and micro-inverter on the individual modules boosted the voltage supply for the standalone and grid connected systems, respectively [4, 8]. In series configuration, the individual module has to be installed with MPPT or bypass diode in order to exploit enough power from the series configuration.

*Corresponding Author's Email: stephen.nnamchi@kiu.ac.ug (S.N. Nnamchi)
URL: https://www.jree.ir/article_137215.html

Please cite this article as: Nnamchi, S.N., Nnamchi, O.A., Nwaigwe, K.N., Jagun, Z.O. and Ezenwankwo, J.U., "Effect of technological mismatch on photovoltaic array: Analysis of relative power loss", ***Journal of Renewable Energy and Environment (JREE)***, Vol. 8, No. 4, (2021), 77-89. (https://doi.org/10.30501/jree.2021.272915.1189).

Otherwise, failure or defect of one of the cells could be catastrophic in the generation of power, leading to hotspot, which impairs the efficiency of the semi-conductor materials in the photovoltaic modules, causing the disappearance of the junction that drives the charge carriers round the circuit [9].

Reconfiguration of the photovoltaic system has been discovered to be an effective means of achieving significant power harvest from photovoltaic devices [10]. Techniques for reconfiguring photovoltaic system include Total-Cross-Tied (TCT) technique, Bridge-Linked (BL) approach, Honeycomb (HC) method, Ladder Interconnection (LAD) technique, and the Su Do Ku logical pattern [11]. Reconfiguring the photovoltaic system is aimed at increasing the output power from the photovoltaic modules arranged in series-parallel configuration. Notwithstanding, the cost of the auxiliary installation and increment in output power ranging from 4.1-10 % [12] ought to be balanced. However, increasing the components of most engineering systems tend to increase the capital cost of the system and subsequently decrease the efficiency of the system. Introducing more linking wires by the virtue of reconfiguring the photovoltaic device may cause a greater voltage drop in the wires, which could affect the output power negatively while sustaining the output current from being cut off or diminished. Thus, parallel configuration requires a thick wire to carry current to the converter within a limited distance not beyond 3.408 m, while the series connection requires a thin wire that has the capacity to carry generated current beyond a distance of over 34.08 m [13]. The demerits of low-output current and voltage discredits a purely series and parallel configuration in the absence of the current and voltage ancillaries, respectively. However, series-parallel configuration has the potential to boost the output power even in the phase of shadings [14].

Most of the findings on the best technique for the reconfiguring photovoltaic device were based on the simulated results in different Nominal Operating Conditions (NOC), Nominal Operating Cell Temperature (NOCT), or PVUSA Test Condition (PTC). This approach is challenged by unevenly distributed global irradiance. Moreover, some of the cells may be under the nominal operating condition. Thus, there is a salient need to consider standard test condition, STC, which is not susceptible to most of these problems enumerated above while carrying out the performance analysis of different modules and array configuration. Research works [15, 16] support that at STC, Air Mass (AM) of 1.5 gives the best distribution of the spectrum and invariably uniform distribution of irradiance on the modules and arrays. The STC data from the manufacturer's sheet are equivalent to the measured or experimental data. This power is the output of the cells making up a module. Besides, an ideal or conventional model describing the behavior of the photovoltaic device is not configurationally suitable for generating the current-voltage (I-V) curves and power-voltage (P-V) curves because the number of series and parallel modules is not incorporated in this model. Thus, a modified model that integrates the number of series and parallel modules has to be employed for the purpose of generating I-V and P-V characteristic curves, which truly unveils the performance characteristics of different modules and array configurations [17, 18]. It is generally asserted that series resistance increases the output voltage, while parallel resistance increases the output current of modules and arrays. In the same vein, series configuration increases the output voltage, whereas parallel configuration increases the output current [19].

The resulting effect of hybridizing both the series and parallel configurations deserves a general verification and proof, which is the main driver of the present work. Besides, the current work tends to show additional inherent mismatch (variation in electrical and thermal properties of the semiconductors) emanating from the erroneous configuration of an array with the modules of different number of cells (known as technological mismatch), which causes Relative Power Losses (RPL) above 3 % against the common mismatch [6], which is known to cause RPL between 0.53-3 % [20]. The RPL is based on the difference between the fill factor of cells and that of the module.

Thus, the present work is aimed at showing module or array configuration that is least susceptible to technological mismatch or most efficient configuration by considering the performance curves of the series, parallel and series-parallel configuration for the modules or array with a uniform (homogeneous) and non-uniform (heterogeneous) electrical and thermal characteristics.

2. THE EQUIVALENT CIRCUIT MODEL

The equivalent circuit model that depicts the helio-photovoltaic phenomenon is diagrammatically represented in Figures 1a-1c. In accordance with Kirchhoff's nodal law, the output current in the equivalent circuit model in non-standard test conditions is modeled as follows [21, 22]:

$$\begin{aligned} I = n_p I_{ph} - n_p I_D - n_p I_p \\ = n_p I_{ph} \\ - n_p I_0 \left(\exp\left(\frac{\frac{V}{n_s} + \frac{IR_s}{n_p}}{n_p A V_T} \right) - 1 \right) \\ - n_p \frac{\frac{V}{n_s} + \frac{IR_s}{n_p}}{R_p} \end{aligned} \quad \text{or} \quad (1)$$

$$\begin{aligned} I = n_p I_{ph} - n_p I_D - n_p I_p \\ = n_p I_{ph} \\ - n_p I_0 \left(\exp\left(\frac{\frac{n_p V}{n_s} + IR_s}{n_p A V_T} \right) - 1 \right) \\ - \frac{\frac{n_p V}{n_s} + IR_s}{R_p} \end{aligned}$$

However, the output current in the equivalent circuit in the standard test condition (0) is modeled as follows:

$$\begin{aligned} I = n_p I_{ph\_0} - n_p I_{D\_0} - n_p I_{p\_0} \\ = n_p I_{ph\_0} \\ - n_p I_{0\_0} \left(\exp\left(\frac{\frac{n_p V}{n_s} + IR_{s\_0}}{n_p A_0 V_T} \right) - 1 \right) \\ - \frac{\frac{n_p V}{n_s} + IR_{s\_0}}{R_{p\_0}} \end{aligned} \quad (2)$$

where A = ideality factor ($1 \leq A \leq 2$ [23, 24]), I = the output current (A), I_D = diode current (A), I_0 = diode reverse or saturation current (A), I_p = shunt current (A), I_{ph} = photon current (A), n_p = number of parallel modules (-), n_s = number

of series modules (-), R_p = shunt or parallel resistance (Ω), R_s = series resistance (Ω), V= the output voltage (V) and V_T = thermal voltage (V).

The model and nodal analysis of the Helio-photovoltaic circuit is made feasible by considering the three important standard conditions [25]: the short circuit, SC (in standard condition, 1), the maximum power point, mpp (in standard condition, 2), and open circuit, OC (3) in standard condition 1 ($I = I_{sc}$, $V = 0$), standard condition 2 ($I = I_{mpp}$, $V = V_{mpp}$), and standard condition 3 ($I = 0$, $V = V_{oc}$).

These standard conditions are imposed on Equation (2) to obtain the following three standard analytical equations:

For standard condition, 1 ($I = I_{sc}$, $V = 0$):

$$I_{sc} = n_p I_{ph\_0} - n_p I_{0\_0}\left(\exp\left(\frac{I_{sc}R_{s\_0}}{n_p A_0 V_T}\right) - 1\right) - \frac{I_{sc}R_{s\_0}}{R_{p\_0}} \quad (3)$$

For $R_{s\text{-}0} = 0$, Equation (3) becomes:

$$n_p I_{ph\_0} = I_{sc} \quad (4)$$

For standard condition, 2 ($I = I_{mpp}$, $V = V_{mpp}$):

$$I_{mpp} = n_p I_{ph\_0} - n_p I_{0\_0}\left(\exp\left(\frac{\frac{n_p V_{mpp}}{n_s} + I_{mpp}R_{s\_0}}{n_p A_0 V_T}\right) - 1\right) - \frac{\frac{n_p V_{mpp}}{n_s} + I_{mpp}R_{s\_0}}{R_{p\_0}} \quad (5)$$

For standard condition, 3 ($I = 0$, $V = V_{oc}$):

$$0 = n_p I_{ph\_0} - n_p I_{0\_0}\left(\exp\left(\frac{\frac{n_p V_{oc}}{n_s}}{n_p A_0 V_T}\right) - 1\right) - \frac{\frac{n_p V_{oc}}{n_s}}{R_{p\_0}} \quad (6)$$

, respectively.

Equation (3) can be re-written as follows:

$$n_p I_{ph\_0} = n_p I_{sc} + n_p \frac{I_{sc}R_{s\_0}}{R_{p\_0}} + n_p I_{0\_0}\left(\exp\left(\frac{I_{sc}R_{s\_0}}{n_p A_0 V_T}\right) - 1\right) = n_p \frac{R_{p\_0} + R_{s\_0}}{R_{p\_0}} I_{sc} + n_p I_{0\_0}\left(\exp\left(\frac{I_{sc}R_{s\_0}}{n_p A_0 V_T}\right) - 1\right) \quad (7)$$

Since $n_p \frac{R_{p\_0}+R_{s\_0}}{R_{p\_0}} I_{sc} \gg n_p I_{0\_0}\left(\exp\left(\frac{I_{sc}R_{s\_0}}{n_p A_0 V_T}\right) - 1\right)$, Equation (7) can be approximated as follows [26]:

$$n_p I_{ph\_0} \approx n_p \frac{R_{p\_0} + R_{s\_0}}{R_{p\_0}} I_{sc} \quad (8)$$

In an ideal case, $\frac{V_{oc}}{R_{p\_0}} \to 0$, and $I_{ph\_0} = I_{sc}$ according to Equation (4); thus, Equation (6) can be expressed as:

$$n_p I_{0\_0} = \frac{n_p I_{sc}}{\left(\exp\left(\frac{I_{sc}R_{s\_0}}{n_p A_0 V_T}\right) - 1\right)} \quad (9)$$

Rearranging Equation (5) gives an expression for the shunt or parallel resistance, R_{p_0}, in the equivalent circuit as follows:

$$R_{p\_0} = \frac{\frac{n_p V_{mpp}}{n_s} + I_{mpp}R_{s\_0}}{n_p I_{ph_0 - n_p I_{0\_0}}\left(\exp\left(\frac{\frac{n_p V_{mpp}}{n_s} + I_{mpp}R_{s\_0}}{n_p A_0 V_T}\right) - 1\right) - I_{mpp}} \quad (10)$$

However, the minimum and initial values of $R_{p\_0,min}$ are given as [22]:

$$R_{p\_min} = \frac{n_p}{n_s}\left(\frac{V_{mpp}}{I_{sc} - I_{mpp}} - \frac{V_{oc} - V_{mpp}}{I_{mpp}}\right) \quad (11)$$

The ancillary terms found in Equation (1 or 2) are defined as follows:

The thermal voltage, V_T (V), is defined as [21, 27]:

$$V_T = \frac{n_p K_B T}{q_c} \quad (12)$$

where K_B = Boltzmann constant (J/K), q_c= electron charge (C), T = nominal operating temperature (K).

The ideality factor in standard test condition, A_0 (-) can be expressed as [23, 24]:

$$A_0 = \frac{I_{mpp}V_{oc}}{I_{sc}V_{mpp}};\ 1 \le A_0 \le 2 \quad (13)$$

Similar to Equation (7 or 8), Equation 13 can be improved in terms of R_p and R_s for non-standard test conditions as:

$$A_0 = \frac{R_{p\_0} + R_{s\_0}}{R_{p\_0}} \frac{I_{mpp}V_{oc}}{I_{sc}V_{mpp}};\ 1 \le A_0 \le 2 \quad (14)$$

The series resistance in Equation (10) is defined as [22]:

$$R_{s\_0} = \frac{n_p}{n_s}\left(1 - \frac{I_{mpp}V_{mpp}}{I_{sc}V_{oc}}\right)\left(\frac{V_{oc}}{I_{sc}} - \frac{V_{mpp}}{I_{mpp}}\right) = \frac{n_p}{n_s}(1 - FF)\left(\frac{V_{oc}}{I_{sc}} - \frac{V_{mpp}}{I_{mpp}}\right) \quad (15)$$

where FF (-) is the fill-factor.

We determined the values of the following constants, I_{ph_0}, I_{0_0}, A_0, R_{p_0}, and R_{s_0} from Eqs. 7 or 8, 9, 14, 10, and 15, respectively. Then, the I-V and P-V characteristic data are generated by employing Newton-Raphson scheme as follows [27]:

$$I_m = I_{m-1} - \frac{f(I_{m-1})}{f'(I_{m-1})} \quad (16)$$

The function, $f(I_{m-1})$ is obtained from Equation (2) by fixing the values of the voltage, V:

$$f(I_{m-1}) = n_p I_{ph\_0} - n_p I_{0\_0}\left(\exp\left(\frac{\frac{n_p V}{n_s} + I_{m-1}R_{s\_0}}{n_p A_0 V_T}\right) - 1\right) - \frac{\frac{n_p V}{n_s} + I_{m-1}R_{s\_0}}{R_{p_{0\_0}}} - I_{m-1} = 0 \quad (17)$$

However, the derivative of $f(I_{m\text{-}1})$, $f'(I_{m\text{-}1})$ is obtained by differentiating Equation (17) while holding the voltage constant:

$$f'(I_{m-1}) = \frac{I_{0\_0}R_{s\_0}}{A_0 V_T}\exp\left(\frac{\frac{n_p V}{n_s} + I_{m-1}R_{s\_0}}{n_p A_0 V_T}\right) - \frac{R_{s\_0}}{R_{p_{0\_0}}} - 1 \quad (18)$$

where m is a subscript designating the iteration.

The relative power loss, RPL (%), per module is given in Equation (19) according to Ref. [20] as follows:

$$\mathrm{RPL} = \frac{\sum \mathrm{nP}_{\mathrm{measured,cells}} - \sum \mathrm{nP}_{\mathrm{computed,module}}}{\sum \mathrm{nP}_{\mathrm{measured,cells}}} \quad (19)$$

where n is the number of cells and P(W) is the power.

However, the present study defined RPL (%) as a function of Fill Factor (FF) in Equation (20):

$$\mathrm{RPL} = \frac{\mathrm{FF}_{\mathrm{measured,cells}} - \mathrm{FF}_{\mathrm{computed,cells}}}{\mathrm{FF}_{\mathrm{measured,cells}}} \quad (20)$$

where the fill factor of the measured and matched series or parallel configuration [20] is expressed in Equation (21) as follows:

$$\mathrm{FF}_{\mathrm{measured,cells}} = \frac{\sum_{j=1}^{n} I_{mpp,j} V_{mpp,j}}{\sum_{j=1}^{n} I_{sc,j} V_{oc,j}} \quad (21)$$

However, the fill factor of computed and mismatched series and parallel module [20] is expressed in Equation (22) as follows:

$$\mathrm{FF}_{\mathrm{computed,series\ module}} = \frac{P_{max,series}}{I_{sc,min} \sum_{j=1}^{n} V_{oc,j}}$$
$$\mathrm{FF}_{\mathrm{computed,parallel\ module}} = \frac{P_{max,paraallel}}{V_{oc,max} \sum_{j=1}^{n} I_{sc,j}} \quad (22)$$

3. METHOD

3.1. The conceptual model

Five different circuit configurations of modules and arrays were considered in the search for optimum output power: series configuration (Figure 1a), parallel configuration (Figure 1b), and equal series-parallel (S=P) configuration (Figure 1c).

3.2. Input data

The input constants and variables to the computational scheme in Section 2.4. are summarized in Table 1 in Standard Test Condition (STC). The numerical values were obtained from literatures [28-31].

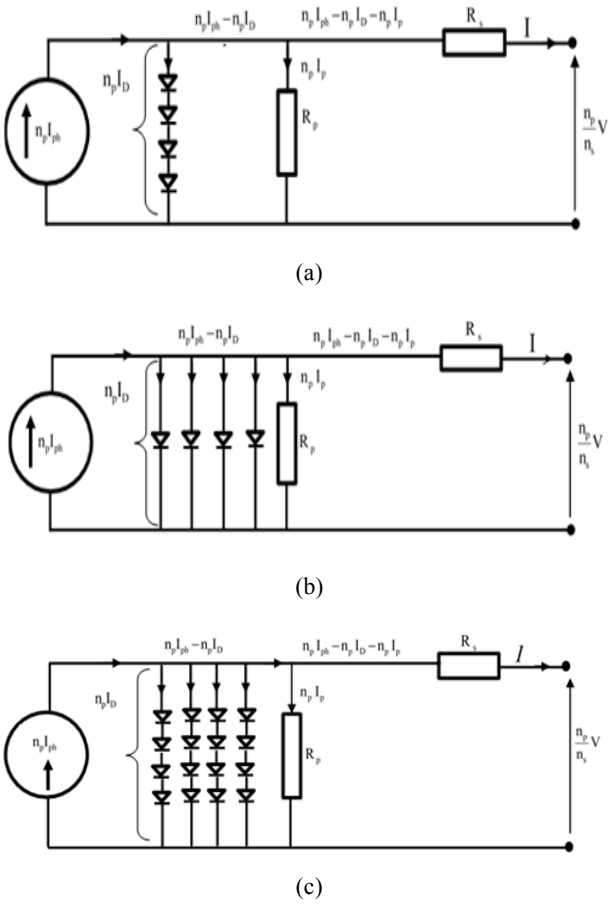

Figure 1. Equivalent circuit diagram of: (a) series configuration, (b) parallel configuration, (c) equal series-parallel configuration

Table 1. Data for different modules at AM=1.5 and G=1000 (W/m^2)

S#	Constant/variable	Sym.	Unit	Value			
1	Module type	-	-	MSX-60 [28]	SPSM-220D [29]	TW325P-72 [30]	ASP-400M [31]
2	Maximum output power	P_{max}	kW	0.060	0.220	0.325	0.400
3	Number of cells in series	n_s	-	36	60	72	96
4	Number of cells in parallel	n_p	-	1	1	1	1
5	Short circuit current in STC	I_{sc}	A	3.8	7.77	9.28	8.56
6	Open circuit voltage in STC	V_{oc}	V	21.1	36.24	45.60	60.00
7	Current at maximum power point	I_{mpp}	A	3.5	7.35	8.75	8.04
8	Voltage at maximum power point	V_{mpp}	V	17.1	29.94	37.10	49.08
9	Temperature coefficient of short circuit current	k_i	%/K	0.065	0.040	0.041	0.037
10	Temperature coefficient of open circuit voltage	k_v	%/mV	-80	-30	-31	-24
11	Temperature at STC	T_0	K	298.15	298.15	298.15	298.15
12	Irradiance at STC	G_0	W/m^2	1000	1000	1000	1000
13	Boltzmann constant	K_B	J/K	1.381×10^{-23}	1.381×10^{-23}	1.381×10^{-23}	1.381×10^{-23}
14	Electron charge	q_c	C	1.6×10^{-19}	1.6×10^{-19}	1.6×10^{-19}	1.6×10^{-19}
15	Energy gap for c-Si	E_g	eV	1.11	1.11	1.11	1.11
16	Ideality factor in STC	A_0	–	1.13994	1.14709	1.16155	1.13378
17	Parallel resistance in STC (min.)	$R_{p0,min}$	Ω	1.55159	1.17381	2.50609	0.98438
18	Series resistance at STC (min.)	R_{s0}	Ω	0.00470	0.00215	0.00218	0.00187

19	Diode saturation or reverse current	I_{0_0}	A	7.94727×10^{-09}	1.00385×10^{-08}	5.7959×10^{-09}	4.23354×10^{-09}
20	Photon or light current	I_{ph0}	A	3.81150	7.78424	9.30109	8.57628
21	Fill factor	FF	–	0.748	0.781	0.768	0.779

3.3. Computational scheme

The computational scheme in Figure 2 gives the logical flow and the strategic design of the analysis in order to address the key objectives of this work. At a glance, Figure 2 indicates three drops at the first summing point. Thus, three analytic routes are created for series, parallel, and series-parallel configurations, whereas the second summing point indicates the module or array type, which could be either a matched or mismatched configuration. The matched module or array consists of panels of homogeneous electrical and thermophysical properties, whereas the matched module or array consists of panels of heterogeneous electrical and thermophysical properties.

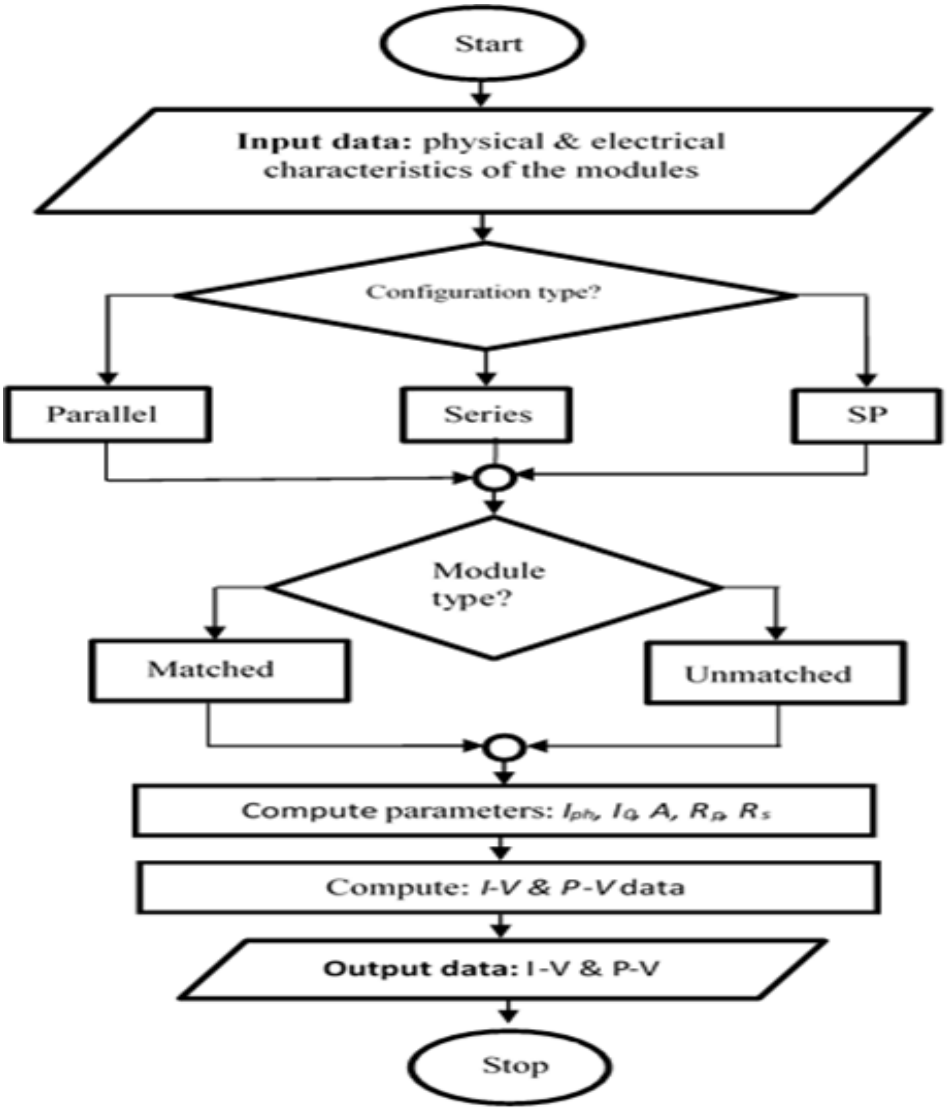

Figure 2. Flow chart for array configuration and computation of RPL

4. RESULTS AND DISCUSSION

4.1. Result presentation

Table 2 shows the estimated values $\{I_{ph}, I_0, A, R_p. R_s\}$ for the five-parameter model, which is capable of driving the simulated output power very close to the measured output power in the standard test condition with a negligible difference between the computed and measured output power. These sets of constants were substituted into Eqs. 16-18 to obtain the I-V and P-V curves for the four selected demonstration modules (MSX-60, SPSM-220D, TW325P-72, ASP-400M). The I-V and P-V curves for the demonstration modules are shown in Figure 3. Moreover, the measured output power rates in Table 1 (and simulated output power in Table 2) for the modules, MSX-60, SPSM-220D, TW325P-72, ASP-400M are 0.05985 (0.06003), 0.22006 (0.22045), 0.32463 (0.32659), 0.39460 (0.40137) kW were respectively in good agreement, which indicates that the equivalent circuit parameters were aptly determined. Thus, these results validate the authenticity of the proposed equivalent circuit models presented in Eqs. 1-18.

Table 2. The computed model parameters for the selected modules in standard test condition (25 °C, AM=1.5 and 1 kW/m²)

Parameter	Symbol	Unit	Computed value			
			MSX-60	SPSM-220D	TW325P-72	ASP-400M
Number of cells	n	-	36	60	72	96
Photon current	I_{ph}	A	3.81150	7.78424	9.30109	8.57628
Diode reverse or saturation current	I_0	A	7.94727×10^{-09}	1.00385×10^{-08}	5.7959×10^{-09}	4.23354×10^{-09}
Ideality factor	A	—	1.14339517	1.1491926	1.16418801	1.13593746
Shunt or parallel resistance	R_p	Ω	3.04991945	9.19608693	2.50609225	3.31810158
Series resistance	R_s	Ω	0.00479001	0.00214437	0.00218206	0.00188495
Maximum output power	P_{max}	kW	0.06003	0.22045	0.32659	0.40137

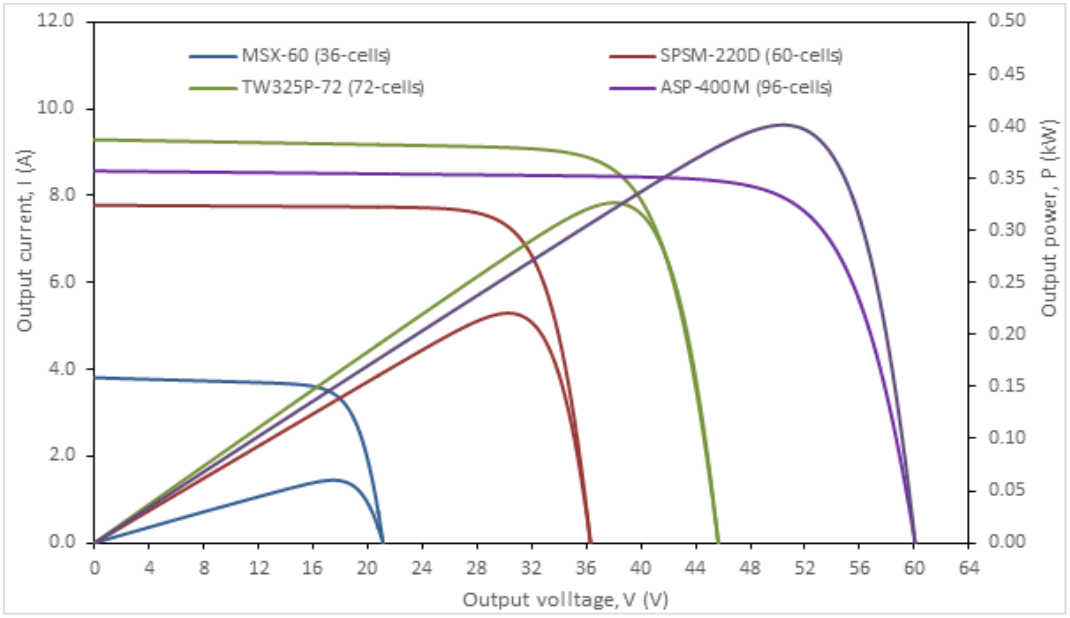

Figure 3. I-V and P-V curves for the individual demonstration modules

4.2. Discussion of results

For number of cells, n, ranging from 36 to 96, the maximum output power, which is the key performance yardstick, increased with increasing number of cells; however, for n > 96, the efficiency of the module decreased [14], which could be attributed to open circuit defect losses due to predominance of series configuration. Thus, modules with a high number of cells (n > 96) should not be used in setting up a PV plant as inevitable open circuit losses will favor mismatch losses in such modules. This is in agreement with the thermodynamic principle, which asserts that the efficiency of a system decreases as the number of components increases; thus, the modules with the number of cells above 96 cells were not included in the analysis in order the results clean and unflawed.

Figures 4 (a-d) and Figure 4e show the I-V and P-V curves for the four matched and mismatched modules in series configuration with the same and different electrical and thermal characteristics, respectively. The behavior of these curves is identical to those of weak and strong cells connected in series [20]. The weak cell dictates the magnitude of current, but the voltage cumulatively builds up. The module with the smallest number of cells (MSX-60) dominated the value of current, although the voltage tends to increase as the modules of the large number of cells were added [9]. From Figure 4e, the maximum output power of four mismatched modules (MSX-60 + SPSM-220D + TW325P-72 + ASP-400M) gave 0.4644 kW , but those of the four matched modules of MSX-60, SPSM-220D, TW325P-72, and ASP-400M gave maximum output power rates of 0.2406, 0.8825, 1.3065, and 1.6057 (kW), respectively. Apparently, the relative power loss was determined when comparing the power obtained from the matched to mismatched modules for the S configuration mentioned in the objective. The output power of the matched modules (MSX-60) was less than that of the mismatched modules, implying that the total number of cells in those matched modules was less than that of cells in the mismatched modules for modules (SPSM-220D, TW325P-72 and ASP-400M), and vice versa. Thus, once there are a commensurate number of cells (non-redundancy), the effect of power loss in matched and mismatched modules can be accurately determined. Thus, a common number of cells need to be observed before establishing the Real RPL (RRPL) which is the reason why the present work adopted the fill factor in computing RRPL.

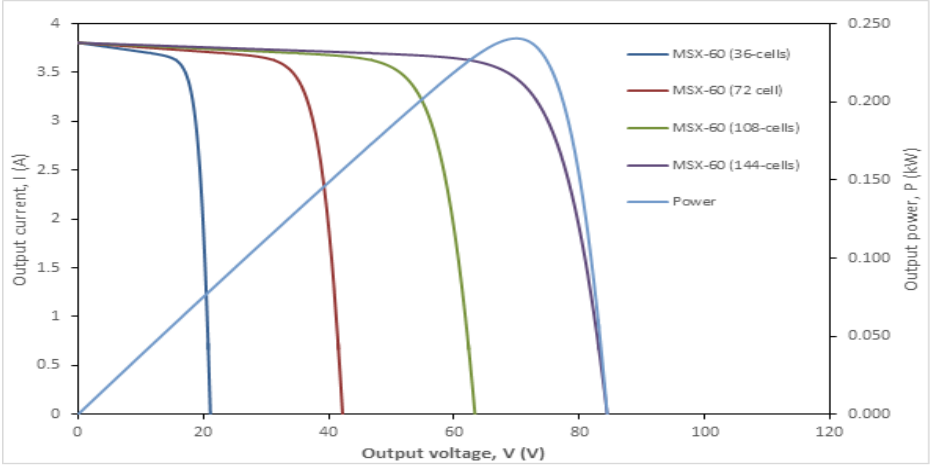
MSX-60 (36-cells)
MSX-60 (72 cell)
MSX-60 (108-cells)
MSX-60 (144-cells)
Power
Output current, I (A)
Output power, P (kW)
Output voltage, V (V)

(a)

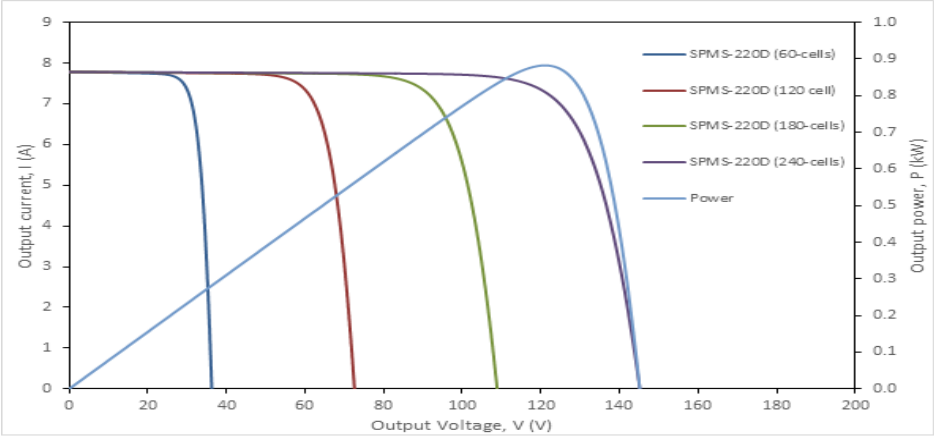
SPMS-220D (60-cells)
SPMS-220D (120 cell)
SPMS-220D (180-cells)
SPMS-220D (240-cells)
Power
Output current, I (A)
Output power, P (kW)
Output Voltage, V (V)

(b)

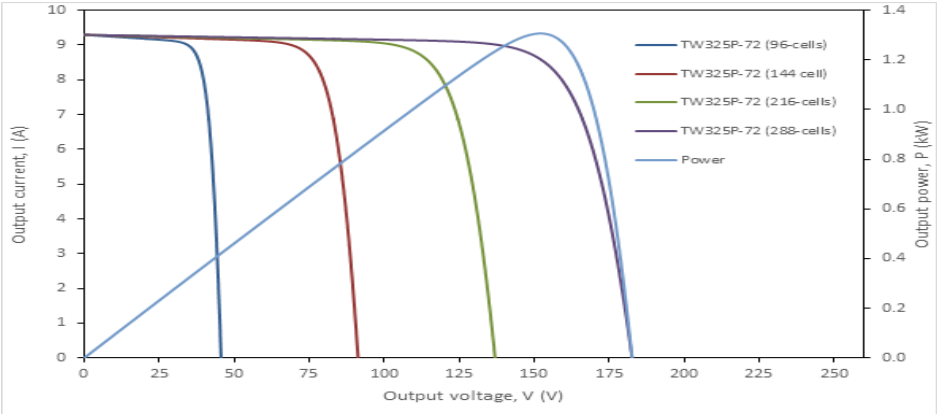
TW325P-72 (96-cells)
TW325P-72 (144 cell)
TW325P-72 (216-cells)
TW325P-72 (288-cells)
Power
Output current, I (A)
Output power, P (kW)
Output voltage, V (V)

(c)

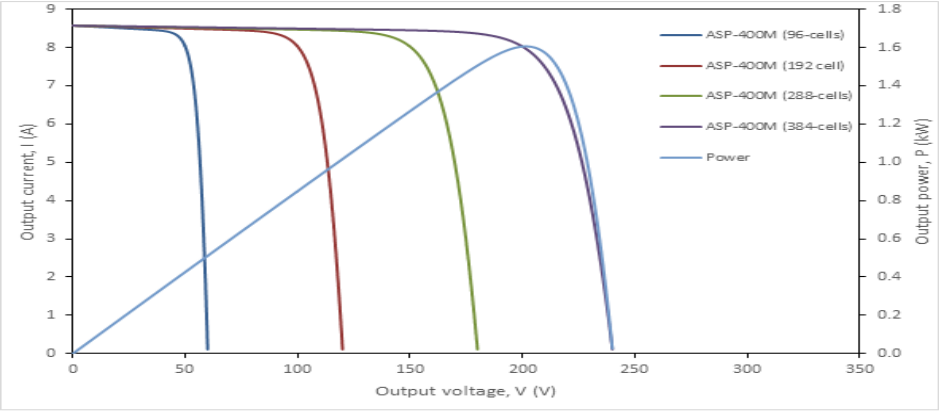
ASP-400M (96-cells)
ASP-400M (192 cell)
ASP-400M (288-cells)
ASP-400M (384-cells)
Power
Output current, I (A)
Output power, P (kW)
Output voltage, V (V)

(d)

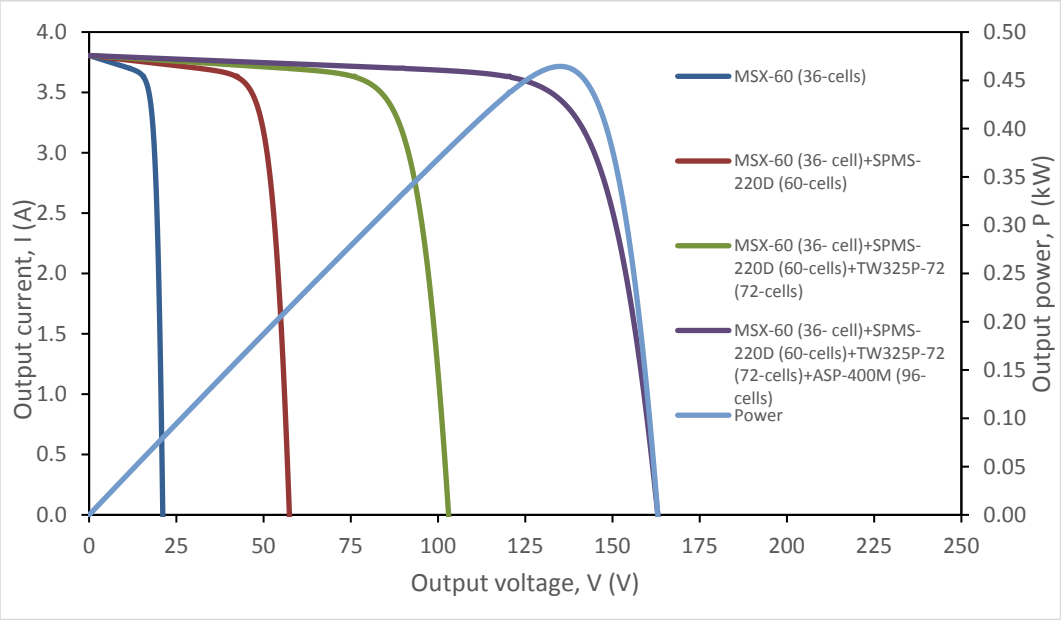

(e)

Figure 4. I-V and P-V curves for the matched: (a) MSX-60 series(S) configuration, (b) SPMS-220D series(S) configuration, (c) TW325P-72 series(S) configuration, (d) ASP-400M series(S) configuration and (e) I-V and P-V curves for the mismatched series(S) configuration

Quantitatively, the four matched modules of SPSM-220D, TW325P-72, and ASP-400M gave higher maximum output power than those of four mismatched modules (MSX-60 + SPSM-220D + TW325P-72 + ASP-400M) at excess values of 0.4181, 0.8421 and 1.1413 (kW), respectively. Apparently, there is no advantage to combining mismatched modules with different electrical and thermal characteristics in series configuration. It simply amounts to a substantial power loss in mismatched array and should be avoided by designers and installers of PV modules. Also, Table 3 supports that more RPL is associated with mismatched modules, whereas close to zero RPL is associated with the technologies of matched modules [20]. Moreover, power losses due to defects in the open circuit voltage are significant in mismatched modules. In order to avert the problem of RPL in the series configuration, the present work recommends the application of matched modules as a palliative measure.

Table 3. Relative power loss in series configuration

S#	Module	Characteristic	n_cell	Power, P (kW)	Measured Fill factor, $FF_{measured}$	Computed Fill factor, $FF_{computed}$	RPL (%)	Figure
1	MSX-60	Matched (4)	144	0.2406	0.75	0.75	0.0	4a
2	SPSM-220D	Matched (4)	240	0.8825	0.78	0.78	0.0	4b
3	TW325P-72	Matched (4)	288	1.3065	0.77	0.77	0.0	4c
4	ASP-400M	Matched (4)	384	1.6057	0.78	0.78	0.0	4d
5	All	Mismatched (4)	264	0.4644	0.77	0.75	2.6	4e

Figures 5 (a-d) and Figure 5e show the I-V and P-V curves for the four matched and mismatched modules in a parallel configuration, respectively. The former and latter modules have the same and different electrical and thermal characteristics, respectively. The behaviors of these curves are akin to those of weak and strong cell connection in parallel configuration. The stronger module dictates the magnitude of the voltage applied, but the current cumulatively builds up. Therefore, the module with the highest number of cells (ASP-400M) dominates the output voltage, although the output current tends to increase as the modules of the lower number of cells were added [19], whereas Figure 5e gives the maximum output power of the four mismatched modules (MSX-60 + SPSM-220D + TW325P-72 + ASP-400M) as 1.370 kW, but those of the four matched modules (MSX-60, SPSM-220D, TW325P-72 and ASP-400M) in Figures 5 (a-d) gave maximum output power of 0.24060, 0.88255, 1.3065 and 1.6057 kW, respectively.

However, having four mismatched modules of MSX-60, SPSM-220D, TW325P-72, and ASP-400M in parallel configuration gave much maximum output power (1.370 kW) compared to those of series configuration (0.4644 kW). Consequently, the RPL in parallel configuration was suppressed to 1.2 % in Table 5, since the maximum output of the mismatched parallel configuration is higher than that of the series counterpart in Table 4, but the RPL was enhanced to 2.6 %. This phenomenon simply buttresses the fact that the parallel configuration remains more resistant to short circuit defects. However, the influence of short circuit defects becomes significant, and this could be suppressed by introducing power electronics device (the MPPT tracker) or DC-DC or micro-inverter to minimize RPL in parallel configuration [19]. Therefore, parallel configuration is superior to series configuration in case of mismatch in technological configuration [4]. This observation becomes obvious if the equivalent circuit model analysis is carried out at normalized or optimum shunt resistance; otherwise, the RPL cannot be trivial if the shunt resistance approaches infinity as the maximum output power is being reduced [20].

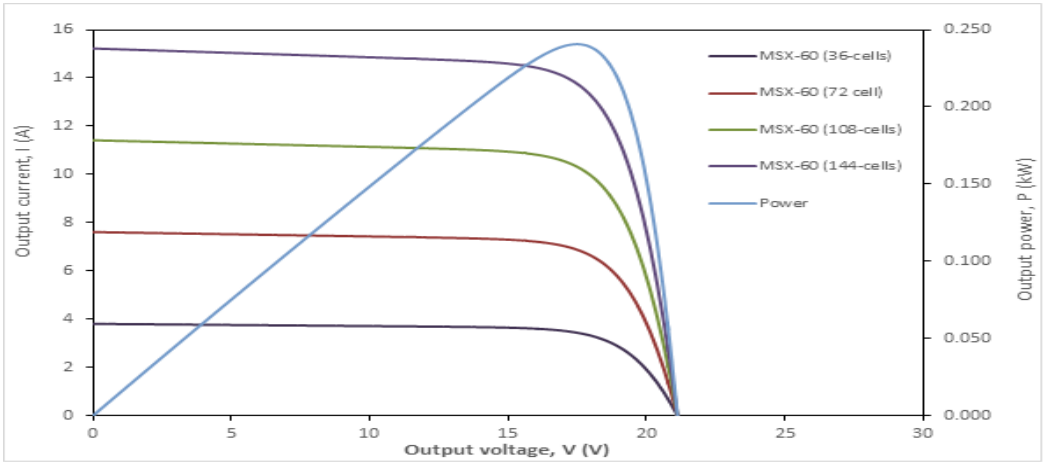
MSX-60 (36-cells)
MSX-60 (72 cell)
MSX-60 (108-cells)
MSX-60 (144-cells)
Power
Output current, I (A)
Output power, P (kW)
Output voltage, V (V)

(a)

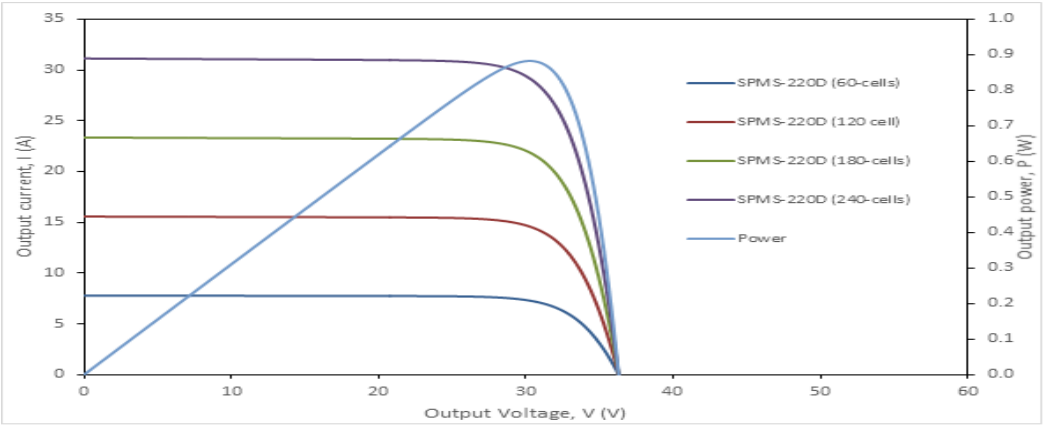
SPMS-220D (60-cells)
SPMS-220D (120 cell)
SPMS-220D (180-cells)
SPMS-220D (240-cells)
Power
Output current, I (A)
Output power, P (W)
Output Voltage, V (V)

(b)

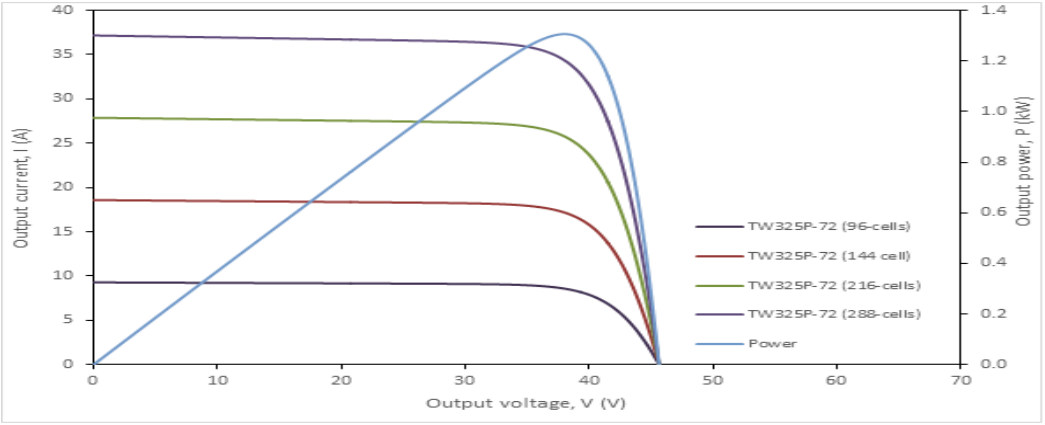
TW325P-72 (96-cells)
TW325P-72 (144 cell)
TW325P-72 (216-cells)
TW325P-72 (288-cells)
Power
Output current, I (A)
Output power, P (kW)
Output voltage, V (V)

(c)

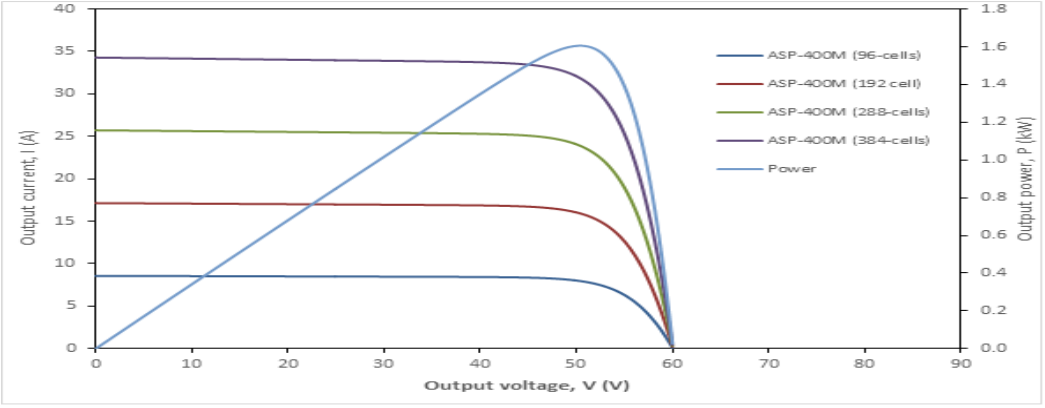
ASP-400M (96-cells)
ASP-400M (192 cell)
ASP-400M (288-cells)
ASP-400M (384-cells)
Power
Output current, I (A)
Output power, P (kW)
Output voltage, V (V)

(d)

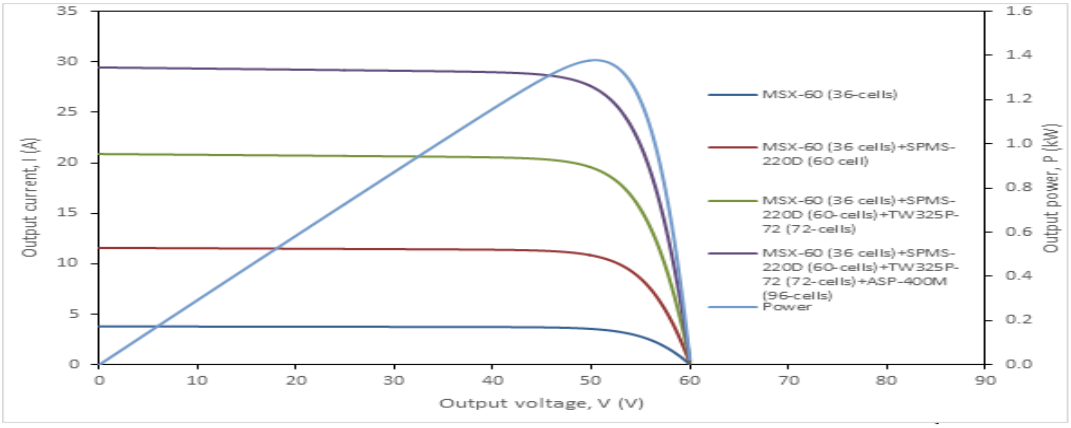

(e)

Figure 5. I-V and P-V curves for the matched: (a) MSX-60 parallel (P) configuration, (b) SPMS-220D parallel (P) configuration, (c) TW325P-72 parallel (P) configuration, (d) ASP-400M parallel (P) configuration and (e) I-V and P-V curves for the mismatched parallel (P) configuration

Table 4. Relative power loss in parallel configuration

S#	Module	Characteristic	n_cell	Power, $P_{computed}$ (kW)	Measured Fill factor, $FF_{measured}$	Computed Fill factor, $FF_{computed}$	RPL (%)	Figure
1	MSX-60	Matched (4)	144	0.2406	0.75	0.75	0.0	5a
2	SPSM-220D	Matched (4)	240	0.8825	0.78	0.78	0.0	5b
3	TW325P-72	Matched (4)	288	1.3065	0.77	0.77	0.0	5c
4	ASP-400M	Matched (4)	384	1.6057	0.78	0.78	0.0	5d
5	All	Mismatched (4)	264	1.3700	0.77	0.76	1.3	5e

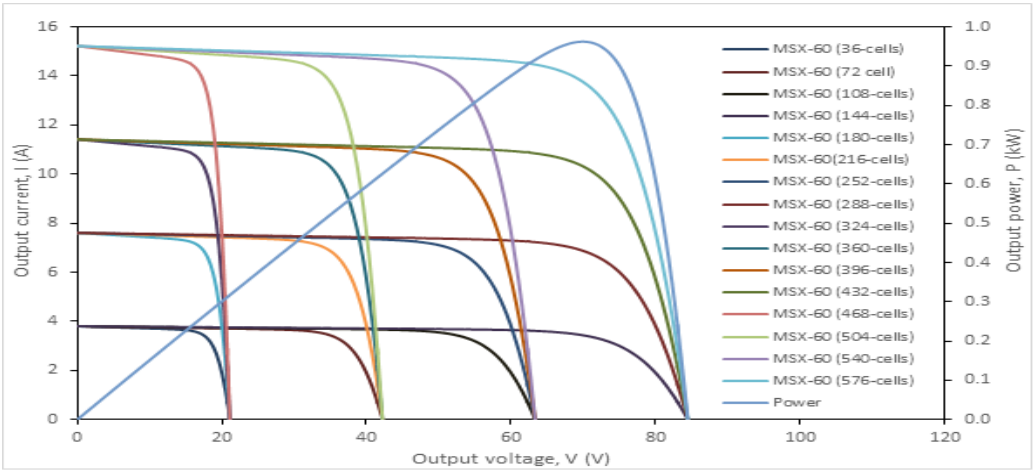

(a)

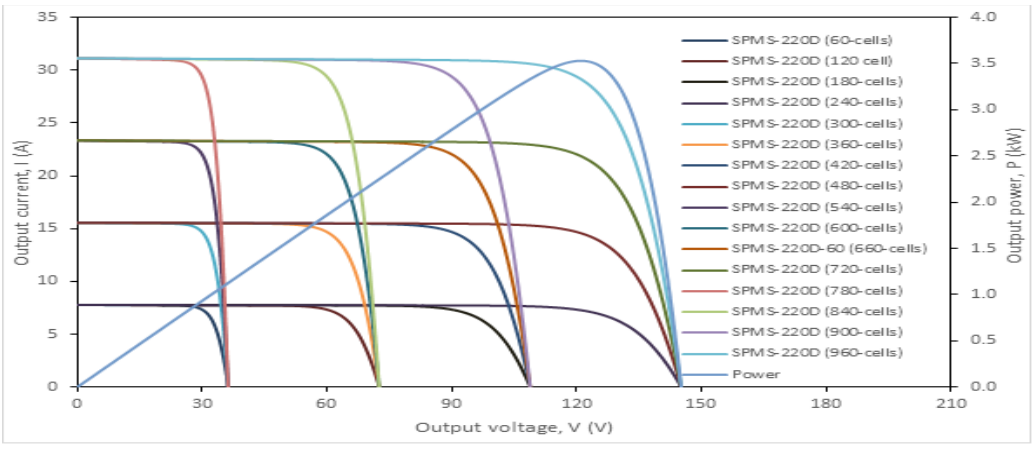

(b)

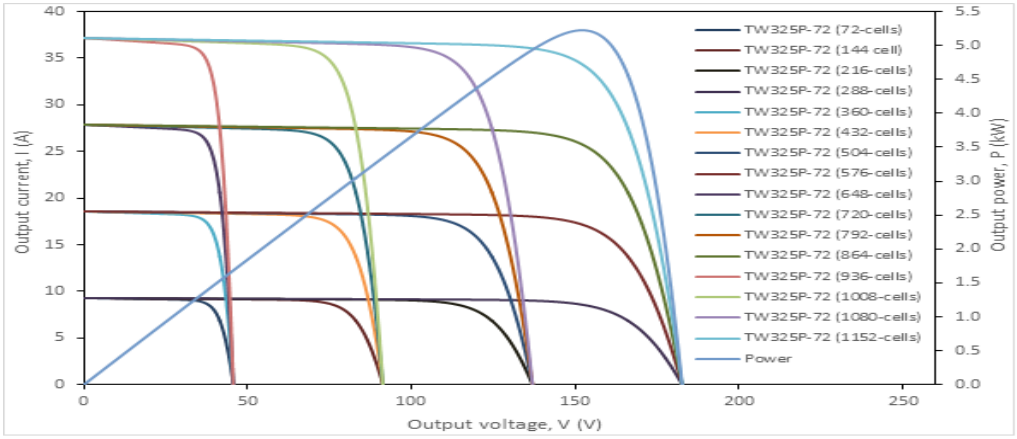

(c)

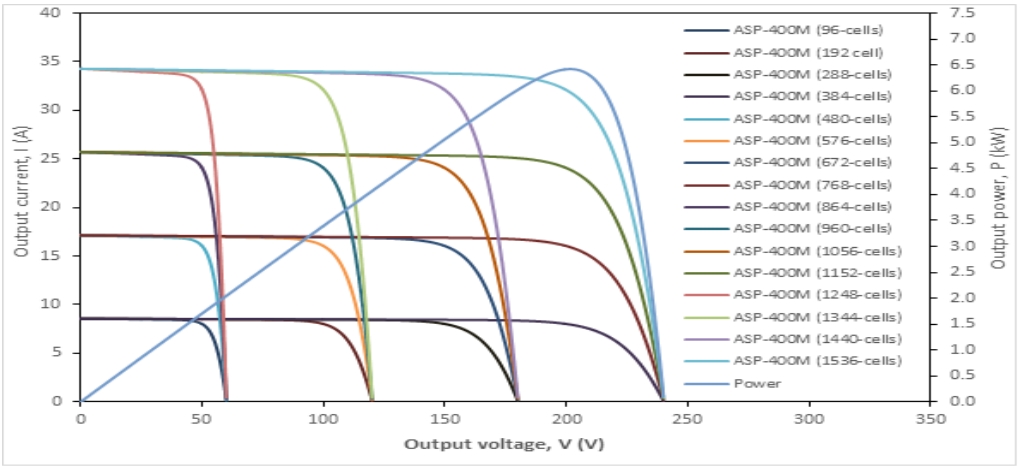

(d)

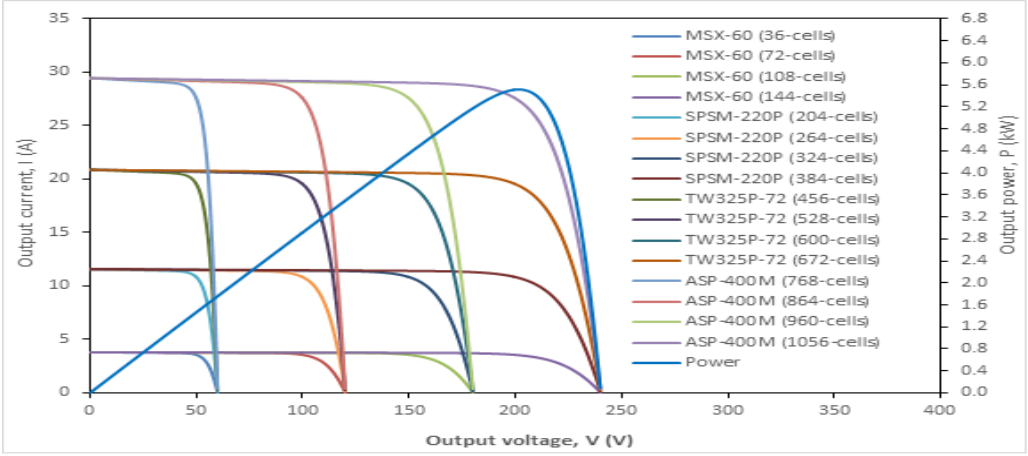

(e)

Figure 6. I-V and P-V curves for the: (a) MSX-60 matched array, (b) SPMS-220D matched array, (c) TW325P-72 matched array, (d) ASP-400M matched array and (e) I-V and P-V curves for the mismatched array

Figures 6 (a-d) present the maximum output power of equal series-parallel configuration of sixteen matched modules (MSX-60, SPSM-220D, TW325P-72, ASP-400M) which gave maximum output power rates of 0.9625, 3.5301, 5.2260, 6.4229 kW, respectively, but those of sixteen mismatched modules (MSX-60 + SPSM-220D + TW325P-72 + ASP-400M) in Figure 6e gave 5.5169 kW in Table 5. Notably, the characteristics of series-parallel array are similar to those of parallel modules, sequel to the four strings (or blocks) responsible for lowering RPL to 1.3 %, as reported in Tables 4 and 5. Thus, increasing the number of strings minimizes the inherent RPL in an array. Also, the matched technology in Tables 3-5 showed a trivial RPL, which implies that the total output power of the cells is approximately equal to that of the module. This indicates that the electrical and thermal properties of the cells and the modules are in alignment. Hence, designers and installers of photovoltaic plants should adhere to use of modules or arrays of matched or uniform electrical and thermal properties to enhance output power.

Moreover, by comparing the RPL of mismatched technologies in Tables 3 and 4 (or 5), the RPL associated with the series configuration (2.6 %) is twice that of the parallel

configuration (1.3 %) and these results are in agreement with those of Vicente et al. [20]. This implies that open circuit defect is more pronounced in series configuration and more than a short circuit defect in parallel configuration. This could be remedied by simply increasing the number of blocks or strings in the design of photovoltaic arrays or by avoiding the use of mismatched modules in the design of photovoltaic plants.

Table 5. Relative power loss in series-parallel configuration in Figure 1c

S#	Module	Characteristic	n_cell	Power, $P_{computed}$ (kW)	Measured Fill factor, $FF_{measured}$	Computed Fill factor, $FF_{computed}$	RPL (%)	Figure
1	MSX-60	Matched (16)	576	0.9625	0.75	0.75	0.0	6a
2	SPSM-220D	Matched (16)	960	3.5301	0.78	0.78	0.0	6b
3	TW325P-72	Matched (16)	1152	5.2260	0.77	0.77	0.0	6c
4	ASP-400M	Matched (16)	1536	6.4229	0.78	0.78	0.0	6d
5	All	Mismatched (16)	1056	5.5169	0.77	0.76	1.3	6e

5. CONCLUSIONS

A configuration analysis of the modules and arrays was successfully carried out via real equivalent circuit model for matching and mismatched: series (S), parallel (P), and series-parallel (SP) configurations in standard test conditions. Comparison of the maximum output power for the first two configurations showed that for the equal number of mismatched modules, the parallel configuration (P) was superior to series configuration (S) due to less RPL associated with the parallel configuration. Moreover, parallel configuration (P) had a greater tendency to resist inhomogeneity in electrical and thermal characteristics of modules, leading to relative power losses in an array. However, there was no discrepancy in the maximum output power for different matched configurations (S and P). The relative power loss was more recurrent in mismatched series configuration due to open circuit defect. Thus, the application of mismatched modules with heterogeneous electrical and thermal characteristics should be avoided in order to minimize power losses in modules or arrays. Pertinently, the present work suggests the application of power electronics device as a means of curbing the RPL in parallel configuration and the application of integral bypass diode as a means of minimizing the RPL in series configuration. Furthermore, mismatched modules should be avoided when designing and installing photovoltaic power plants to enhance power generation from power plants.

6. ACKNOWLEDGEMENT

This work was not funded by any organization.

NOMENCLATURE

A	Ideality factor
AM	Air mas
BL	Bridge-linked interconnection
DC	Direct curren
FF	Fill-factor
HC	Honeycomb interconnection
I	Current
I-V	Current-voltage
K	Boltzmann constant
LAD	Ladder interconnection
MPPT	Maximum power point tracking
NOC	Nominal operating cell temperature
OC	Open circuit
P	Parallel configuration
PTC	PVUSA test condition
P-V	Power-voltage
PVUSA	Photovoltaic USA
R	Resistance
RPL	Relative power losses
RRPL	Real relative power losses
S	Series configuration
SC	Short circuit
SP	Series-parallel configuration
STC	Standard test condition
T	Cell operating temperature
TCT	Total-cross-tied interconnection
V	Voltage

REFERENCES

1. Balram, G., Anitha, S. and Deshmukh, A., "Utilization of renewable energy sources in generation and distribution optimization", ***Proceedings of the International IOP Conference Series: Material Science Engineering, Vol. 981, International Confetrence on Recent Advancements in Engineering and Management (ICRAEM-2020)***, Warangal, India, (October 9-10, 2020), 042054. (https://doi.org/10.1088/1757-899X/981/4/042054).
2. Williams, B.K. and Nichols, J.D., "Optimization in natural resources conservation", In: Guntenspergen, G., Eds, Application of threshold concepts in natural resource decision making, Springer, New York, NY, (2014), 45-65. (https://doi.org/10.1007/978-1-4899-8041-0_4).
3. Marodkar, M.M., "Study of pv array configuration and its effects on performance under nonuniform irradiance", ***Proceedings of International Conference on Electrical, Electronics, Signals, Communication and Optimization (EESCO)***, Visakhapatnam, India, (Jan. 24-25, 2015), 1-5. (https://doi.org/10.1109/EESCO.2015.7253902).
4. Burhanudin, K., Kamarzaman, N.A., Samat, A.A.A., Tajudin, A.I., Ramli, S.S. and Hidayat, N., "An improved photovoltaic array configuration for photovoltaic system in the presence of maximum power point tracking during partial shading condition", ***Indonesian Journal of Electrical Engineering and Computer Science***, Vol. 6, No. 2, (2017), 301-309. (http://doi.org/10.11591/ijeecs.v6.i2.pp301-309).
5. Fan, Q., An, Q., Lin, Y., Xia, Y., Li, Q., Zang, M., Su, W., Peng, W., Zang, C., Liu, F., Hou, L., Zhu, W., Yu, D., Xiano, M., Moon, E., Zang, F., Anthopoulos, T.D., Linganas, O. and Wang, E., "Over 14 % efficiency all-polymer solar cells enabled by a low bandgap polymer acceptor with low energy loss and efficient charge separation", ***Energy & Environment Science***, Vol. 13, No. 12, (2020), 1-27. (https://doi.org/10.1039/D0EE01828G).
6. Chikate, B.V. and Sadawarte, Y.A., "The factors affecting the performance of solar cell", ***International Journal of Computer Applications, Proceedings on International Conference on Advancements in Engineering and Technology (ICAET 2015), (ICQUEST 2015)***, No. 1, (2015), 4-8. (https://www.https://www.ijcaonline.org/proceedings/icquest2015/number1/22976-2776).
7. Srinivasan, A., Devakirubakaran, S. and Sundaram, B.M., "Mitigation of mismatch losses in solar pv system–two-step reconfiguration approach", ***Solar Energy***, Vol. 206, (2020), 640-654. (https://doi.org/10.1016/j.solener.2020.06.004).
8. Mahmoud, Y. and El-Saadany, E.F., "Enhanced reconfiguration method for reducing mismatch method for reducing mismatch", ***IEEE Journal of Photovoltaics***, Vol. 99, (2017), 1-9. (https://doi.org/10.1109/JPHOTOV.2017.2752708).
9. Bonthagorla P.K and Mikkili S., "Performance analysis of PV array configurations (SP, BL, HC and TT) to enhance maximum power under

non-uniform shading conditions", ***Engineering Reports***, Vol. 2, (2020), e12214. (https://doi.org/10.1002/eng2.12214).

10. Mohammadnejad, S., Khalafi, A. and Ahmadi S.M., "Mathematical analysis of total-cross-tied photovoltaic array under partial shading condition and its comparison with other configurations", ***Solar Energy***, Vol. 133, (2016), 501-511. (https://doi.org/10.1016/j.solener.2016.03.058).
11. Christabel, S.C., Srinivasan, A., Winston, D.P. and Kumar, B.P., "Reconfiguration solution for extracting maximum power in the aged solar pv systems", ***Journal of Electrical Engineering***, Vol. 16, No. 3, (2016), 440-446. (https://www.researchgate.net/publication/319502192_Reconfiguration_solution_for_extracting_maximum_power_in_the_aged_solar_PV_systems).
12. Renogy, R., "Learn series and parallel", (2017). (https://www.renogy.com/learn-series-and-parallel/), (Accessed: 07 October 2017).
13. Fei, L., Guo, S., Walsh, T.M. and Aberle, G.A., "Improved pv module performance under partial shading condition", ***Energy Procedia***, Vol. 33, (2013), 248-255. (https://doi.org/10.1016/j.egypro.2013.05.065).
14. Pendem S.R. and Mikkili S., "Modeling, simulation and performance analysis of solar pv array configurations (series, series–parallel and honey-comb) to extract maximum power under partial shading conditions", ***Energy Reports***, Vol. 4, (2018), 274-287. (https://doi.org/10.1016/j.egyr.2018.03.003).
15. Ferahtia, S., Djerioui, A., Zeghlache, S. and Houari, A., "A hybrid power system based on fuel cell, photovoltaic source and supercapacitor", ***SN Applied Science*** Vol. 2, No. 940, (2020). (https://doi.org/10.1007/s42452-020-2709-0).
16. Nguyen, X.H. and Nguyen, M.P., "Mathematical modeling of photovoltaic cell/module/arrays with tags in MATLAB/SIMULINK", ***Environmental Systems Research***, Vol. 4, (2015), 24. (https://doi.org/10.1186/s40068-015-0047-9).
17. Salem, F.A., Matrawy, K.K. and Mahrous, A.F., "Mathematical modeling of PV array with different performance parameters", ***International Journal of Control, Automation and Systems***, Vol. 4, No. 2, (2015). (http://www.researchpub.org/journal/jac/jac.html).
18. Vicente, P.D., Pimenta, T.C. and Ribeiro, E.R., "Photovoltaic array reconfiguration strategy for maximization of energy production", ***International Journal of Photoenergy***, Vol. 11, (2015), 592383. (http://doi.org/10.1155/2015/592383).
19. Fornie´s, E., Naranjo, F., Mazo, M. and Ruiz, F. "The influence of mismatch of solar cells on relative power loss of photovoltaic modules", ***Solar Energy***, Vol. 97, No. 2, (2013), 39-47. (https://doi.org/10.1016/j.solener.2013.08.004).
20. Nnamchi, S.N., Mundu, M.M., Busingye, J.D. and Ezenwankwo, J.U., "Extrinsic modeling and simulation of helio-photovoltaic system: A case of single diode model", ***International Journal of Green Energy***, Vol. 16, No. 6, (2019), 450-467. (https://doi.org/10.1080/15435075.2019.1578659).
21. Nnamchi, S.N. and Nnamchi, O.A., "Perturbation of diminutive solar irradiance and extreme semiconductor temperature on the output current and voltage: The translation of electrical characteristics into thermal characteristics", ***Journal of Solar Energy Research***, Vol. 4, No. 2, (2019b). 92-106. (https://doi.org/10.1080/15435075.2019.1578659).
22. Yahyaoui, I., Specifications of photovoltaic pumping systems in agriculture: Sizing, fuzzy energy management and economic sensitivity analysis, Elsevier, (2016), 121-133. (https://www.elsevier.com/books/specifications-of-photovoltaic-pumping-systems-in-agriculture/yahyaoui/978-0-12-812039-2).
23. Ahmad, T., Sobhan, S. and Nayan, M.F., "Comparative analysis between single diode and double diode model of PV cell, concentrate different parameters effect on its efficiency", ***Journal of Power and Energy Engineering,*** Vol. 4, (2016), 31-46. (https://doi.org/10.4236/jpee.2016.43004).
24. Baba, A.O., Liu, G. and Chen, X., "Classification and evaluation review of maximum power point tracking methods", ***Sustainable Futures***, Vol. 2, (2020), 100020. (https://doi.org/10.1016/j.sftr.2020.100020).
25. Hayt, W.H., Kemmerly, J.E. and Durbin, S.M., Engineering circuit analysis, 9th Ed., McGraw-Hill, New York, (2020). (https://www.aldeatdo.com/wp-content/uploads/2019/09/William_Hart_Hayt_Jack_E_Kemmerly_Steven_M_Durbz-lib.org_.pdf).
26. Belkassmi,Y., Rafiki, A., Gueraoui, K., Bonkoungou, D., Koalaga, Z. and Njomo, D., "Modeling and simulation of photovoltaic module based on one diode model using MATLAB/SIMULINK ", ***Proceedings of International Conference on Engineering & MIS (ICEMIS)***, Monastir, Tunisia, (2017). (https://doi.org/10.1109/icemis.2017.8272965).
27. Nnamchi, S.N., Nnamchi, A.O., Sanya, O.D., Mundu, M.M. and Gabriel, V., "Dynamic analysis of performance of photovoltaic generators under moving cloud conditions", ***Journal of Solar Energy. Research***, Vol. 5, No. 2, (2020), 453-468. (https://doi.org/10.22059/jser.2020.304561.1158).
28. Solarex D., "Msx-60 and msx-64 photovoltaic module", (2020). (https://www.solarelectricsupply.com), (Accessed: 12 August 2017).
29. Shangpin S.D., "Poly-crystalline solar module spsm-22", (2020). (http://www.wxsunpower.com/images/new/new05.jpg), (Accessed: 15 August 2017).
30. Tongwei S.D., "Specifications of tw305p-72 polycrystalline solar module", (http://www.tw-solar.com/en/Uploads/2014/0124/256bf277.pdf.), (Accessed: 16 August 2020).
31. Manufacturer, D.S., "Advanced solar photonics asp-400m solar", (http://www.solardesigntool.com/components/module-panel-solar/Advanced-Solar-Photonics/1737/ASP-400M/specification-data-sheet.html), (Accessed 17 August 2020).

JREE: Vol. 8, No. 4, (Autumn 2021) 90-100

Journal of Renewable Energy and Environment

Research Article

Journal Homepage: www.jree.ir

Performance Analysis of a Novel Compressed Carbon Dioxide Storage Model Integrated with Solar Energy

Samira Jafari, Mehran Ameri *

Department of Mechanical Engineering, School of Engineering, University of Shahid Bahonar, P. O. Box: 76175-133, Kerman, Kerman, Iran.

PAPER INFO

Paper history:
Received 11 February 2021
Accepted in revised form 22 September 2021

Keywords:
Exergy Analysis,
Energy Storage,
Carbon Dioxide,
Solar Energy

ABSTRACT

As a result of growing energy demand, shortage of fossil fuel resources, climate change, and environmental protection, the need for renewable energy sources has been growing rapidly. However, there is an urgent need to cope with intermittency and fluctuation of renewable energies. Various energy storage systems are considered as appropriate solutions to the above-mentioned problem. In the present manuscript, a novel compressed carbon dioxide energy storage system was proposed. Furthermore, an extra thermal energy storage with Therminol VP-1 as a working fluid, coupled with Parabolic Trough Collector (PTC), was added to the system. This integration is conducive to rising the inlet temperature of turbines and reducing the work load that should be done by the compressors. In the present study, a method based on software product including Engineering Equation Solver (EES) for determining thermodynamic characters per component and System Advisor Model (SAM) was employed to model the solar field for a desired location. Energy and exergy analyses were conducted to evaluate the whole cycle performance during charging and discharging periods. In this study, the city of Kerman located in the south-eastern part of Iran, with Direct Normal Incidence (DNI) of 950 $\frac{W}{m^2}$, was selected for the present modeling. The results of a random day (June 22/2019) at time 15:00 represented the exergy efficiency of 66.98 % and the round trip efficiency of 93.14 %. High exergy efficiency and round trip efficiency of this system make this idea applicable to enhancing the total performance of the entire system.

https://doi.org/10.30501/jree.2021.272790.1188

1. INTRODUCTION

In recent years, much attentions has been given to renewable energy sources such as solar photovoltaic, wind, geothermal, biofuel, biomass, tidal, etc. as a result of two major concerns including climate change and energy security.

It should be kept in mind that these renewable energy sources are subject to a major drawback, namely intermittent and fluctuating nature. As a reasonable solution to the above-mentioned problem, various methods have been proposed. Energy storage process includes changing the form of available electricity to another, which can again be converted easily to electricity. A proper energy storage method can be used to make a balance between electricity supply and demand. Moreover, energy storage methods can guarantee grid stability and security. There are diverse methods such as pumped-hydro, compressed air, liquid air, and compressed carbon dioxide to store energy.

Pumped Hydro Energy Storage (PHES) method is among the most common energy storage technologies as a result of its large-scale capacity and economic benefits [1]. PHES method employs cheap electricity during off-peak hours to pump water from a smaller source to a larger one. On the contrary, during peak hours, the water gathered in the larger source is freed in order to activate hydro turbine and generate electricity. The energy efficiency of the installed PHES plants worldwide has been reported to be between 70 % and 80 % with capacities of 1000-1500 MW, in order. It should be noted that this method suffers topography and geology constraints as a major difficulty. In other words, a typical pumped hydro energy storage system acquires sufficient elevation difference between its reservoirs. Owing to the low energy density of pumped hydro energy storage, this technology needs either a large amount of water or a noticeable height difference between sources [2].

Another large-scale thermal energy storage method is Compressed Air Energy Storage (CAES) method. In comparison with PHES method, CAES-based technologies are independent of massive amount of water and significant height difference between the reservoirs [3]. The initial notion behind using compressed air for energy storage was suggested by Gay in 1948 in a patent [4]. Following the excessive demand for energy in the last decades of 1960, CAES becomes more practical [5]. CAES method has two principal sub-categories: Diabatic CAES (D-CAES) and Adiabatic CAES (A-CAES).

In the case of D-CAES method, when the demand is low, the entrance air is compressed and fed into the ground tanks or underground cavities. Subsequently, when the demand is high, the air gathered in the cavities is drawn up using excess

*Corresponding Author's Email: ameri_mm@mail.uk.ac.ir (M. Ameri)
URL: https://www.jree.ir/article_137352.html

Please cite this article as: Jafari, S. and Ameri, M., "Performance analysis of a novel compressed carbon dioxide storage model integrated with solar energy", ***Journal of Renewable Energy and Environment (JREE)***, Vol. 8, No. 4, (2021), 90-100. (https://doi.org/10.30501/jree.2021.272790.1188).

electricity and, afterwards, its temperature increases through natural gas in the combustion chamber. Then, the gas is expanded in the turbine to produce electric power. As previously described, the effect of greenhouse gases can be observed in the case of D-CAES method as a result of combustion process. In order to resolve this problem, A-CAES method has been proposed. In this method, a central thermal storage unit is used as a substitute for pre-coolers and post-heaters in the compressed air energy storage method [6].

In A-CAES procedure, whilst there is excess electricity available, the air is compressed. Then, the air goes across the thermal storage unit and eventually it is kept in the reservoir which can be located under the ground or over it. In case of high demand, the compressed air collected in the reservoir is drawn up to the thermal storage unit to be heated again. Thereafter, it goes across the turbine to generate electricity. A-CAES reduces the need for combustion chamber. The theoretical efficiency of this method was reported to be 70 % [6].

Both of the previously described compressed air-based energy storage methods require large cavities whether under or above the ground to store compressed air. In order to resolve this difficulty, researchers are interested in using liquid air as a storage medium [3].

In the process of Liquid Air Energy Storage (LAES), in addition to heat recovery and heat storage due to the compression process, the capacity of cold energy storage has been used to liquefy the air for storage [5].

During the discharge period, the liquid air is extracted from storage tanks and is pumped to higher pressure. Afterwards, the air is evaporated to the superheated state and eventually, it leads to production of high pressure gas can be used for operating turbines and generating electric power [7].

In 1997, Smith [8] was the first who suggested that recovery of cold energy from liquid air for use in the liquefaction process can enhance the storage efficiency. Although this method is characterized by some advantages including reducing the volume of compressed air and increasing the energy storage capacity [5], it is subject to some drawbacks including the need for a significantly low critical temperature which increases the need for precise insulation. Moreover, liquid air and its vapor can rapidly freeze body tissue and make many materials brittle [3].

Recently, integration of energy storage systems with carbon dioxide as the working fluid is one of the newest and most reliable methods for designing thermo-electric energy storage systems. Table (1) represents the thermo physical properties of carbon dioxide as working fluid [9].

Table 1. Thermo-physical properties of carbon dioxide [9]

Fluid name	ASHRAE No. Level for safety	Critical temperature (°C) Pressure (Bar)	ODP	GWP 100yr	ds/dT
Carbon dioxide	R744 A1	30.98 73.8	0	1	-8.27

According to Table (1), carbon dioxide is a natural, environmentally benign refrigerant. What's more, its Global Warming Potential (GWP) is low and its Ozone Depleting Potential (ODP) indicates zero result. In addition, carbon dioxide is an inexpensive, non-explosive and cost-effective option [10]. The aforementioned reasons make carbon dioxide an acceptable choice as a working fluid. New researches have focused on using carbon dioxide as a storage medium [11].

Mercangoz et al. [12] in 2012 suggested a carbon dioxide power cycle coupled with an electrical energy storage system. In their study, hot water and ice were used as storage materials. They concluded that the efficiency of this method was higher than that of the compressed air energy storage method and lower than that of the pumped hydro energy storage method.

Thereafter, Wang et al. [3] in 2015 presented a storage method based on liquid compressed air carbon dioxide. Their new system included high and low temperature storage units. Moreover, an additional organic Rankine cycle was designed to take full advantage of waste heat. Their results demonstrated that in comparison with the compressed air energy storage, their method exhibited higher energy generated per unit volume (EVR) and its efficiency could reach 56-64 %.

In 2016, to ensure the enhancement of energy storage density, Liu et al. [13] designed a storage system containing two saline aquifers as storage media in a close cycle for storing energy. They conducted energy and exergy analysis for the cycle. The exergy efficiency was reported to be 51.56 % for the supercritical carbon dioxide and 53.02 % for the transcritical carbon dioxide.

In 2019, Liu et al. [14] discussed conventional and advanced exergy analyses for a two-stage transcritical compressed carbon dioxide energy storage system. Their conclusion exhibited that the exergy efficiency of the cycle could reach up to 59 %.

In 2020, Yuan Zhang et al. [17] proposed an integrated system including transcritical carbon dioxide energy storage and Organic Rankine Cycle (ORC). They employed advanced exergy methods to optimize the performance of the entire cycle. They reported the exergy efficiency to be 34.62 %.

Later on, in 2020, Yuan Zhang et al. [1] presented a carbon dioxide storage method with low-temperature thermal storage in order to restore the heat in the compression process. In their research, in addition to parametric analysis, they used genetic algorithm to optimize key parameters. Finally, the round-trip efficiency, exergy efficiency, and thermal efficiency of this method were reported to be 41.4 %, 45.4 %, and 59.7 %, respectively.

Thereafter, Yuan Zhang et al. [18] in 2021 carried out conventional and advanced exergy analyses on the compressed carbon dioxide energy storage system and compressed air energy storage system under low-temperature conditions. They measured the exergy efficiency of compressed carbon dioxide as 56.28 % and 63.93 % for the similar compressed air energy storage.

Subsequently, Yuan Zhang et al. [19] in 2021 analyzed thermodynamic features of a compressed carbon dioxide energy storage system including carbon dioxide Brayton cycle, low-temperature thermal energy storage, and cold energy storage. They reported the exergy efficiency at 55.3 % under real conditions.

There are two commercial plants including Huntorf plant of 290 MW in Germany (1978) and McIntosh plant of 110 MW in America (1991). These plants operate based on compressed air energy storage [13]. In these plants, in the charging step, the heat produced from the compression process is released directly to the environment and the cooled compressed air is stored in a massive salt cavern. Furthermore, natural gas is employed to heat the compressed air in the discharging

process. For the above-stated reasons, the total system efficiency of these plants is recorded to be low (e.g., Huntorf plant efficiency is 42 % and McIntosh plant efficiency is 54 %). These operations yield an increase in the emission of carbon dioxide [13].

In order to achieve higher efficiency and energy storage density, attempts have been made in the form of suggestions to use carbon dioxide as the working fluid due to its greater density which causes a smaller volume for storage tank, compared to the compressed air. At the same time, employing solar power in place of natural gas during discharging step eliminate the carbon dioxide emission.

In the present paper, a combination of compressed carbon dioxide power cycle and concentrating solar power plant has been employed to generate and store electrical energy simultaneously. The novelty of the present study lies in the employment of a parabolic trough collector with the intention of supplying the energy required for preheating the entrance working fluid of the turbines. This approach leads to the enhancement of turbines' output power. Furthermore, in the current investigation, supercritical compressed carbon dioxide is used as liquid carbon dioxide with lower performance efficiency employed in similar conducted studies. This research is structured as in the following. First, the methodology employed in this article is discussed. Then, the schematic of the proposed cycle, its components, and its performance are introduced. Next, the thermodynamic modeling is introduced. Later, exergy analysis is presented. Eventually, the results are carried out in the last part.

2. METHOD

2.1. Methodology

In the present study, integration of software-based and manual calculations was employed to model the proposed cycle. Engineering Equation Solver (EES) was opted due to its thermodynamic database of high accuracy to model individual components. Since the open-source System Advisor Model (SAM) software is capable of analyzing concentrating solar power systems including parabolic trough, it has been selected for the present modeling. SAM software requires a weather data TMY file to begin the modeling process for a desired location. Afterwards, design point parameters should be specified. Then, solar field parameters including collectors, receivers, and thermal storage systems must be determined. Eventually, by means of the aforementioned data, the modeling can be completed.

2.2. Description of proposed system

A schematic of the proposed system is given in Figure (1). The main components of this system can be addressed as Compressors 1 & 2, Turbines 1 & 2, Coolers 1 & 2, Heaters 1, 2 & 3, Throttle valves 1 & 2, High-pressure carbon dioxide storage tank, Low-pressure carbon dioxide storage tank, Cold water tank, Hot water tank, Hot TV-oil tank, Cold TV-oil tank, Parabolic Trough collector, and Pump.

The performance of this cycle is divided into charging and discharging processes.

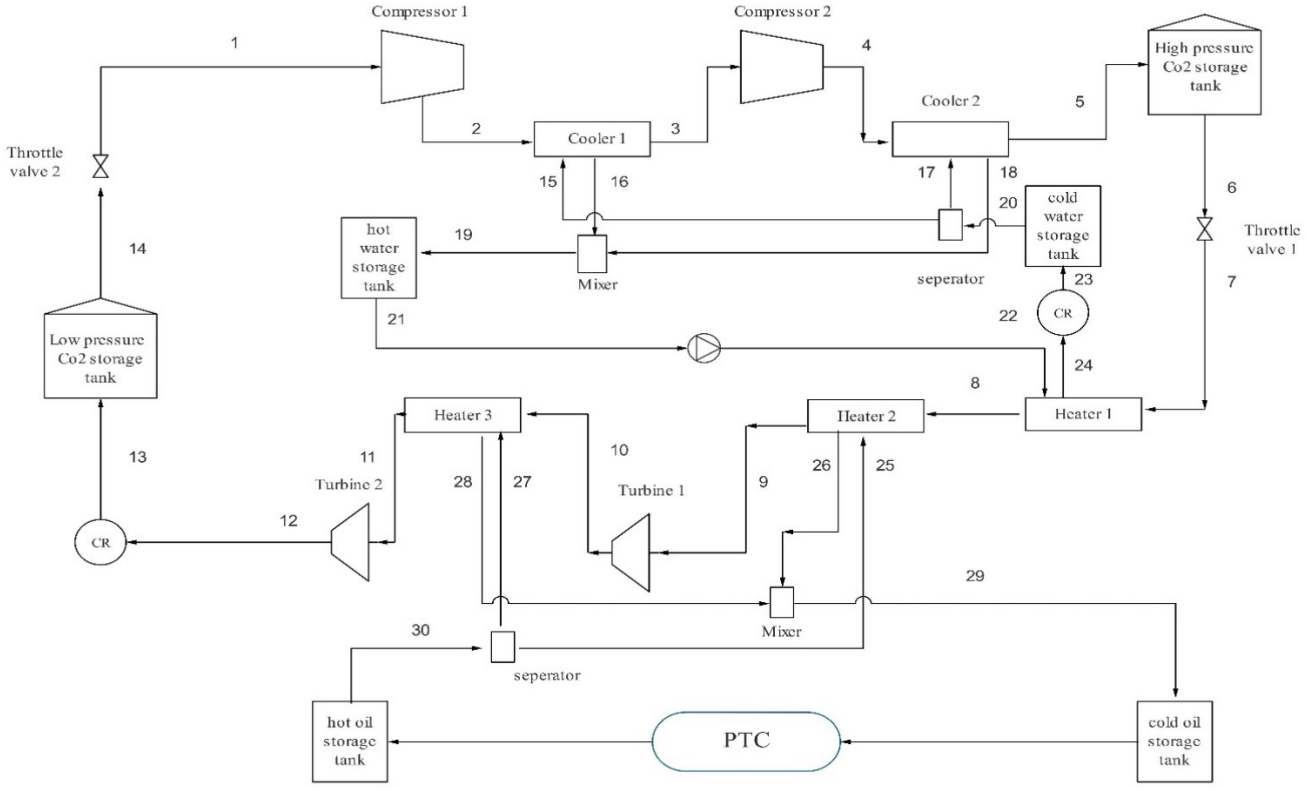

Figure 1. Schematic of the proposed system

2.2.1. Charging process

During off-peak hours, carbon dioxide is compressed by means of excess energy in hand. Then, compressed carbon dioxide is stored in a high-pressure storage tank. The details of this process are described below:

Stream 14: This stream contains low-pressure liquid carbon dioxide (1 Mpa), which is extracted from the low-pressure carbon dioxide storage tank.

Stream 1: This stream is the outlet stream of throttle valve 2 whose pressure has been reduced to 0.7 Mpa. Then, it goes into Compressor 1.

Stream 2: The compressed carbon dioxide exits Compressor 1 in Stream 2. Meanwhile, the temperature of carbon dioxide decreases by means of cold water (Stream 15) through Cooler 1.
Stream 3: It is the outlet of Compressor 1 whose temperature is set to be 313.15 K to keep it supercritical.
Stream 4: It is the outlet of Compressor 2 whose temperature similarly decreases via cold water (Stream 17).
Stream 5: It is the exiting stream of Compressor 2 whose temperature is 313.15 K and its pressure is 20 Mpa and it approaches the high-pressure carbon dioxide tank.

2.2.2. Discharging process

During peak hours, the stored compressed carbon dioxide is used to activate turbines to generate electricity.
Stream 6: It is the outlet stream of the high-pressure carbon dioxide storage tank.
Stream 7: The temperature and pressure of Stream 6 after passing through throttle valve 1 are reduced. Next, it goes through Heater 1 whose temperature increases by means of hot water (Stream 22) which is recovered from the hot water tank.
Stream 8: It is the exiting stream of Heater 1 fed into Heater 2.
Stream 9: It is the outlet stream of Heater 2 whose temperature increases by means of hot oil stream (Stream 25).
Stream 10: It is the exiting stream of Turbine 1 which goes to Heater 3 and its temperature rises via hot oil stream 27 in the same manner.
Stream 11: It is the outlet stream of Heater 3 which goes to Turbine 2.
Stream 12: This stream exchange heat with a massive amount of air creates an environment where its temperature reaches ambient temperature.
Stream 13: It is the outlet stream of cooler which is stored in a low-pressure carbon dioxide tank storage.

3. PERFORMANCE ANALYSIS METHOD

This section includes thermodynamic modeling. First, the assumption used in this modeling were introduced. Subsequently, energy analysis containing individual component role and modeling is discussed. At last, exergy analysis is investigated.

3.1. Assumptions

The following assumptions are taken into account in order to simulate the proposed cycle in this article [14].

1) A constant isentropic efficiency value is set for compressors, turbines, and heat exchangers.
2) The heat exchange between system components and environment is ignored.
3) The pressure loss in pipes is neglected.
4) The pressure loss in heat exchangers is set to 0.02 Mpa.

3.2. Energy analysis

According to the first law of thermodynamics, energy balance can be written as in Eq. (1):

$$\dot{Q} - \dot{W} + \sum_i \dot{m}_i h_i - \sum_o \dot{m}_o h_o = 0 \quad (1)$$

In Eq. 1, $\dot{Q}$ represents net heat input, $\dot{W}$ is net power output, $\dot{m}$ is the mass flow rate, and h is the specific enthalpy. It should be noted that subscripts i and o refer to inlet and outlet stream, respectively [15].

In this study, a two-stage compression and expansion cycle is employed. Throughout the proceeding sections, individual components will be discussed.

3.2.1. Compressor model

During the charging process, the input power of each compressor is derived from Eq. (2):

$$\dot{w}_{c_1} = \dot{m}_1(h_2 - h_1)$$
$$\dot{w}_{c_2} = \dot{m}_3(h_4 - h_3) \quad (2)$$

where w is input power, $\dot{m}$ is mass flow rate of carbon dioxide, subscripts c_1 and c_2 stand for Compressors 1 and 2 in Figure (1), and subscripts 1, 2, 3, and 4 denote the streams depicted in Figure (1) [1].

The isentropic efficiency of the compressors can be calculated using Eq. (3):

$$\eta_{c_1} = \frac{(h_{2,is} - h_1)}{(h_2 - h_1)}$$
$$\eta_{c_2} = \frac{(h_{4,is} - h_3)}{(h_4 - h_3)} \quad (3)$$

In the aforementioned equation, subscripts is stands for the isentropic process [1].

3.2.2. Turbine model

During the discharging process, the outlet power of each turbine can be calculated by Eq. (4):

$$\dot{w}_{T_1} = \dot{m}_9(h_9 - h_{10})$$
$$\dot{w}_{T_2} = \dot{m}_{12}(h_{11} - h_{12}) \quad (4)$$

where subscripts T_1 and T_2 stand for the turbines depicted in Figure (1) and subscripts 9, 10, 11, and 12 denote the streams shown in Figure (1) [1].

The isentropic efficiency of turbines can be driven from Eq. (5):

$$\eta_{T_1} = \frac{(h_9 - h_{10})}{(h_9 - h_{10,is})}$$
$$\eta_{T_2} = \frac{(h_{11} - h_{12})}{(h_{11} - h_{12,is})} \quad (5)$$

Subscripts is refers to the isentropic process [1].

3.2.3. Throttle valve model

Since the throttling process is isentropic, Eq. (6) is valid for modeling throttle valves:

$$h_7 = h_6$$
$$h_1 = h_{14} \quad (6)$$

Subscripts 1, 6, 7, and 14 are in line with the streams represented in Figure (1) [14].

3.2.4. CR model

CR functions like an after cooler in this cycle. As it is discussed previously in the literature, it is assumed that in this step, the working fluid and carbon dioxide exchange heat with plenty of air to reach the environment temperature [15]. Therefore, carbon dioxide condenses in gaseous state. Then, it can be stored in a low-pressure storage tank.

3.2.5. High-pressure and low-pressure carbon dioxide tank model

The state variation of carbon dioxide as a working fluid has not been considered during charging and discharging process in this study. Therefore, the inlet and outlet conditions do not vary in Eq. (7).

$$h_6 = h_5$$
$$h_{14} = h_{13} \quad (7)$$

where subscripts 5, 6, 13, and 14 are related to streams shown in Figure (1) [14].

Based on the assumptions made about storage tanks and throttle valves, only inlet conditions of storage tank and outlet conditions of the valve should be taken into account. The pressure and temperature difference can be calculated through Eq. (8).

$$P_7 = P_5 - \Delta P_{5-7}$$
$$T_7 = T_5 - \Delta T_{5-7} \quad (8)$$

where P refers to pressure, T denotes temperature, $\Delta P_{5\text{-}7}$ refers to pressure difference between States 5 and 7, and $\Delta T_{5\text{-}7}$ denotes temperature difference between States 5 and 7 [15].

3.2.6. Cooler and heater model

The heat exchange rate in heat exchangers shown in Figure (1) can be calculated through Eq. (9) [1].

$$Q_{cooler,1} = \dot{m}_2(h_2 - h_3) = \dot{m}_{15}(h_{16} - h_{15})$$
$$Q_{cooler,2} = \dot{m}_4(h_4 - h_5) = \dot{m}_{17}(h_{18} - h_{17})$$
$$Q_{heater,1} = \dot{m}_{22}(h_{22} - h_{24}) = \dot{m}_7(h_8 - h_7) \quad (9)$$
$$Q_{heater,2} = \dot{m}_8(h_9 - h_8) = \dot{m}_{25}(h_{25} - h_{26})$$
$$Q_{heater,3} = \dot{m}_{10}(h_{11} - h_{10}) = \dot{m}_{27}(h_{27} - h_{28})$$

where subscripts 4, 5, 7, 8, 9, 10, 11, 17, 18, 22, 24, 27, and 28 refer to the streams shown in Figure (1) [14].

The well-known parameter of the heat exchanger, namely heat exchange effectiveness, can be calculated using Eq (10).

$$\varepsilon_{cooler,1} = \frac{\dot{m}_{15}(h_{15} - h_{16})}{Q_{cooler1,max}} = \frac{\dot{m}_2(h_2 - h_3)}{Q_{cooler1,max}}$$
$$\varepsilon_{cooler,2} = \frac{\dot{m}_{17}(h_{17} - h_{18})}{Q_{cooler2,max}} = \frac{\dot{m}_4(h_4 - h_5)}{Q_{cooler2,max}}$$
$$\varepsilon_{heater,1} = \frac{\dot{m}_7(h_8 - h_7)}{Q_{heater1,max}} = \frac{\dot{m}_{22}(h_{22} - h_{24})}{Q_{heater1,max}} \quad (10)$$
$$\varepsilon_{heater,2} = \frac{\dot{m}_8(h_9 - h_8)}{Q_{heater2,max}} = \frac{\dot{m}_{25}(h_{25} - h_{26})}{Q_{heater2,max}}$$
$$\varepsilon_{heater,3} = \frac{\dot{m}_{10}(h_{11} - h_{10})}{Q_{heater3,max}} = \frac{\dot{m}_{27}(h_{27} - h_{28})}{Q_{heater3,max}}$$

where subscripts 2, 3, 4, 5, 7, 8, 9, 10, 11, 15, 16, 17, 18, 22, 24, 25, 26, 27, and 28 denote the streams depicted in Figure (1) and the subscript max represents the maximum heat exchange occurring in heat exchanger [14].

3.3. Exergy analysis

Exergy is the maximum useful possible work which transforms the system from a specific state to equilibrium with the environment.

The exergy of each stream of the former desired system can be calculated using Eq. (11) [14]:

$$E = \dot{m}[h - h_0 - T(s - s_0)] \quad (11)$$

In Eq. (10), $\dot{m}$ is the mass flow rate of the working fluid, h is the specific enthalpy of the stream, and S is the specific entropy of the stream. h_0 and S_0 are specific enthalpy and entropy in the dead state, respectively.

Exergy analysis is calculated based on the second-law of thermodynamics to identify the source value of thermodynamic inefficiencies.

For each component, exergy of product, ($\dot{E}_P$), as the expected outlet should be calculated. Furthermore, exergy of fuel ($\dot{E}_F$), which is the consumed exergy of the component, is evaluated [20].

The exergy balance can be written as Eq. (12) [14]:

$$\dot{E}_F = \dot{E}_P + \dot{E}_D \quad (12)$$

where ($\dot{E}_D$) is the waste exergy of the component due to irreverssibilities. ($\dot{E}_P$) and ($\dot{E}_F$) of individual subsystems in the previously mentioned cycle are given in Table (2), where E represents exergy of each stream shown in Figure (1).

Table 2. ($\dot{E}_P$) and ($\dot{E}_F$) of individual subsystems

Component	$\dot{E}_P$	$\dot{E}_F$
Compressor 1	E[2]-E[1]	$\dot{W}_{compressor1}$
Compressor 2	E[4]-E[3]	$\dot{W}_{compressor2}$
Cooler 1	E[16]-E[15]	E[2]-E[3]
Cooler 2	E[18]-E[17]	E[4]-E[5]
Throttle valve 1	E[7]	E[6]
Throttle valve 2	E[1]	E[14]
Heater 1	E[8]-E[7]	E[22]-E[24]
Heater 2	E[9]-E[8]	E[25]-E[26]
Heater 3	E[11]-E[10]	E[27]-E[28]
Turbine 1	$\dot{W}_{turbine1}$	E[9]-E[10]
Turbine 2	$\dot{W}_{turbine2}$	E[11]-E[12]

The exergy efficency of each component derived from Eq. (13) [14]:

$$\in_{component} = \frac{\dot{E}_P}{\dot{E}_F} \times 100\ \% \quad (13)$$

where $\in$ shows the efficiency of each component.

The relative exergy destruction per component is calculated using Eq. (14) [14]:

$$\in_r = \frac{\dot{E}_{D,r}}{\dot{E}_{D,total}} \times 100\ \% \quad (14)$$

where the subscript D denotes destruction and subscript r is calculated according to each component.

In the case of energy storage syatems, it is quite usual to introduce several parameters so as to evaluate the performance of the energy storing system. Commonly, round-trip efficiency is one of these parameters. According to Eq. (15), the mentioned efficiency is defined as the ratio of total output power denoting the capability of electricity generation in the discharge mode by means of turbines to the net input power of the system reflecting the compressor work in the charging mode. Overall, the higher the round-trip efficiency, the less the energy loss in the storage process [15].

$$\mathrm{RTE} = \frac{(\dot{w}_{\mathrm{turbine},1}+\dot{w}_{\mathrm{turbine},2})t_{\mathrm{discharge}}}{(\dot{w}_{\mathrm{compressor},1}+\dot{w}_{\mathrm{compressor},2})t_{\mathrm{charge}}} \quad (15)$$

The exergy efficiency of the whole cycle is calculated as in Eq. (16) [15]:

$$\mathrm{Exergy}_{\mathrm{efficiency}} = 1 - \left(\frac{\text{Total exergy destruction}}{\text{Inlet exergy to the cycle}}\right) \quad (16)$$

4. RESULTS AND DISCUSSION

4.1. RESULTS

In order to confirm the validity of the present model, some model components were validated based on the similar data existing in the literature. The data for the purpose of comparison were collected from reference [14]. The obtained results are presented in Table (3).

Table 3. Comparison between the present results and those of Ref. [14]

Component	$\dot{E}_{D,r}$ (kW)	$\dot{E}_{D,r}$ (kW) [14]	Relative error (%)
Compressor	181.4	181.60	0.1101
Turbine	154.6	152.89	1.118
Heat exchanger	254.9	259.10	1.62
Cooler	53.62	53.34	0.525
Throttle valve	47.93	47.94	0.02

The results of the simulation of the proposed cycle are given here. In order to measure the thermodynamic properties of carbon dioxide and Therminol VP-1 oil, a software product called Engineering Equation Solver (EES) is employed. The environment temperature and pressure are set to be 298.15 K and 0.1 MPa for simulation. Mass flow rate of working fluid in the main cycle is considered to be 13.88 kg/s for both charging and discharging cycles. In the present case, charging and discharging periods are both considered to be 6 hours. The main initial parameters of this cycle are listed in Table (4). The initial parameters have been selected so that they can be similar to those of reference [14] in order to make an appropriate comparison between final results.

Table 4. Initial parameters [14]

Parameter	Unit	Value
Ambient temperature	K	298.15
Ambient Pressure	Mpa	0.1
Pressure of high-pressure storage tank	Mpa	20
Pressure of low-pressure storage tank	Mpa	1
Δp of the throttle valve 1	Mpa	0.3
Δp of the throttle valve 2	Mpa	3
Isentropic efficiency of turbines	%	85
Isentropic efficiency of compressors	%	85
Isentropic efficiency of heat exchangers	%	85

Furthermore, conventional exergy analysis has been carried out for this specific system. Thermodynamic properties per state of the proposed cycle are shown in Table (5).

In order to analyze the impact of compressor isentropic efficiency on the performance of the entire cycle, the value of isentropic efficiency of compressors is considered to vary from 80 % to 95 % while other parameters are kept unchanged. Based on Figure (2), upon increasing the efficiency of compressors, both RTE and exergy efficiency values rise as a result of the better performance of compressors.

Table 5. Thermodynamic properties of each state of the cycle

Stream	Working fluid	T (K)	P (MPa)	H (kj/kg)	S ($\frac{\mathbf{kj}}{\mathbf{kgK}}$)	E (kj/kg)
1	Carbon dioxide	295	0.7	-9.477	-0.3903	1573
2	Carbon dioxide	443.9	3.74	117.6	-0.3465	3288
3	Carbon dioxide	313.2	3.72	-23.36	-0.7229	2813
4	Carbon dioxide	474.9	19.87	93.85	-0.6854	4407
5	Carbon dioxide	313.2	19.85	-229.6	-1.539	3271
6	Carbon dioxide	313.2	19.85	-229.6	-1.539	3271
7	Carbon dioxide	311.4	16.85	-229.6	-1.527	3218
8	Carbon dioxide	420.2	16.83	26.46	-0.8104	3941
9	Carbon dioxide	620.2	16.81	284	-0.3053	5605
10	Carbon dioxide	476.4	4.08	150.6	-0.2904	3540
11	Carbon dioxide	628.6	4.06	315.5	0.01233	4711
12	Carbon dioxide	491.4	0.9855	176.9	0.0274	2551
13	Carbon dioxide	298.2	0.9655	-9.297	-0.4479	1826
14	Carbon dioxide	298.2	0.9655	-9.297	-0.4479	1826
15	Water	298.2	1	105.7	0.3667	1.574

16	Water	422	1	627.8	1.83	396.5
17	Water	298.2	1	105.7	0.3667	2.962
18	Water	448.4	1	742.3	2.093	1037
19	Water	439.3	1	702.6	2.004	1427
20	Water	298.2	1	105.7	0.3667	4.536
21	Water	439.3	1	702.6	2.004	1427
22	Water	439.4	1.3	703	2.004	1431
23	Water	298.2	0.98	105.7	0.3667	4.303
24	Water	362.2	1	373.9	1.181	375.6
25	Therminol VP-1 oil	655.5	0.1	754.7	1.638	4934
26	Therminol VP-1 oil	564.7	0.1	535.1	1.278	2910
27	Therminol VP-1 oil	655.5	0.1	754.7	1.638	3179
28	Therminol VP-1 oil	564.7	0.1	535.1	1.278	1875
29	Therminol VP-1 oil	564.7	0.1	535.1	1.278	4785
30	Therminol VP-1 oil	655.5	0.1	754.7	1.638	8114

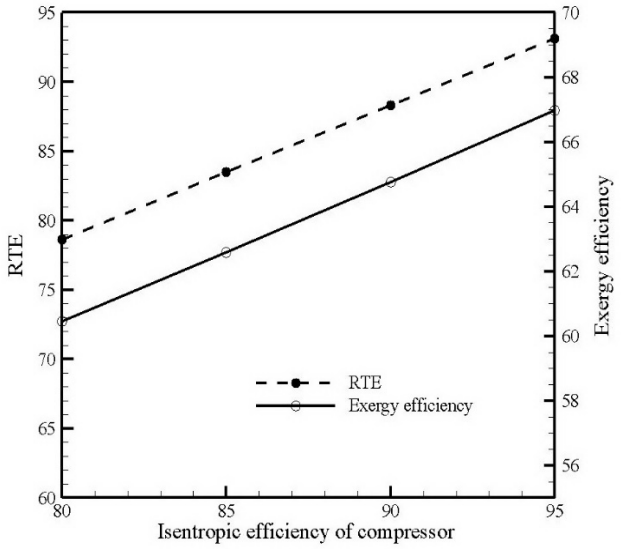

Figure 2. Impact of isentropic efficiency of compressors on the cycle performance

In a similar manner, the impact of changes in the turbine isentropic efficiency on RTE and exergy efficiency is presented in Figure (3).

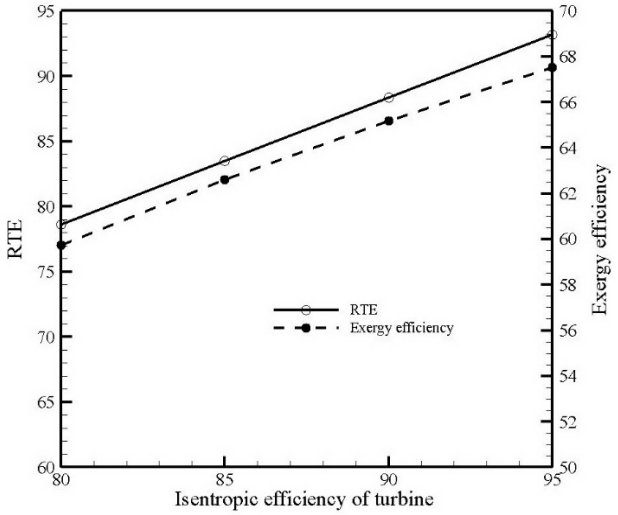

Figure 3. Impact of isentropic efficiency of turbines on the cycle performance

By the same token, upon improving the performance of turbines, RTE and exergy efficiency increase.

Figure (4) presents the exergy destruction and exergy efficiency of each constituent of the entire system.

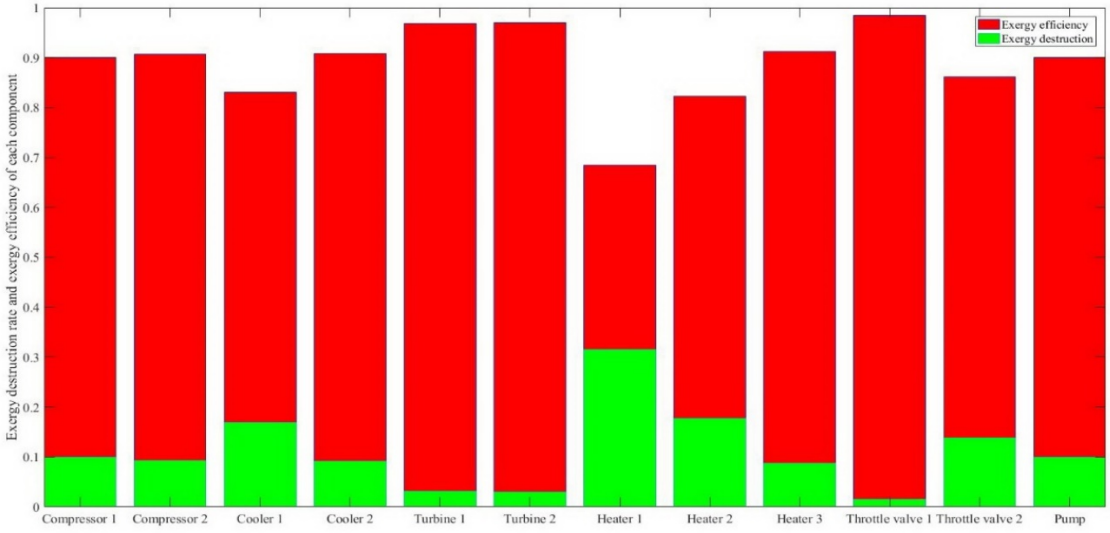

Figure 4. Comparison between exergy efficiency and exergy destruction of individual components

Moreover, the relative exergy destruction percentage of individual components is given in Figure (5).

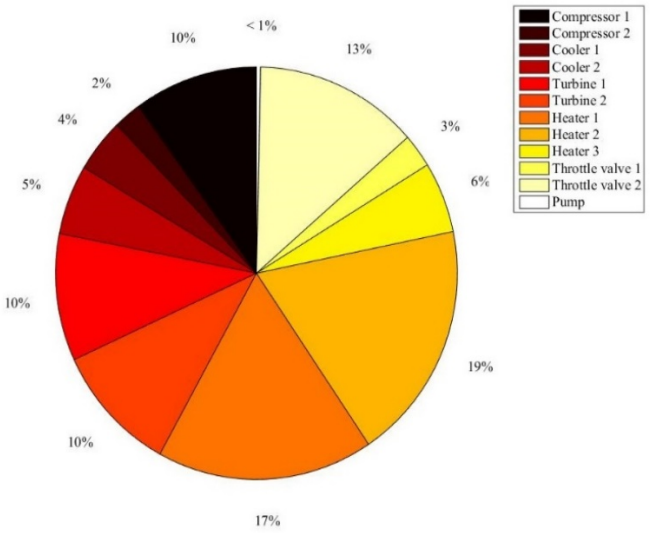

Figure 5. Relative exergy percentage of individual components

From the above stated results, Heater 2 and pump have the largest and smallest shares of relative exergy destruction, respectively. Most of the constituents represent high exergy efficiency (more than 80 %) except Heater 1, which is 68.42 %. Of note, Heater 1 uses hot water from the hot water storage tank to recover it in the cycle and the temperature of carbon dioxide increases from 311.4 K to 420.2 K. This increase is greater through Heater 2 and Heater 3 due to the higher thermal capacity of Therminol VP-1 than water.

In this paper, a Parabolic Trough Collector (PTC) was suggested as a resource for the system to enhance the cycle performance. As was mentioned formerly in this paper, the principal drawback of renewable sources is their instability and fluctuating nature. In order to cope with this trouble, thermal storage tanks have been designed to balance the required energy.

In this study, System Advisor Model (SAM) version 2020.2.29 developed by the National Renewable Energy Lab (NREL) was employed to design a parabolic trough collector. To this end, SAM software was utilized due to its user-friendly environment, its open-source platform, and up-to-date meteorological data available. It is also a well-known software product for designing both performance and financial model.

The principal design parameters of the suggested parabolic through collector due to SAM database is given in Table (6).

In order to initialize the simulation, meteorological data are to be added to the software. The required data for this paper are downloaded from the website "nsrdb.nrel.gov" with station ID2697736.

Table 6. Design parameters of PTC

DNI	**950** $\frac{\mathbf{W}}{\mathbf{m^2}}$
HTF hot temperature	664.15 K
Hours of storage	6 h

The meteorological data utilized in this study originate from Kerman province located in Iran at latitude of 30.29 and longitude of 57.06. The exact date on 06/22/2019 is determined as the typical day for simulating the operation of the aforementioned system.

Figure (6) presents the Direct Normal Incidence (DNI) on the surface and dry bulb temperature with respect to the aforesaid day.

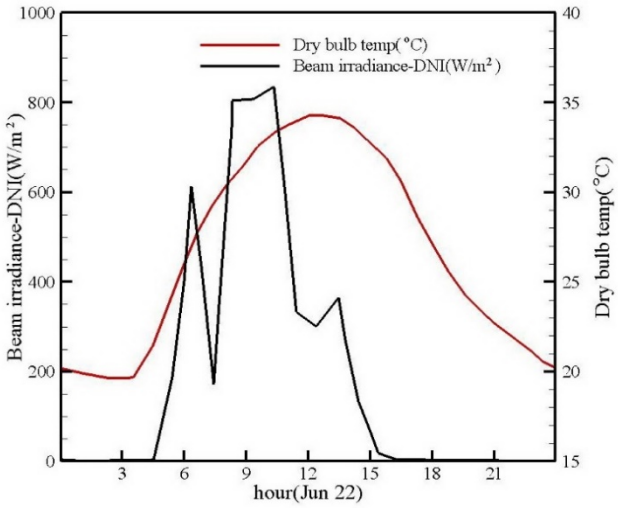

Figure 6. DNI and dry bulb temperature of the selected day (6/22/2019)

According to Figure (6), the dry bulb temperature increases within the time interval starting at 5:00 in the morning to around 14:00 in the afternoon. Furthermore, DNI profile presents that the solar field has the potential to supply sufficient heat in the discharge mode when the sun goes down.

System design, solar field, collector, receiver, and thermal storage parameters, as shown in Table (7), should be fed to the SAM software first.

Table 7. Characteristics of PTC

Characteristics	**Value**
Total plant capacity	111 MWe
Total land area	1.4 × (solar field area) m^2
Collectors and solar field	
Collector type	Skye fuel sky through
Number of loops	181
Single loop aperture	5248 m^2
Solar multiple	2
Water usage per wash	0.7 L/m^2 aperture
Row spacing	15
Thermal receiver and HTF properties	

Receiver type	Schott PTR80
Absorber tube inner diameter	0.076 m
Absorber tube outer diameter	0.08 m
Glass envelope inner diameter	0.115 m
Glass envelope outer diameter	0.12 m
Absorber material type	304 L
HTF type	Therminol VP-1
Design loop outlet temperature	391 ℃
Design loop inlet temperature	293 ℃
Boiler operating pressure	100 bar
Thermal energy storage	
Full load hours of TES	6 h
Storage type	Two tanks
Storage fluid	Therminol VP-1
Tank diameter	65.026 m
Tank height	12 m
Tank loss coefficient	$0.4\ {}^{W}/_{m^2K}$
Estimated heat loss	1.38695 MWt

Afterwards, the temperature inside the storage tanks, mass flow rate of the working fluid and further cycle properties can be modeled using SAM software.

Amongst the various heat transfer fluids, Therminol VP-1 is considered to be a suitable choice due to its high specific heat capacity [17]. The hot Therminol VP-1 temperature profile in the hot storage tank is depicted in Figure (7).

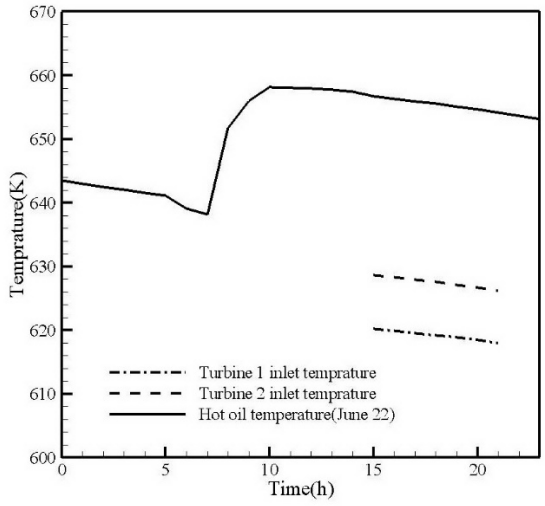

Figure 7. Hot oil temperature profile for the hot storage tank

According to Figure (7), from the early hours in the morning to the noon, the temperature of the oil in hot storage tank increases due to sunshine. Then, in the afternoon from 15:00 to 21:00 in the evening when available sunshine dims, the temperature of hot oil lessens as a result of heat dissipation to the environment.

In this paper, it is considered that the system starts to discharge in the time range of 15:00 to 21:00 for 6 full hours. The turbine inlet temperature plays an important role in the cycle performance. In order to investigate this impact, the inlet temperature changes for Turbines 1 and 2 are shown in Figure (7). Subsequently, based on the whole performance of the system in the discharge mode is presented in Figure (8).

Based on Figures (7) and (8), from 15:00 to 21:00, the temperature of hot oil and the inlet temperature of turbines are reduced simultaneously. Therefore, the RTE decreases from 93.14 % to 92.74 %. In the same manner, the exergy efficiency lessens from 66.98 % to 66.72 %. This slight difference in efficiencies through time represents that the sun fluctuations during the day have a minor effect on the functionality of the system due to role of storage tanks.

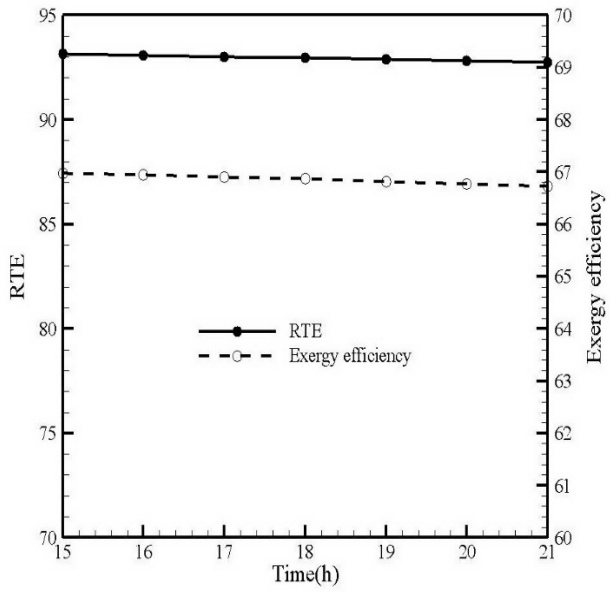

Figure 8. Performance analysis of the system in the discharge mode

In order to demonstrate the capability of the present modeling, a comparison between the present results and similar work done by Liu [14] was made.

Table 8. Comparison in exergy efficiency obtained in the present study and reference [14]

	Present study	**Liu [14]**
Exergy efficiency (%)	66.98	59

As it is obvious from Table (8), the exergy efficiency of the present study model is higher than that of the reference.

5. CONCLUSIONS

This paper presented the integration between compressed carbon dioxide energy storage and parabolic trough collector. Furthermore, energy and exergy analyses were conducted for every individual constituent. Moreover, the fluctuating nature of the sun in parabolic trough collector in the discharging mode was taken into account on an hourly basis, from 15:00 to 21:00. The principal concluding remarks can be addressed as follows:

-Exergy efficiency and round-trip efficiency of the system for a random day (22 June/2019) at 15:00 was reported to be 66.98 % and 93.14 %, respectively, being higher than the previous data reported in the literature [14].

-All the components had high exergy efficiency above 80 % except Heater 1 with an exergy efficiency rate of 68.42 %.

-After a while, throughout the discharging period, the inlet temperatures of both Turbines 1 and 2 decreased and exergy efficiency and round-trip efficiency were reduced.

6. ACKNOWLEDGEMENT

The authors gratefully acknowledge the editor and reviewers for their contribution to completing this manuscript.

NOMENCLATURE

C_p	Specific heat capacity (Kj/Kg.K)
E	Exergy flow rate (KW)
h	Specific enthalpy (Kj/Kg)
$\dot{m}$	Mass flow rate (Kg/s)
P	Pressure (MPa)
Q	Heat flow rate (KW)
S	Entropy (Kj/Kg.K)
T	Temperature (K)
t	Time (s)
W	Power (KW)
Greek letters	
η	Efficiency (%)
Subscripts	
0	Dead state
c	Compressor
D	Destruction
F	Fuel
HST	High Pressure Storage Tank
is	isentropic
LST	Low Pressure Storage Tank
max	Maximum
P	Product
t	Turbine
Abbreviations	
A-CAES	Adiabatic CAES
CAES	Compressed Air Energy Storage
CR	Cooler
D-CAES	Diabatic CAES
DNI	Direct Normal Incidence
EES	Engineering Equation Solver
EVR	Energy Generated per Unit Volume
Eq.	Equation
HTF	Heat Transfer Fluid
GWP	Global Warming Potential
LAES	Liquid Air Energy Storage
NREL	National Renewable Energy Lab
ODP	Ozone Depleting Potential
PHES	Pumped Hydro Energy Storage
RTE	Round-Trip Efficiency
SAM	System Advisor Model

REFERENCES

1. Zhang, Y., Yao, E., Zhang, X. and Yang, K., "Thermodynamic analysis of a novel compressed carbon dioxide energy storage system with low-temperature thermal storage", ***International Journal of Energy Research***, Vol. 44, No. 8, (2020), 6531-6554. (https://doi.org/10.1002/er.5387).
2. Rehman, S., Al-Hadhrami, L. and Alam, M., "Pumped hydro energy storage system: A technological review", ***Renewable and Sustainable Energy Reviews***, Vol. 44, (2015), 586-598. (https://doi.org/10.1016/j.rser.2014.12.040).
3. Wang, M., Zhao, P., Wu, Y. and Dai, Y., "Performance analysis of a novel energy storage system based on liquid carbon dioxide", ***Applied Thermal Engineering***, Vol. 91, (2015), 812-823. (https://doi.org/10.1016/j.applthermaleng..08.081).
4. (https://patents.google.com/patent/US2433896A/en).
5. Zhou, Q., Du, D., Lu, C., He, Q. and Liu, W., "A review of thermal energy storage in compressed air energy storage system", ***Energy***, Vol. 188, (2019). (https://doi.org/10.1016/j.energy.2019.115993).
6. Kere, A., Goetz, V., Py, X., Olives, R., Sadiki, N. and Mercier, E., "Dynamic behavior of a sensible-heat based thermal energy storage", ***Energy Procedia***, Vol. 49, (2014), 830-839. (https://doi.org/10.1016/j.egypro.2014.03.090).
7. Guizzi, G.L., Manno, M., Tolomei, L.M. and Vitali, R.M., "Thermodynamic analysis of a liquid air energy storage system", ***Energy***, Vol. 93, No. 1977, (2015) 1639-1647. (https://doi.org/10.1016/j.energy.2015.10.030).
8. Baxter, J.W. and Bumby, J.R., "Fuzzy control of a mobil robotic vehicle", ***Proceedings of the Institution of Mechanical Engineers, Part I : Journal of Systems and Control Engineering***, Vol. 209, No. 2, (1995). (https://doi.org/10.1243/PIME_PROC_1995_209_369_02).
9. Chen, H., Goswami, D.Y. and Stefanakos, E.K., "A review of thermodynamic cycles and working fluids for the conversion of low-grade heat", ***Renewable and Sustainable Energy Reviews***, Vol. 14, No. 9, (2010), 3059-3067. (https://doi.org/10.1016/j.rser.2010.07.006).
10. Rony, R.U., Yang, H., Krishnan, S. and Song, J., "Recent advances in transcritical CO_2 (R744) heat pump system: A review", ***Energies***, Vol. 12, No. 3, (2019). (https://doi.org/10.3390/en12030457).
11. Alami, A.H., Hawili, A., Hassan, R., Al-Hemyari, M. and Aokal, K., "Experimental study of carbon dioxide as working fluid in a closed-loop compressed gas energy storage system", ***Renewable Energy***, Vol. 134, (2019), 603-611. (https://doi.org/10.1016/j.renene.2018.11.046).
12. Mercangöz, M., Hemrle, J., Kaufmann, L., Z'Graggen, A. and Ohler, C., "Electrothermal energy storage with transcritical CO_2 cycles", ***Energy***, Vol. 45, No. 1, (2012), 407-415. (https://doi.org/10.1016/j.energy.2012.03.013).
13. Liu, H., He, Q., Borgia, A., Pan, L., and Oldenburg, C.M., "Thermodynamic analysis of a compressed carbon dioxide energy storage system using two saline aquifers at different depths as storage reservoirs", ***Energy Conversion and Management***, Vol. 127, (2016), 149-159. (https://doi.org/10.1016/j.enconman.2016.08.096).
14. Liu, Z., Liu, B., Guo, J., Xin, X. and Yang, X., "Conventional and advanced exergy analysis of a novel transcritical compressed carbon dioxide energy storage system", ***Energy Conversion and Management***, Vol. 198, No. July, (2019), 111807. (https://doi.org/10.1016/j.enconman.2019.111807).
15. Zhang, Y., Yang, K., Hong, H., Zhong, X. and Xu, J., "Thermodynamic analysis of a novel energy storage system with carbon dioxide as working fluid", ***Renewable Energy***, Vol. 99, (2016), 682-697. (https://doi.org/10.1016/j.renene.2016.07.048).
16. Bishoyi, D. and Sudhakar, K., "Modeling and performance simulation of 100 MW LFR based solar thermal power plant in Udaipur India", ***Resource-Efficient Technologies***, Vol. 3, No. 4, (2017), 365-377. (https://doi.org/10.1016/j.reffit.2017.02.002).
17. Zhang, Y., Liang, T., Yang, C., Zhang, X. and Yang, K., "Advanced exergy analysis of an integrated energy storage system based on transcritical CO_2 energy storage and Organic Rankine Cycle", ***Energy Conversion and Management***, Vol. 216, No. April, (2020), 112938. (https://doi.org/10.1016/j.enconman.2020.112938).

18. Zhang, Y. and Yao, E., "Comparative analysis of compressed carbon dioxide energy storage system and compressed air energy storage system under low-temperature conditions based on conventional and advanced exergy methods", ***Journal of Energy Storage***, Vol. 35, No. October 2020, (2021). (https://doi.org/10.1016/j.est.2021.102274).

19. Zhang, Y., Yao, E., Tian, Z., Gao, W. and Yang, K., "Exergy destruction analysis of a low-temperature compressed carbon dioxide energy storage system based on conventional and advanced exergy methods", ***Applied Thermal Engineering***, Vol. 185, No. August 2020, (2021), 116421. (https://doi.org/10.1016/j.applthermaleng.2020.116421).

20. Kreith, F., "CRC Handbook of Thermal Engineering", **Cycle**, (2000), (https://www.springer.com/gp/book/9783540663492).

Journal of Renewable Energy and Environment

Research Note

Journal Homepage: www.jree.ir

Evaluation of Power Performance of a PV Module with MPPT Solution Using MATLAB Simulation

Md. Tamim Hossain, Md. Atiqur Rahman, Suman Chowdhury *

Department of Electrical and Electronic Engineering, International University of Business Agriculture and Technology, Dhaka-1230, Bangladesh.

PAPER INFO

Paper history:
Received 25 February 2021
Accepted in revised form 22 September 2021

Keywords:
PV,
MPPT,
Incremental Conductance,
Boost Converter,
MATLAB,
Solar Power

ABSTRACT

In the context of increasing emission of greenhouse gasses in the environment due to fossil fuel burning, this paper attempts to describe the significance of Maximum Power Point Tracking (MPPT) by investigating the power performance of photovoltaic modules with MATLAB simulation. MPPT algorithm was employed to secure maximum power from PV module. The boost converter whose pulse is linked to MPPT algorithm restricts the flow of load power and controls the current and voltage of PV panels. The whole design of the solar model, boost converter, and MPPT controlled algorithms was done in the SIMULINK to prioritize the system in simulation. The main concept employed in this paper was to develop a power generation process with MPPT algorithm and to provide information for future use. In this paper, all simulations along with the PV power generation process were done in MATLAB. This research could potentially play a vital role in mitigating the world fuel crisis.

https://doi.org/10.30501/jree.2021.274901.1193

1. INTRODUCTION

The world remains challenged by the difficulties and constraints associated with energy generation. Societies are developing alongside new technology every day. New technology needs greater power which in turn increases the fuel cost of the power plant. Power generation and transmission cost are increasing day by day, which incurs a greater cost for customers [1]. Burning fossil fuel in every generating station produces a large amount of greenhouse gasses. Emission of CO_2 is increasing due to burning of fossil fuel which may increase the temperature of the environment by 20-60 Celsius up to the year 2100 [2]. The cost of electric power can be reduced using renewable energy sources like wind, solar, and hydropower nuclear reaction. Solar energy is considered a low-cost system with less maintenance and lower energy loss [3]. Photovoltaic systems play a vital role in ensuring a peaceful and clean environment because they do not contribute to global warming [4]. Moreover, a Photovoltaic (PV) power system represents a popular renewable energy system. Solar power demand increases day by day due to such advantages as (i) direct electric power access, (ii) little maintenance cost, and (iii) no noise [5]. The PV operation provides maximum power to its load. The output current and voltage depend on the radiation of the sunlight and the temperature of the solar cell [6]. Upon increase in sunlight radiation, the current of solar cell increases; in addition, when the temperature increases by the sunlight, the voltage of the solar cell increases. This paper runs the power performance of PV module in MATLAB to prove the potentiality of solar cells in near future

2. SIMULATION OF PV MODULE

For simulation purposes, an equivalent circuit model of PV cell is required, as given in Figure 1.

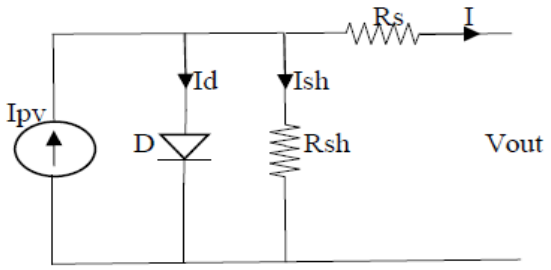

Figure 1. Single diode SIMULINK model of PV cells

Table 1 shows the PV module specifications. The simulation employed to determine the power performance of the PV module is carried out in MATLAB using the specifications provided in the table.

PV array is designed when modules with various arrangements are connected [7]. A significant amount of power can be retrieved by making connections among a series of PV modules in a PV array [8]. The connection among a fixed number of PV cells is known as PV module [9] and it provides no current to the load in case of any disconnection from the load [10].

*Corresponding Author's Email: suman@iubat.edu (S. Chowdhury)
URL: https://www.jree.ir/article_137353.html

Please cite this article as: Hossain, Md.T., Rahman, Md.A. and Chowdhury, S., "Evaluation of power performance of a PV module with MPPT solution using MATLAB simulation", ***Journal of Renewable Energy and Environment (JREE)***, Vol. 8, No. 4, (2021), 101-107. (https://doi.org/10.30501/jree.2021.274901.1193).

The V-I characteristics curve of the solar module is shown in Figure 2.

Table 1. Data sheet of JKM295P model

Parameters	Values
Maximum power (P_{max})	295 W
Maximum power voltage (V_{mp})	36.6 V
Maximum power current (I_{mp})	8.15 A
Open-circuit voltage (V_{op})	45.1 V
Short-circuit current (I_{sc})	8.76 A
Number of series cells (N_s)	72
Number of parallel cells (N_p)	1
Energy band gap (A)	1.1 eV

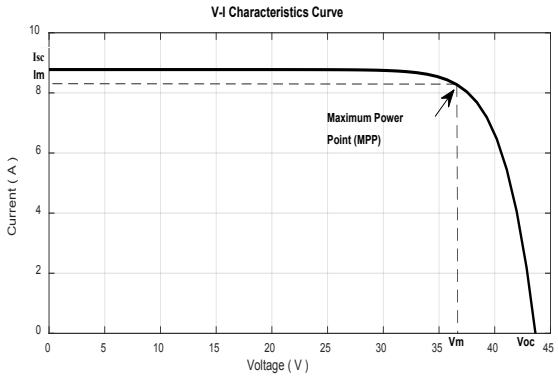

Figure 2. V-I characteristics curve of PV module

The V-I characteristics curve is obtained for the solar model JKM295P. Here, the main parameters include maximum short-circuit current and maximum open-circuit voltage. On the maximum power point with high output efficiency, the fill factor should be 0.5-0.82 [11].

The V-P characteristics curve is shown in Figure 3. Based on the power curve, it is seen that the power reaches around 300 W with the maximum power point voltage V_m. The maximum power P relies on the PV module voltage V, which is the terminal voltage of the PV module [12]. The maximum power point voltage provides maximum power from the module.

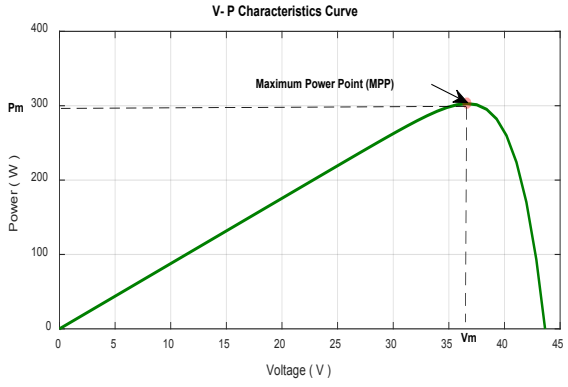

Figure 3. V-P characteristics curve of PV module

The MPPT algorithm plays a vital role in obtaining maximum power despite possible variations in instant radiation. MPPT selects the duty cycle that determines the boost converter switching using MOSFET [13]. Weather changes continuously upon every changes in radiation caused by earth rotation, which in turn induces changes in the PV current, voltage, and power. Incremental Conductance (IC) algorithm makes the array voltage suitable for obtaining maximum power from PV array [14]. PV module current and voltage are unstable if the MPPT algorithm is not applied. Increasing the module current can damage load electrical devices [15]. Installing solar power modules with a proper series-parallel combination can protect the connected electrical device. An alternating and convenient way of obtaining maximum power from solar array is to connect boost converter to the load. The block diagram for the whole project is shown in Figure 4.

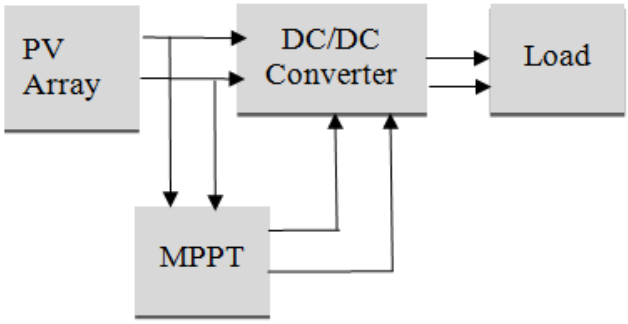

Figure 4. Block diagram of solar MPPT

The PV array generates the voltage and current using the radiation from sunlight. The unstable PV module voltage and current can damage the load electrical device. Therefore, the incremental conductance algorithm can increase the generated power by selecting a proper duty cycle that provides the required power to the electrical device.

3. MATHEMATICAL MODEL OF PV MODULE

The developed equation from the equivalent circuit is as follows:

$$I = Iph - Id - Ish \quad (1)$$

where I is the photovoltaic current. The photon current and the diode current are denoted by I_{ph} and I_d, respectively. The shunt resistor current is I_{sh}.

The following equation can be considered for PV module:

$$I = Iph - Is\{\exp\frac{q(V+IRs)}{k*Tc*A} - 1\} - Ish \quad (2)$$

where I_{ph} is the photon current which is generated by the sunlight radiation, q is the electric charge ($1.60*10^{-19}$ C), and the Boltzmann's constant k is ($1.38*10^{-23}$ J/K). T_c is the cell's temperature, A defines ideality factor, and R_s, I_{sh} are series and shunt resistors, respectively.

Photon current of the PV module is developed from sunlight irradiation and the mathematical equation of the photon current is expressed as follows:

$$Iph = Isc + Ki * \{Tc - Tref\} * \frac{G}{Gn} \quad (3)$$

Here, the symbols are short-circuit current (I_{sc}), short-circuit current temperature coefficient (K_i), cell temperature (T_c), and Cell's reference temperature (T_{ref}). (G) and (G_n) are the solar irradiation and nominal solar irradiation, respectively, in Standard Test Condition (STC). Figure 5 shows the MATLAB

SIMULINK model employed in illustrating the photon current characteristics. The saturation current (I_s) of PV cells varies with respect to the temperature of the solar cell. The mathematical equation of solar cell saturation current is as follows:

$$Is = Irs * (\frac{Tc}{Tref})3 * \exp * \{q * Eg * (\frac{1}{Tref} - \frac{1}{Tc})\} \quad (4)$$

Figure 6 shows the MATLAB SIMULINK model for saturation current. I_{rs} is the reverse saturation current of the PV solar cell. Energy bandgap (E_g) depends on the materials used in semiconductor. The solar cell is made of silicon and the bandgap for silicon is 1.2 eV.

$$Irs = \frac{Isc}{\exp * \frac{q * Voc}{k * Tc * A} - 1} \quad (5)$$

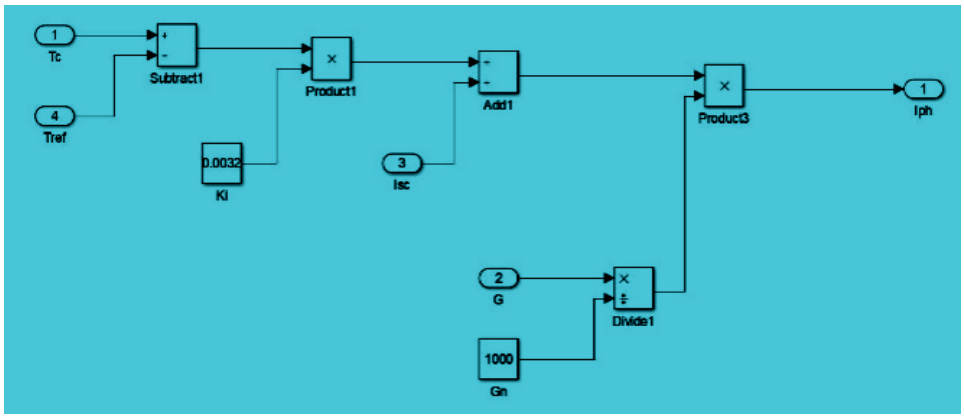

Figure 5. SIMULINK diagram for equation of photon current in PV module

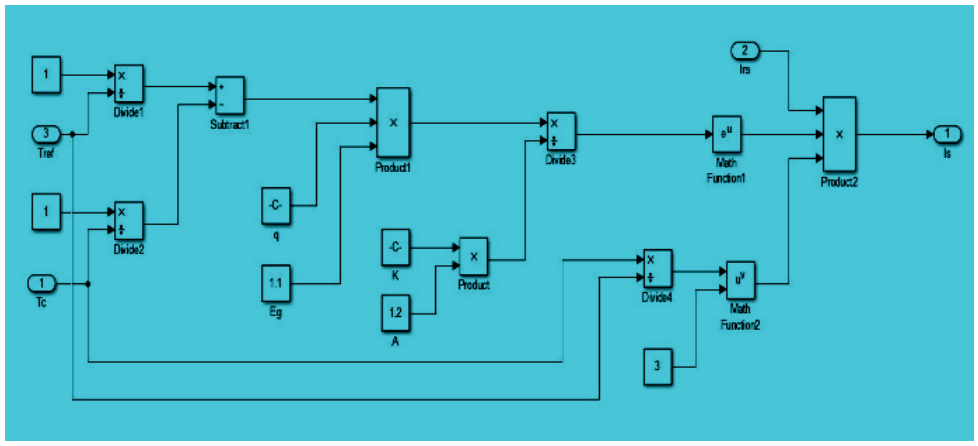

Figure 6. SIMULINK diagram for equation of saturation current for PV module

In the equation, the symbols are short-circuit current (I_{sc}), diode ideality factor (A), and the open-circuit voltage (V_{oc}). The output current and short-circuit current of PV cell result from sunlight radiation and cell temperature. This is developed by the MATLAB SIMULINK model. The PV module is made using the series-parallel combination. Thus, the developed mathematical equation for the array is given by Equation (6).

$$Ipv = Np * Iph - NpIs\{\exp\frac{q(\frac{V}{Ns} + \frac{IRs}{Np})}{k * Tc * A}\} - 1\} - \{\frac{\frac{NpV}{Ns} + IRs}{Rsh}\} \quad (6)$$

For characterizing the output current of the PV module, the SIMULINK model is established in Figure 7. The equation also defines V-I and V-P curves that find the Maximum Power Point (MPP) of the PV module. The whole equation is developed by the MATLAB SIMULINK model in Figure 8.

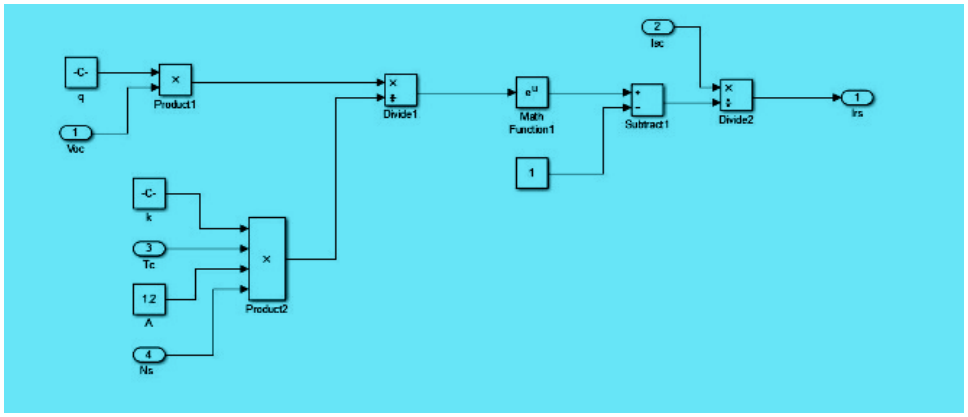

Figure 7. SIMULINK diagram for equation of reverse saturation current for PV module

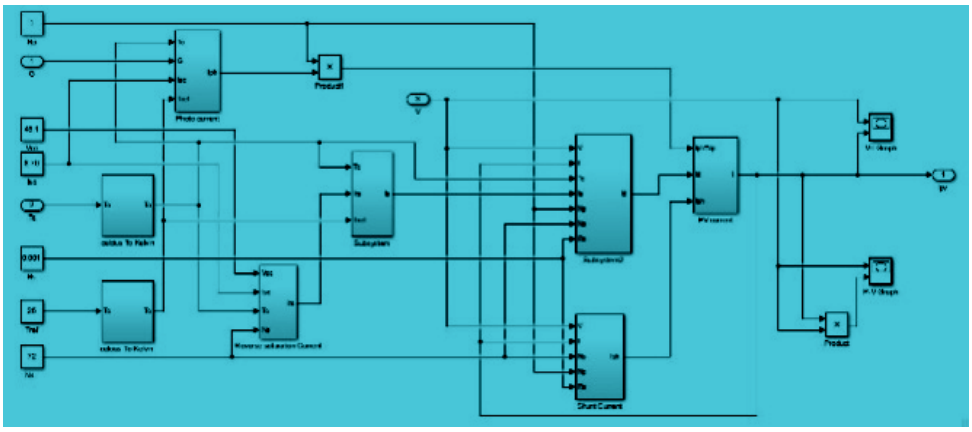

Figure 8. SIMULINK model for equation of PV load current

4. INCREMENTAL CONDUCTANCE AS AN MPPT SOLUTION

The output current and the voltage of the PV module vary with respect to the continuous change of the solar radiation and temperature. To stabilize the output voltage and to obtain the maximum power from the PV module, an MPPT algorithm is required to transfer maximum power to the load. The unwanted duty cycle is modified so that the MPP can be implemented fully. To meet the MPP condition, the duty cycle needs to be adjusted for obtaining the fixed position, because rapid variation of duty cycle may hamper the function of the device connected to load. The SIMULINK model together with the MATLAB function of MPPT algorithm is shown in Figure 9.

Incremental Conductance (IC) of MPPT algorithm is designed to achieve maximum power in different weather conditions. The block diagram of Incremental Conductance is shown in Figure 10.

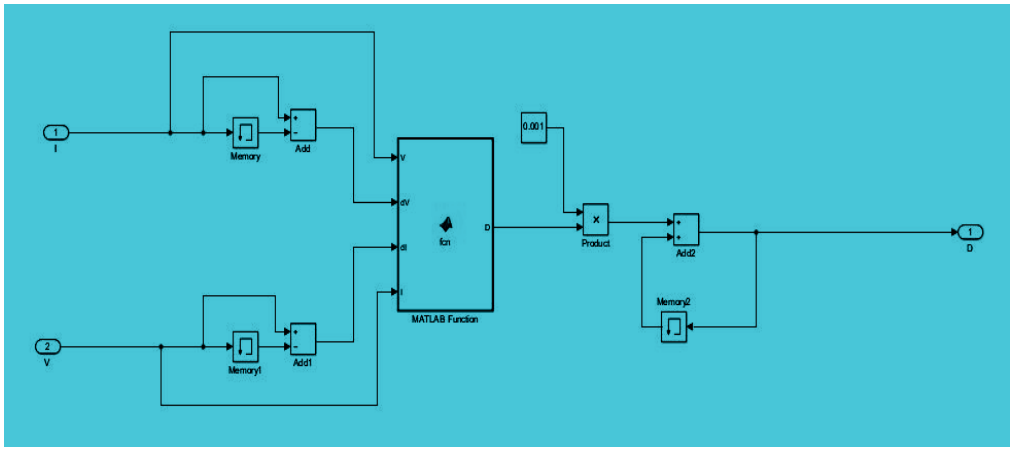

Figure 9. MPPT SIMULINK model with MATLAB function

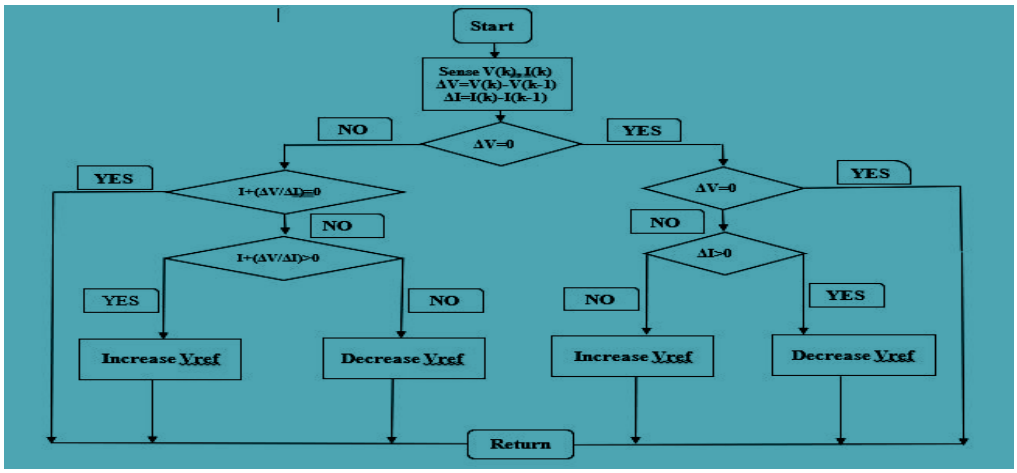

Figure 10. Incremental Conductance MPPT algorithm

The incremental conductance algorithm can fix the output more rapidly than the Perturb and Observe (P & O) algorithm method [16]. This model is used to ensure the Incremental Conductance (dI/dV) of PV array to measure the power changes with respect to the change in voltage (dP/dV), where (I/V) is the array conductance or instantaneous conductance

[17]. MPPT is designed with the boost converter. Boost converter boosts the input voltage to make it equal to the load voltage. The buck converter decreases the output voltage to increase the output current [18].

5. BOOST CONVERTER FOR PV MODULE

The MOSFET works like a switch, as shown in Figure 11. When the switch is turned off, diode works as reverse bias resisting current flow. However, when the switch is turned on, diode is in forward bias which results the current to the load. Inductor and capacitor values are constant for measuring the duty cycle.

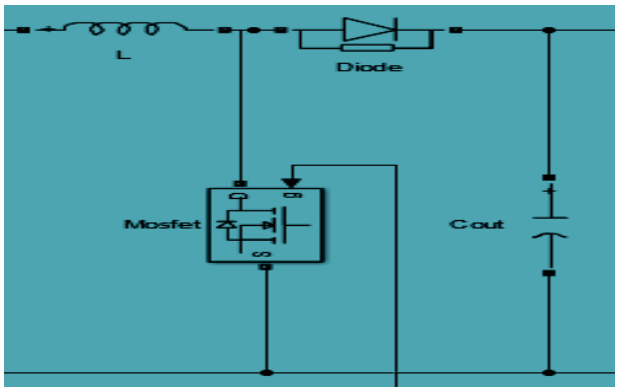

Figure 11. Boost converter of PV module

Duty cycle D can be measured through the following equation:

$$\text{Duty cycle, } D=1-\frac{Vout}{Vin}*\eta \quad (7)$$

Output voltage is V_{out}, Input voltage is V_{in}, and η is the efficiency of the boost converter.

Capacitor value can be determined using the following equation:

$$C=\frac{Io(max)*D}{Fs*\Delta Vc} \quad (8)$$

I_o (max) is the maximum output current, F_s is the frequency, and ΔVc is the capacitor ripple voltage ranging from 1 % to 5 % of output voltage.

$$\text{Inductor, } L=\frac{Vmin*D}{Fs*\Delta Il} \quad (9)$$

V_{min} is the minimum voltage and ΔI_L is the ripple inductor current. The ripple current value varies from 20 % to 40 % of inductor current based on the rule of Thumb.

6. SIMULATION RESULT FOR PV MODULE WITH MPPT SOLUTION

Figure 12 shows simulation for output duty cycle. As mentioned earlier, IC reaches the MPP very faster than Perturb and Observe (P & O) algorithm method.

Here, Figure 13 defines the maximum current characteristics due to the Incremental Conductance (IC) algorithm in MPPT.

Similarly, Figure 14 shows the output power characteristics obtained in the load depending on the output current and voltage of the solar cell.

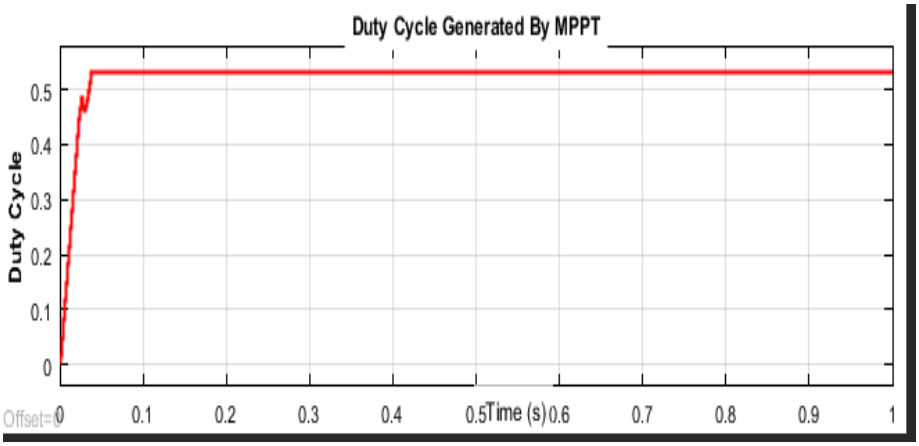

Figure 12. Duty cycle

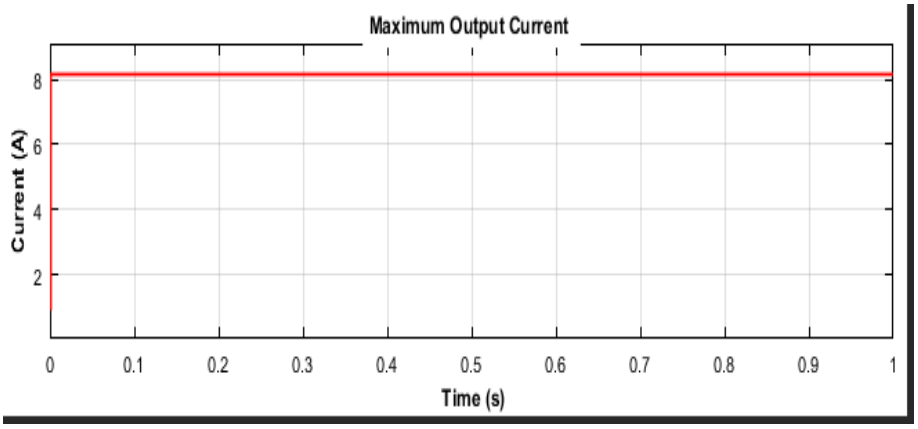

Figure 13. Maximum output current characteristics

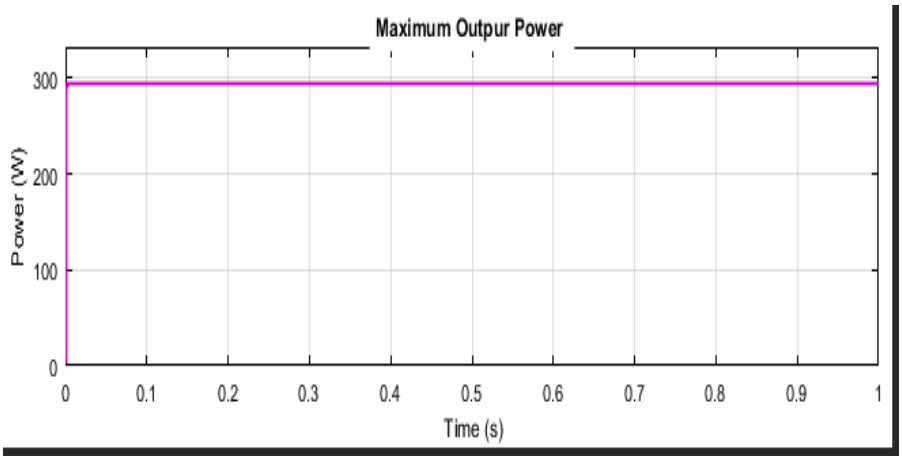

Figure 14. Maximum output power characteristics

7. CONCLUSIONS

The aim of every resource is to generate more power in a cost-effective manner without damaging the environment and to improve PV module to distribute a significant generation of electric power. Incremental Conductance (IC) provides maximum power with different weather conditions in different critical places. This study investigated whether the incremental conductance would work faster and provide maximum power with different radiation degrees of sunlight. The boost converter provided maximum efficiency and reliability in reducing the ripple current and voltage. Load-connected electrical device was saved by boost converter and load resistor was added to deliver limited power. Overall observation of this SIMULINK investigation indicated that some factors like low power generation cost, low maintenance cost, immunity against climatic variations were helpful in developing economic changes.

8. ACKNOWLEDGEMENT

We are heartily grateful to Department of Electrical and Electronic Engineering, International University of Business Agriculture and Technology (IUBAT) for the valuable support for our research.

REFERENCES

1. Bhagwat, P.C., Richstein, J.C., Chappin, E.J.L. and De Vries, L.J., "The effectiveness of a strategic reserve in the presence of a high portfolio share of renewable energy sources", ***Utilities Policy***, Vol. 39, (2016), 13-28. (https://doi.org/10.1016/j.jup.2016.01.006).
2. Singh, B.R. and Singh, O., "Global trends of fossil fuel reserves and climate change in the 21st century", In: Khan, Sh. (Ed.), Fossil fuel and environment, Chapter 8, InTech, India, (2012), 167-192. (https://doi.org/10.13140/2.1.1079.8084).
3. Sheik Mohammed, S. and Devaraj, D., "Simulation of incremental conductance MPPT based two phase interleaved boost converter using MATLAB/SIMULINK", ***Proceedings of 2015 IEEE International Conference on Electrical, Computer and Communication Technologies (ICECCT)***, Coimbatore, India, (2015), 1-6. (https://doi.org/10.1109/ICECCT.2015.7225987).
4. Chandwani, A. and Kothari, A., "Design, simulation and implementation of Maximum Power Point Tracking (MPPT) for solar based renewable systems", ***Proceedings of 2016 International Conference on Electrical Power and Energy Systems (ICEPES)***, Bhopal, India, (2016). (https://doi.org/10.1109/ICEPES.2016.7915987).
5. Chiu, C.-S., "T-S fuzzy Maximum Power Point Tracking control of solar power generation systems", ***IEEE Transactions on Energy Conversion***, Vol. 25, No. 4, (2011), 1123-1132. (https://doi.org/10.1109/TEC.2010.2041551).
6. Carrasco, J.A., de Quiros, F.G., Alaves, H. and Navalon, M., "An analog Maximum Power Point Tracker with pulsewidth modulator multiplication for a solar array regulator", ***IEEE Transactions on Power Electronics***, Vol. 34, No. 9, (2019), 8808-8815. (https://doi.org/10.1109/TPEL.2018.2886887).
7. Atiq, J. and Kumar Soori, P., "Modelling of a grid connected solar PV system using MATLAB/SIMULINK", ***International Journal of Simulation: Systems, Science and Technology***, Vol. 17, No. 41, (2017), 45.1-45.7. (https://doi.org/10.5013/IJSSST.a.17.41.45).
8. Said, S., Massoud, A.M., Benammar, M. and Ahmed, Sh., "A MATLAB/SIMULINK-based photovoltaic array model employing SimPowerSystems toolbox", ***Journal of Energy and Power Engineering***, Vol. 6, (2012), 1965-1975. (https://www.academia.edu/2887497/A_Matlab_Simulink_Based_Photovoltaic_Array_Model_Employing_SimPowerSystems_Toolbox?auto=download).
9. Said, S., Massoud, A.M., Benammar, M. and Ahmed, Sh., "Development of generalized photovoltaic model using MATLAB/SIMULINK", ***Proceedings of the World Congress on Engineering and Computer Science***, San Francisco, USA, (2008). (http://s2i.bordeaux.free.fr/Espace%20Terminale/Ressources/Projet/ProjetASI/2.%20Development%20of%20Generalized%20Photovoltaic%20Model%20using%20Matlab.pdf).
10. Murshed, N., Khan Tushar, Md.S. and Chowdhury, S., "Power performance analysis of PV module with dc to dc buck converter", ***Advanced Journal of Graduate Research***, Vol. 1, No. 9, (2019), 27-39. (https://doi.org/10.21467/ajgr.8.1.27-39).
11. Sheik Mohammed, S., "Modeling and simulation of photovoltaic module using MATLAB/SIMULINK", ***International Journal of Chemical and Environmental Engineering***, Vol. 2, No. 5, (2013), 24-32. (https://www.researchgate.net/publication/301602460_Mathematical_Modeling_and_Digital_Simulation_of_PV_Solar_Panel_using_MATLAB_Software).
12. Surya Suresh, K. and Vishnu Prasad, M., "PV cell based five level inverter using multicarrier PWM", ***International Journal of Modern Engineering Research (IJMER)***, Vol. 1, No. 2, 545-551. (chrome-extension://efaidnbmnnnibpcajpcglclefindmkaj/viewer.html?pdfurl=http%3A%2F%2Fwww.ijmer.com%2Fpapers%2Fvol%25201%2520issue%25202%2FAP012545551.pdf&clen=701280&chunk=true).
13. Ilyas, A., Ayyub, M., Rizwan Khan, M., Jain, A. and Aslam Husain, M., "Realisation of incremental conductance MPPT algorithm for solar photovoltaic system", ***International Journal of Ambient Energy***, Vol. 39, No. 8, (2018), 873-884. (https://doi.org/10.1080/01430750.2017.1354322).
14. Sarathi Maji, P., Dikshit, S. and Mohapatra, S., "Modelling and simulation of photovoltaic model using incremental conductance algorithm", ***International Journal of Engineering and Management Research***, Vol. 4, No. 2, (2012), 205-211. (https://www.ijemr.net/DOC/ModellingAndSimulationOfPhotovoltaicModelUsingIncrementalConductanceAlgorithm(205-211)626d1cf0-bc09-476b-a1fe-205846b3a526.pdf).
15. Ritu, Verma, N., Mishra, Sh. and Shukla, S., "Implementation of solar based PWM fed two phase interleaved boost converter", ***Proceedings of International Conference on Communication, Control and Intelligent***

Systems (CCIS), (2015), 470-476. (https://doi.org/10.1109/CCIntelS.2015.7437962).

16. Sreenivasa Rao, K. and Mahesh, M., "ARM based solar tracking system", ***International Journal of Modern Engineering Research (IJMER)***, Vol. 2, No. 4, (2012), 2504-2507. (chromeextension://efaidnbmnnnibpcajpcglclefindmkaj/viewer.html?pdfurl=http%3A%2F%2Fwww.ijmer.com%2Fpapers%2FVol2_Issue4%2FDA2425042507.pdf&clen=492184&chunk=true).
17. Chandwani, A. and Kothari, A., "Comparative study of Maximum Power Point Tracking algorithms", *Progress in Photovoltaics: Research and Applications,* Vol. 11, (2003), 47-62. (https://doi.org/10.1002/pip.459).
18. Glasner, I. and Appelbaum, J., "Advantage of boost vs. buck topology for Maximum Power Point Tracker in photovoltaic systems", ***Proceedings of 19th Convention of Electrical and Electronics Engineers in Israel***, Jerusalem, Israel, (1996), 355-358. (https://doi.org/10.1109/EEIS.1996.566988).

Journal of Renewable Energy and Environment

Research Article

Journal Homepage: www.jree.ir

Thermodynamic Investigation of a Trigeneration ORC Based System Driven by Condensing Boiler Hot Water Heat Source Using Different Working Fluids

Aref Razmjoo, Iraj Mirzaee *, Nader Pourmahmoud

Department of Mechanical Engineering, Faculty of Engineering, Urmia University, Urmia, West Azerbaijan, Iran.

PAPER INFO

Paper history:
Received 04 March 2021
Accepted in revised form 27 September 2021

Keywords:
Organic Rankine Cycles (ORCs),
LNG Cold Energy,
Condensing Boiler,
Working Fluid,
Thermodynamics Analysis

ABSTRACT

This study conducts thermodynamic analysis on three trigeneration cycles including Organic Rankine Cycle (ORC), Liquefied Natural Gas (LNG) cold energy, and absorption refrigeration cycle in order to select appropriate working fluids. Different types of ORC cycles including simple ORC, regenerative, and ORC with Internal Heat Exchange (IHE) were investigated. For those types, the operation of six working fluids with different thermodynamic behaviors (R141b, R124, R236fa, R245fa, R600, and R123) was evaluated. In power plants, a low-grade heat source was provided by condensing boiler hot water energy while the thermal sink was prepared by cold energy of LNG. The effect of boiler temperature variation on energy and exergy efficiencies was investigated. According to the derived results, regenerative ORC-based systems possessed maximum energy and exergy efficiencies, while simple ORC and ORC with internal heat exchanger exhibited approximately the same quantities. Also, among these analyzed working fluids, R141b had the maximum energetic and exergetic efficiencies, while R124 and R236fa had minimum performance.

https://doi.org/10.30501/jree.2021.273786.1191

1. INTRODUCTION

Much effort is required to put a stop to global warming and ozone depletion. To reduce CO_2 emissions, applying effective technologies is necessary. One of the efficient systems to get electricity from low/medium temperature heating is applying Organic Rankine Cycle (ORC). These days, ORC systems have proved to be a perfect technology to turn low-grade heat into applicable electricity or work. In ORC systems, organic fluids are used instead of water in steam power cycles. Modifying the configuration of the cycle and improving the working fluid are some of the methods for enhancing the efficiency of an ORC system. Finding a suitable working fluid that matches the heat source is essential to enhancing the efficiency.

Producing power from low/medium-grade heat sources using ORC systems is one of the appealing subjects that has attracted the attention of the researchers [1-3]. Maizza et al. [4] investigated waste energy recovery using the ORC cycle and studied the properties of some working fluids. Their results demonstrated the role the analytical criteria in selecting the most favorable working fluid in terms of thermodynamics. Wang et al. [5] simulated a modified regenerative ORC cycle using solar energy. According to their results, the cycle performance would increase with increasing inlet temperature and pressure of the turbine. They also proved that R245fa and R123 had better thermodynamic performance. Safarian and Aramoun [6] employed the first and second law of thermodynamics for evaluation of applying R113 as the working fluid in the modified ORC. Among the studied systems, the maximum energy and exergy efficiencies belong to the ORC system with both turbine bleeding and regeneration. Four ORC systems were analyzed by Mosaffa et al. [7] exploiting geothermal energy as the heat source and LNG cold energy as the thermal sink. Among the studied cycles, the regenerative and IHE systems had maximum thermal and exergy efficiencies. Habibzadeh and Jafarmadar [8] investigated applying ten working fluids in an ORC cycle to recover the engine waste heat. They studied the role of various factors in the system efficiency and introduced the most proper working fluid. Results indicated that in the studied ranges, R134a had the best performances. On the other hand, cyclohexane possessed the least appropriate fluid. Behnam et al. [9] studied thermodynamically and economically the performance of a trigeneration system using geothermal. The system included a single-stage absorption refrigeration system, a single-stage evaporation desalination system, and an organic Rankine cycle. The findings showed that a production capacity of 0.662 kg/s freshwater, 161.5 kW power, and 246 kW heat load could be obtained when the geothermal water temperature was set to 100 °C. Akrami et al. [10] investigated a geothermal-based multi-generation energy system in which heating, electricity, hydrogen, and cooling were produced. The system included a domestic water heater to produce heating, an Organic Rankine Cycle to produce electricity, a proton exchange membrane electrolyzer to produce hydrogen, and an absorption refrigeration cycle to

*Corresponding Author's Email: i.mirzaee@urmia.ac.ir (I. Mirzaee)
URL: https://www.jree.ir/article_137507.html

Please cite this article as: Razmjoo, A., Mirzaee, I. and Pourmahmoud, N., "Thermodynamic investigation of a trigeneration ORC based system driven by condensing boiler hot water heat source using different working fluids", ***Journal of Renewable Energy and Environment (JREE)***, Vol. 8, No. 4, (2021), 108-115. (https://doi.org/10.30501/jree.2021.273786.1191).

produce cooling. From the results, 34.98 % and 49.17 % were calculated for the energy and exergy efficiencies, respectively. In a study by Yagli et al. [11], ORC system was used as the downstream cycle of a gas turbine. Various working fluids were investigated and compared. For the turbine inlet pressure between 10-25 bar, benzene had the best performing working fluid. At higher pressures, R123 had the highest performance. Wang et al. [12] analyzed a combined power plant to produce power and cooling in which ORC was applied to generate power. For finding the most appropriate working fluid, zeotropic mixtures were investigated. The results revealed that Isopentane (30 %) and R142b (70 %) zeotropic mixture had the highest efficiency. Mosaffa and Garousi Farshi [13] investigated the effect of using zeotropic mixture in an organic Rankine cycle for a salinity gradient solar pond-based power generation system. For increasing power generation, LNG cold energy is applied as a heat sink. The results showed that R245ca/R236ea mixture possessed an optimal thermal performance. In another study, a combined ORC and LNG regasification was studied by Choi et al. [14]. Results showed that the higher the total conductance for system design, the higher the heat duty should ORC take. Sun et al. [15] studied the selection of suitable configuration including single-stage Rankine Cycles (RC), two-stage RCs, and a regenerative-reheat RC using cold energy of LNG and low-grade heat. According to the optimization of eight working fluids, it was found that the best choice was the modified single-stage RC. Moreover, it was stated that for reheat RC, wet working fluids were better, while dry and isentropic fluids were better for regenerative RC and regenerative-reheat RC. Tian et al [16] investigated the performance of zeotropic and pure fluids in an ORC system. The heat source for the system was the waste heat of the ship engine and the heat sink was LNG. It was concluded that the zeotropic mixtures did not always have better performance than pure fluids. The results indicated that the maximum energy and exergy efficiencies were 22.09 % and 23.28 %.

In this paper, a novel combined cycle was introduced for power and cooling using a condensing boiler. Although in some researches, a combination of ORC and LNG is investigated, but to the knowledge of the authors, there are no studies in which condensing boiler was applied as the heat source. The purpose of the present study is to thermodynamically model and investigate the performances of the simple ORC, the regenerative ORC, and ORC with IHE in different operating conditions in terms of energy and exergy. In this paper, the Organic Rankine Cycle (ORC) and the absorption chiller are considered as upstream and downstream cycles, respectively. In this system, the energy required for the ORC evaporator and absorption chiller generator is prepared by condensing boiler hot water as the heat source while the heat sink is provided by LNG cold energy. Six working fluids with various thermodynamic behaviors have been chosen to analysis and comparison thermodynamically.

2. SYSTEM DESCRIPTION

Figure 1 provides the three different types of ORC systems and absorption refrigeration systems as well as LNG cold energy: (a) simple ORC, (b) ORC with IHE, and (c) regenerative ORC.

In a simple ORC, after absorbing the heat from condensing boiler hot water in the evaporator, the working fluid vaporizes to a saturated vapor at high pressure and temperature and is expended in the turbine to produce electricity. The exhausted working fluid leaving the turbine is condensed in the condenser by applying low-temperature natural gas. The saturated liquid is pumped to the preheater before entering the evaporator to complete the cycle. In the IHE ORC configuration, to enhance the efficiency of the system, part of the energy of the turbine exhaust stream is recovered by an internal heat exchanger. A Feed Organic Heater (FOH) is added for modifying a simple ORC system to a regenerative ORC. The organic fluid exiting the first pump is mixed by a hot turbine extracted stream. The stream leaving the FOH is saturated liquid. The hot ORC turbine leaving stream is applied as the heat source for the natural gas power generation system. In the LNG cycle, the saturated liquid low-temperature LNG is extracted and pumped into the ORC condenser and changes to saturated vapor. Then, in a heat exchanger, it is further heated which enters the turbine. After expansion and power generation, the natural gas is sent to the gas supplying system. For operating the absorption refrigeration system as the cooling subsystem, the hot water of condensing boiler provides a heat source to the generator. In this system, water and LiBr are the refrigerant and absorbent, respectively. The strong concentration of water solution in the absorber is pumped to the generator. In the generator, the solution is boiled out and the water vapor is separated from the solution. The vapor flows through the condenser and rejects heat and then, for providing a cooling effect, expands to the pressure of the evaporator. To complete the cycle, in the absorber, a weak solution stream from the generator and refrigerant stream from the evaporator should solve with each other.

3. WORKING FLUID SELECTION

Organic fluids are capable of operating at a very low temperature and pressure which is one of the advantages of ORC systems over the Rankine cycles. The selection of a suitable working fluid can improve the thermal and exergetic efficiency of ORC. The organic working fluids can be categorized into 3 categories (dry, wet, isentropic) dependant on the saturation vapor curve slope in the T-s diagram. The most suitable working fluid can be selected according to two important factors: possessing the highest efficiency when applying in a cycle and being eco-friendly working fluid, which means near-zero ODP and low GWP characteristics. In this paper, 6 working fluids (R141b, R124, R236fa, R245fa, R600, R123) were elected for thermodynamic analysis of the suggested system. The properties of the six chosen organic fluids are mentioned in Table 1.

4. THERMODYNAMICS APPROACH

4.1. Thermodynamics assumptions

For the thermodynamic investigation of the suggested combined cycles, the following assumptions are considered:

- Pressure and heat losses in all types of equipment are considered zero.
- All processes of components in the cycles are in a steady state.
- The condition of organic fluid is saturated vapor and saturated liquid in the evaporator and condenser, respectively.

- For natural gas simulation, it is assumed to be pure methane. The LNG is saturated liquid in the storage tank under the pressure of P0, while it changes to saturated vapor after passing through the condenser.

For thermodynamics analysis, it is sufficient to apply governing equations (conservation of mass and energy) to each component. These mentioned relations are needed to be applied to each part of the proposed system. Some of the required thermodynamics balance equations in this analysis are presented in Table 2.

Table 1. Properties of the candidate working fluids [17]

Fluid	M (g/mol)	T_{cri} (°C)	P_{cri} (bar)	T_b (°C)	ODP	GWP (100yr)	ASHRAE-SL	TYPE
R141b	116.95	204.35	42.12	32	0.12	7.2	NA	Isentropic
R124	136.48	122.28	36.2	-11.96	0	<1	A1	Isentropic
R236fa	152.04	124.92	32	-0.5	0	98	A1	Dry
R245fa	134	154.1	36.5	15.1	0	10	B1	Dry
R600	58.12	152	38	-1	0	~20	A3	Dry
R123	153	183.7	36.6	27.8	0.02	0.77	B1	Dry

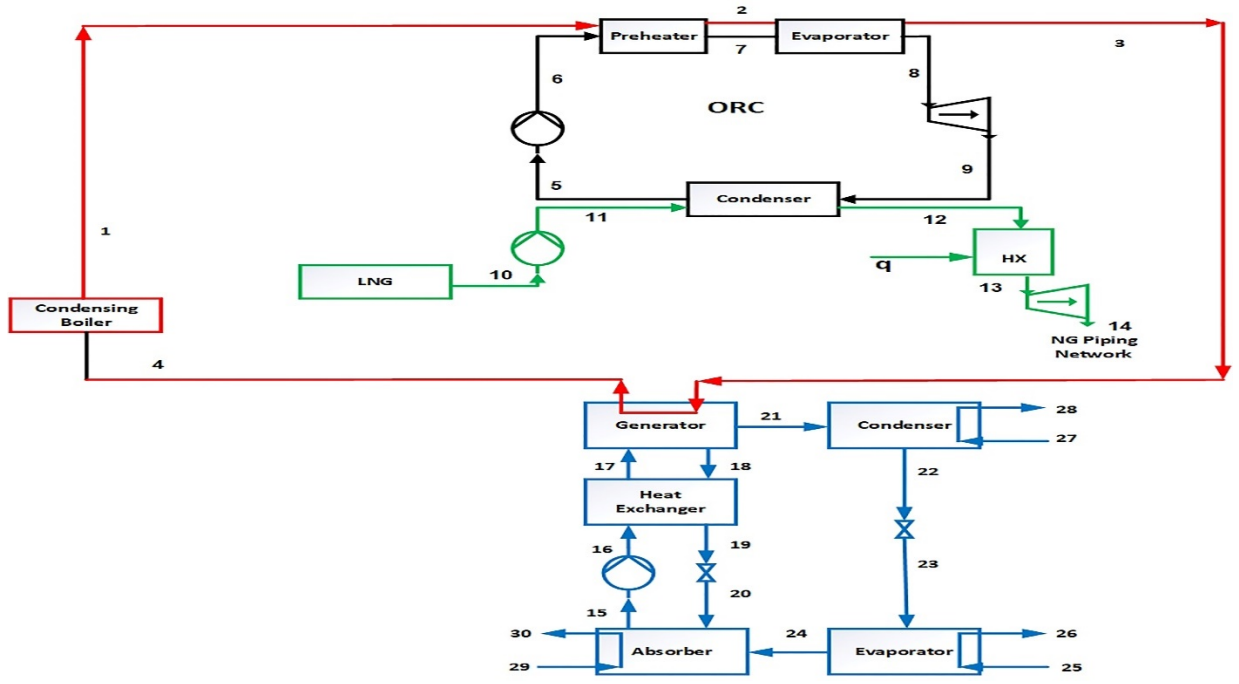

(a)

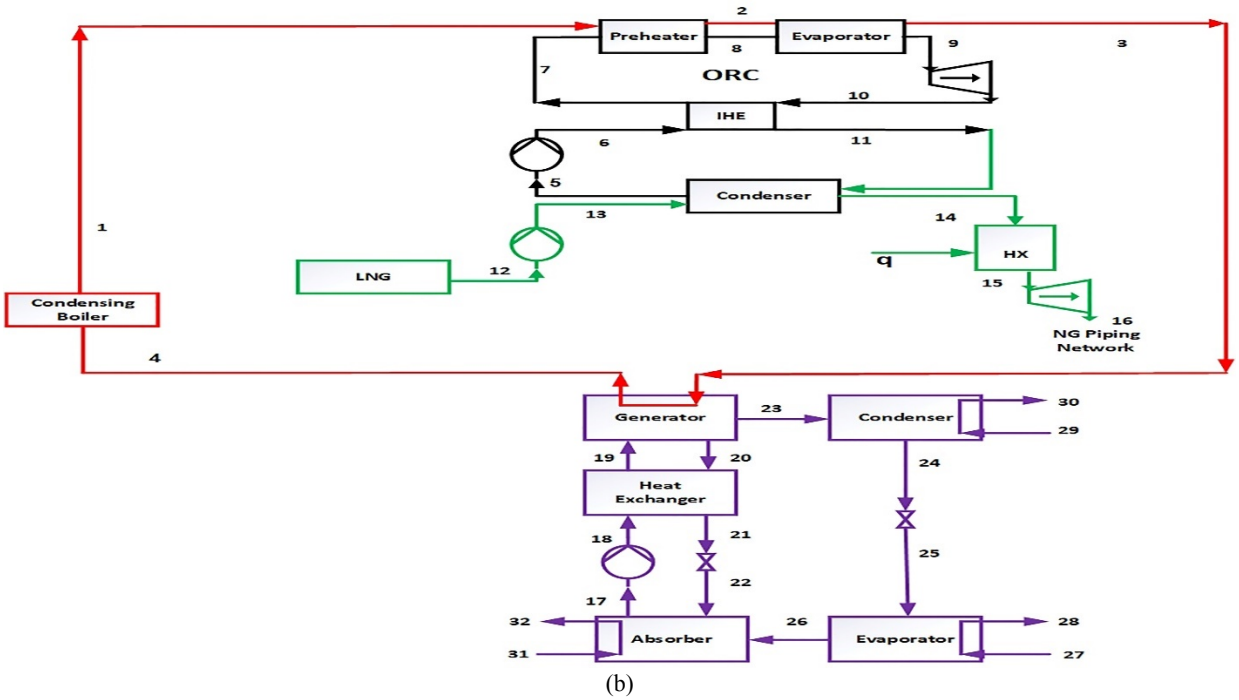

(b)

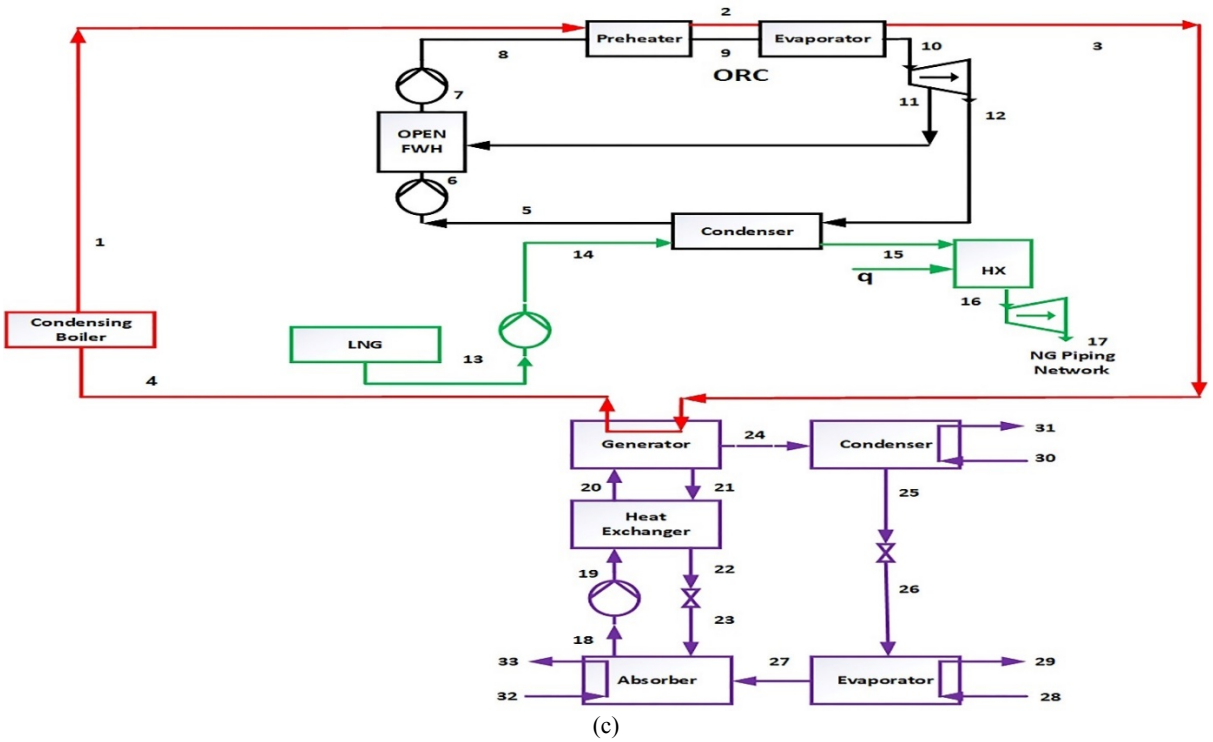

(c)

Figure 1. Cycle configuration: (a) simple, (b) ORC with IHE, and (c) regenerative ORC

Table 2. Some equations used in the thermodynamic analysis of the basic proposed system [18]

Component	Energy	Exergy
ORC		
Pump	$\dot{W}_p = \frac{\dot{m}_5 (h_6 - h_5)}{h_p}$	$\dot{m}_5 (e_5 - e_6) - \dot{W}_p$
Preheater	$\dot{Q}_{preh} = \dot{m}_6 (h_7 - h_6)$	$\dot{m}_2 e_2 + \dot{m}_7 e_7 - \dot{m}_1 e_1 - \dot{m}_6 e_6$
Evaporator	$\dot{Q}_{eva} = \dot{m}_7 (h_8 - h_7)$	$\dot{m}_9 e_9 + \dot{m}_8 e_8 - \dot{m}_2 e_2 - \dot{m}_7 e_7$
Turbine	$\dot{W}_t = \dot{m}_8 (h_8 - h_9)\, h_t$	$\dot{m}_8 (e_8 - e_9) - \dot{W}_t$
Condenser	$\dot{Q}_{con} = \dot{m}_9 (h_9 - h_5)$	$\dot{m}_9 (e_9 - e_5) - \dot{Q}_{con} (1 - \frac{T_0}{T_{con}})$
LNG		
Pump	$\dot{W}_p = \frac{\dot{m}_{10} (h_{11} - h_{10})}{h_p}$	$\dot{m}_{10} (e_{10} - e_{11}) - \dot{W}_p$
Heat exchanger	$\dot{Q}_{cool} = \dot{m}_{12} (h_{13} - h_{12})$	$\dot{m}_{12} (e_{12} - e_{13}) - \dot{Q}_{cool} (1 - \frac{T_0}{T_{cool}})$
Turbine	$\dot{W}_t = \dot{m}_{12} (h_{12} - h_{13})\, h_t$	$\dot{m}_{12} (e_{12} - e_{13}) - \dot{W}_t$
ARC		
Pump	$\dot{W}_p = \frac{\dot{m}_{15} (h_{16} - h_{15})}{h_p}$	$\dot{m}_{15} (e_{15} - e_{16}) - \dot{W}_p$
Expansion valve 1	----------	$\dot{m}_{19} (e_{20} - e_{19})$
Absorber	$\dot{Q}_{abs} = \dot{m}_{20} h_{20} + \dot{m}_{24} h_{24} - \dot{m}_{15} h_{15}$	$\dot{m}_{24} e_{24} + \dot{m}_{20} e_{20} - \dot{m}_{15} e_{15} + \dot{m}_{29} (e_{29} - e_{30})$
Generator	$\dot{Q}_{gen} = \dot{m}_{21} h_{21} + \dot{m}_{18} h_{18} - \dot{m}_{17} h_{17}$	$\dot{m}_3 (e_3 - e_4) + \dot{m}_{17} e_{17} - \dot{m}_{18} e_{18} - \dot{m}_{21} e_{21}$
Condenser	$\dot{Q}_{con} = \dot{m}_{21} (h_{21} - h_{22})$	$\dot{m}_{21} (e_{21} - e_{22}) - \dot{m}_{27} (e_{27} - e_{28})$
Expansion valve 2	----------	$\dot{m}_{22} (e_{23} - e_{22})$
Evaporator	$\dot{Q}_{eva} = \dot{m}_{24} (h_{24} - h_{23})$	$\dot{m}_{23} (e_{23} - e_{24}) - \dot{m}_{25} (e_{25} - e_{26})$

For thermodynamic analysis, a thermodynamics code is programmed using Engineering Equation Solver (EES), which is in good agreement with the works of other authors. Table 3 summarizes the basic assumptions and input parameters to simulate and analyze the systems.

Table 3. Thermodynamic parameters conditions considered in this study

Parameter	Value
Hot water inlet temperature	120 °C
Mass flow rate of hot water	255 kg s^{-1}
Hot water return temperature	20 °C
Evaporating temperature of the organic fluid	105 °C
Condensing temperature of the organic fluid	-35 °C
Turbine isentropic efficiency	85 %
Pump isentropic efficiency	90 %
ARC mass flow rate	150 kg s^{-1}
Effectiveness of heat exchanger	60 %
Ambient temperature	25 °C
Ambient pressure	101.3 kPa
LNG turbine inlet pressure	6500 kPa
NG network pressure	3000 kPa
ARC evaporator temperature	7 °C
ARC Generator temperature	80 °C
ARC Condenser temperature	35 °C
ARC Absorber temperature	40 °C

4.2. Model validation

For accurate measurement in the present work, the simple ORC system was validated under the same conditions using three different working fluids with Saleh et al. [19] and Hamdi et al. [20]. Table 4 depicts very good agreement believed to be satisfactory in most engineering problems.

Table 4. System validation of the present study and references [19] and [20]

Fluid	Mass flow rate (Kg s^{-1})	η_{ORC} (%)	Turbine exit temperature (°C)	References
R245fa	33.24	12.54	50.7	[13]
	33.21	13.13	47.79	[14]
	32.46	13.11	47.45	This study
Isopentane	17.44	12.75	58.47	[13]
	17.42	13.21	58.32	[14]
	17.05	13.06	57.55	This study
R600	17.75	12.58	48.43	[13]
	17.60	13.21	45.94	[14]
	16.83	13.22	48.35	This study

5. RESULTS AND DISCUSSION

Figures 2-4 compare the thermodynamic parameters including thermal efficiency, exergy efficiency, and net output power of the cycle obtained for simple, IHE, and regenerative ORC proposed cycles. R141b, R124, R236fa, R245fa, R600, and R123 are the working fluids investigated in the proposed systems. Figure 2 shows thermal efficiency, exergy efficiency, and net power output for the introduced working fluids and for the three different ORC system configurations. The comparison has been done under the same operating conditions for all configurations. It is inferred that for some of the studied fluids, the system efficiencies and net power are the same for the three different configurations. As a result, it can be expressed that a suitable fluid for the system depends on the configuration, and vice versa. According to the results, among the studied working fluids, R141b and R124 had the maximum and minimum thermal efficiencies, respectively. The same trend can be seen for the exergy efficiency and net power. It is concluded that the range of energy efficiencies for the simple ORC, IHE ORC, and regenerative ORC includes (27.83-30.02), (28.07-30.17), and (28.69-38.21) %, respectively. These exergy efficiency values were (16.62-20.37), (16.88-20.63), and (17.99-29.14) %. Finally, (8460-10804), (8722-10962), and (9383-16045) were obtained for net output power. Results depicted that among the three studied systems, the regenerative ORC-based system exhibited the best performance.

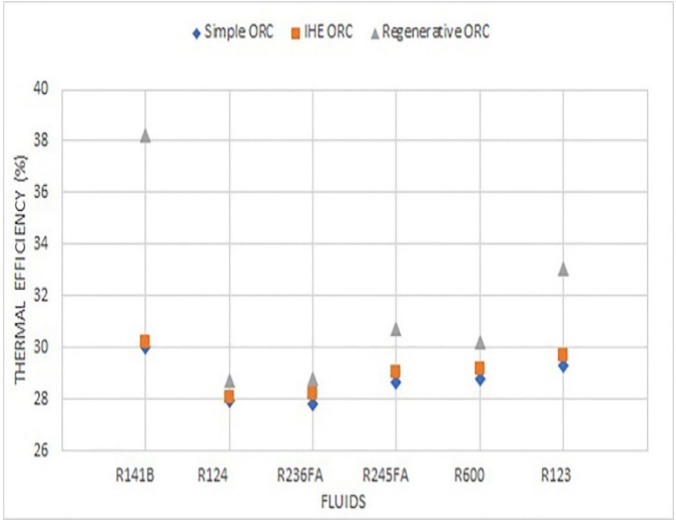

(a)

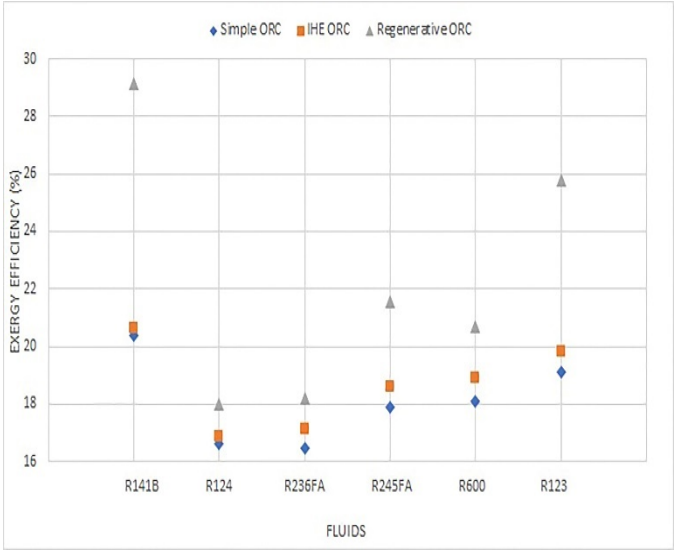

(b)

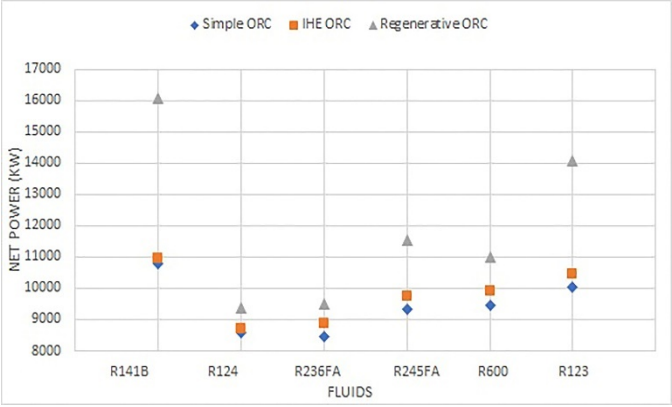

(c)

Figure 2. Comparison of thermodynamic parameters: (a) thermal efficiency, (b) exergy efficiency, and (c) net output power

Figure 3 displays the alteration of the thermal efficiency for the simple, IHE, and regenerative ORC-based configurations with the boiler temperature. We notice that for all configurations and working fluids, the energy efficiencies decrease with the increasing boiler temperature. The more energy the boiler produces, the less thermal efficiency the cycle can generate. The reason is that when the temperature of the boiler increases, the boiler produced heat increases and the net power of the system decreases. The rate of the produced heat in the boiler is greater than that of cooling effect and the net power of the system. The figures show that for the studied systems, R141b has the best performance among the set of considered fluids, while R124 and R236fa show the worst performance. Moreover, it is observed that the effect of increasing boiler temperaure is higher in the regenerative ORC than other configurations.

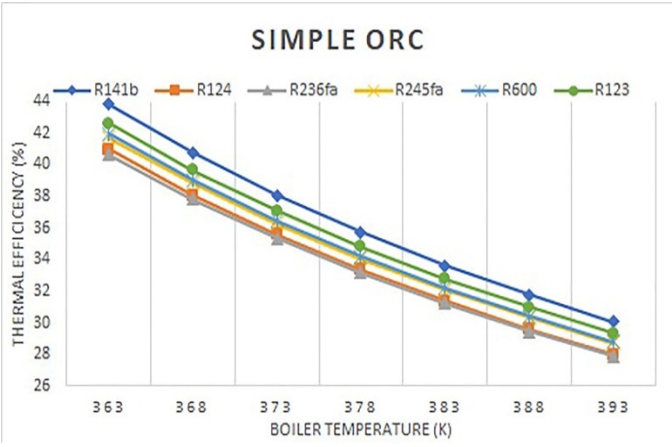

(a)

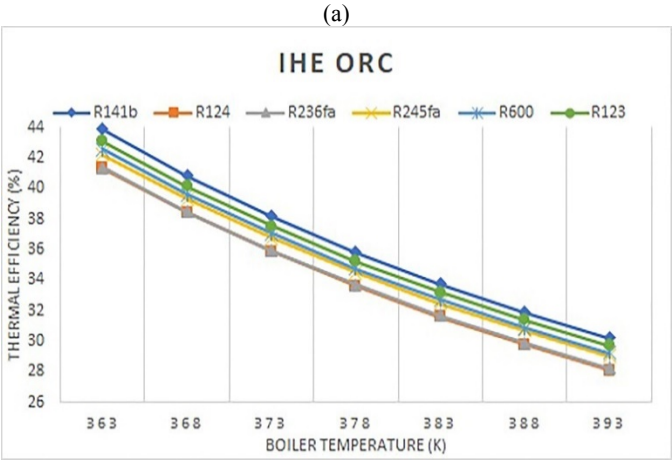

(b)

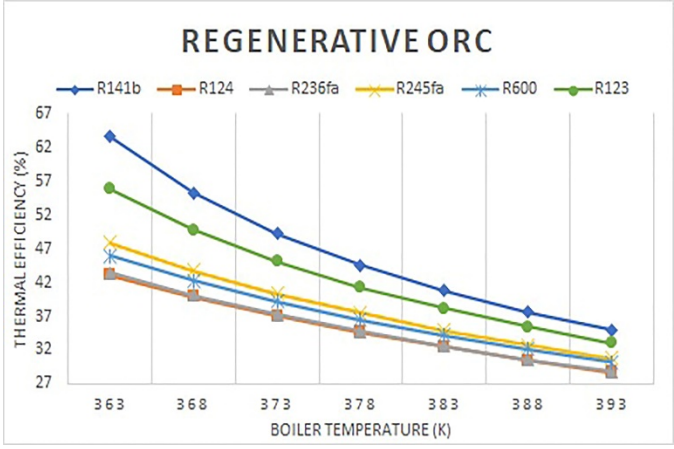

(c)

Figure 3. Variation in thermal efficiency versus boiler temperature: (a) simple ORC, (b) IHE ORC, and (c) regenerative ORC

Figure 4 depicts the variation in exergy efficiency versus boiler tempearature. According to the graphs, by increasing boiler temperature from 363 to 393 Kelvin, exergy efficiency of the three studied configurations is reduced. The extent of decrease in the exergy efficiency in the regenerative ORC system is more obvious. The reason for the decrease in the efficiency of the proposed systems is that by increasing the temperature of the boiler, the net power produced by the system is reduced and the boiler exergy increases. The extent of increase in boiler exergy is higher than that of the decrease in the net power output. Therefore, the exergy efficiency of the system decreases.

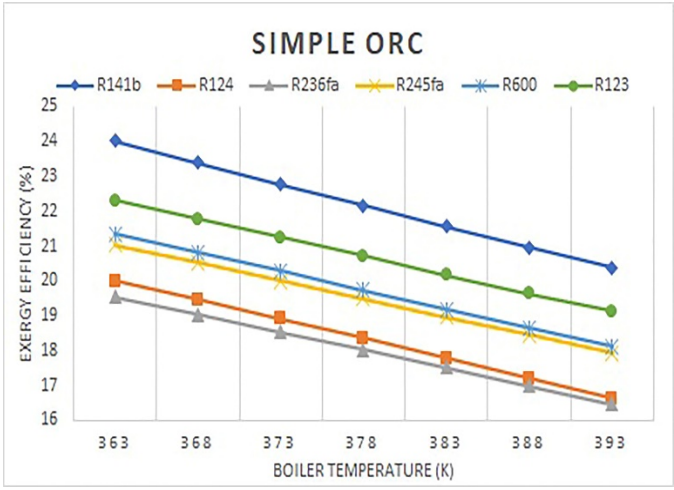

(a)

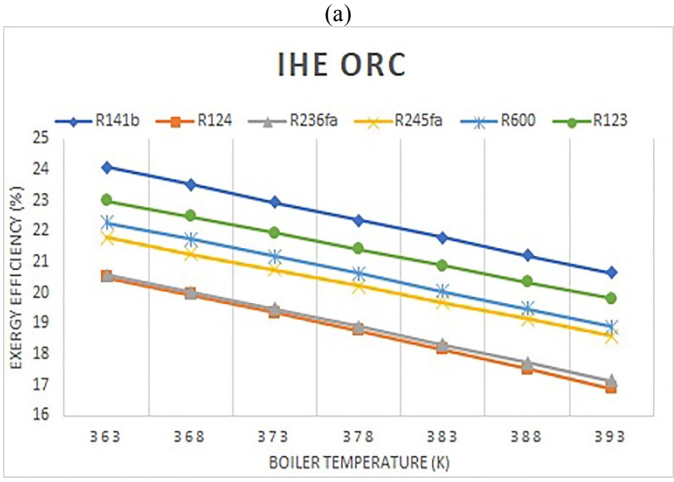

(b)

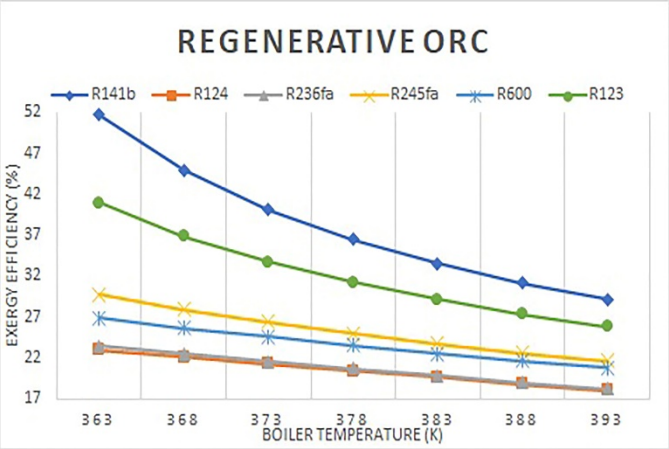

(c)

Figure 4. Variation of exergy efficiency versus boiler temperature: (a) simple ORC, (b) IHE ORC, and (c) regenerative ORC

6. CONCLUSIONS

In this paper, a thermodynamic analysis was conducted for a trigeneration system composed of ORC, LNG cold energy, and absorption refrigeration system which can efficiently recuperate the energy for condensing boiler hot fluid as a low-temperature heat source and entirely utilize LNG cold energy as a heat sink. The efficiency of the three main types of ORC systems, namely simple, internal heat exchanger, and regenerative ORCs are considered. Six working fluids (R141b, R124, R236fa, R245fa, R600, and R123) were analyzed and compared in the studied system from the thermodynamic standpoint.

Some of the obtained results can be summarized as follows:

- Among the presented working fluids, R141b had the highest thermal efficiency, exergy efficiency, and net power, while R124 and R236fa had the lowest amounts and the system with regenerative ORC had the maximum energy and exergy efficiencies.
- Thermal efficiencies for simple, IHE, and regenerative ORC ranged between (27.83-30.02), (28.07-30.17), and (28.69-38.21) %, respectively.
- Thermal efficiencies for simple, IHE, and regenerative ORC ranged between (27.83-30.02), (28.07-30.17), and (28.69-38.21) %, respectively.
- Exergy efficiencies for simple, IHE, and regenerative ORC ranged between (16.62-20.37), (16.88-20.63), and (17.99-29.14) %, respectively.
- Net power output for simple, IHE, and regenerative ORC ranged between (8460-10804), (8722-10962), and (9383-16045), respectively
- Increasing the boiler temperature would decrease the thermal and exergy efficiencies in all systems.

7. ACKNOWLEDGEMENT

The authors are grateful to Urmia University for the financial support of this study.

NOMENCLATURE

e	Specific exergy (kJ/kg)
h	Specific enthalpy (kJ/kg)
ṁ	Mass flow rate (kg/s)
Q̇	Heat transfer rate (kW)
T	Temperature (°C)
Ẇ	Power (kW)
Greek letters	
η	Thermal efficiency (%)
Subscripts	
0	Ambient
1, 2, 3, …	Cycle locations
abs	Absorber
con	Condenser
cool	Cooling
eva	Evaporator
gen	Generator
p	Pump
preh	Preheater
t	Turbine

REFERENCES

1. Peris, B., Navarro-Esbrí, J., Mol´es, F. and Mota-Babiloni, A., "Experimental study of an ORC (Organic Rankine Cycle) for low grade waste heat recovery in a ceramic industry", ***Energy***, Vol. 85, (2015), 534-542. (https://doi.org/10.1016/j.energy.2015.03.065).
2. Chatzopoulou, M.A. and Markides, C.N., "Thermodynamic optimisation of a high-electrical efficiency integrated internal combustion engine–Organic Rankine Cycle combined heat and power system", ***Applied Energy***, Vol. 226, (2015), 1229-1251. (https://doi.org/10.1016/j.apenergy.2018.06.022).
3. Koç, Y., Yağlı, H. and Kalay, I., "Energy, exergy, and parametric analysis of simple and recuperative organic rankine cycles using a gas turbine-based combined cycle", ***Journal of Energy Engineering***, Vol. 146, No. 5, (2020), 04020041. (https://ascelibrary.org/doi/10.1061/(ASCE)EY.1943-7897.0000693).
4. Maizza, V. and Maizza, A., "Unconventional working fluids in organic Rankine cycles for waste energy recovery systems", ***Applied Thermal Engineering***, Vol. 21, (2001), 381-390. (https://doi.org/10.1016/S1359-4311(00)00044-2).
5. Wang, M., Wang, J., Zhao, Y., Zhao, P. and Dai, Y., "Thermodynamic analysis and optimization of a solar-driven regenerative Organic Rankine Cycle (ORC) based on flat-plate solar collectors", ***Applied Thermal Engineering***, Vol. 50, (2013), 816-825. (https://doi.org/10.1016/j.applthermaleng.2012.08.013).
6. Safarian, S. and Aramoun, F., "Energy and exergy assessments of modified Organic Rankine Cycles (ORCs)", ***Energy Reports***, Vol. 1, (2015), 1-7. (https://doi.org/10.1016/j.egyr.2014.10.003).
7. Mosaffa, A.H., Mokarram, N.H. and Farshi, L.G., "Thermoeconomic analysis of combined different ORCs geothermal power plants and LNG cold energy", ***Geothermics***, Vol. 65, (2017), 113-125. (https://doi.org/10.1016/j.geothermics.2016.09.004).
8. Habibzadeh, A. and Jafarmadar, S., "Thermodynamic based working fluid selection for high-temperature waste heat recovery of a turbocharged diesel engine using Organic Rankine Cycle", ***Journal of Renewable Energy and Environment (JREE)***, Vol. 6, (2019), 16-23. (https://doi.org/10.30501/jree.2019.99360).
9. Behnam, P., Arefi, A. and Shafii, M.B., "Exergetic and thermoeconomic analysis of a trigeneration system producing electricity, hot water, and freshwater driven by low-temperature geothermal sources", ***Energy Conversion and Management***, Vol. 157, (2018), 266-276. (https://doi.org/10.1016/j.enconman.2017.12.014).
10. Akrami, E., Chitsaz, A., Nami, H. and Mahmoudi, S.M.S., "Energetic and exergoeconomic assessment of a multi-generation energy system based on indirect use of geothermal energy", ***Energy***, Vol. 124, (2017), 625-639. (https://doi.org/10.1016/j.energy.2017.02.006).
11. Yaglı, H., Koç, Y. and Kalay, H., "Optimisation and exergy analysis of an Organic Rankine Cycle (ORC) used as a bottoming cycle in a cogeneration system producing steam and power", ***Sustainable Energy Technologies and Assessments***, Vol. 44, (2021). (https://doi.org/10.1016/j.seta.2020.100985).
12. Wang, N., Zhang, S., Fei, Z., Zhang, W., Shao, L. and Sardari, F., "Thermodynamic performance analysis a power and cooling generation system based on geothermal flash, organic Rankine cycles, and ejector refrigeration cycle; Application of zeotropic mixtures", ***Sustainable Energy Technologies and Assessments***, Vol. 40, (2020), 100749. (https://doi.org/10.1016/j.seta.2020.100749).

13. Mosaffa, A.H. and Garousi Farshi, L., "Thermodynamic feasibility evaluation of an innovative salinity gradient solar ponds-based ORC using a zeotropic mixture as working fluid and LNG cold energy", ***Applied Thermal Engineering***, Vol. 186, (2021). (https://doi.org/10.1016/j.applthermaleng.2020.116488).
14. Choi, H.W., Na, S., Hong, S.B., Chung, Y., Kim, D.K. and Kim, M.S., "Optimal design of organic Rankine cycle recovering LNG cold energy with finite heat exchanger size", ***Energy***, Vol. 217, (2021). (https://doi.org/10.1016/j.energy.2020.119268).
15. Sun, Z., Zhao, Q., Wu, Z. and Lin, K., "Thermodynamic comparison of modified Rankine cycle configurations for LNG cold energy recovery under different working conditions", ***Energy Conversion and Management***, Vol. 239, (2021), 114141. (https://doi.org/10.1016/j.enconman.2021.114141).
16. Tian, Z., Zeng, W., Gu, B., Zhang, Y. and Yuan, X. "Energy, exergy, and economic (3E) analysis of an organic Rankine cycle using zeotropic mixtures based on marine engine waste heat and LNG cold energy", ***Energy Conversion and Management***, Vol. 228, (2021), 113657. (https://doi.org/10.1016/j.enconman.2020.113657).
17. Saleh, B., "Performance analysis and working fluid selection for ejector refrigeration cycle", ***Applied Thermal Engineering***, Vol. 107, (2016), 114-124. (https://doi.org/10.1016/j.applthermaleng.2016.06.147).
18. Ehyaei, M.A., Ahmadi, A., Assad, M.E.H. and Rosen, M.A., "Investigation of an integrated system combining an Organic Rankine Cycle and absorption chiller driven by geothermal energy: Energy, exergy, and economic analyses and optimization", ***Journal of Cleaner Production***, Vol. 258, (2020). 120780. (https://doi.org/10.1016/j.jclepro.2020.120780).
19. Saleh, B., Koglbauer, G., Wendland, M. and Fischer, J., "Working fluids for low temperature Organic Rankine Cycles", ***Energy***, Vol. 32, (2007), 1210-1221. (https://doi.org/10.1016/j.energy.2006.07.001).
20. Hamdi, B., Mabrouk, M.T., Kairouani, L. and Kheiri, A. "Analysis and optimization of three main organic Rankine cycle configurations using a set of working fluids with different thermodynamic behaviors", ***The European Physical Journal Applied Physics***, Vol. 78, (2017), 1-11. (https://doi.org/10.1051/epjap/2017170088).

ABSTRACTS

Green Synthesis of Heteroatom Doped Graphene from Natural and Chemical Precursors for Oxygen Reduction Reaction

Sedigheh Sadegh Hassani [a], Leila Samiee [b*]

[a] *Catalysis Research Division, Research Institute of Petroleum Industry (RIPI), Tehran, Tehran, Iran.*
[b] *Energy Technology Research Division, Research Institute of Petroleum Industry (RIPI), Tehran, Tehran, Iran.*

PAPER INFO

Paper history:
Received 10 November 2020
Accepted in revised form 12 June 2021

Keywords:
Alkaline Fuel Cell,
Fuel Cell,
Graphene,
Electrocatalyst,
Natural Resources

ABSTRACT

In the present work, natural biomass and chemical materials were applied as the heteroatom resources for modifying the Porous Graphene (PG) structure by pyrolysis method at 900 ºC. The physical and chemical characterizatons were performed by means of Scanning Electron Microscopy (SEM), Brunauer–Emmett–Teller (BET), Raman Spectroscopy, N_2 Adsorption-Desorption, and X-ray Photo-electron Spectroscopy (XPS). Furthemore, the behavior of the prepared materials was investigated by Cyclic Voltammetry (CV) and Rotating Disk Electrode (RDE). The obtained results indicated that doping of heteroatoms into the graphene framework was possible using a low-cost and environment-friendly biomass material as well as chemical sources. Moreover, one-step quarternary and tersiary co-doped graphene could be acheived using natural biomass. The prepared electrocatalysts using grape leaves and sulfur trioxide pyridine complex exhibit higher electrocatalytic performance as exampled which conducted the electrocatalyst in $4e^-$ pathway and showed high stability in methanol solutions during the process, confirming their considerable potential to Oxygen Reduction Reaction (ORR) as an electro-catalyst. Moreover, the onset potential of Gl300G-900 and GSP 900 (0.93 V vs RHE) is almost equal to the Pt/C 20 wt % (0.99 V vs RHE). These optimal prepared cathodes (Gl300G-900 and GSP 900) in the Microbial Fuel Cell (MFC) test lead to considerable power densities of 31.5 mW m^{-2} and 30.9.mW m^{-2}, which are close to 38.6 mW m^{-2} for the Pt/C 20 wt % cathode.

https://doi.org/10.30501/jree.2021.255422.1157

چکیده

در کار حاضر، مواد شیمیایی و زیست‌توده طبیعی به عنوان منابع هترواتمی به منظور اصلاح ساختار گرافن با روش پیرولیز در دمای ۹۰۰ °C استفاده شد. تعیین مشخصات فیزیکی و شیمیایی با استفاده از میکروسکوپ الکترونی روبشی (SEM)، بورنر-امت-تلر (BET)، طیف‌سنجی رامان، جذب-واجذب نیتروژن و طیف سنجی فوتوالکترون پرتو ایکس (XPS) انجام شد. علاوه بر این، رفتار مواد تهیه شده به‌وسیله الکترود دیسک چرخان (RDE) و ولتامتری چرخه‌ای (CV) مورد مطالعه قرار گرفت. نتایج به دست آمده نشان داد که دوپ کردن هترواتمها در چارچوب گرافن با استفاده از یک ماده زیست‌توده با هزینه کم و دوستدار محیط‌زیست، به خوبی منابع شیمیایی امکان‌پذیر است. علاوه بر این، سنتز گرافن دوپ شده چهارتایی و سه‌تایی تک مرحله‌ای با استفاده از زیست‌توده طبیعی قابل دستیابی است. الکتروکاتالیست تهیه شده با استفاده از برگ مو و سولفور تری اکسید پیریدین کمپلکس، عملکرد الکتروکاتالیستی بالایی را نشان می‌دهد و کاتالیست را در طول فرآیند در مسیر ۴ الکترونی هدایت می‌کند، همراه با پایداری بیشتر و تحمل بالاتر متانول نسبت به Pt/C ۲۰ wt % که پتانسیل قابل توجه آنها را به واکنش احیای اکسیژن به عنوان یک الکتروکاتالیست تأیید می‌کند.

Reuse of Wood-Based Industrial Wastewater through Optimization of Electrocoagulation Process Using Aluminum and Iron Electrodes

Abotaleb Bay [a], Payam Ghorbannezhad [b*], Javad Yazdan-Moghadam [c], Rahim Aali [d]

[a] *Environmental Health Research Center, Golestan University of Medical Sciences, Gorgan, Golestan, Iran.*
[b] *Department of Biorefinery Engineering, Faculty of New Technologies Engineering, Shahid Beheshti University, Tehran, Tehran, Iran.*
[c] *Center of Research and Development at Golestan Cellulose Group, Kimia Choob Golestan Inc. Company, Gorgan, Golestan, Iran.*
[d] *Research Center for Environmental Pollutants, Qom University of Medical Sciences, Qom, Qom, Iran.*

PAPER INFO

Paper history:
Received 06 November 2020
Accepted in revised form 06 July 2021

Keywords:
Electrocoagulation,
Iron,
Aluminum,
Medium Density Fiberboard,
Reuse Water

ABSTRACT

The wastewater treatment of Medium Density Fiberboard (MDF) is a harsh process because of its contents of high suspended solids, chemical oxygen demand, high molecular weight of lignin, and fatty acids. Electrocoagulation (EC) process was used for efficient removal of pollutants and reusing the water. The impact of aluminum and iron as sacrificial anodes on removal of Chemical Oxygen Demand (COD), Total Suspended Solid (TSS), turbidity, and Total Solid (TS) were investigated. A full quadratic model was deployed to optimize the EC process variables for pretreatment of MDF effluent through response surface methodology. The model results confirmed that the COD and TSS removal efficiency was enhanced upon increasing voltage and residence time; hence, other pollutants initially increased and then, decreased at higher levels. The comparison between aluminum and iron electrodes indicated that the polluted removal efficiencies of aluminum were higher than the iron electrode for MDF wastewater. The optimum values of voltage and residence time for electrocoagulation of MDF wastewater with aluminum were 33 V and 25 min, which resulted in 93 %, 89 %, 67 %, and 76 % for COD, TSS, turbidity, and TS removal, respectively. The implementation of electrocoagulation provided a possibility for reusing water and reducing water consumption in the MDF manufacturing process.

https://doi.org/10.30501/jree.2021.256108.1159

چکیده

تصفیه فاضلاب تخته فیبر دانسیته متوسط (MDF) به دلیل حجم زیاد مواد معلق جامد (TSS)، اکسیژن خواهی شیمیایی (COD)، وزن مولکولی زیاد لیگنین و اسیدهای چرب، فرآیندی بسیار سخت است. فرآیند انعقاد الکتریکی برای حذف بهینه آلودگی‌ها و استفاده مجدد از آب، به‌کار گرفته شده است. تأثیر آلومینیوم و آهن به عنوان قطب آند بر روی حذف COD، کل مواد معلق جامد (TSS)، شفافیت و مواد کل (TS) بررسی شده است. مدل آماری مجذور کامل، جهت بهینه‌سازی متغیرهای مستقل فرآیند (ولتاژ و زماند ماند) برای پیش‌تیمار فاضلاب MDF با روش سطح پاسخ به‌کار گرفته شد. نتایج بدست آمده نشان می‌دهد که میزان COD و TSS با افزایش ولتاژ و زمان ماند، بیشتر می‌شوند، درصورتی که دیگر آلودگی‌ها، ابتدا روند افزایشی و سپس کاهشی داشته‌اند. مقایسه الکترودهای آلومینیوم و آهن نشان می‌دهد که کارایی حذف آلودگی برای فاضلاب صنایع MDF به‌وسیله الکترودهای آلومینیوم بهتر از الکترود آهن است. مقدار بهینه ولتاژ و زمان ماند برای فرآیند انعقاد الکتریکی فاضلاب MDF با آلومینیوم، ولتاژ ۳۳ ولت و زمان ماند ۲۵ دقیقه می‌باشد که منجر به حذف ۹۳ درصد COD، ۸۹ درصد TSS، ۶۷ درصد شفافیت و ۷۶ درصد مواد کل شده است. اجرای فرآیند انعقاد الکتریکی موجب بازگردانی آب و کاهش مصرف آب در صنایع MDF شده است.

Production of Hydrogen via Renewable Energy and Investigation of Water Molecular Changes During Electrolysis Process

Iessa Sabbe Moosa [a], Hussein A. Kazem [b*], Laila Masoud Rashid Al-Iessi [c]

[a] *Research Cooperator with Public Authority for Water, Al-Buraimi Province, P. C.: 512, Oman.*
[b] *Faculty of Engineering, Sohar University, Sohar, P. C.: 311, Oman.*
[c] *Public Authority for Water, Al-Buraimi Province, P. C.: 512, Oman.*

PAPER INFO

Paper history:
Received 01 December 2020
Accepted in revised form 03 August 2021

Keywords:
Electrolysis,
Hydrogen,
Chemical-Physical Actions,
Eclectic Dipoles,
Dielectric Strength,
Transpiration

ABSTRACT

Studies on renewable energy are essential topics that help find new energy sources to replace fossil sources and promote environment friendliness. Hydrogen is the most practical alternative energy carrier source that meets the mentioned purposes. The mass of hydrogen element in the Earth's water was calculated and found to be about 2.1×10^{20} kg, which is greater than the mass of the world oil reserves by about 9×10^{5} times. In addition, essential details of water molecular arrangement were investigated in order to better understand the electrolysis of water. Also, the energy of covalent and hydrogen bonds per molecule of water was theoretically calculated and found to be about 8.17×10^{-19} J/molecule and 3.87×10^{-20} J/molecule, respectively. In the electrolysis process, two stages should be undertaken: the first stage was to break hydrogen bonds between water molecules, in which all water eclectic dipoles would align in the direction of the Applied Electric Field across the electrolysis unit. The second stage was to break water covalent bonds to generate H_2 and O_2 gases. Moreover, the lowest cost to generate one kg of hydrogen (0.4 $/kg) by electrolysis method using solar energy was about 0.4 $, which has already been proven, while this value was about 2.8 $/kg upon considering the average price of electricity of Oman in comparison.

https://doi.org/10.30501/jree.2021.260034.1167

چکیده

تحقیقات بر روی انرژی‌های تجدیدپذیر از موضوعات اساسی است که به یافتن منابع جدید انرژی جهت جایگزینی با منابع فسیلی کمک کرده و دوستی با محیط‌زیست را ارتقاء می‌دهد. هیدروژن عملی‌ترین حامل انرژی جایگزین است که اهداف مذکور را برآورده می‌کند. جرم عنصر هیدروژن در آب زمین در حدود $۲/۱ \times ۱۰^{۲۰}$ کیلوگرم محاسبه شده که از جرم ذخایر نفتی جهان حدود ۹×۱۰^{۵} برابر بیشتر است. بعلاوه، جزئیات اصلی آرایش مولکولی آب به منظور درک بهتر الکترولیز آب مورد بررسی قرار گرفت. همچنین، انرژی پیوندهای کووالانسی و هیدروژنی بر هر مولکول آب به ترتیب حدود $۸/۱۷ \times ۱۰^{-۱۹}$ ژول بر مولکول و $۳/۸۷ \times ۱۰^{-۲۰}$ ژول بر مولکول بصورت نظری محاسبه شد. در فرآیند الکترولیز، دو مرحله بایستی انجام گیرد: مرحله اول شکست پیوندهای هیدروژنی بین مولکول های آب بوده که در آن همه دو قطبی‌های چند سازگانی آب در جهت میدان الکتریکی اعمال شده در سراسر واحد الکترولیز هم‌راستا می‌شوند. مرحله دوم شکستن پیوندهای کووالانسی آب برای تولید گازهای H_2 و O_2 بود. بعلاوه، کمترین هزینه برای تولید یک کیلوگرم هیدروژن (۰/۴ دلار بر کیلوگرم) با روش الکترولیز با استفاده از انرژی خورشیدی حدود ۰/۴ دلار بود که قبلاً محقق شده است، در حالیکه این مقدار با در نظر گرفتن قیمت متوسط برق عمان جهت مقایسه، حدود ۲/۸ دلار بر کیلوگرم بود.

Effect of Covering Aperture of Conical Cavity Receiver on Thermal Performance of Parabolic Dish Collector: Experimental and Numerical Investigations

Sina Eterafi [a], Shiva Gorjian [a*], Majid Amidpour [b]

[a] *Department of Biosystems Engineering, Factuly of Agriculture, Tarbiat Modares University (TMU), P. O. Box: 14115-111, Tehran, Tehran, Iran.*
[b] *Department of Energy System Engineering, Factuly of Mechanical Engineering, K. N. Toosi University of Technology, P. O. Box: 19395-1999, Tehran, Tehran, Iran.*

P A P E R I N F O

Paper history:
Received 06 April 2021
Accepted in revised form 10 August 2021

Keywords:
Experimental Analysis,
Conical Cavity Receiver,
Ultra-White Glass Cover,
Parabolic Dish Concentrator

A B S T R A C T

In this study, the effect of covering the aperture area of a conical cavity receiver with an ultra-white glass on operational parameters of a Parabolic Dish Collector (PDC) was numerically and experimentally investigated under climate conditions of Tehran (35.44° N latitude and 51.10° longitude). The main components of the experimental setup include a dish reflector, a conical cavity receiver, Heat Transfer Fluid (HTF), hydraulic and cooling cycle, and a sun tracker. For this purpose, a conical cavity receiver with an ultra-white glass cover on its aperture was numerically modeled in Fortran software. During the evaluation, environmental parameters including ambient temperature, solar radiation, and wind speed were considered as inputs of the model. The results revealed fair agreement between the numerical and experimental data with the maximum error of approximately 4.63 % and 7.89 % for receivers with and without the glass cover on the aperture, respectively. For a steady-state analysis, the mean values of useful energy ($\dot{Q}_u$) absorbed by the receiver were calculated as 1,253.25 W and 987.68 W, while thermal efficiency (η_{th}) of the receiver was calculated as 52.61 % and 40.69 % for receivers with and without glass cover, respectively. The results revealed that both η_{th} and $\dot{Q}_u$ followed a similar trend of the variations in the HTF's temperature between the inlet and outlet of the receiver. Also, the overall heat loss coefficient (U_l) and the collector heat removal factor (F_r) were calculated as 420.76 W/m^2°C and 0.62 for the conical cavity receiver with the glass cover.

https://doi.org/10.30501/jree.2021.275871.1194

چکیده

در این مطالعه، تأثیر پوشاندن دهانه‌ی گیرنده‌ی حفره‌ای مخروطی با یک پوشش شیشه‌ای فوق شفاف بر پارامترهای عملکردی یک متمرکزکننده‌ی سهموی بشقابی (PDC) به صورت تجربی و عددی تحت شرایط آب و هوایی تهران مورد بررسی قرار گرفت. اجزای اصلی سامانه‌ی مورد مطالعه شامل منعکس‌کننده، گیرنده‌ی حفره‌ای مخروطی، سیال انتقال حرارت (HTF)، چرخه‌ی هیدرولیک و خنک‌کننده و ردیاب دو محوره‌ی نوری است. در این مطالعه، یک گیرنده‌ی حفره‌ای مخروطی با استفاده از یک پوشش شیشه‌ای فوق شفاف روی دهانه‌ی آن، به صورت عددی در نرم افزار Fortran مدل‌سازی شد. در این ارزیابی، پارامترهای محیطی از جمله تابش خورشید، دمای محیط و سرعت باد به عنوان ورودی‌های مدل در نظر گرفته شدند. نتایج نشان داد که توافق خوبی بین داده‌های عددی و تجربی با حداکثر خطای تقریبی ۴/۶۳ ٪ و ۷/۸۹ ٪ برای گیرنده‌های با و بدون پوشش شیشه روی دهانه‌ی حفره وجود دارد. مقدار متوسط انرژی مفید جذب‌شده ($\dot{Q}_u$) توسط گیرنده و بازده حرارتی (η_{th}) گیرنده در بازه‌ی ساعت‌های کاری پایدار سامانه، برای گیرنده‌ی دارای پوشش شیشه‌ای و بدون پوشش شیشه‌ای به ترتیب ۱۲۵۳/۲۵ W و ۹۸۷/۶۸ W و ۵۲/۶۱ ٪ و ۴۰/۶۹ ٪ محاسبه شدند. نتایج نشان دادند که راندمان حرارتی و انرژی مفید جذب‌شده در سامانه، هر دو روند مشابهی با اختلاف دمای HTF در ورودی و خروجی گیرنده را طی می‌کنند. همچنین، ضریب حذف حرارت متمرکزکننده (F_r) و ضریب تلفات حرارتی کل (U_l) برای گیرنده‌ی حفره‌ای مخروطی با پوشش شیشه‌ای در دهانه آن ۰/۶۲ و ۴۲۰/۷۶ W/m^2°C محاسبه شدند.

Effect of Nano Fluids on the Thermal Performance and Efficiency of Linear Fresnel Collector in Hot Summer Months

Najmeh Salehi [a], Arash Mirabdolah Lavasani [a*], Ramin Mehdipour [b], Mohammad Eftekhari Yazdi [a]

[a] *Department of Mechanical Engineering, School of Engineering, Central Tehran Branch, Islamic Azad University, Tehran, Iran.*
[b] *Department of Mechanical Engineering, Faculty of Engineering, Tafresh University, Tafresh, Markazi, Iran.*

PAPER INFO

Paper history:
Received 12 September 2020
Accepted in revised form 15 August 2021

Keywords:
Linear Fresnel Collectors,
Direct Steam Generation,
Critical Heat Flux,
Thermal Efficiency,
Nanofluid,
Look Up Table

ABSTRACT

One of the best and most important types of concentrating solar power plants is the linear Fresnel collector. The thermal performance and application of absorber in a solar power plant can be enhanced using direct steam generation technology. A particular discrepancy between the present study and others lies in our attempt at applying a new method for calculating critical heat flux based on Look-up Table. In the current study, effects of nanofluid on the length of the critical heat flux and convection heat transfer coefficient were investigated. The nanoparticles considered in this study were aluminum, silver, nickel, and titanium dioxide at concentrations of 0.01, 0.1, 0.3, 0.5, 1 and 2 %. Modeling results revealed that the heat transfer coefficient increased upon enhancing the volumetric concentration of nanoparticles, thereby improving this coefficient at 2 vol. % nickel nanoparticles, which was 10.6 % above the value of pure water. On the other hand, thermal efficiency was enhanced when nickel nanoparticles were dispersed in pure water such that increase rates of thermal efficiency equaled 11.2, 10.8 and 11.3 % in the months of June, July, and August, respectively, when the volume concentration of nanoparticles was 0.5 %.

https://doi.org/10.30501/jree.2020.243043.1141

چکیده

یکی از مهمترین انواع متمرکزکننده‌های نیروگاه خورشیدی، متمرکزکننده‌های خطی فرزنل می‌باشند و عملکرد حرارتی جاذب در نیروگاه خورشیدی با استفاده از تکنولوژی تولید مستقیم بخار بهبود می‌یابد. تفاوت ویژه این تحقیق با سایر تحقیقات، استفاده از یک روش جدید در زمینه محاسبه شار حرارتی بحرانی بر مبنای جدول LUT می‌باشد. در مطالعه حاضر، اثر نانوسیال بر موقعیت شار حرارتی بحرانی و ضریب انتقال حرارت جابجایی بررسی شد. نانوذرات درنظر گرفته شده در این مطالعه، آلومینیوم، نقره، نیکل و دی اکسید تیتانیوم با غلظت‌های ۰/۰۱، ۰/۱، ۰/۳، ۰/۵، ۱ و ۲ درصد می‌باشند. نتایج مدلسازی نشان داده‌اند که با افزایش غلظت حجمی نانوذرات، ضریب انتقال حرارت افزایش یافته است، که به موجب آن بهترین نتیجه بر روی نقطه شار حرارتی بحرانی در نانوذرات نیکل با غلظت حجمی ۲ درصد حاصل شد، به‌طوری‌که نسبت به آب خالص، معادل ۱۰/۶ درصد بهبود یافته است. از سوی دیگر، در مورد راندمان حرارتی هنگامی که نانوذرات نیکل با غلظت حجمی ۰/۵ درصد در آب خالص پخش می‌شوند، برای این ویژگی در ماه های ژوئن، جولای و آگوست به ترتیب افزایشی معادل ۱۱/۲، ۱۰/۸ و ۱۱/۳ درصد به‌دست آمده است.

An Experimental and Analytical Study of Influential Parameters of Parabolic trough Solar Collector

Daryoosh Borzuei, Seyed Farhan Moosavian, Abolfazl Ahmadi *, Rouhollah Ahmadi *, Kourosh Bagherzadeh

School of New Technologies, Department of Energy Systems Engineering, Iran University of Science & Technology, Tehran, Tehran, Iran.

PAPER INFO

Paper history:
Received 14 December 2020
Accepted in revised form 17 August 2021

Keywords:
Solar Collector,
PTC,
Heat Transfer Fluid,
Vacuum Tube,
Analytical Study

ABSTRACT

Energy plays a vital role in all human life activities. Due to the problems caused by fossil fuels in recent decades such as global warming, greenhouse gas emissions, ozone depletion, etc., the use of renewable and clean energy has been considered. An experimental facility for the acquisition of reliable data from Parabolic Trough Solar Collectors (PTCs) was established to develop a robust analytical model. A wide range of Heat Transfer Fluid (HTF) flow rates (0.0372-0.1072 kg/s) and solar radiation (400-900 W/m^2) were used to determine PTC parameters such as the outlet temperature of HTF loss and temperature distribution. Vacuum conditions in the receiver were considered effective in terms of thermal efficiency. Also, three types of HTF including two oil fluids (Syltherm 800 and S2) and water were examined. The temperature distribution showed that when Syltherm 800 or S2 passed through the absorber tube, the outlet temperature was higher than water: 2.84 % for Syltherm 800 and 3.72 % for S2. Since the absorber tube temperature was much higher than water, the heat loss in this condition was considered for oil HTF. Of note, the results demonstrated that use of the vacuum tube could diminish heat loss for the oil HTF. The effect of solar intensity increases from 600 W/m^2 to 900 W/m^2 on the maximum temperature of the receiver tube indicated that when Syltherm 800 was used as an HTF, this temperature increased by 35.1 % (from 167 °C to 219 °C), while this percentage was 32.7 % and 6.8 % for S2 and water, respectively.

https://doi.org/10.30501/jree.2021.261647.1172

چکیده

انرژی در تمام فعالیتهای زندگی انسان نقش حیاتی دارد. با توجه به مشکلات ناشی از سوختهای فسیلی در دههای اخیر، مانند گرم شدن کره زمین، انتشار گازهای گلخانه ای، تخریب لایه اوزون و ...، استفاده از انرژیهای تجدیدپذیر مورد توجه قرار گرفته است. پژوهشی تجربی برای دستیابی به دادههای قابل اعتماد از طریق کلکتورهای خورشیدی سهموی برای ایجاد یک مدل تحلیلی قوی انجام شده است. برای تحلیل برخی پارامترهای کلکتورهای خورشیدی مانند دمای خروجی و حرارت اتلافی و توزیع دما، از دبی جریان سیال کاری (۰/۱۰۷۲–۰/۰۳۷۲ کیلوگرم بر ثانیه) و تابش خورشید (۹۰۰-۴۰۰ وات بر مترمربع) استفاده میشود. وجود شرایط خلأ در فاصله لوله جاذب و کاور از نظر بازده حرارتی، تأثیرات مثبتی را ایجاد میکند. همچنین، سه نوع سیال کاری شامل دو روغن (Syltherm 800 و S2) و آب مورد بررسی قرار گرفت. توزیع دما نشان میدهد که وقتی Syltherm 800 یا S2 از لوله جاذب عبور میکند، دمای خروجی بالاتر از آب است. نکته قابل توجه، نتایج نشان میدهد که استفاده از لوله خلأ میتواند اتلاف حرارت در روغنها را کاهش دهد. تأثیر افزایش شدت خورشید از ۶۰۰ وات بر مترمربع به ۹۰۰ وات بر مترمربع بر روی حداکثر دمای سطح لوله جاذب افزایش نشان میدهد که در صورت استفاده از Syltherm 800 به عنوان سیال کاری، این دما ۳۵/۱ ٪ افزایش مییابد، درحالیکه درصورت استفاده از S2 و آب این افزایش به میزان ۳۲/۷ و ۶/۸ درصد خواهد بود.

Renewable Energy-Based Systems on a Residential Scale in Southern Coastal Areas of Iran: Trigeneration of Heat, Power, and Hydrogen

Mehdi Jahangiri [a*], Fatemeh Karimi Shahmarvandi [b], Reza Alayi [c]

[a] *Department of Mechanical Engineering, Shahrekord Branch, Islamic Azad University, Shahrekord, Iran.*
[b] *Department of Biomedical Engineering, Shahrekord Branch, Islamic Azad University, Shahrekord, Iran.*
[c] *Department of Mechanical Engineering, Germi Branch, Islamic Azad University, Germi, Iran.*

PAPER INFO

Paper history:
Received 14 December 2020
Accepted in revised form 21 August 2021

Keywords:
CO_2 Penalty,
Interest Rate,
Fuel Cell,
Gas Boiler

ABSTRACT

The use of small-scale Combined Heat and Power (CHP) to meet the electrical and thermal needs of buildings has grown exponentially and plans have been made in Iran to expand these systems. In view of the above, in the present work, for the first time, sensitivity analysis has been performed on the parameters of natural gas price, annual interest rate, and the price of pollutant penalties. The CHP system studied included fuel cell, biomass generator, solar cell, wind turbine, and gas boiler. The techno-econo-enviro simulations were performed by HOMER software and the study area was Abadan. The use of a dump load to convert excess electricity into heat and heat recovery in a biomass generator and fuel cell are other advantages presented by the present work. The minimum Cost of Energy (COE) is 1.16 $/kWh. The results also showed that the use of biomass generators was economical when the annual interest rate was 30 %. The significant effect of using dump load on the required heat supply and the lowest price per kg of hydrogen produced equal to $ 35.440 are other results of the present work. In general, the results point to the superiority of solar radiation potential over wind energy potential of the study area and the prominent role of dump load in providing heat on a residential scale is clearly seen. Also, for the current situation, using biomass is not cost-effective.

https://doi.org/10.30501/jree.2021.261980.1170

چکیده

استفاده از تولید همزمان برق و حرارت در مقیاس کوچک و برای تأمین نیازهای الکتریکی و حرارتی ساختمان‌ها رشد فزاینده‌ای داشته و در ایران نیز برنامه‌ریزی‌هایی جهت گسترش این سیستم‌ها صورت گرفته است. با توجه به موارد مطرح شده، در کار حاضر برای نخستین بار با استفاده از شبیه‌سازی‌های انجام شده توسط نرم‌افزار HOMER، به آنالیز حساسیت تأثیر قیمت گاز طبیعی، نرخ بهره سالیانه و قیمت جریمه آلاینده‌ها روی عملکرد فنی-اقتصادی-زیست‌محیطی یک سیستم تولید همزمان برق و حرارت شامل پیل سوختی، ژنراتور زیست‌توده، سلول خورشیدی، توربین بادی و بویلر گازسوز در شهر آبادان پرداخته شده است. استفاده از یک dump load برای تبدیل برق مازاد به حرارت و بازیافت حرارت در ژنراتور زیست‌توده و پیل سوختی از دیگر مزیت‌های کار حاضر هستند. کمترین میزان قیمت انرژی تولیدی برابر ۱/۱۶ دلار به ازای هر کیلووات ساعت می‌باشد. همچنین نتایج نشان دادند که استفاده از ژنراتور زیست‌توده هنگامی صرفه اقتصادی دارد که نرخ بهره سالیانه ۳۰ ٪ باشد. تأثیر چشمگیر استفاده از dump load در تأمین حرارت مورد نیاز و کمترین قیمت هر کیلوگرم هیدروژن تولیدی برابر با ۳۵/۴۴۰ دلار، از دیگر نتایج کار حاضر می‌باشند. در مجموع نتایج کار حاضر حاکی از برتری پتانسیل تابش خورشید بر پتانسیل انرژی باد در منطقه مورد بررسی بوده و نقش پررنگ dump load در تأمین حرارت در مقیاس مسکونی به‌وضوح دیده می‌شود. همچنین برای شرایط فعلی، استفاده از زیست‌توده مقرون به صرفه نمی‌باشد.

Effect of Technological Mismatch on Photovoltaic Array: Analysis of Relative Power Loss

Stephen Ndubuisi Nnamchi [a*], Onyinyechi Adanma Nnamchi [b], Kevin Nnanye Nwaigwe [c], Zaid Oluwadurotimi Jagun [d], Johnson Ugochukwu Ezenwankwo [a]

[a] *Department of Mechanical Engineering, School of Engineering and Applied Sciences, Kampala International University, P. O. Box: 20000 Ggaba, Kansanga, Kampala, Uganda.*
[b] *Department of Agricultural Engineering and Bio Resources, Michael Okpara University of Agriculture, Umudike, Umuahia, Nigeria.*
[c] *Department of Mechanical Engineering, Faculty of Engineering and Technology, University of Botswana, Gaborone, Botswana.*
[d] *Department of Computer Engineering, Olabisi Onabanjo University, Ibogun, Nigeria.*

PAPER INFO

Paper history:
Received 13 February 2021
Accepted in revised form 20 September 2021

Keywords:
Configuration (S, P, SP),
Photovoltaic,
Mismatched Array,
Relative Power Loss,
Computational Scheme

ABSTRACT

This study conducts a comparative evaluation of the performance of modules and the arrays under standard test conditions. An equivalent circuit model was developed alongside a computational scheme. The model input data were obtained from the manufacturer's specification datasheets. They were used to analyse the maximum Fill Factor (FF) and Relative Power Losses (RPL) for Parallel (P), Series (S) and Series-Parallel (SP) configurations. For matching modules, the RPL was insignificant, but for mismatched modules, the parallel configuration (P) and series-parallel (SP) yielded RPL of 1.3 %, while the series configuration (S) produced RPL of 2.6 %. Thus, short circuit defects associated with the P and SP configuration were well below the open circuit defects associated with the series configuration (S). These results clearly show that the large photovoltaic plant needs to be configured with multiple blocks or strings of SP configuration in order to suppress RPL. In addition, the designer and installers of large solar power plants should adopt modules with uniform electrical and thermal properties in the construction of large solar power plants. The trivial RPL associated with the matched modules should be taken into consideration, as well.

https://doi.org/10.30501/jree.2021.272915.1189

چکیده

این مطالعه، ارزیابی مقایسه‌ای عملکرد ماژول‌ها و آرایه‌ها را در شرایط استاندارد آزمایش انجام می دهد. یک مدل مدار معادل در کنار یک طرح محاسباتی توسعه داده شد. داده‌های ورودی مدل از برگه‌های مشخصات سازنده به‌دست آمده است. از آنها برای تجزیه و تحلیل حداکثر تغییرات ضریب پوششی (FF) و افت توان نسبی (RPL) برای تنظیمات موازی (P)، سری (S) و سری-موازی (SP) استفاده شد. برای تطبیق ماژول‌ها، RPL ناچیز بود، اما برای ماژول‌های ناهماهنگ، پیکربندی موازی (P) و سری-موازی (SP)، RPL ایجاد شده ۱/۳ ٪ می‌باشد، در حالی که پیکربندی ردیف (S)، RPL تولید شده ۲/۶ ٪ می‌باشد. بنابراین، نقص‌های اتصال کوتاه مرتبط با پیکربندی P و SP بسیار کمتر از نقص‌های مدار باز مرتبط با پیکربندی سری (S) بود. این نتایج به وضوح نشان می‌دهد که نیروگاه بزرگ فتوولتائیک برای کاهش RPL، نیاز به پیکربندی با چندین بلوک یا رشته پیکربندی SP دارد. علاوه براین، طراح و نصب‌کننده نیروگاه‌های بزرگ خورشیدی باید در ساخت نیروگاه‌های بزرگ خورشیدی از ماژول‌هایی با خواص الکتریکی و حرارتی یکنواخت استفاده کنند. RPL ناچیز مرتبط با ماژول‌های منطبق نیز باید مورد توجه قرار گیرد.

Performance Analysis of a Novel Compressed Carbon Dioxide Storage Model Integrated with Solar Energy

Samira Jafari, Mehran Ameri *

Department of Mechanical Engineering, School of Engineering, University of Shahid Bahonar, P. O. Box: 76175-133, Kerman, Kerman, Iran.

PAPER INFO

Paper history:
Received 11 February 2021
Accepted in revised form 22 September 2021

Keywords:
Exergy Analysis,
Energy Storage,
Carbon Dioxide,
Solar Energy

ABSTRACT

As a result of growing energy demand, shortage of fossil fuel resources, climate change, and environmental protection, the need for renewable energy sources has been growing rapidly. However, there is an urgent need to cope with intermittency and fluctuation of renewable energies. Various energy storage systems are considered as appropriate solutions to the above-mentioned problem. In the present manuscript, a novel compressed carbon dioxide energy storage system was proposed. Furthermore, an extra thermal energy storage with Therminol VP-1 as a working fluid, coupled with Parabolic Trough Collector (PTC), was added to the system. This integration is conducive to rising the inlet temperature of turbines and reducing the work load that should be done by the compressors. In the present study, a method based on software product including Engineering Equation Solver (EES) for determining thermodynamic characters per component and System Advisor Model (SAM) was employed to model the solar field for a desired location. Energy and exergy analyses were conducted to evaluate the whole cycle performance during charging and discharging periods. In this study, the city of Kerman located in the south-eastern part of Iran, with Direct Normal Incidence (DNI) of 950 $\frac{W}{m^2}$, was selected for the present modeling. The results of a random day (June 22/2019) at time 15:00 represented the exergy efficiency of 66.98 % and the round trip efficiency of 93.14 %. High exergy efficiency and round trip efficiency of this system make this idea applicable to enhancing the total performance of the entire system.

https://doi.org/10.30501/jree.2021.272790.1188

چکیده

با افزایش نیاز به انرژی، کمبود منابع فسیلی، تغییرات اقلیمی و حفاظت از محیط‌زیست، نیاز به منابع انرژی تجدیدپذیر افزایش پیدا کرده است. برای حل مشکل ذات نوسانی و متناوب انرژی های نو، روش‌های ذخیره‌سازی متنوعی معرفی شده‌اند. در تحقیق حاضر، یک روش ذخیره‌ی انرژی جدید بر پایه‌ی دی‌اکسیدکربن ارائه شده است. در ادامه، یک واحد ذخیره‌ی انرژی گرمایی مجزا با سیال کاری ترمینول وی‌پی-۱ که با کلکتور سهموی خطی ترکیب شده است، به سیستم اضافه شده است. این عمل منجر به افزایش دمای ورودی توربین و در نهایت کاهش کار انجام شده توسط کمپرسورها می‌شود. در این مطالعه، از ترکیب نرم‌افزارهای EES برای تعیین خصوصیات ترمودینامیکی هر جزء و SAM برای مدل‌سازی میدان خورشیدی استفاده شده است. در ادامه آنالیز انرژی و اگزرژی انجام شده است تا عملکرد کل سیستم در طول زمان شارژ و دشارژ بررسی شود. در این مقاله، شهر کرمان واقع در جنوب شرق کشور ایران با مقدار تشعشع نرمال ۹۵۰ $\frac{W}{m^2}$ برای بررسی نتایج انتخاب شده است. نتایج برای یک روز انتخابی (۲۲ماه ژوئن سال ۲۰۱۹) در ساعت سه بعد از ظهر بازده اگزژی ۶۶/۹۸ ٪ و بازده انرژی ۹۳/۱۴ ٪ را نشان می‌دهند. بازده‌های بالا نمایان‌گر عملکرد قابل قبول سیستم است.

Evaluation of Power Performance of a PV Module with MPPT Solution Using MATLAB Simulation

Md. Tamim Hossain, Md. Atiqur Rahman, Suman Chowdhury *

Department of Electrical and Electronic Engineering, International University of Business Agriculture and Technology, Dhaka-1230, Bangladesh.

PAPER INFO

Paper history:
Received 25 February 2021
Accepted in revised form 22 September 2021

Keywords:
PV,
MPPT,
Incremental Conductance,
Boost Converter,
MATLAB,
Solar Power

ABSTRACT

In the context of increasing emission of greenhouse gasses in the environment due to fossil fuel burning, this paper attempts to describe the significance of Maximum Power Point Tracking (MPPT) by investigating the power performance of photovoltaic modules with MATLAB simulation. MPPT algorithm was employed to secure maximum power from PV module. The boost converter whose pulse is linked to MPPT algorithm restricts the flow of load power and controls the current and voltage of PV panels. The whole design of the solar model, boost converter, and MPPT controlled algorithms was done in the SIMULINK to prioritize the system in simulation. The main concept employed in this paper was to develop a power generation process with MPPT algorithm and to provide information for future use. In this paper, all simulations along with the PV power generation process were done in MATLAB. This research could potentially play a vital role in mitigating the world fuel crisis.

https://doi.org/10.30501/jree.2021.274901.1193

چکیده

با رویکرد به انتشار فزاینده‌ی گازهای گلخانه‌ای به محیط‌زیست در اثر سوزاندن سوختهای فسیلی، این مقاله می‌کوشد بر اهمیت «ردیابی نقطهٔ بیشینه توان دریافتی (MPPT)» با کمک گرفتن از شبیه‌سازی بوسیله نرم افزار MATLAB برای بررسی عملکرد توان خروجی آرایه‌های فتوولتائیک تأکید کند. الگوریتم MPPT برای تضمین بالاترین توان خروجی از آرایه فتوولتائیک بکار گرفته شد. مبدل تقویت‌کننده که پالس آن به الگوریتم MPPT متصل است، جریان توان بار را محدود کرده و جریان و ولتاژ پانل‌های فتوولتائیک را کنترل می‌کند. طراحی یکپارچه‌ی مدل خورشیدی، مبدل تقویت‌کننده و الگوریتم‌های ردیابی نقطهٔ بیشینه توان دریافتی در محیط سیمولینک (SIMULINK) به انجام رسید تا اولویت‌بندی اجزای سامانه در شبیه‌سازی مراعات شود. مفهوم اصلی بکارگرفته شده در این مقاله، توسعه فرایند تولید توان الکتریکی با استفاده از الگوریتم ردیابی نقطه بیشینه توان دریافتی و فراهم‌سازی اطلاعات سودمند برای بهره‌گیری‌های آینده بوده است. همه شبیه‌سازی‌ها همراه با فرایند تولید توان در پنل‌های خورشیدی فتوولتائیک در محیط نرم افزار MATLAB انجام شد. پژوهش حاضر می‌تواند نقشی کلیدی در تخفیف بحران جهانی سوخت ایفا کند.

Thermodynamic Investigation of a Trigeneration ORC Based System Driven by Condensing Boiler Hot Water Heat Source Using Different Working Fluids

Aref Razmjoo, Iraj Mirzaee*, Nader Pourmahmoud

Department of Mechanical Engineering, Faculty of Engineering, Urmia University, Urmia, West Azerbaijan, Iran.

PAPER INFO

Paper history:
Received 04 March 2021
Accepted in revised form 27 September 2021

Keywords:
Organic Rankine Cycles (ORCs),
LNG Cold Energy,
Condensing Boiler,
Working Fluid,
Thermodynamics Analysis

ABSTRACT

This study conducts thermodynamic analysis on three trigeneration cycles including Organic Rankine Cycle (ORC), Liquefied Natural Gas (LNG) cold energy, and absorption refrigeration cycle in order to select appropriate working fluids. Different types of ORC cycles including simple ORC, regenerative, and ORC with Internal Heat Exchange (IHE) were investigated. For those types, the operation of six working fluids with different thermodynamic behaviors (R141b, R124, R236fa, R245fa, R600, and R123) was evaluated. In power plants, a low-grade heat source was provided by condensing boiler hot water energy while the thermal sink was prepared by cold energy of LNG. The effect of boiler temperature variation on energy and exergy efficiencies was investigated. According to the derived results, regenerative ORC-based systems possessed maximum energy and exergy efficiencies, while simple ORC and ORC with internal heat exchanger exhibited approximately the same quantities. Also, among these analyzed working fluids, R141b had the maximum energetic and exergetic efficiencies, while R124 and R236fa had minimum performance.

https://doi.org/10.30501/jree.2021.273786.1191

چکیده

تجزیه و تحلیل ترمودینامیکی برای انتخاب سیال عامل مناسب برای سه‌چرخه تولید سه‌گانه شامل چرخه آلی رانکین (ORC) ، گاز طبیعی مایع (LNG) و چرخه تبرید جذبی انجام می‌گیرد. انواع مختلف چرخه‌های رانکین آلی (ORC) از جمله چرخه رانکین آلی پایه، چرخه رانکین آلی با بازیاب و چرخه رانکین آلی با تبادل حرارت داخلی (IHE) بررسی شده است. برای انواع مختلف، عملکرد شش سیال عامل با رفتارهای ترمودینامیکی مختلف (R141b، R124، R236fa، R245fa، R600 و R123) ارزیابی شده است. این نیروگاه‌ها از انرژی آب گرم دیگ بخار چگالشی به عنوان منبع گرمای دما پایین و از انرژی سرد LNG به عنوان چاه حرارتی استفاده می‌کنند. تأثیر تغییرات دمای بویلر بر بازدهی انرژی و اگزرژی مورد بررسی قرار گرفت. بر اساس نتایج استخراج شده، بالاترین بازده انرژی و اگزرژی برای سیستم مبتنی بر چرخه رانکین آلی با بازیاب به دست می‌آید، درحالی‌که سیستم چرخه رانکین آلی ساده و با تبادل حرارت داخلی تقریباً مقادیر مشابهی را نشان می‌دهند. همچنین، در میان این سیال عامل‌های بررسی شده، R141b بالاترین بازده انرژی و اگزرژی را نشان می‌دهد درحالی‌که R124 و R236fa پایین‌ترین عملکرد را نشان می‌دهند.

CONTENTS

Journal Homepage: www.jree.ir